Biochemical, cellular and structural studies on vascular receptors and ligands

Faheem Shaik

Submitted in accordance with the requirements for the

Doctor of Philosophy

Faculty of Biological Sciences

University of Leeds

United Kingdom

January 2020

DEDICATION

This thesis is dedicated to the memory of my beloved mother, Malin Begum.
She was my inspiration to complete this thesis.

ACKNOWLEDGMENTS

Firstly, I would like to thank my supervisor Dr Vas Ponnambalam for giving me an opportunity to undertake a PhD in his group. I thank him for giving me confidence, support, and for being a best supervisor anyone could ask for. His door was always open for both scientific and non-scientific conversations, and made my time in Leeds enjoyable. I would like to express my sincere gratitude to Dr Mike Harrison for his advice and guidance. Special thanks for his patience and continuous source of wisdom. I would also like to thank Dr Stephen Muench for his support and optimism. I must thank everyone at the EM facility for their support, especially Dr Shaun Rawson for helping me acquire my EM data.

I would like to thank Dr Gareth Fearnley and Dr Izma Abdul Zani for passing down their knowledge for me to start in the lab. I would like to thank past and present members of the Ponnambalam lab; Dr Gina Smith, Jonathan De Siqueira, Gary Cuthbert, Joanna Mitchell, Areej Alzahrani, Barney Roper, Dr William Critchley, Sandie Lai, Hala Ahmed and Queen Saikia. It's been great pleasure working with you guys. A special thanks to my squash and gym buddy Dr Andrew Tsatsanis for his constant distraction and support.

It has been great to have met these amazing people: Dr Robert Bedford, Sophie Hesketh, Dr Jack Goode, Fatema Mouswani, Maali Ahmed, Christian Nathan, Conny Leistner, Catherine Hodgson, Philipa Malko, Bolin Wang and Yu Ma. Thank you for making my time at Leeds memorable. Finally, I also thank my father and my brothers for their support and help.

ABSTRACT

Vascular endothelial growth factor receptors (VEGFRs) regulate fundamental cellular responses such as cell proliferation, survival, and migration, and thus play key roles in angiogenesis and vascular physiology in higher eukaryotes such as vertebrates. The intracellular signaling pathways associated with VEGFRs have been well studied and characterised. However, there is a lack of understanding of their mechanism of activation. In this study, mammalian cell lines for tetracycline-inducible expression of VEGFR1, VEGFR2 and VEGFR3 were developed. A strategy was devised for expression, solubilisation and purification of VEGFR2. The first negative stain electron microscopy (neg stain-EM) observation of full-length VEGFR2 produced various negative stain class averages of VEGFR2 dimer bound to VEGF-A ligand. By biochemical and structural means, we also unraveled the process of differential activation of VEGFR2, its modulation on the cell membrane in multiple states against the previously reported ‘one structure’ model.

Also implicated in cardiovascular disease, lectin-like low-density lipoprotein receptor-1 (LOX-1) is a member of the scavenger receptor family that binds to oxidized low-density lipoprotein (OxLDL). It is also proposed to activate downstream signal transduction that causes pro-atherogenic processes such as endothelial dysfunction, foam cell formation and apoptosis. LOX-1 does not recognize the native form of OxLDL, and the mechanism of ligand recognition by LOX-1 is unknown. Moreover, the structural changes brought about by LDL oxidation are also unknown. This study revealed that LOX-1 forms higher order multimers with OxLDL. Using cryo-electron microscopy (cryo-EM), the first 3D *de novo* model of the OxLDL particle was proposed. These studies also investigated the structural differences between native LDL (nLDL) and OxLDL, and identified that oxidation of LDL causes tighter packing of lipids and unravels hithero inaccessible binding domains of ApoB-100 (protein component) of the lipoprotein, which is recognized by LOX-1 receptor. This starts to provide some insight into a crucial event in the progression of atherosclerosis.

TABLE OF CONTENTS

LIST OF TABLES

LIST OF FIGURES

ABBREVIATIONS

Akt	protein kinase B
ALK	anaplastic lymphoma kinase
ApoB-100	apolipoprotein B-100
ATP	adenosine triphosphate
CD-36	cluster of differentiation 36
CTLD	c-type lectin-like domain
DDM	N-dodecyl-β-D-maltoside
DMEM	dulbecco’s modified eagle medium
ECGM	endothelial cell growth medium
EGFR	epidermal growth factor receptor
EM	electron microscopy
ER	endoplasmic reticulum
FGFR	fibroblast growth factor receptor
FRT	flippase recognition target
HDL	high density lipoprotein
HEK 293	human embryonic kidney 293 cells
HIF-1	hypoxia inducible factor-1
HMG-CoA	β-Hydroxy β-methylglutaryl-CoA
HUVEC	human umbilical cord vein endothelial cells
IDL	intermediate density lipoprotein
IGFR	insulin growth factor receptor
JMD	juxta membrane domain
KIT	proto-oncogene c-KIT
LC-MS	liquid chromatography mass spectrometry
LDL/nLDL	native low-density lipoprotein
LDLR	low-density lipoprotein receptor
LOX-1	lectin-like oxidised low-density lipoprotein receptor-1
MAPK	mitogen-activated protein kinase

Neg stain-EM	negative stain electron microscopy
NMR	nuclear magnetic resonance
ORF	open reading frame
OxLDL	oxidised low-density lipoprotein
PBS	phosphate buffer saline
PDGFR	platelet derived growth factor receptor
PI3K	phosphoinositide 3-kinase
PIGF	placental growth factor
PKC	protein kinase C
PLCγ1	phopholipase C gamma 1
PMSF	phenylmethylsulfonyl fluoride
PVDF	polyvinylidene difluoride
RTK	receptor tyrosine kinases
SAXS	small-angle x-ray scattering
SDS-PAGE	sodium dodecyl polyacrylamide gel electrophoresis
SH2	Src homology 2
SMA	styrene-maleic acid
SR-A1	scavenger receptor type-1
SR-A2	scavenger receptor type-2
sVEGFR1	soluble VEGFR1
sVEGFR2	soluble VEGFR2
TRK	tropomyosin receptor kinase
VEGF	vascular endothelial growth factor
VEGFRs	vascular endothelial growth factor receptors
VLDL	very low-density lipoprotein

CHAPTER 1

INTRODUCTION

1. Structure and Function of Membrane Receptors

The membrane that encloses a biological unit such as a cell provides a physical barrier between the cell interior and the extracellular environment. All eukaryotic cells have a similar basic membrane phospholipid bilayer with typically 25 Å thickness, embedded with various proteins that help the cell to carry out its functions. Proteins that are associated with the cell membrane make up about half the biological mass of the membrane (Freedman, 2012). Some proteins are bound peripherally to either side of the membrane, whereas other membrane proteins pass through the membrane bilayer once or more. These integral membrane proteins serve as a connection between the internal and external environments of a cell. Membrane proteins are both structurally and functionally very diverse, and play critical roles in the biology of the cell, from the controlled physical movement of ions and molecules into or out of the cell (transport) to the transmission of information (signal transduction) (Chiu, 2012). Membrane proteins are an important focus of study, as ~70% of current drug targets are membrane proteins (Bakheet and Doig, 2009), and continue to be key targets for new drug development (Overington et al., 2006).

Based on their topology within the lipid bilayer, membrane proteins are mainly classified into two types: membrane-associated peripheral proteins and integral membrane proteins. Peripheral membrane proteins, also known as extrinsic proteins, usually adhere to the membrane bilayer via ionic and hydrophobic interactions with polar headgroups of membrane-associated phospholipids or indirectly by association with integral membrane proteins. Peripheral membrane proteins are present on both the extracellular membrane surface and intracellular cytosolic face (Ariöz, 2014). Examples of intracellular peripheral proteins include actin and spectrin, cytoskeletal proteins primarily involved in shaping the cells, and protein kinase C which plays a crucial role in signal transduction.

Integral membrane proteins, also known as intrinsic proteins, are transmembrane proteins that extend across the bilayer either as single α-helix or multiple α-helices (e.g. G-protein coupled receptors, ligand- or voltage-gated ion channels, transporters: Fig. 1.1). or as barrels of β-sheets (e.g. bacterial porins) The fold of integral membrane proteins is such that they traverse the lipid bilayer, typically with the structure on either side of the membrane exposed to the aqueous phase (Whitelegge, 2013). Integral membrane receptors can be further classified into different types based on their structure and function: ion channels, G-protein-coupled receptors, and enzyme-associated receptors (Fig. 1.1). Ion channels contain multiple transmembrane domains which facilitate passage of ions through the membrane. Channel opening can be in response to ligands such as neurotransmitters ('ligand-gated' channels such as the nicotinic acetylcholine receptor (Miyazawa et al., 1999), or to changes in transmembrane electrical potential ('voltage-gated' ion channels, such as the K_v channels (Grizel et al., 2014). G-protein coupled receptors (GPCRs) are also known as 7 transmembrane domain receptors, since they contain 7 transmembrane α-helices (Shibuya, 2011a). GPCRs are the largest group of integral transmembrane receptors that are activated by ligands such including a wide range of neurotransmitters (including monoamine, catecholamine and peptide), hormones (such as growth hormone, glucagon) or can be light-sensitive (e.g. rhodopsin-like receptors) (von Heijne, 2006, Rosenbaum et al., 2009, Kroeze et al., 2003). Enzyme-linked receptors usually consist of a single transmembrane domain with an enzyme activity embedded within sequences in the cytoplasmic domain. Therefore, membrane receptor now becomes an active enzyme itself. Receptor tyrosine kinases are one such example of membrane receptors with intrinsic enzymatic activity. Other examples include receptor-like tyrosine phosphatases, histidine kinase receptors, histidine kinase-associated receptors and receptor serine/threonine kinases (Waller and Sampson, 2018, Lalan et al., 2011).

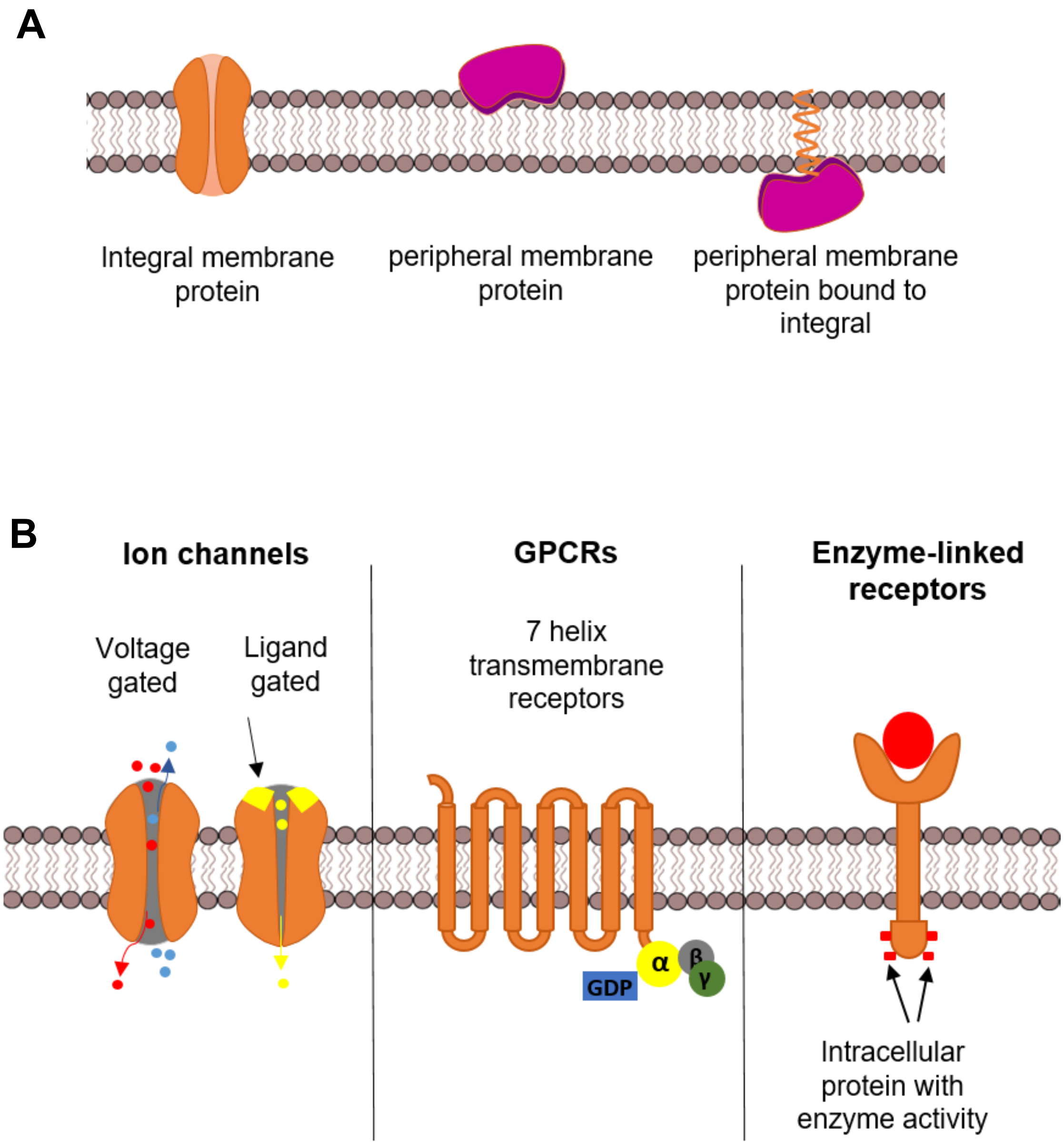

Figure 1.1. Schematic overview of types of membrane proteins. (A) Typical membrane proteins in cell membrane. Membrane bound integral (intrinsic), peripheral (extrinsic), and integral bound peripheral membrane proteins. **(B)** Overview of types of integral membrane proteins based on their function: Ion channels, G-protein coupled receptors (GPCRs) and enzyme-linked receptors (RTKs).

1.1. Receptor Tyrosine Kinases (RTKs)

Receptor tyrosine kinases (RTKs) are transmembrane glycoproteins that possess a cytosolic tyrosine kinase activity and they are key regulators in important cellular responses such as metabolism, survival, migration, proliferation, differentiation, motility and organ development (Ullrich and Schlessinger, 1990). There are 90 human genes that encode proteins with tyrosine kinase activity, amongst these 58 genes encode specific RTKs. These can be divided into 20 RTK subfamilies (Fig. 1.2). RTKs are another major regulatory cell surface signalling entities similar to G-coupled protein receptors. The RTK families include vascular endothelial growth factor receptors (VEGFRs), epidermal growth factor receptors (EGFRs), insulin and insulin-like growth factor receptors (InsR, IGFR), fibroblast growth factor receptors (FGFRs) and platelet-derived growth factor receptors (PDGFRs). RTK signalling has been shown to play crucial roles in cancer development and progression, and are therefore important therapeutic targets (Schlessinger, 2014).

All RTKs have an overall similar architecture with an extracellular ligand-binding domain, a single α-helical transmembrane domain, and a cytoplasmic domain that contains a juxtamembrane region, a tyrosine kinase domain (~300 residues), and a flexible carboxyl-terminal tail (~100-200 residues) (Figure 1.2). The extracellular domains in the different RTKs vary within the sub-families, with different binding motifs that are highly conserved, enabling ligand specificity, recognition and binding. Ligands can bind to RTKs with high specificity, thereby preventing unwanted signalling. Most RTKs are postulated to exist as monomers which form homo- or heterodimers upon ligand binding, leading to conformational changes that lead to activation of the cytoplasmic domain containing tyrosine kinase activity. The studies presented in this thesis will mainly focus on VEGFRs and their ligands.

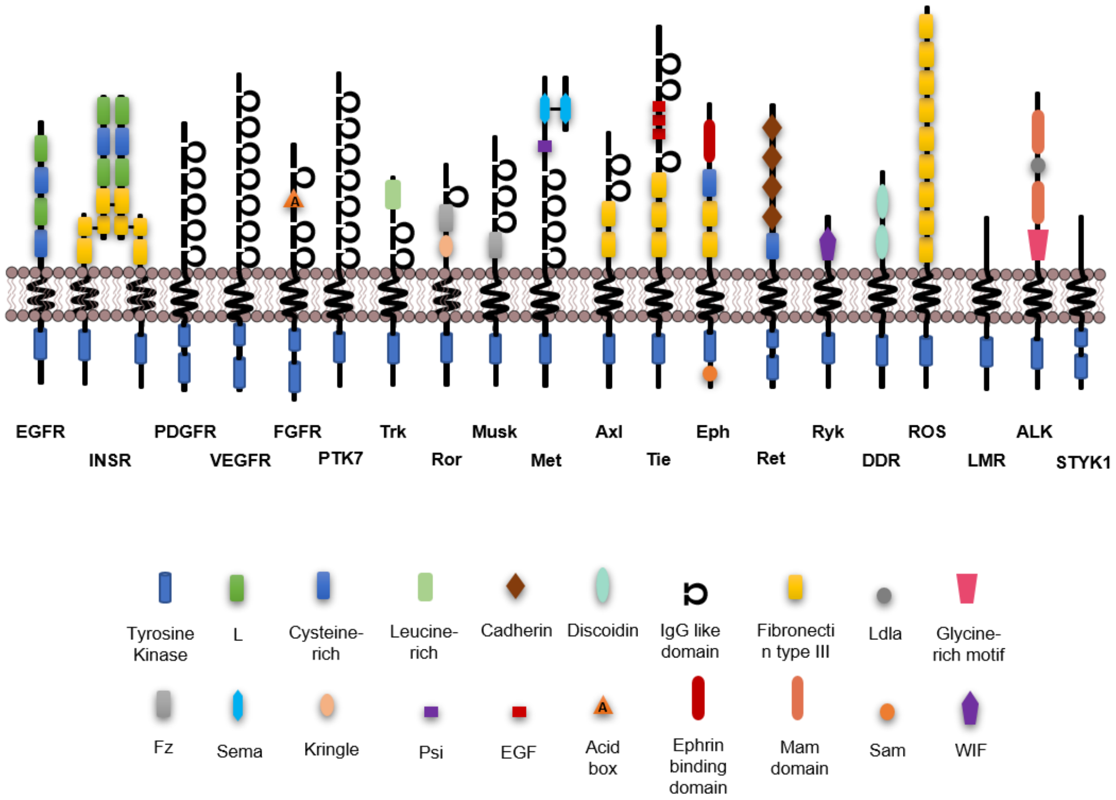

Figure 1.2. Schematic of architecture of receptor tyrosine kinases. All 20 RTK subfamilies comprise an extracellular ligand-binding domain, an α-helical transmembrane domain, juxtamembrane domain, an enzymatic tyrosine kinase domain and a carboxy terminal tail region. The extracellular domains of RTKs display relatively high primary sequence variability compared to other domains. All RTKs are postulated to exist as free monomers except for insulin receptor subfamily which are preassembled multimers.

1.1.1. Vasculogenesis, angiogenesis, and lymphangiogenesis

The *de novo* formation of vascular network during embryonic stage is known as vasculogenesis, whereas angiogenesis describes the sprouting of new blood vessels from pre-existing ones. Both vasculogenesis and angiogenesis are dependent upon the regulation by vascular endothelial growth factors (VEGFs) and their interaction with various membrane receptors expressed on endothelial cells. Physiological vasculogenesis and angiogenesis are essential features in embryogenesis (Fig. 1.3). In adults, angiogenesis is involved in tissue regeneration, vascular remodelling, maintenance and wound healing. However, abnormal angiogenesis is associated with variety of diseases such as tumour neovascularisation, rheumatoid arthritis, diabetic retinopathy and age-related macular degeneration (Overington et al., 2006). The first experimental study that linked tumour progression or dependency on angiogenesis was conducted in the late 1930s (Folkman, 2008, Ribatti, 2008, Pezzella et al., 2015) by isolating rabbit tumour cells and demonstrating that an unknown diffusible substance released from the tumours stimulated the sprouting of new blood vessels. Later studies showed that tumours can continuously derive new capillaries from the host blood vessels (Algire et al., 1945). This established the concept that development of capillary vascular network around the cancer cells is crucial for growth and metastasis. As the cancer cells are either dormant or necrotic in the absence of blood supply, tumour neovascularization triggered by cancer cells stimulates supply of nutrients and enables metastasis (Tammela and Alitalo, 2010, Stacker et al., 2014). Hence by supplying nutrients to cancer cells, tumour angiogenesis is a major contributory factor in growth of various types of cancers.

Lymphangiogenesis on the other hand is the growth and formation of new lymphatic vessels. This regulates immune function, wound healing and fluid homeostasis, whereas the dysfunctional lymph vessels are associated with inadequate immune response and progression of cancer (Tammela and Alitalo, 2010). Similar to angiogenesis, abnormal lymphangiogenesis promoted by VEGFs lead to enlargement and sprouting of new lymphatic vessels in and around the cancer cells which promote the metastatic spread of cancer

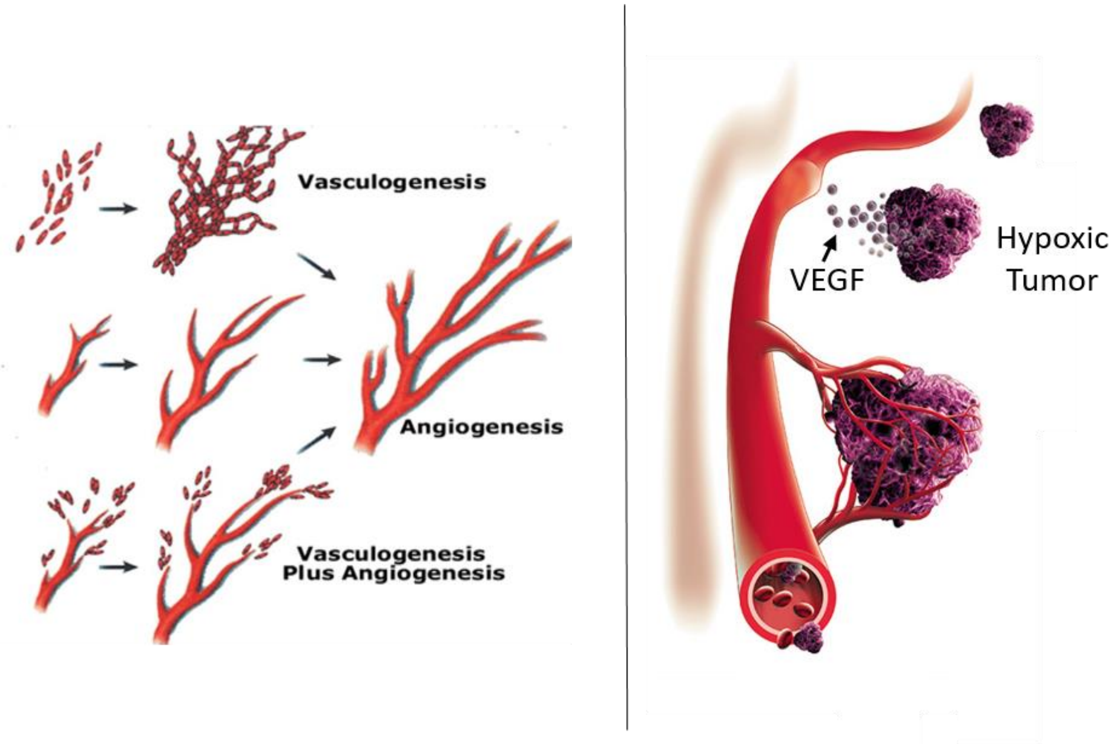

Figure 1.3. Vasculogenesis and angiogenesis in health and cancer. (A) Vasculogenesis requires the aggregation of endothelial progenitor cells (angioblasts) in the developing embryo, whereas angiogenesis requires the sprouting of new blood vessels from pre-existing ones. In normal physiology both vasculogenesis and angiogenesis occur at the same time for neovascularization. Reproduced from (Llevadot and Asahara, 2002) **(B)** Under hypoxic conditions, tumour cells promote stabilisation of hypoxia inducible factor 1a (HIF-1a) which upregulates VEGF-A synthesis. Increased VEGF-A synthesis and secretion enables VEGFR-stimulated signal transduction in nearby endothelial cells and thus tumour angiogenesis. Image reproduced from Llevadot and Asahara, 2002.

(Stacker et al., 2014). Initially it was thought that only blood vessels were directly involved in metastasis of cancer whereas lymphatic vessels are not involved directly but have a passive role. Various clinical and experimental studies have shown that the changes in lymphatic vessels directly promote cancer metastasis but unlike blood vessels they are not involved in primary tumour growth which is promoted by angiogenesis (Matsumoto et al., 2013).

Studying the growth factors and cell surface receptors that regulate the endothelial cell proliferation and migration is important for understanding the biology of angiogenesis and lymphangiogenesis, and to characterise their pathological role in cancer. Understanding the underlying molecular mechanisms of how the endothelial receptors are activated, their structure and regulation of function has huge significance in improving the diagnosis and therapeutic cancer treatment (Sini et al., 2006).

1.1.2. Introduction to vascular endothelial growth factor receptors (VEGFRs) and their ligands (VEGFs)

The VEGF family has multiple isoforms encoded by each VEGF-related gene, and there are differences in biological activity within closely related VEGF variants (Whitelegge, 2013). VEGF ligands bind to VEGFRs which belong to type IV receptor tyrosine kinase family, there are three VEGFRs, VEGFR1 (historically known as Flt1), VEGFR2 (KDR, Flk1) and VEGFR3 (Flt4) (Whitelegge, 2013). Similar to all RTKs, VEGFRs possess a cytoplasmic tyrosine kinase activity which regulate the signal transduction for pathways that are linked to proliferation, migration and metabolism of especially endothelial cells, thereby lead to vasodilation, blood vessel formation and remodelling (Whitelegge, 2013, Lemmon and Schlessinger, 2010, Ferrara et al., 2003)**.** Both VEGFR1 and VEGFR2 are involved in regulation of angiogenesis whereas VEGFR3 is majorly involved in lymphangiogenesis (Matsumoto et al., 2013, Sini et al., 2006). VEGF genes encode seven growth factors namely VEGF-A, VEGF-B, VEGF-C. VEGF-D, VEGF-E, VEGF-F and placental growth factor (PIGF) (Banai et al., 1994, Otrock et al., 2007). VEGF-A, VEGF-B, VEGF-C, VEGF-D, and PIGF are found in most metazoan species, whereas VEGF-E is encoded by parapoxvirus and VEGF-E is found in snake venom (Abraham et al., 2000, Ebos et al., 2004). VEGFs are also known to interact with some non-RTKs such as heparin sulphate proteoglycans (HSPGs), neuropilin-1 (NRP1) and neuropilin-2 (NRP2) (Cebe-Suarez et al., 2006, Baldwin et al., 2004, Whitelegge, 2013, Fong et al., 1995). All VEGFs are homodimers stabilised by two disulphide bridges between each monomer (Fig. 1.4).

1.1.2.1. VEGF-A

VEGF-A is also known as vascular permeability factor (VPF). It is usually a homodimer formed by the arrangement of two anti-parallel VEGF-A monomers with a receptor binding site at each pole (Olsson et al., 2006). VEGF-A specifically binds to VEGFR1 and VEGFR2 expressed on endothelial cells, and can also bind NRP1 and NRP2 co-receptors expressed on the vascular endothelium and neurons (Hoeben et al., 2004). The pattern of VEGF-A expression is dependent of the *VEGF-A* gene which encodes at least 8 exons. Alternative splicing of the primary RNA transcript can generate at least 9 VEGF-A splice isoforms such as VEGF-A$_{121}$, VEGF-A$_{145}$, VEGF-A$_{148}$, VEGF-A$_{162}$, VEGF-A$_{165}$, VEGF-A$_{165b}$, VEGF-A$_{183}$, VEGF-A$_{189}$ and VEGF-A$_{206}$ (Fig. 1.4E) The expression of VEGF-A is known to be upregulated by hypoxia, p53 gene mutations, thyroid stimulating hormone and nitric oxide (NO). The *VEGF-A* promoter is dependent on activation by the hypoxia inducible factor-1 (HIF-1) which is composed of α and b subunits (Banai et al., 1994, Takahashi and Shibuya, 2005). All the VEGF-A splice isoforms stimulate VEGFR tyrosine kinase activity except for VEGF$_{165b}$, which has been was proposed to negatively regulate VEGFR activity (Takahashi and Shibuya, 2005). VEGF-A is the most potent pro-angiogenic growth factor compared to other VEGFs and the deletion of the *VEGFA* gene in mice shows embryonic lethality even with the loss of only a single allele (Carmeliet et al., 1996).

1.1.2.2. VEGF-B

VEGF-B is encoded by the *VEGFB* locus and consists of eight exons and six introns. Alternative splicing of the VEGF-B primary RNA transcript generates two splice isoforms, VEGF-B_{167} and VEGF-B_{186} (Fig. 1.4F). These VEGF-B isoforms only bind to VEGFR1, but not VEGFR2 or VEGFR3. Upon VEGF-B binding and activation of VEGFR1, it induces poor signalling and found to have negligible effect in inducing blood vessel growth (Otrock et al., 2007, Grunewald et al., 2010). The role of VEGF-B is still unclear, but mice lacking a functional *VEGFB* locus have smaller hearts, impaired angiogenic response and decreased capillary density (Abraham et al., 2000). However, VEGF-B is essential for blood vessel survival (Li et al., 2009).

1.1.2.3. VEGF-C and VEGF-D

There are no known isoforms for VEGF-C and VEGF-D, and both growth factors are identical at N and C terminals; a feature which is not present in other VEGFs. They are cleaved by the furin protease via a two-step process (Shibuya, 2011a, Takahashi and Shibuya, 2005). An initial proteolysis step produces premature variants which bind and activate both VEGFR2 and VEGFR3. However, these VEGFs have higher affinity towards VEGFR3 and very low affinity for VEGFR2. A second proteolysis step produces the mature VEGF forms that have high affinity for both VEGFR2 and VEGFR3 (Stuttfeld and Ballmer-Hofer, 2009). VEGF-C is essential for the sprouting of lymphatic vessels from embryonic vein, thereby crucial in lymphangiogenesis. However, it is also involved in promoting lymphangiogenesis in various types of cancers (Ikeda et al., 2014). In VEGF-C knockout mice, embryo lymphatic lineage was observed but development of lymphatic vessels were not seen, with embryonic lethality at a late stage due to lack of lymphatic vessels (Karkkainen et al., 2004).

Similarly, mature VEGF-D binds to both VEGFR2 and VEGFR3, therefore promotes both angiogenesis and lymphangiogenesis. Expression of VEGF-D by cancer cells is known to promote metastasis (Stacker et al., 2001). There are no known isoforms for VEGF-D, it is present in most tissues but more adequately in skin and lungs. Interestingly, out of all the VEGFs expressed in humans, VEGF-D is the only growth factor that is dispensable, as VEGF-D knockout mice were healthy, fertile with normal body mass and no abnormalities in lymphatic vessel development or function were observed (Baldwin et al., 2005).

1.1.2.4. PIGF

Placental growth factor (PIGF) is predominantly expressed in placenta. The human *PIGF* gene has 7 exons, with alternative RNA splicing producing four isoforms such as PIGF-1 ($PIGF_{131}$), PIGF-2 ($PIGF_{152}$), PIGF-3 ($PIGF_{203}$) and PIGF-4 ($PIGF_{224}$) (Fig. 1.4F). All isoforms of PIGF recognize and bind to VEGFR1, but not VEGFR2 and VEGFR3 (Autiero et al., 2003, Otrock et al., 2007). Deletion of *PIGF* impairs angiogenesis, inflammation and wound healing (Carmeliet et al., 2001, Autiero et al., 2003). However, PlGF upregulation is associated with pathological angiogenesis (Odorisio et al., 2002).

1.1.2.5. VEGF-E

The *VEGFE* gene is absent from animal species but is found in parapoxvirus which infects sheep but rarely infects humans. *VEGFE* encodes four splice isoforms VEGF-E_{NZ-2}, VEGF-E_{NZ-7}, VEGF-$E_{NZ-10,}$ and VEGF-E_{D1701}, which all only bind to VEGFR2 and act as pro-angiogenic factors by promoting pathological angiogenesis in sub-cutaneous lesions infected by the virus (Kiba et al., 2003). Even though VEGF-E selectively binds to VEGFR2, the amino acid sequence of VEGF-E is less than 25% identical to VEGF-A (Cebe-Suarez et al., 2008). Unlike VEGF-A, all isoforms of VEGF-E selectively bind to VEGFR2 but not VEGFR1. Thus, VEGF-E isoforms have the potential to be candidates for selectively targeting VEGFR2-specific responses towards pro-angiogenic therapy.

1.1.2.6. VEGF-F

VEGF-F is found in *Trimereserus flavoviridis* snake venom but not expressed in humans. VEGF-F has no isoforms and selectively binds to VEGFR2, which leads to vascular permeability but very weak cell proliferation. The sequence of VEGF-F is ~50% identical to that of VEGF-A (Shibuya, 2011a). VEGF-F is however more

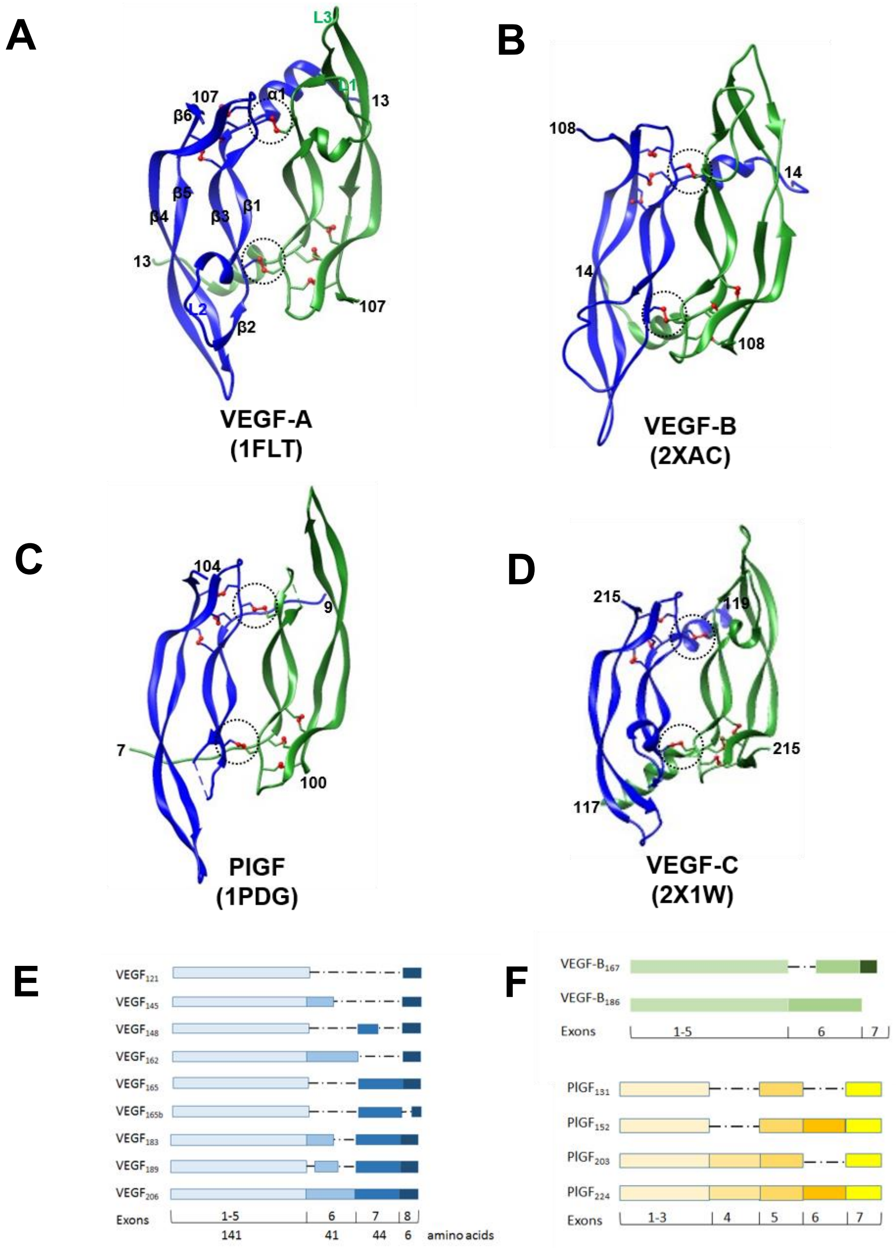

Figure 1.4. Structures of VEGF ligands and splice variants. Homodimer structures of **(A)** VEGF-A (PDB ID:1FLT), L1, L2 ans L3 are the loops involved in binding contacts with VEGFRs, **(B)** VEGF-B (PDB ID: 2XAC), **(C)** PIGF (PDB ID: 1PDG) and **(D)** VEGF-C (PDB ID: 1PDG). Each VEGF has one α-helix and 7 β-sheets. The homodimeric complex is stabilised by two disulphide bridges between two monomers (red ball and stick represented in circles). **(E)** Alternative splicing of *VEGFA* primary RNA transcript can produce at least 9 isoforms if VEGF-A. **(F)** VEGF-B can exist as two isoforms and PlGF can exist as four isoforms.

potent than VEGF-A, with both *in vivo* and *in vitro* studies having shown that the heparin-binding domain at the C-terminus of VEGF-F competitively inhibits VEGF-A binding to VEGFR2 (Takahashi et al., 2004).

1.1.2.7. VEGFR1

The first identification of a VEGF-specific receptor was VEGFR1 (fms-like tyrosine kinase, Flt1). Human VEGFR1 contains 1312 amino acids (Table 1.1), is glycosylated, and the mature VEGFR1 protein is ~180 kDa in size. This protein is relatively widely expressed in the endothelium, epithelial tissues, immune and nervous systems and is present on tumour cells (de Vries et al., 1992). VEGFR1 expression is upregulated by hypoxia involving the HIF-1 complex (Ramakrishnan et al., 2014). The *VEGFR1* promoter also contains a hypoxia-responsive element (HRE) sequence which enables HIF-1α binding and control of *VEGFR1* gene expression (Gerber et al., 1997). VEGFR1 binds all isoforms of VEGF-A, VEGF-B, and PlGF with ~10-20 picomolar affinity (K_d) (Fig. 1.5). VEGFR1 knockout mice exhibit embryonic lethality and die in mid-gestation due to abnormal blood vessel formation and excessive endothelial cell proliferation (Baldwin et al., 2004, Fong et al., 1995). Interestingly, VEGFR1 kinase domain-defective mice showed normal development and angiogenesis with no vascular defects (Hiratsuka et al., 1998). There is an alternative soluble form (soluble VEGFR1, sFlt1) of VEGFR1, a splice variant which acts as an inhibitor for VEGFR activity (Ferrara et al., 2003). The soluble splice variant acts as a decoy receptor and a negative regulator for VEGFR2 by binding to VEGF-A, thereby decreasing local concentrations of growth factor and limiting VEGF-A binding to VEGFR2 (Takahashi and Shibuya, 2005). Soluble VEGFR1 is also involved in maintaining the photoreceptor avascular area in the eye, further discussed in section 1.1.6.2.

1.1.2.8. VEGFR2

Human VEGFR2 (KDR/Flk-1) contains 1337 amino acids (Table. 1.1) and the molecular mass of immature non-glycosylated VEGFR2 is ~160 kDa. Mature VEGFR2 is 200-230 kDa, heavily glycosylated and largely expressed in vascular and lymphatic endothelial cells. VEGFR2 binds to all isoforms of VEGF-A, VEGF-

C, VEGF-D, and VEGF-E with relative high binding affinity (Fig. 1.5). VEGFR2 affinity towards VEGF-A is ~75-125 pM which is much higher compared to other VEGFs it binds to. However, VEGFR2 has 5-10-fold lower affinity for VEGF-A when compared to VEGFR1. VEGFR2 is considered as the predominant mediator of physiological and pathological angiogenesis as it mediates the angiogenic and vascular-permeability enhancing effects of VEGF-A (Ferrara et al., 2003). VEGFR2 knockout mice die mid-gestation with no organised blood vessels observed in the embryo which are normally seen at mid-gestation period. This unlike VEGFR1 KO mice, where an abnormal vascular network development was observed (Shalaby et al., 1995, Fong et al., 1995).

A soluble form of VEGFR2 (sVEGFR2) has been identified in mouse and human plasma (Ebos et al., 2004). The distinct function of sVEGFR2 is still unclear, although recent studies suggest a connection between breast cancer and sVEGFR2 levels; higher levels of sVEGFR2 in plasma could increase the breast cancer risk (Harris et al., 2016).

1.1.2.9. VEGFR3

Mature VEGFR3 (FLT-4) is ~195 kDa in size and has very high affinity towards VEGF-C and VEGF-D (Fig. 1.5). VEGFR3 contains 1339 amino acids but undergoes cleavage with Ig-like domain D5 in the ER into 2 chains which are subsequently re-attached by a single disulphide bond. Unlike VEGFR1 and VEGFR2, VEGFR3 is predominantly involved in lymphangiogenesis and not known to play significant role in angiogenesis. Mouse deficient for VEGFR3 resulted in defective blood vessel formation in mouse embryos. Even though vasculogenesis and angiogenesis were observed in VEGFR3 KO mice, vessels were abnormally organised with defective lumen which resulted in cardiovascular failure of the embryo (Dumont et al., 1998). Similar to VEGFR1 and VEGFR2, VEGFR3 exists in a soluble variant (Harris et al., 2016). sVEGFR3 is known to be expressed in corneal endothelial cells; the truncated VEGFR3 (sVEGFR3) in cornea has anti-lymphangiogenic properties and binds both VEGF-C and VEGF-D therefore could act as a decoy receptor for both ligands. This could block the

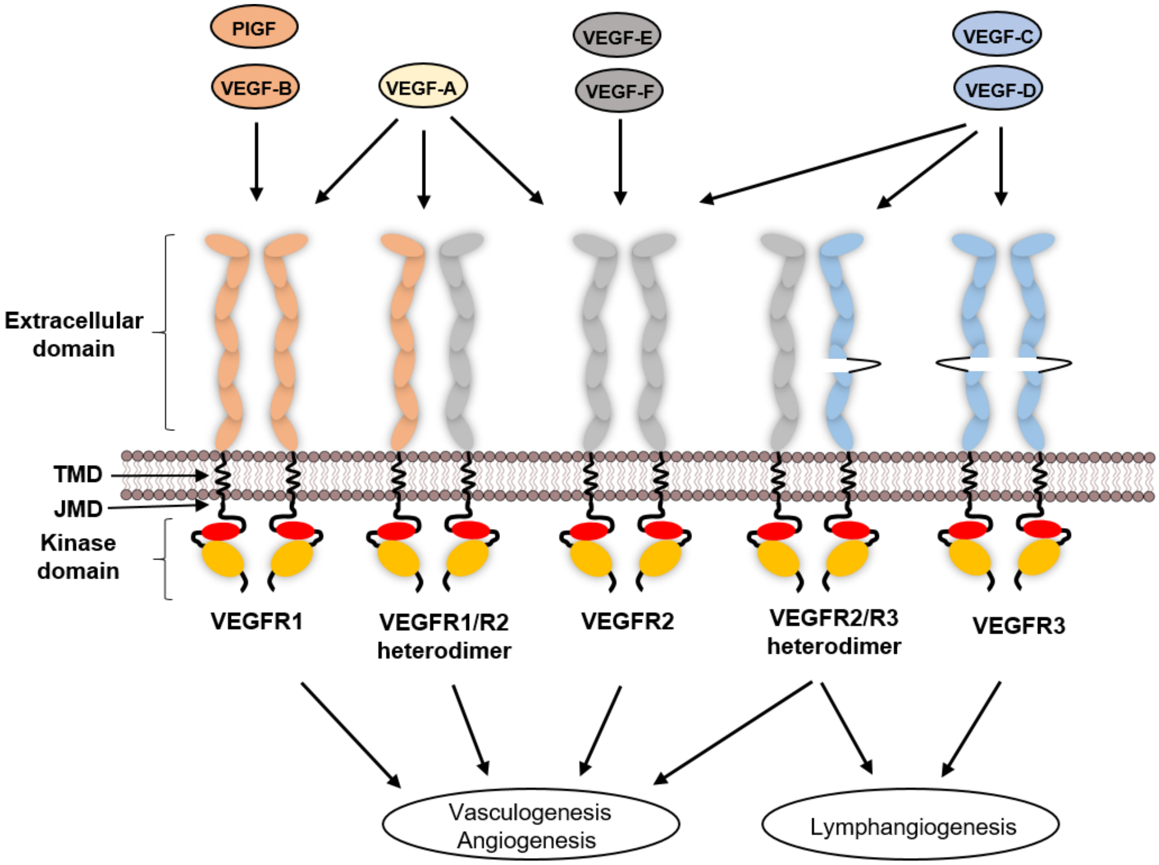

Figure 1.5. Schematic representation of VEGFR membrane protein structure and ligand-binding specificity. VEGFR1 and specific ligands (orange), VEGFR2 and specific ligands (grey), and VEGFR3 and specific ligands (green). Ligands shown in other colours bind to more than one VEGFR. In VEGFR3, the 5th extracellular Ig-like domain is cleaved and attached to the rest of the chain with a disulphide bond. VEGFR1 and VEGFR2 can form heterodimers, whereas VEGFR3 can form heterodimers with VEGFR2. VEGFR1 and VEGFR2 play a major role in angiogenesis, whereas VEGFR3 is mainly involved in lymphangiogenesis

lymphangiogenesis promoted by VEGFR3 signal transduction (Singh et al., 2013). sVEGFR3 is also involved in supressing allosensitization and promoting survival of corneal allografts (Emami-Naeini et al., 2014).

1.1.3. Structural features of VEGFR domains

1.1.3.1. VEGFR extracellular domains

VEGFRs that are inactive are thought to be in a monomeric state. However, using ligand binding studies (Emami-Naeini et al., 2014) and mathematical modelling, Harris et al. (Harris et al., 2016) postulated the presence of both free monomers and non-activated or resting dimers. Conventionally, VEGF binding to VEGFR extracellular domain is postulated to trigger dimer formation, tyrosine kinase activation and downstream signalling, similar to other RTKs (Whitelegge, 2013). The extracellular domain of VEGFRs are similar with seven Ig-like domains which are primarily involved in ligand binding, except in VEGFR3, where domain D5 is cleaved and reattached via a disulphide bridge (Fig. 1.5). Ligand interaction with VEGFR extracellular domains and their dimerisation has been extensively studied using various structural methods. Crystal structures of various Ig domains of soluble VEGFRs with or without bound VEGF have been solved (Table. 1.2). Ballmer-Hofer and colleagues have recently produced a high-resolution structure of soluble VEGFR1 bound to VEGF-A: this structure now reveals how ligand-induced dimerisation in VEGFR1 mediated by domains D1 and D2 leads to homotypic interactions between D4, D5, and D7 (Emami-Naeini et al., 2014). In case of both VEGFR1 and VEGFR2, domains D2 and D3 are crucial in ligand recognition and binding, which enables the transmission of conformational changes towards the cytoplasmic domain which activate the tyrosine kinase (Ruch et al., 2007b, Emami-Naeini et al., 2014). Binding of VEGFR3 to VEGF ligand is similar with binding sites involving contacts with residues lying between D1 to D3; furthermore, structural rearrangements and contacts between D4 and D7 domains of dimers are crucial for VEGFR3 tyrosine kinase activation (Leppanen et al., 2013).

1.1.3.2. VEGFR transmembrane domains

The transmembrane domain of VEGFRs is α-helical and hydrophobic in nature, consisting of 21 residues for VEGFR1 and 22 residues for both VEGFR2 and VEGFR3. These α-helices pass through the lipid bilayer and VEGFR activation is postulated to be dependent upon the orientation of transmembrane α-helices, which also influences the stability of VEGFR complex (Singh et al., 2013). Ballmer-Hofer and colleagues demonstrated an increase in VEGFR2 tyrosine kinase activity caused by mutations of two amino acids (G770E and F777E) in transmembrane domain; using NMR they detected ~180° rotation (i.e helix spin around its own axis) of the mutant VEGFR2 transmembrane domain compared to inactive wild-type (Karkkainen et al., 2004, Singh et al., 2013). Such evidence further supports the view that the orientation and conformational changes in the extracellular Ig-like domains triggered by VEGF binding causes substantial rotational changes in transmembrane domain which further influences the rearrangement of cytoplasmic domains relative to each other within an active receptor dimer. In other words, the growth factor binding signal is transmitted from outside to inside via conformational changes that involve changes in position of the TM helices.

1.1.3.3. VEGFR cytoplasmic domains

The cytoplasmic domain of each VEGFR has a juxtamembrane domain (JMD), followed by a split tyrosine kinase domain (~300-330 residues) followed by a flexible C-terminal tail or carboxy terminus (Hubbard, 1999, Stuttfeld and Ballmer-Hofer, 2009). The JMD is present immediately after the transmembrane domain and although its function is unclear, it is implicated in activation and inhibition of tyrosine kinase activity (Gille et al., 2000), replacing the JMD of VEGFR1 with JMD of VEGFR2 caused significant increase in VEGFR1 tyrosine kinase activity. This further demonstrated the difference in role of JMD in tyrosine kinase activation of each RTK (Baldwin et al., 2005).

The tyrosine kinase domain of VEGFRs consists of approximately 300-330 residues with a typical ‘split’ configuration into N- lobe, and C-lobe, similar to most

RTKs. Crystal structures of tyrosine kinase of VEGFR2 with various tyrosine kinase inhibitors (TKIs) has been resolved by various groups (Table. 1.2). The resolved kinase structures of VEGFR2 showed ATP binding core within the juncture of N- and C- lobes which is in common with other RTKs (Fig. 1.6A) (Felmeden et al., 2003, Chen et al., 2002). The N- lobe mainly consists of an α-helix (αC), five anti-parallel β-sheets (β1-β5), and a glycine-rich region (841-846) with a hydrophobic residue (F845) close to ATP-binding pocket. The C-lobe is larger in comparison to N-lobe and it consists of seven α- helices (αD-αI and αEF), four β-sheets (β6-β9), a catalytic loop and an activation region. The catalytic loop contains a conserved HRP motif (residues 1026-1028), whereas the activation loop starts with conserved DFG motif (residues 1046-1048) and ends with APE motif (residues 1073-1075). For most protein kinases, the DFG and APE motifs in the activation loop regulates protein kinase activity. VEGFR2 also contains a key signature KEDD (K868-E885-D1028-D1046) residues which regulate the tyrosine kinase activation and inhibitor binding (Boocock, 1990) (Fig. 1.6A and 1.6B). There is very limited information on how the kinase is activated in VEGFR1 and VEGFR3 as the kinase structures are not yet resolved. There are various tyrosine specific-phosphorylation sites spread throughout the cytoplasmic domain which regulate different downstream signalling activities.

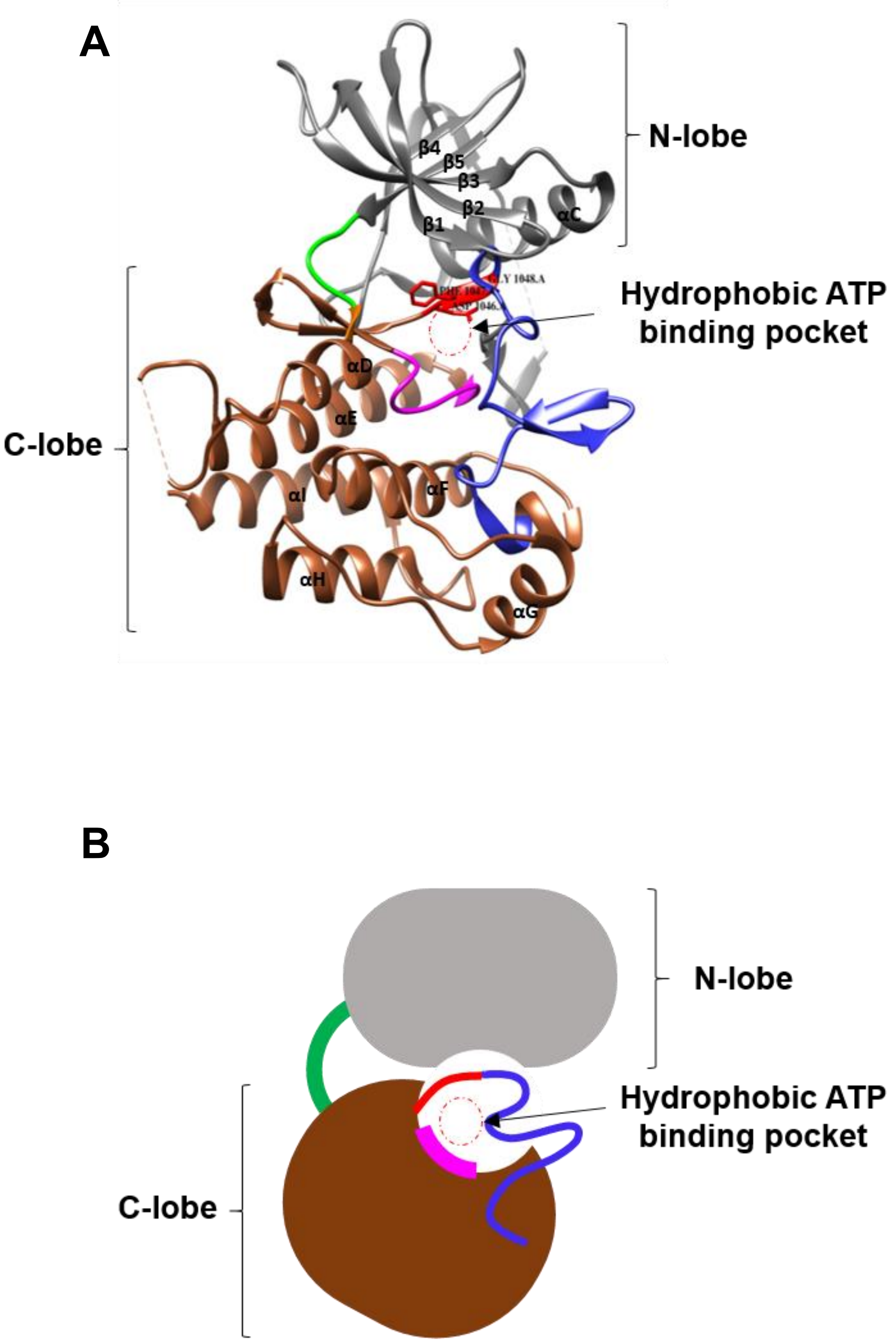

Figure 1.6. Representation of VEGFR2 kinase domain. (A) Crystal structure of VEGFR2 kinase, N lobe is shown in grey, C-lobe in brown, the hinge region which connects the N and C lobes is shown in green, catalytic loop in magneta and the activation loop in blue with conserved DFG motif of activation segment in red. Both α-helices and β-sheets are labelled from αC-αI and β1-β5 respectively. (PDB code : 4AGD). **(B)** Schematic representation of inactive VEGFR2 kinase showing hinge region (green), catalytic loop (magneta), activation loop (blue) and ATP binding domain.

Table 1.1. Peptide length homology information of different domains of VEGFRs. (source: uniprot)

Details	VEGFR1	VEGFR2	VEGFR3
Swiss UniProt ID	P17948	P35968	P35916
Full length	1338	1356	1363
Signal peptide	26 (1-26)	19 (1-19)	24 (1-24)
Receptor chain	1312 (27-1338)	1337 (20-1356)	1339 (25-1363)
Extracellular domain	732 (27-758)	745 (20-764)	751 (25-775)
Ig1	92 (32-123)	65 (46-110)	98 (30-127)
Ig2	64 (151-214)	67 (141-207)	63 (151-213)
Ig3	98 (230-327)	97 (224-320)	108 (219-326)
Ig4	87 (335-421)	87 (328-414)	85 (331-415)
Ig5	126 (428-553)	128 (421-548)	131 (422-552)
Ig6	99 (556-654)	110 (551-660)	117 (555-671)
Ig7	87 (661-747)	87 (667-753)	87 (678-764)
Transmembrane domain	22 (759-780)	21 (765-785)	21 (776-796)
Cytoplasmic domain	558 (781-1338)	571 (786-1356)	567 (797-1363)

Table 1.2. Relevant details for high-resolution VEGFR/VEGF complex structures available on Protein Database (PDB).

Complex	PDB Code	Resolution (Å)	Domains	Method	Reference
VEGFR1/VEGF-A	1FLT	1.7	Domain 2	X-ray diffraction	(Wiesmann et al., 1997)
VEGFR1/VEGF-A	1QTY	2.7	Domain 2	X-ray diffraction	(Park et al., 2012)
VEGFR1/PIGF	1RV6	2.45	Domain 2	X-ray diffraction	(Christinger et al., 2004)
VEGFR1/VEGF-B	2XAC	2.71	Domain 2	X-ray diffraction	(Iyer et al., 2010)
VEGFR1/VEGF-A	5T89	4	Domain 1-6	X-ray diffraction	(Markovic-Mueller et
VEGFR2	3KVQ	2.7	Domain 7	X-ray diffraction	(Yang et al., 2010b)
VEGFR2/VEGF-A	3V2A	3.2	Domains 2 & 3	X-ray diffraction	(Brozzo et al., 2012)
VEGFR2/VEGF-C	2X1W	2.7	Domains 2 & 3	X-ray diffraction	(Leppanen et al., 2010)
VEGFR2/VEGF-C	2X1X	3.1	Domains 2 & 3 in tetragonal	X-ray diffraction	(Leppanen et al., 2010)
VEGFR2 Kinase Domain	1VR2	2.4	Kinase Domain	X-ray diffraction	(McTigue et al., 1999)
VEGFR2/VEGF-E	3V6B	3.2	Domains 2 & 3	X-ray diffraction	(Brozzo et al., 2012)
VEGFR2 mutant dimeric	2MEU	-	Transmembrane domain	NMR	(Karkkainen et al., 2004)
VEGFR2 dimeric	2M59	-	Transmembrane domain	NMR	(Karkkainen et al., 2004)
VEGFR3/VEGF-C	4BSK	4.2	Domains 1 & 2	X-ray diffraction	(Leppanen et al., 2013)
VEGFR3 ECD	4BSJ	2.5	Domains 4 & 5	X-ray diffraction	(Leppanen et al., 2013)

1.1.4. Mechanism of activation of VEGFRs

Many structural studies have been performed on VEGFRs, including using x-ray crystallography, NMR and single-particle electron microscopy (Table. 1.2). However, no full-length structure is determined. Therefore, using the structural information of ECD and kinase domains, it was postulated how ligand binding to extracellular Ig domains and the conformational changes in the extracellular domain leads to catalytic activation and phosphorylation of tyrosine residues. All individual Ig domain structures determined by x-ray crystallography show interaction between a dimeric ligand and receptor interactions to form 1:1 complex at domains 2 and 3 (Fig. 1.7A), and the recently reported VEGFR-1/VEGF-A ECD structure revealed the interaction of three loops of VEGF-A (L1, L2 and L3) (Fig. 1.4A) to D2 and D3 domains VEGFR-1, it also revealed that homotypic receptor-receptor interactions between domains D4, D5 and D7 are essential to carry the signal downstream (Imoukhuede and Popel, 2012). In VEGFR2, Ballmer-Hofer and colleagues were successful in inhibiting ligand binding, receptor dimerization, and finally kinase activation by isolating designed ankyrin repeat proteins (DARPins) that interact with D2 and D3 (Hyde et al., 2012a). These DARPins specific for VEGFR2 D4 and D7 domains were able to block tyrosine kinase activation and RTK signalling but did not prevent ligand binding and RTK dimerisation (Jopling et al., 2014). Ligand-induced dimerisation and torsional changes in the extracellular domain bring the kinase domain into active orientation through allosteric effects, with both N and C lobes opening with respect to each other and giving ATP access to the cleft located between the N- and C-lobes. In the cleft, the adenine ring of ATP form hydrogen bonds with hinge region of the tyrosine kinase; the ribose and triphosphate moieties form hydrogen bonds with the conserved DFG and APE motifs essential for regulating kinase activity. The activation loop also plays a crucial role in unblocking the substrate-binding site, thereby leads to active conformation of kinase and phosphorylation of tyrosine residues (Mittar et al., 2009). This demonstrates the specific role of each domain, their importance, and how they are interconnected to finally activate the enzyme activity of the RTK.

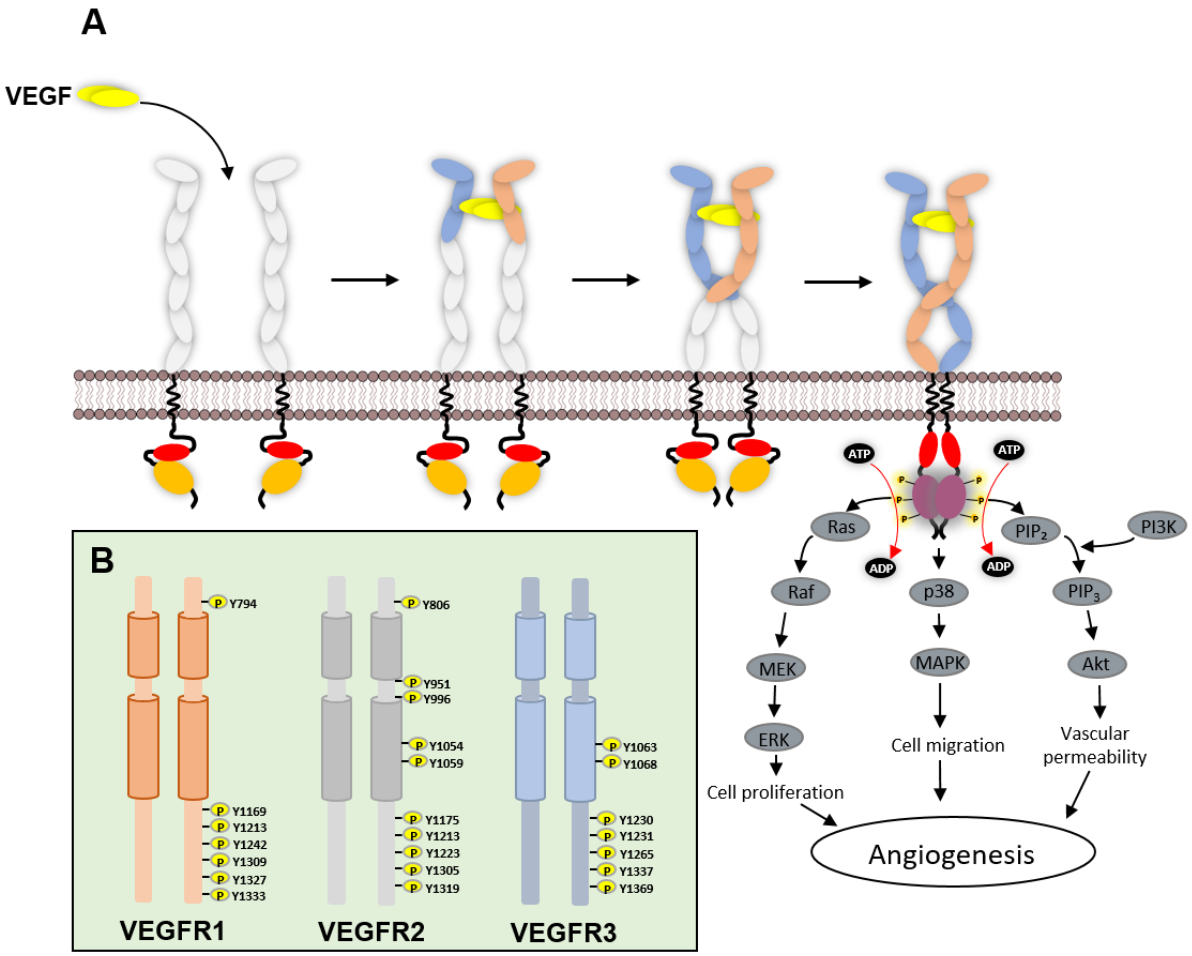

Figure 1.7. Generic representation of VEGFR signal transduction. (A) Schematic representation of mechanism of VEGFR activation and downstream signalling pathways. A covalently linked VEGF dimer (yellow) binds to second and third extracellular IgG like domains of VEGFR that leads to dimerisation of receptors with homophilic contacts between IgG-like domains 5 and 7. The complex is also stabilised with additional contacts at transmembrane and juxtamembrane regions that leads to phosphorylation of various tyrosine kinase residues which trigger downstream pathways such as Ras-Raf-MEK-Erk pathway, p38-MAPK pathway and PI3K-Akt pathway**. (B)** Various tyrosine residues that undergo phosphorylation in each VEGFR.

1.1.5. Phosphorylation and signal transduction by activated VEGFRs

The activated VEGFRs recruit and phosphorylate adaptors and enzymes that regulate a wide variety of cellular and biological responses in different cells and tissues. Similar to all other RTKs, VEGFRs have tyrosine autophosphorylation sites that act as recognition motifs for signalling mediator proteins, and hence are important for downstream signalling. Even though VEGFR1 is postulated as a negative regulator of VEGF-A mediated signal transduction, it undergoes phosphorylation at specific tyrosine sites (Y794, Y1169, Y1213, Y1242, Y1309, Y1327 and Y1333) that allows binding of adaptor proteins (such as SH2 domain proteins) and phospholipase PLCγ1 (Fig. 1.7B) (Sawano et al., 1997, Igarashi et al., 1998a, Igarashi et al., 1998b, Hainfeld et al., 1999). Recruitment of phospholipase PLCγ1 to the plasma membrane triggers PIP_2 hydrolysis to IP_3 (causing cytosolic calcium ion flux) and DAG (which activates protein kinase C, PKC). These tyrosine phosphorylation sites are present within different regions of the cytoplasmic domain of VEGFR1.

VEGFR2 is major RTK which is involved in promoting VEGF-A regulated angiogenesis. Activated VEGFR2 exhibits tyrosine phosphorylation at Y801, Y951, Y996, Y1054, Y1059, Y1175, Y1214, Y1223, Y1305, Y1309 and Y1319 (Fig. 1.7B). The VEGFR2-Y801 phosphorylation site is present in the JMD, and other phospho-epitopes such as Y951, Y996, Y1054 and Y1059 are located within the kinase domain, whereas the remaining phosphotyrosine sites lie within the ~200 residue C-terminal flexible tail region. Phosphorylation of VEGFR2-Y801 within the JMD is postulated to be an initial step in tyrosine kinase activation (Hainfeld et al., 1999). Furthermore, generation of the VEGFR2-pY801 epitope is linked to phosphatidylinositol 3-kinase (PI3K) and protein kinase B (PI3K/Akt) signalling, and downstream activation of endothelial nitric oxide synthase (eNOS) (Blanes et al., 2007). The appearance of the VEGFR2-pY1059 epitope is linked to cytosolic Ca^{2+} ion rise, MAPK activation and endothelial cell proliferation, whereas the appearance of the VEGFR2-pY951 epitope is linked to endothelial cell migration (Zeng et al., 2001). The appearance of the VEGFR2-pY1175 epitope within the C-terminal tail is a key signature of VEGF-A binding to

VEGFR2, and this epitope directly enables the recruitment of PLCγ1 via SH2-domain-mediated recognition. Recruitment of PLCγ1 to the plasma membrane leads to PIP_2 hydrolysis, and one consequence is activation of the MAPK pathway linked to cell proliferation (Sase et al., 2009a).

VEGFR3 plays a major role in lymphangiogenesis. Activation of VEGFR3 leads to phosphorylation on residues Y1063, Y1068, Y1230, Y1231, Y1265, Y1337 and Y1363 (Fig. 1.7B). Phosphorylation sites Y1063 and Y1068 are located within the tyrosine kinase domain whereas the remaining phosphotyrosine residues are present within the flexible C-terminal tail region. Similar to VEGFR1 and VEGFR2, activation and tyrosine phosphorylation of VEGFR3 can activate PI3K/Akt, PKC and MAPK signal transduction pathways (Olsson et al., 2006).

1.1.6. VEGFRs and ligand are linked to disease states

Expression of VEGFRs and their ligands are linked to various types of disease states, primarily cancer, some forms of blindness and inflammatory conditions; increasingly, such links are also evident in neurodegenerative pathologies. As VEGFRs are also associated with neuronal development, especially VEGFR1 and VEGFR2, which play a divergent role in embryonic neurogenesis

1.1.6.1. Involvement of VEGF signalling in cancer

In healthy humans, VEGF-related ligands are primarily involved in physiological angiogenesis: a hypoxic environment can trigger the expression of VEGF-A and specific VEGFRs. This promotes the ‘angiogenic switch’ which results in endothelial cell proliferation and migration to form new blood vessels, which creates a microenvironment around tumours and cause them to grow exponentially beyond their minimal size.

Blood vessels promoted by tumour cells have a distinct morphological feature and abnormal pattern when compared to normal blood vessels (Viallard and Larrivée, 2017). They don’t contain vascular smooth muscle cells (VSMCs) and reported to have a disorganised and immature vascular network with dilated lumen, high permeability and excess hypoxia. This is caused by abnormal levels of VEGF-A

Table 1.3. List specific VEGFRs involved various cancer types and their progression.

Cancer type	Receptor	Other RTKs	Reference
Non-small cell lung cancer (NSCLC)	VEGFR1, VEGFR2	EGFR, FGFR, PDGFR, ALK	(Piperdi et al., 2014, Forde and Ettinger, 2013)
Pancreatic cancer	VEGFR1, VEGFR2, VEGFR3	EGFR, PDGFR, c-KIT, IGFR, RON	(Xiao et al., 2014, Fink et al., 2016)
Renal cell carcinoma (RCC)	VEGFR1, VEGFR2, VEGFR3	PDGFR, FGFR, MET, KIT Axl	(Alonso-Gordoa et al., 2019, Hsieh et al., 2017)
Thyroid cancer	VEGFR1, VEGFR2, VEGFR3	PDGFR, FGFR, RET, c-KIT	(Cabanillas and Habra, 2016, Corrado et al., 2017)
Oral cancer	VEGFR1, VEGFR2	EGFR, FGFR	(Lin et al., 2016, Hwang-Bo et al., 2016)
Hepatocellular carcinoma (HCC)	VEGFR1 and VEGFR2	PDGFR, Raf	(Longo et al., 2017, Meng et al., 2017)
Gastrointestinal tumour	VEGFR2	EGFR, PDGFR, c-MET, IGFR	(Lian et al., 2019, Scott, 2018)
Chronic myeloid leukemia (CML)	VEGFR2	KIT, RET, TRK, FGFR	(Lakkireddy et al., 2016)
Breast cancer	VEGFR2	EGFR, IGFR, PDGFR, FGFR	(Zhu and Zhou, 2015)
Colorectal cancer	VEGFR1, VEGFR2, VEGFR3	EGFR, IGFR, KIT, TRK, c-MET	(Bhattacharya et al., 2017, Zhu et al., 2016)
Glioblastoma multiforme	VEGFR2, VEGFR3	EGFR, MET, RET, KIT	(Weathers and de Groot, 2015, Zhang et al., 2010)

and VEGFRs in tumour cells, therefore VEGF-A/VEGFR signalling axis is involved progression of numerous cancers such as pancreatic cancer, metastatic renal-cell cancer, breast cancer, oral cancer, thyroid cancer and lung cancer (Table. 1.3) (Lin et al., 2016, Costache et al., 2015, Choueiri and Motzer, 2017, Srabovic et al., 2013, Kilic et al., 2016).

1.1.6.2. Age-related macular degeneration (AMD)

sVEGFR1 expressed in photoreceptor cells play a crucial role in maintaining the avascularity of the cornea and retina in the eye. There is evidence that suggests that the decrease in sVEGFR1 levels in photoreceptor cells leads to increased free VEGF-A which stimulates VEGFRs and pathological angiogenesis (Shibuya, 2014). Abnormal angiogenesis promoted by VEGF/VEGFR system in oedema of retina causes age-related macular degeneration (AMD), a progressive chronic disease and leading cause of irreversible age-related blindness in elderly people (Shao et al., 2016, Yang et al., 2016).

1.1.6.3. Amyotrophic lateral sclerosis (ALS)

In contrast, recent studies performed using cell culture and rodent models suggest a link between VEGF-A levels and amyotrophic lateral sclerosis (ALS), a progressive neurodegenerative disorder in adults. In cell culture, VEGF-A has shown to protect motor neurons against stimuli which promote the pathogenesis of ALS (Tolosa et al., 2008). In transgenic rodent models, VEGF-A has also shown neuroprotective effects, thereby delaying the disease (Tovar-y-Romo et al., 2007, Zheng et al., 2004). However the evidence in human case studies is less compelling, and more research is needed to conclusively establish the role of VEGF-A in ALS (Sathasivam, 2008). Also, there is increasing evidence that suggest the effect of VEGF-A on neurons that regulate axon guidance, axon growth, neuron migration and survival.

1.1.6.4. Multiple sclerosis (MS)

Multiple sclerosis (MS) is a chronic autoimmune inflammatory neurological disease that affects the central nervous system (CNS). In the CNS, tight regulation of endothelial cell properties is vital for the functioning of the blood brain barrier (BBB) function. Alteration of BBB permeability is one of the pathological hallmarks in MS. The role of angiogenesis in abnormal blood brain barrier is still unclear (Lengfeld et al., 2014). However, there is enough evidence that suggest VEGF-A is one such factor that promotes BBB permeability, amongst other factors such as tumour necrosis factor-α (TNF-α) and interferon-γ (IFN-γ) (Girolamo et al., 2014).

Disruption of BBB permeability triggers the infiltration of lymphocytes, macrophages and various mediators into CNS. The migration of monocytes is in response to VEGF-A-mediated VEGFR1 activation (Barleon et al., 1996). The attack of immune cells on oligodendrocytes cells of CNS also suggest that angiogenesis play a vital role in progression of MS (Girolamo et al., 2014). MS lead to severe physical and mental hindering that lead to disabilities in adults. In most cases it start as a reversible cognitive incapacitation, this often lead into severe progressive degeneration (Ghasemi et al., 2017, Goldenberg, 2012).

1.1.6.5. Parkinson’s disease (PD)

Parkinson’s disease is a neurodegenerative disorder which is characterised by degeneration of dopamine generating neurons in the *substantia nigra*. Patients with PD suffer with dementia and psychological issues (Poewe et al., 2008). The mechanisms that lead to neurodegeneration in PD still remain unclear (Carmeliet and de Almodovar, 2013). However, dysfunctional BBB and alteration of blood vessels are reported to be crucial factors that promote PD (Janelidze et al., 2015). Low levels of VEGF-A and VEGF-B are known to exhibit neuroprotective effects in PD. However, overexpression of VEGF-A was reported in the *substantia nigra* of patients with PD (Wada et al., 2006). As we know that VEGF-A levels can promote neurogenesis, one possibility is that the upregulation of VEGF-A expression in the *substantia nigra* is to promote neurogenesis by vascular remodelling (Wada et al., 2006).

1.1.6.6. Alzheimer’s disease (AD)

Similar to ALS and PD, Alzheimer’s disease (AD) is a neurological disorder associated with dysfunctional BBB. AD is the most common of all neurological disorders which lead to decline in consciousness and loss of memory in elderly people. The gradual deposition of β-amyloid peptide (Aβ) caused by neurofibrillary tangles (NFT) and senile plaques in brain parenchyma is the main characteristic in pathology of AD (Weller and Budson, 2018, Schachter and Davis, 2000). In patients with AD, the VEGF-A levels in plasma is found to be higher compared to healthy individuals (Cho et al., 2017). Both VEGFR1 and VEGFR2 are known to be expressed in neurons (Jin et al., 2002, Navaratna et al., 2009). The study conducted by Harris and colleagues showed an AD-associated decline in VEGFR1 expression but a rise in sVEGFR1 levels; however VEGFR2 levels remained unchanged (Harris et al., 2018). It is still unclear whether the elevated VEGF-A levels activate the VEGFR1 and contribute towards impaired angiogenesis. Interestingly, the Aβ peptide competes with VEGF-A to directly recognise and bind to the extracellular domain of VEGFR2 *in vitro*, thereby acting as an antagonist for VEGFR2 with anti-angiogenic activity (Patel et al., 2010). However, the molecular mechanism of anti-angiogenic characteristics of Aβ is still unknown.

1.1.6.7. Other diseases

Increased VEGF-A expression is also associated with progression of osteoarthritis: this comprises of conditions such as cartilage degeneration, subchondral bone cysts, bone sclerosis and synovitis (Hamilton et al., 2016). Angiogenesis promoted by VEGF/VEGFRs is also involved in various other diseases such as pre-eclampsia, rheumatoid arthritis, psoriasis, systemic lupus erythematosus and proliferative retinopathy (Felmeden et al., 2003).

1.1.7. VEGFR targeted treatments in cancer

As described earlier in section 1.1.1, angiogenesis is not only a physiological process but also contribute to pathological conditions such as tumour growth and progression. Therefore, targeting the pro-angiogenic output that promotes cancer is crucial in cancer therapy. Various methods are being employed to tackle cancer therapy; however, few approaches can successfully and selectively block VEGFR functionality for cancer treatment and this is explored in this section.

1.1.7.1. Protein-based therapies

Currently there are a few clinically approved humanised monoclonal antibodies that bind to the circulating VEGF-A with high affinity. These drugs prevent VEGF-A interaction with VEGFRs, which blocks endothelial responses and tumour neovascularisation (Kong et al., 2017, Yang et al., 2017). Bevacizumab (Avastin) is a humanised IgG_1 monoclonal antibody that binds all VEGF-A isoforms and blocks VEGFR2 signalling. Bevacizumab is clinically approved as part of multimodal treatments for advanced non-small cell lung cancer (NSCLC), advanced colorectal cancer (CRC), metastatic breast cancer, renal cell cancer and advanced glioblastoma multiforme (Mukherji, 2010, Kazazi-Hyseni et al., 2010). Ranibizumab is a humanised antibody based on a single antigen-binding site (Fab) derived from Bevacizumab but has much higher VEGF-A binding affinity. The original Bevacizumab has divalent binding sites for VEGF-A but Ranibizumab is a monovalent species (Fig. 1.8) (Ferrara et al., 2006). Ranibizumab is clinically approved for use in ocular diseases involving aberrant angiogenesis such as wet AMD: the smaller monovalent Fab molecules more easily diffuse into the ocular environment compared to full-size antibodies (Shahsuvaryan, 2017, Ferrara et al., 2006). The use of synthetic proteins is being increasingly explored to target angiogenesis in disease states. One such example is Aflibercept (Zaltrap, VEGF TrapEye), a synthetic or artificial protein which contains the high-affinity VEGF-A binding site from VEGFR1 fused to dimerisation domains from VEGFR2, further linked to a humanised Fc portion to recruit the immune system (Al-Halafi, 2014). Such a construct in effect acts as a 'VEGF ligand trap' that inhibits angiogenesis. Aflibercept also binds to other VEGF family members, including VEGF-A, VEGF-B, and PIGF and reduces activation of both VEGFR1 and VEGFR2. The functional effects of Aflibercept in decreasing vascular permeability and neovascularisation (Papadopoulos et al., 2012, Al-Halafi, 2014) has led to clinical approval to treat wet AMD (Freund et al., 2013).

Alternatively, another approach is to directly target the VEGFR extracellular domain thus modulating interaction with VEGF ligand and signalling outcomes. Ramucirumab is a humanised IgG_1 monoclonal antibody that binds VEGFR2 and is approved for advanced gastric cancer (Oholendt and Zadlo, 2015, Singh and Parmar, 2015, Greig and Keating, 2015) and NSCLC (Arrieta et al., 2017, Fuchs et al., 2016). Ramucirumab binds at or close to the VEGF-A binding site on VEGFR2 and blocks ligand binding and VEGFR2 activation (Spratlin et al., 2010, Spratlin, 2011). Several anti-VEGFR2 humanised antibodies are in pre-clinical development and clinical trials. Similar to Ramucirumab mode of action, Tanibirumab (TTAC-0001) is an anti-VEGFR2 antibody also binds to the VEGFR2 extracellular domain and blocks binding of VEGF-A, VEGF-C, VEGF-D and VEGF-E with potent anti-angiogenic activity and tumour growth inhibition in mouse models. Tanibirumab shows effective inhibition of VEGFR2 but not VEGFR1 or VEGFR3 (Lee et al., 2015). Tanibirumab shows positive results in patients with colorectal cancer in phase I clinical trials, and phase II trials are ongoing (Lee et al., 2017).

1.1.7.2. Tyrosine kinase inhibitors (TKIs)

Tyrosine kinase inhibitors (TKIs) are small molecule inhibitors which are water soluble and have amphipathic properties. These TKIs can diffuse through the hydrophobic plasma membrane bilayer and act within the cytosol to inhibit the specific tyrosine kinase activity which is dependent on ATP/ADP cycle. Most TKIs mimic the adenine moiety by forming hydrogen bonds with hinge region of tyrosine kinase, thereby competitively inhibit the ATP binding to the kinase domain. Sunitinib (trade name, Sutent) is an example of VEGFR TKI which is approved for cancer therapy (Roskoski, 2007a) (Fig. 1.8D). Imatinib and Sorafenib are two other examples of small molecule TKIs that selectively block ATP binding to these enzymes.

An alternative approach to target VEGFR activity includes using a class of inhibitors which negatively regulate the tyrosine kinase activity in allosteric manner. These compounds do not bind or inhibit the tyrosine kinase activity directly, but target and inhibit various downstream signal transduction pathways activated by RTKs such as MAPK, p38-MAPK pathway and mTOR signal transduction pathways (Fig. 1.8D). One example is the B-Raf selective inhibitor that also inhibits downstream MEK1/2 and ERK1/2 activity. This drug received FDA approval for treating unresectable or metastatic melanoma in patients carrying the B-Raf-V600E mutation (Kwong-Kwok, 2009, Yang et al., 2010a, Kim et al.). SB203580 is a pyridinyl imidazole inhibitor that targets p38 MAPK (Cuenda et al., 1995) and PDK1, affecting downstream Akt activation and retinoblastoma hyperphosphorylation (Lali et al., 2000). Perifosine is an anti-cancer molecule that inhibits the Akt pathway (Richardson et al., 2012). Dactolosib (BEZ235), Bimiralisib (PQR309), BGT226, SF1126, and GSK2126458 are some examples of Class IV inhibitors developed to target PI3K-Akt-mTOR pathway with dual inhibitory activity towards PI3K and mTOR (Wander et al., 2011). Everolimus is an mTOR inhibitor which has received FDA approval for treating advanced or metastatic renal cell carcinoma in combination with Lenvatinib, a multikinase RTK inhibitor for the VEGFR subfamily (Petiot et al., 2003, Studentova et al., 2018, Glen, 2016). Alpelisib, which inhibits PI3K, has been approved for multimodal therapy in some types of breast cancer (Sidaway, 2019).

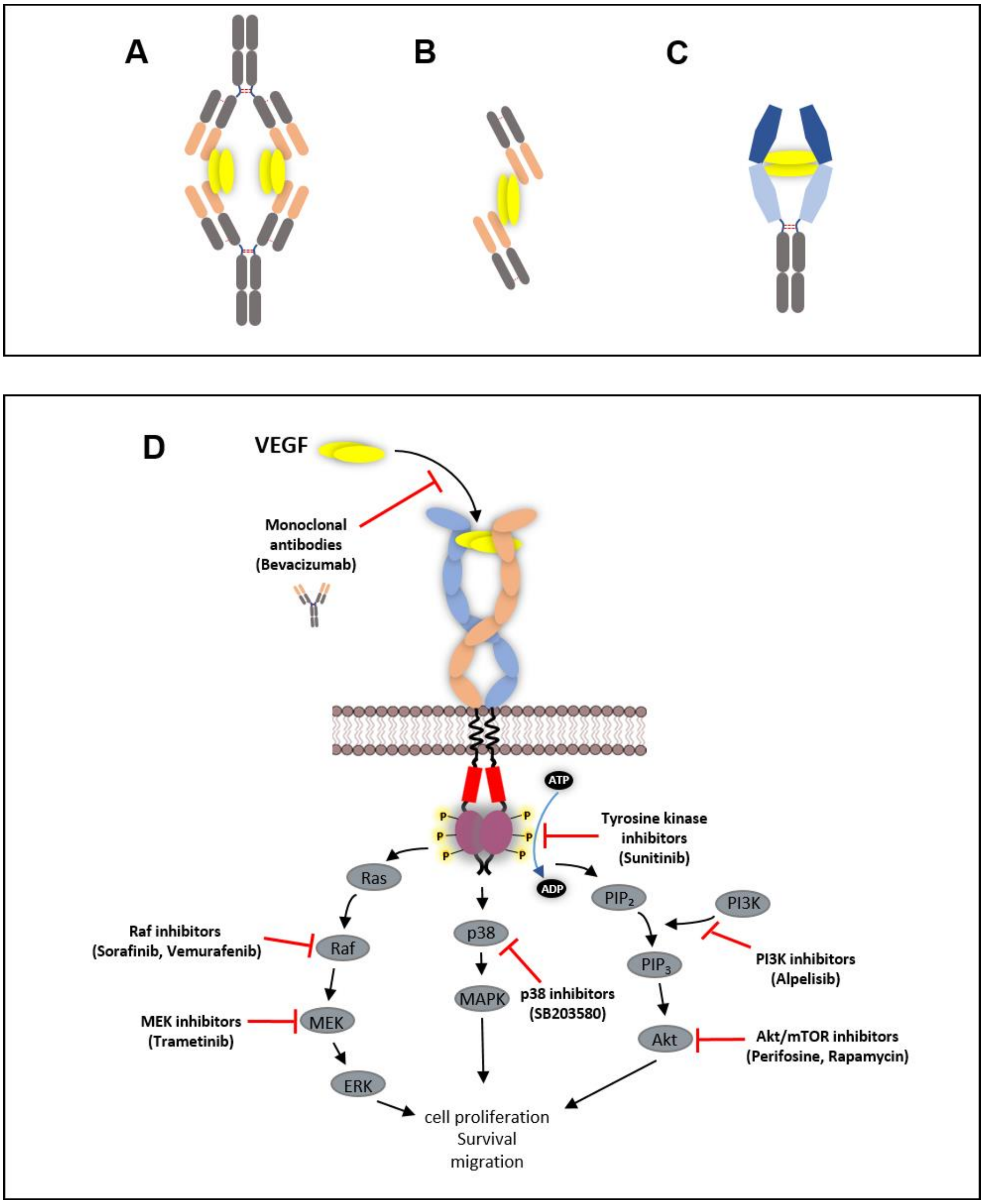

Figure 1.8. Therapeutic targeting of VEGFR function. Cartoon representation of **(A)** Bevacizumab **(B)** Ranibizumab, and **(C)** Aflibercept in targeting VEGFR function. Bevacizumab, Ranibizumab and Aflibercept directly bind to the ligands (VEGFs) thereby neutralising VEGF biological activity. **(D)** VEGFRs can be targeted directly by monoclonal antibodies to inhibit VEGF binding to the extracellular domain of the receptor, Ramucirumab interferes with VEGF ligand binding to the VEGFR. Alternatively, small molecule tyrosine kinase inhibitors (e.g. Sutent) are ATP-like mimetics which bind at or near the ATP-binding site in the TK domain thereby inhibit tyrosine phosphorylation. Other inhibitors of VEGFR signalling pathways can also promote therapeutic benefits.

1.2. Serum lipoproteins and scavenger receptors

Cholesterol and triglycerides are non-polar lipid particles which are important components of human body and involved in function of the cells. Cholesterol is an unsaturated fat or lipid molecule which is a fundamental component of all mammalian cell membranes. These lipids rely on serum lipoproteins for transportation to various organs of the body. Serum lipoproteins are micelle-like globular complexes composed of both proteins and lipids held together by covalent forces. They are mainly involved in transporting cholesterol, triglycerides and specific high-density proteins around the body. Both cholesterol and triglycerides are non-polar lipid particles which can only be transported with lipoproteins in the plasma (Ginsberg, 1998). They can be classified into five different classes based on their size, mobility, density of triglycerides and cholesterol; chylomicrons, very low-density lipoproteins (VLDL), low-density lipoproteins (LDL), intermediate-density lipoproteins (IDL) and high-density lipoproteins (HDL) (Feingold and Grunfeld, Sandhofer, 1994). Specific lipoprotein particles are heavily implicated in atherosclerosis and it is discussed further in section 1.2.4.

Scavenger receptors (SRs) are also cell surface receptors which are expressed on various vascular endothelial cells but predominantly on macrophages. The family of scavenger receptors bind to variety of modified lipids, phospholipids, pathogens and/or apoptotic cells leading to their internalization and degradation. Binding of scavenger receptors to ligands is implicated in their metabolism, and vascular health, inflammation, and chronic disease state such as atherosclerosis. Scavenger receptors comprises of variety of integral membrane proteins and the super-group are classified into 10 subfamilies in eukaryotic organisms, namely A-J (Abdul Zani et al., 2015, Murphy et al., 2005). These receptors are further divided into subfamilies based in their variation in amino acid sequence. This study is primarily focussed on LOX-1 (lectin type oxidised LDL receptor-1, OLR1, oxidised low-density lipoprotein receptor-1) and its interactions with lipoproteins.

1.2.1. Types of lipoproteins

Chylomicrons (CMs) largely carry large triglycerides which are produced in the intestine and act as transport vehicle for dietary fat (Mansbach and Siddiqi, 2016). These lipid particles are heterogeneous entities which also consists of cholesteryl esters, phospholipids, protein with core triglycerides. The structural protein component of CM is apolipoprotein B-48 (ApoB-48) derived from apolipoprotein B-100 (apoB-100) by the ApoB-48 enzyme editing complex, which is produced by the gut cells (Nakajima et al., 2014). The functional role of CMs is to deliver triglycerides to the peripheral tissues of the body, CMs are associated with chylomicron-retention disease which is an autosomal recessive disease, caused by a mutation of in the SAR1B protein which is responsible for transporting CMs from the endoplasmic reticulum (ER) to Golgi complex (Engelking, 2015).

Very low-density lipoprotein particles (VLDLs) are produced in the liver. Similar to CM, the major components of VLDLs are triglycerides, the major structural protein component of VLDL which is different from chylomicrons and comparatively VLDL is smaller than chylomicrons (Table. 1.4). Intermediate density lipoprotein (IDL) are formed from VLDL particles. In muscle tissues and adipose tissues, triglycerides are removed which leads to the formation of IDL. The skeletal protein of IDL is apoB-100 same as VLDL.

Low-density lipoprotein (LDL) is formed from both VLDL and IDL. LDL contains more cholesterol and less triglycerides that both VLDL and IDL, with ApoB-100 as a major structural protein. Three lipoprotein particles i.e. VLDL, IDL and LDL are involved in pro-atherogenic disease states. However, LDL is a dominant pro-atherogenic lipid particle due to high composition of cholesterol compared to VLDL and IDL. Each LDL particle contains cholesterol esters and triglycerides at the hydrophobic core, surrounded by a lipid monolayer composed of cholesterol, phospholipids, and a single ApoB-100 polypeptide of ~500 kDa. Typically, LDL is recognised and internalised by the low-density lipoprotein receptor (LDLR). Binding of LDL to LDLR leads to endocytosis, trafficking and delivery to lysosomes where it undergoes degradation by proteases, lipases and other enzymes. Cholesterol released from the breakdown of LDL can diffuse through intracellular membranes and can further inhibit the activity of HMG-CoA reductase (Goldstein and Brown, 2009), a key enzyme in cholesterol biosynthesis. The average composition of LDL is ~21% lipoprotein, ~25% phospholipids, ~38% cholesterol esters, ~9% unesterified cholesterol, and ~7% triglycerides (Table. 1.4) (Hevonoja et al., 2000). LDL particles are can pass through the arterial wall and also susceptible to oxidation, this makes them dangerously atherogenic as described in section 1.2.2.

High-density lipoprotein (HDL) particles have different function compared to other lipid particles. Even though HDL comprises of high levels of phospholipids and cholesterol, its role is to transport the cholesterol from peripheral tissues back to the liver, thereby functioning as an anti-atherogenic mechanism which decreases systemic cholesterol levels and aids secretion of cholesterol by mixing with bile and excretion into the gut. In addition, HDL particles are resistant to oxidation and also possess anti- inflammatory and anti- thrombotic properties which further contribute towards their mechanism to inhibit atherosclerosis. HDL doesn’t contain ApoB-100 as a structural lipoprotein, but they contain ApoA-I, Apo-AII, ApoA-IV, ApoC-I, ApoC-II, ApoC-III and Apo-E (Schaefer et al., 2014). HDL is considered as 'good entity' as opposed to VLDL, IDL and LDL which are 'bad entities' or arterial disease-promoting agents.

1.2.2. Oxidised and modified low-density lipoprotein (OxLDL/mLDL)

The concept that oxidative stress and the oxidation of LDL originated from a simple observation by incubation of macrophages with oxidised LDL, not with native LDL leads to cholesterol ester accumulation and atherosclerotic plaque formation (Parthasarathy et al., 2010). The release of reactive oxygen species (ROS) and other oxidising agents by respiring cells can lead to the conversion of LDL to oxidised or modified LDL (OxLDL, mLDL). OxLDL, rather than native LDL. This was postulated in the 1980s to be the key agent for the delivery and accumulation of cholesterol in atherosclerosis (Pirillo et al., 2013b, Henriksen et al., 1981). It is hypothesised that the oxidation of LDL causes change on the surface of the lipid particle, making it electronegative. However, it is unclear how the overall structure of the LDL particle is altered in OxLDL as a consequence of the many different chemical alterations caused by such oxidising or modifying agents. ApoB-100 is the main protein component of OxLDL (Fig. 1.9A), Upon oxidation, OxLDL become specific ligand to a scavenger receptor (LOX-1) whereas it doesn't bind to LOX-1 in its native form or before oxidation (Chen et al., 2002). This is further discussed in section 1.2.4.

Table 1.4. Classification of percentage composition of various lipids in different lipoproteins (Diffenderfer and Schaefer, 2014).

Lipoprotein	**Diameter (Å)**	**Percentage of lipoprotein particle (mass)**				
		Apo-lipoprotein	Cholesterol esters (CE)	Free cholesterol (FC)	Phospholipid (PL)	Triglycerides (TG)
Chylomicron	2000-6000	2	3	2	8	85
VLDL	~600	8	20	2	20	50
LDL	~250	21	38	9	25	7
IDL	~150-170	18	21	7	19	35
HDL	~70-120	41	18	6	31	4

1.2.3. LOX-1 scavenger receptor

The lectin-like oxidised low-density lipoprotein receptor-1 (LOX-1, SR-E1, OLR1) is encoded by gene *OLR1* and it is made up of 6 exons and 7 introns and located on human chromosome 12. It was initially identified as a receptor that specifically recognises the OxLDL on aortic endothelial cells. Wide range of ligands recognised by LOX-1 includes OxLDL, apoptotic bodies, C-reactive protein (CRP), platelets, advanced glycation end products (AGEs) and bacteria. Many of these ligands stimulate LOX-1 mRNA synthesis and protein expression (Draude et al., 1999, Xu et al., 2013).

The LOX-1 expression is largely restricted to endothelial cells, macrophages, smooth muscles and platelets and is elevated by pro-inflammatory stimuli including OxLDL, ROS, glucose and TNFα (Draude et al., 1999). The receptor comprises of 273 amino acids, with a predicted molecular weight of ~40 kDa; fully glycosylated and mature LOX-1 is ~50 kDa by SDS-PAGE. LOX-1 comprises of four domains: a short N-terminal cytoplasmic domain, single transmembrane domain, neck domain or stalk region of ~60-70 residues, and C-type lectin-like domain of ~130 residues (Fig. 1.9B). The stalk region is involved in oligomerization of the receptor, whereas the C-type lectin-like domain is primarily responsible for ligand binding, particularly OxLDL. LOX-1 exists as a homodimer and the analysis of crystal structure suggests that it has a hydrophobic tunnel at the centre of C-type lectin-like domain. LOX-1 is suggested to bind covalently to phospholipid moiety of lysine side chain on ApoB-100 protein component of OxLDL with high affinity. Binding studies of LOX-1/OxLDL are still unclear, but using molecular modelling, it is predicted that the phospholipid moiety of ApoB-100 fits perfectly in the hydrophobic pocket and mutations of specific residues in the hydrophobic pocket inhibits LOX-1 binding to OxLDL (Thakkar et al., 2015). Even though several scavenger receptors bind and recognise OxLDL, the LOX-1 is genetically and functionally linked to heart disease, strokes and Type 2 diabetes. Therefore, understanding and targeting LOX-1 interactions with OxLDL has clinical significance in many serious disease states (Fig. 1.9C).

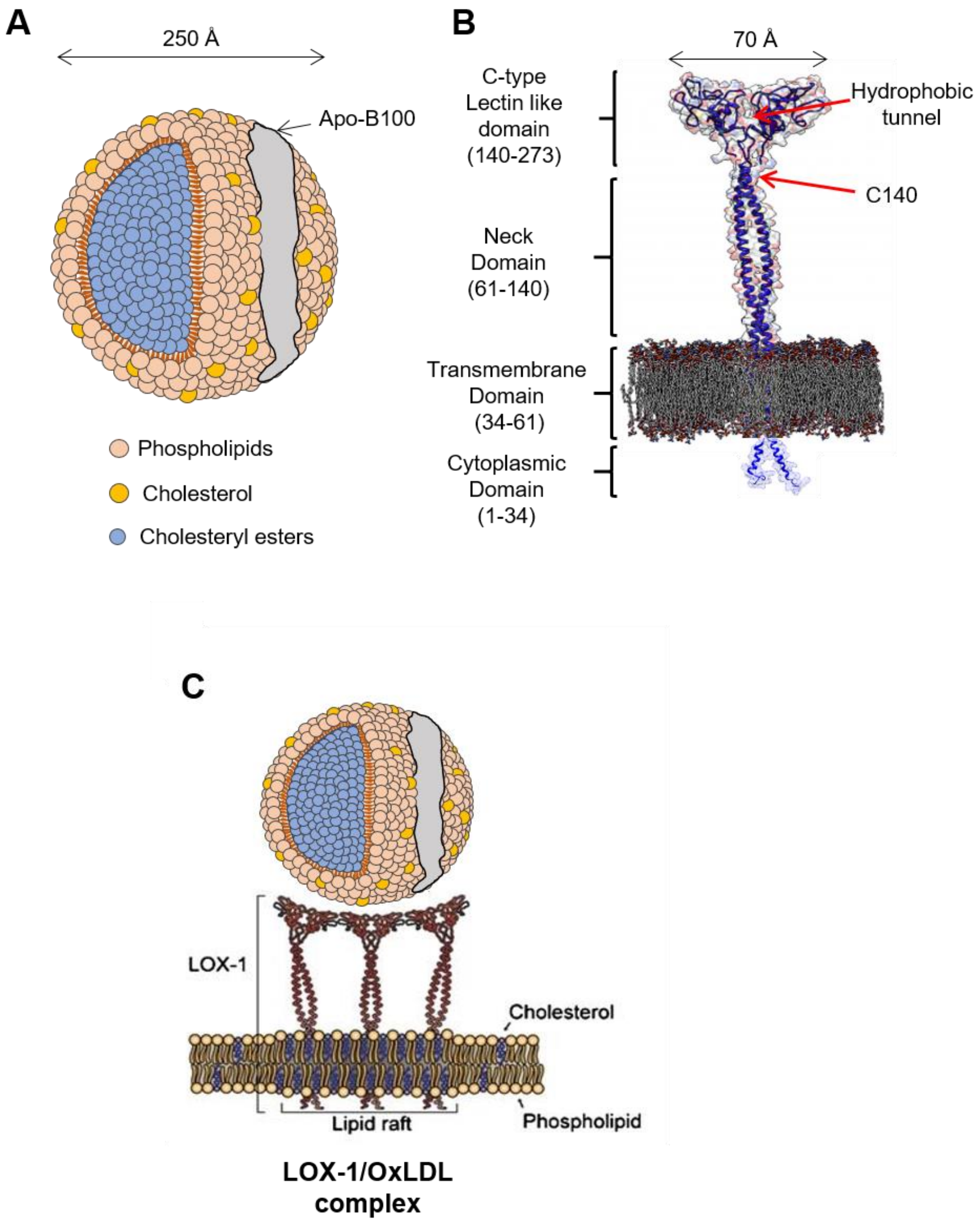

Figure 1.9. Schematic representation of OxLDL and LOX-1 scavenger receptor. (A) Cartoon representation of structure of OxLDL. **(B)** Structural assembly of LOX-1 dimer determined by x-ray crystallography (C-type lectin domain), NMR (neck domain), merged with cartoon illustration (transmembrane and cytoplasmic domain) (adapted from Ohki *et.al*., 2005b), and **(C)** Schematic drawing of LOX-1/OxLDL complex. LOX-1 clustered on cell surface bind to the negatively charged amphiphatic α-helices of OxLDL. C-type lectin domain (CTLD) is preassembled as a homodimer with a disulphide link which is responsible for recognition of OxLDL (adapted from Raniolo et al., 2016).

1.2.4. LOX-1 and OxLDL, and their role in atherosclerosis

Atherosclerosis is a chronic inflammatory disease which characterised by the deposition of dead and dying cells, lipids and fasts that leads to plaque fat-enriched scar or lesion within the walls of arteries. This pro-inflammatory phenomenon causes the initiation and progression fat-engorged lesions that protrude into the arterial lumen, thereby obstructing blood flow; this eventually leads to plaque rupture, blood clot formation (thrombosis) and subsequent acute clinical implications (Lusis, 2000). This is thus a progressive disease and the clinical manifestations include serious cardiovascular diseases (CVD) such as coronary heart disease, peripheral arterial disease, transient ischaemic attack (TIA) and myocardial infarction (MI) (Glass and Witztum, 2001). The abundance of circulating plasma lipid particles e.g. LDL, leading to hypercholesterolaemia is considered to be a primary risk factor that triggers atherosclerosis. The complications and arterial disease states that arise due to atherosclerosis are most common in western societies (Bergheanu et al., 2017).

Atherosclerosis is a multi-factorial disease, all the events and the mechanisms that leads to atherosclerosis are relatively well understood. A key event in disease initiation occurs in the development of 'lipid and fat-enriched' foam cells from macrophages, which then drives the formation of the fatty streak or lesion within the arterial wall (Fig. 1.10). Previously, although it was thought that the foam cells are formed exclusively from smooth muscle cells (SMCs), Steinberg and colleagues were the first to propose that the recognition of modified lipoprotein by membrane receptors on macrophages leads to foam cell formation and fatty streak development (Henriksen et al., 1981, Steinberg, 1987, Steinberg et al., 1989). The events that leads to atherosclerosis can be described by three hypotheses which are different concepts but essential steps in the initiation and progression of the atherosclerosis phenomenon. Firstly, the response-to-injury hypothesis proposed by Ross and Glomset (Ross et al., 1977, Ross, 1993), suggested that an injury to the endothelium (endothelial dysfunction) due to diminished production of nitric oxide synthase (NOS), causes an imbalance between the endothelial relaxing and contracting factors which leads to changes in vascular homeostasis (Hadi et al., 2005). Secondly, the response-to-retention hypothesis (Williams and Tabas, 1995) proposed that the passage of LDLs through the dysfunctional endothelium into the sub-endothelium enables uptake by macrophages leading to foam cell formation. Finally, the oxidative modification hypothesis (Chisolm and Steinberg, 2000) suggests that LDL is modified into OxLDL before being engulfed by macrophages which drives the pro-atherogenic phenotype.

Under normal conditions LOX-1 expression is very low or non-existent; however, under pro-inflammatory conditions and high blood pressure, it is elevated in expression. LOX-1 is then implicated in binding and clearing OxLDL, thereby it’s primary role is to act as a host-defence mechanism (Yoshimoto et al., 2011). However various *in vitro* and *in vivo* studies have provided significance evidence on how the overexpression of LOX-1 is involved in endothelial dysfunction, foam cell formation, and smooth muscle cell migration. LOX-1 is upregulated by pro-inflammatory cytokines, proteoglycans, and vasoconstrictors. Expression of LOX-1 leads to an increase in oxidative stress and ROS production, which further promotes oxidisation of native LDL into OxLDL and development of endothelial cell dysfunction (Fig. 1.10).

Endothelial cells binding to OxLDL via LOX-1 causes a down-regulation of endothelial nitric oxide synthase (eNOS) leading to endothelial dysfunction and apoptosis. The increased circulating levels of LDL is driven by the relatively high pressure in arterial blood vessels past the endothelial monolayer into the sub-endothelial and connective tissue environment, where the LDL is modified into OxLDL by reactive oxygen species (ROS) generated by the surrounding endothelial and vascular smooth muscle cells. The pro-inflammatory stimuli from inflamed endothelial cells attracts the monocytes, whereby monocytes infiltrate into the sub-endothelial layer and accumulate here where they differentiate into macrophages. The dysfunctional endothelium produces reactive oxygen species (ROS) and proinflammatory cytokines which causes monocyte differentiation into macrophages, and further helps macrophage differentiation into foam cells. The scavenger receptors such as CD36, SR-A1, SR-B1, and LOX-1 on macrophages

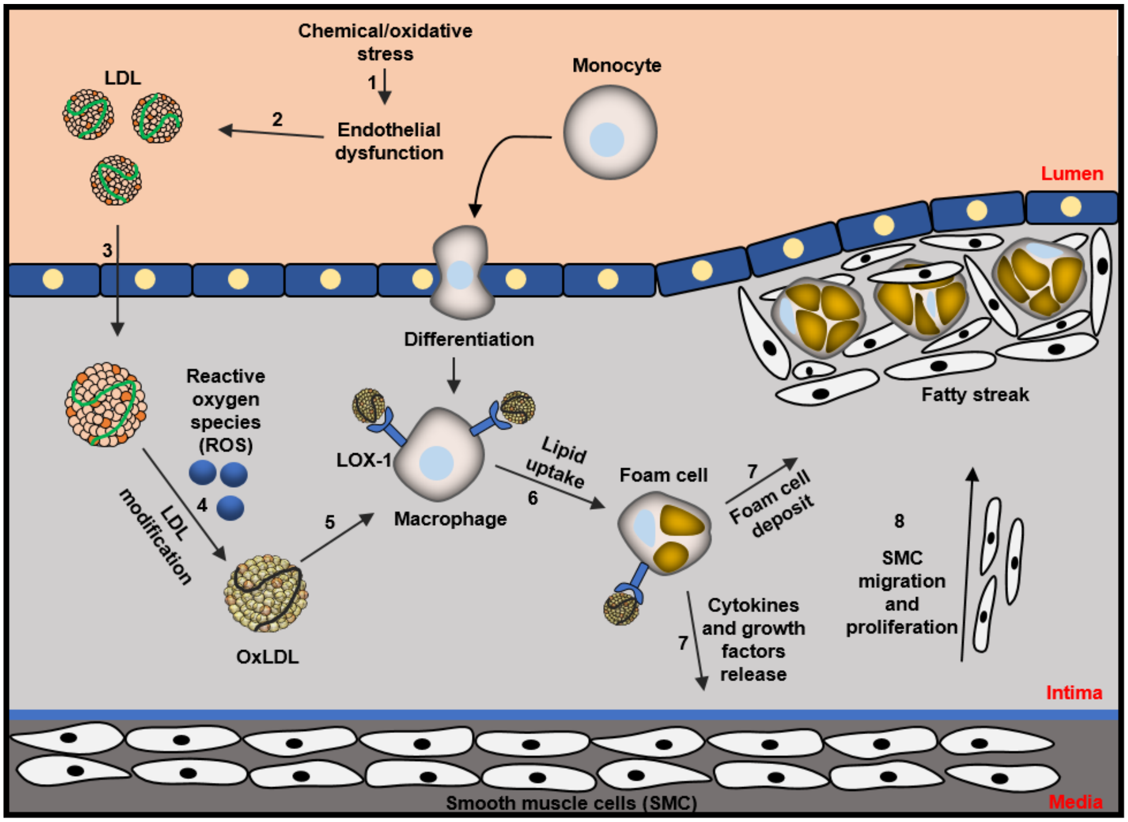

Figure 1.10. Potential role of OxLDL and LOX-1 in foam cell formation and contribution to atherosclerosis. Excess LDL in the circulating bloodstream causes accumulation in the arterial walls operating at relatively high blood pressure (80-120 mm Hg). These accumulated LDLs undergo oxidation into oxidised LDL (OxLDL). Increased OxLDL levels in the sub-endothelial layer triggers migratory cells called macrophages in to recognise, bind OxLDL which promotes conversion of macrophages into lipid-engorged foam cells. These necrotic and aopotitic foam cells release various growth factors and cytokines which also trigger smooth muscle cell migration into the area of the arterial lesion. This fat-enriched atherosclerotic plaque eventually ruptures to cause a blood clot, arterial blockage and tissue death and damage e.g. heart attack or stroke.

recognise and bind to OxLDL thereby engulf these lipid particles, helping the differentiation into foam cells. The presence of OxLDL and/or angiotensin II can also elevate LOX-1 expression in vascular smooth muscle cells (VSMCs), leading to the migration of VSMCs which further 'trap' the foam cells in this locality and further accelerate plaque progression (Fig. 1.10). Formation of plaque deposits pushes the endothelium outwards into the blood vessel lumen, causing a narrowing of arteries, and increased blood pressure. Such abnormal blood flow is an underlying driver for serious disease states. Further disruption of an unstable plaque can cause plaque rupture and blood clot formation (thrombus), which can cause various serious clinical conditions such as angina, myocardial infarction (MI) and stroke.

1.3. Single particle electron microscopy

The conventional techniques such as crystallography and NMR have limitations in solving the structure of membrane proteins; Recent advances in electron microscopes, detector technology and software algorithm have enabled us to determine the near atomic resolution structure of membrane proteins in aqueous environment. Since the aqueous environment preserves the protein in active state conformation, Cryo-EM technique caught the attention of many researchers working on membrane proteins. Recently resolved high resolution membrane protein structures using cryo-EM are, among many; 3.4 Å resolution of TRPV1, γ-secretase at 4.5 Å, ATP-binding cassette transporter (ABC) at 8.2 Å and Slo2.2 Na^+ activated K^+ channel at 4.5 Å. (Lu et al., 2014, Liao et al., 2013, Hite et al., 2015, Vinothkumar, 2015).

1.3.1. Working principle of single particle cryo-EM and negative stain EM

Cryo-electron microscopy is a type of transmission electron microscopy (TEM) which works in much the same way as the optical microscope. Unlike X-ray crystallography, which determine structures from diffraction of 3D crystals, single particle cryo-EM uses computational methods to produce a 3D model based on thousands of views of single particles which are aligned and averaged (Cheng et al., 2015, Cheng, 2015). In this technique a purified homogenous protein sample is applied to thin holey carbon grid and plunge-frozen in liquid ethane (-180 C) using, for example vitrobot (Iancu et al., 2006). Controlled plunge freezing forms a thin layer of vitrified ice across the holes of carbon in which proteins are trapped without any distortion. Ice prevents dehydration of proteins and facilitate in preserving the native conformation (Cheng, 2015). Low dose of electron beam (10-20e^-/$Å^2$) is passed through the grid and projection images are captured using charged coupled device (CCD) cameras or direct electron detection (DED) cameras (Carroni and Saibil, 2016, Glaeser, 2008). The 2D images contain views of the sample in different orientations, based on projection slice theorem the images are positioned using six geometric parameters that include three eular angles, two in-plane positions and a defocus which indicates the direction of an electron beam (Nogales and Scheres, 2015, Cheng, 2015). By aligning the images a 3D computational model is constructed (Nogales and Scheres, 2015). However, various factors influence the resolution of cryo-EM 3D models and has various limitations. Factors such as conformation flexibility of the protein leading to heterogeneity, potential variable oligomerisation state of receptor which leads to further heterogeneity (such as RTKs), membrane protein insolubility at high concentrations leading to aggregation, other limiting factors include potential of membrane protein binding to carbon grid (Glaeser, 2018).

Therefore, to address these issues negative stain-electron microscopy (neg stain-EM) is used before attempting cryo-EM for heterogenous proteins. In negative stain microscopy heavy metal salt such as uranyl acetate is used, the stain added to the sample uniformly covers the grid excluding the protein complexes. When the electron beam is passed through the stained sample it mainly interacts with the stain surrounding the sample but excludes the volume that is occupied by the sample. Hence, the term “negative stain” (Gallagher et al., 2019). The interaction of heavy metal ion with the electron beam produces the optimum phase contrast for imaging the micrographs (Cowley and Bridges, 1979). Negative stain-EM is usually performed to obtain an idea of the homogeneity/heterogeneity of large protein assemblies or to evaluate the quality of the protein (Booth et al., 2011b). It is also possible to build low-resolution preliminary projection models of receptor in various orientations. The initial low-resolution models are further used in combination with cryo-EM to achieve high-resolution (Choi et al., 2018) (Fig. 1.11).

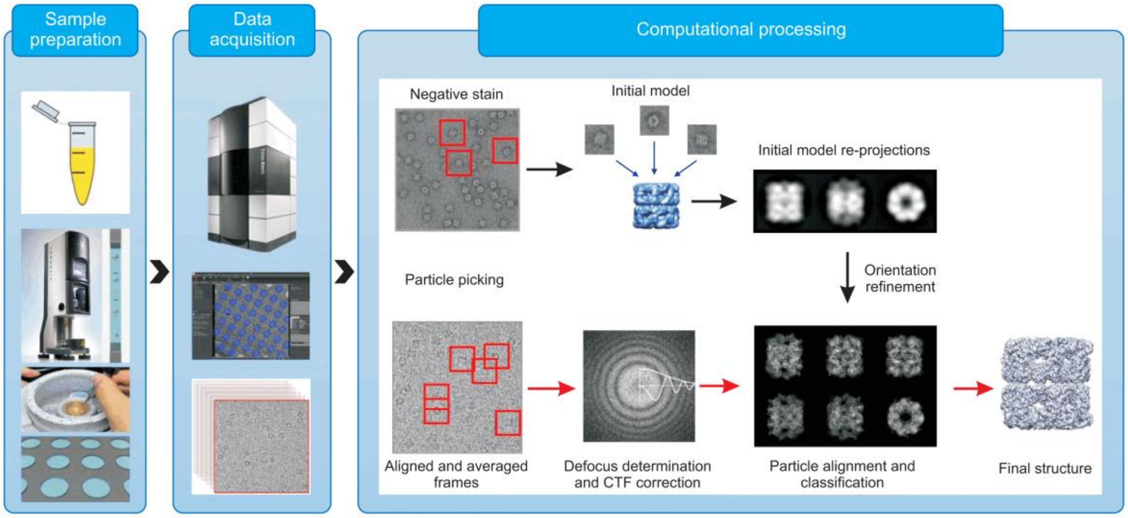

Figure 1.11. Workflow of single-particle analysis for reconstruction of protein. Purified protein samples are screened through negative staining to analyse the concentration and homogeneity/heterogeneity, classification and averaging of contrast images carried out to construct initial models and orientation. Followed by vitrification of proteins by plunge freezing on grids (usually carbon), the micrographs are collected and using computational process three dimensional images are generated from 2-D classes. The 3-D models are refined from initial models to determine the resolution. Reproduced from Choi et al., 2018

1.4. Summary

Cancer is the second leading cause of deaths in the world, the fundamental feature of cancer is abnormal proliferation of various types of cells in the body. Various primary factors known to trigger cancers are genetic mutation, chemical carcinogens, radiation etc. It is a multistep process which involves first initiation step, second stage is development of tumour and the final spread. Over 90% of cancers are malignant in nature which can initiate and effect almost all organs of the body. VEGFRs are members of receptor tyrosine kinase family which are linked to the pathologies of almost all types of cancers, evidence from immense number of studies indicate that VEGFRs and their growth factors are key modulators involved in two key processes such as progression and spread of cancer by inducing angiogenesis which is a major hallmark of cancer. Thus, VEGFs and their receptors are targets for anti-cancer therapy and understanding their mechanism of action would provide invaluable insight into their central role in cancer progression.

On the other hand, atherosclerosis is a primary cause of heart diseases and stroke which reason for leading number deaths around the world. It accounts for over 50% of deaths especially in western societies. It is a systemic process that involve abnormal accumulation of fat deposits in arterial walls by narrowing it down, followed by rupture of foam cells/fat deposits causing clot formation. Thereby, blockage of arteries leads to serious consequences such as heart diseases and stroke. LOX-1, a scavenger receptor on macrophages along with ligand (OxLDL) are directly involved in pathology of plaque formation i.e artherosclerosis. The mechanistic insights of how LOX-1 bind to OxLDL and promote vascular dysfunction is still unknown. Therefore, studying their molecular mechanisms can lead to design novel therapeutics for LOX-1/OxLDL.

1.5. PhD project aims

This project involves two lines of investigation with studies on two distinct types of vascular receptors. Firstly, the study of VEGFRs which are primarily involved in numerous types of cancers triggered by angiogenesis. Despite their importance as crucial cancer targets, no high quality structural and mechanistic data exists for the family of VEGFRs. In first line of investigation, our overall aim is to derive the structural information about VEGFR family, by studying the full-length proteins and possibly resolve the high-resolution structure of one of the receptors. This would require construction of expression vectors for suitable overexpression system, optimization of production by purification recombinant VEGFR proteins. Therefore, specific objectives of this study include

- Expression and purification of VEGFRs in mammalian expression system
- Biochemical and structural analysis of VEGFRs using electron microscopy (EM) approach

Once produced these receptors would be used for structural studies in order to determine the 3D structure model of complexes, other biochemical experiments include dimer formation, activation with an ultimate aim to understand their structural complexity.

The second line of investigation include studying the structural aspects of lipoproteins involved in progressive heart disease such as atherosclerosis. As discussed in the introduction, we lack information on nLDL and OxLDL discrimination towards selectively binding to scavenger receptor (LOX-1). Therefore, the specific objectives of this study include

- Purification LDL and OxLDL and compare their biochemical properties.
- Evaluate the ability of LOX-1 to discriminate between these lipid particles.
- Compare the structure of LDL and OxLDL.
- Evaluate the structure of OxLDL-LOX-1 complexes.

The lipoproteins would be analysed using biochemical and structural experiments. These studies ultimately aim to unravel the in-depth information on structural insight lipoprotein binding to scavenger receptor that mediate heart diseases.

CHAPTER 2

MATERIALS AND METHODS

2.1. General buffers and media solutions

All chemicals were analytical grade and purchased from Sigma-Aldrich or Fisher Scientific unless otherwise stated. All the restriction enzymes were purchased from New England Biolabs.

2.2. Cell lines

Human umbilical vein endothelial cells (HUVECs) were isolated from umbilical cords obtained from patients undergoing elective Caesarean section with informed patient consent at Leeds General Infirmary (LGI). Flp-In^{TM} T-Rex^{TM} Human embryonic kidney cell line (HEK293 Flp-In^{TM} T-Rex^{TM}) were purchased from ThermoFisher Scientific. Human embryonic kidney (HEK293S GnTI^{-}) cell line (ATCC CLR-3022^{TM}) were purchased from American type cell culture collection (ATCC®). HEK293S GnTI cells and HEK293 Flp-In^{TM} T-Rex^{TM} were grown in DMEM (10 % v/v tetracycline-free fetal bovine serum) maintained by incubating at 37˚C in 5% (v/v) CO_2 incubator. HEK293 cells were passaged every 3 days by gentle pipetting without trypsinization and plated at 20-25% confluency.

2.3. Isolation of primary HUVECs

Primary endothelial cells were always obtained fresh from umbilical cords obtained from ethically approved program linked to Leeds General Infirmary (LGI) and Leeds NHS Hospital Trust). The umbilical vein was cannulated with an 18-gauge blunt end needle and flushed with 50 ml PBS containing 10 U/ml penicillin and 100µg/ml streptomycin. The cord was clamped at one end using hemostat and the vein was filled with 0.1% (w/v) type IIS collagenase in MCDB131 (Life Technologies) and then clamped at the other end. The cord was incubated at 37˚C for 20 mins allowing the cells to digest and detach from the cord. The vein was flushed with 50 ml of PBS and the cells were collected. Cells were pelleted via centrifugation at 140 *g* for 5 min at 37˚ C. The supernatant was aspirated and the cells were re-suspended in endothelial cell growth medium (ECGM) containing 10 U/ml penicillin, 100µg/ml streptomycin and 50 ng/ml amphotericin B. Cells were seeded into a 75 cm^2 vented tissue culture flask (Sarstedt) pre-coated with 0.1 % (w/v) pig skin gelatin (PSG). After 24 h, cells were washed 5 times with PBS before replacing with fresh ECGM medium.

2.4. Molecular Biology

Table 2.1. List of plasmids used

Plasmid name	Source
pCMV3-SP-FLAG-VEGFR1	Sino Biological
pCMV3-SP-FLAG-VEGFR2	Sino Biological
pCMV3-SP-FLAG-VEGFR3	Sino Biological
pcDNA5-FRT-TOPO	ThermoFisher Scientific
pOG44	ThermoFisher Scientific
pET-15b-LOX-1	Addgene

2.4.1. Preparation of competent *E.coli XL-10* cells

Competent cells were prepared for transformation of plasmid. XL-10 variant *E. coli* cells (Stratagene) were streaked onto LB agar plates containing 10 µg/ml tetracycline and the plate was incubated overnight at 37˚C. A single colony was picked using a sterile yellow pipette tip and grown in LB medium (with 25 ug/mL tetracycline) in a shaker at 220 rpm overnight at 37˚C. Next day, a 1:100 ratio of overnight culture was added to fresh LB-tetracycline and incubated again on a shaker at 37˚C (220 rpm) for 2.5 hr. When $OD_{550-600}$ reached 0.2-0.4, the cells were harvested by centrifugation at 3000 rpm for 10 min at 4˚C. The supernatant was discarded and the cell pellet re-suspended in ice-cold transformation buffer-I (Tfb-I) (30 mM potassium acetate, 100 mM rubidium chloride, 50 mM manganese chloride, 10 mM calcium chloride, 15 % (v/v) glycerol, pH adjusted to 5.8 using 0.2 M acetic acid) and kept on ice for 5 min. Cells were centrifuged again at 3000 rpm for 10 min at 4˚C, the supernatant discarded, and the cells again re-suspended in ice-cold Transformation buffer-II (Tfb-II) (10 mM MOPS or PIPES, 75 mM calcium chloride, 10 mM rubidium chloride, 15 % (v/v) glycerol, pH adjusted to 6.5 using KOH). After incubation on ice for 30 min, 50µl aliquots were made stored at -80˚C.

2.4.2. Transformation of competent *E.coli* cells

100 ng of ligations or plasmids were added to 50 µl of thawed competent *XL-10* cells and incubated on ice for 30 mins. Cells were heat-shocked for 2 mins using a 42°C water bath and left on ice for 5 mins. 1 ml of sterile LB was added and incubated at 37°C for 1 hr to allow cells to recover. Cells were then streaked onto appropriate LB agar plate containing antibiotics and incubated at 37˚C for 16 h to allow bacterial colonies to grow.

2.4.3. DNA amplification using polymerase chain reaction (PCR)

PCR amplifications were performed using Q5 High Fidelity (HF) polymerase purchased from NEB. Typically, reactions of final volume 50 µl were set as follows

Table 2.2. Composition of PCR reaction mixture

Component	Final concentration
Q5 HF polymerase PCR buffer (5X)	1X
10 mM dNTPs	200 µM
10 µM Forward Primer	0.5 µM
10 µM Forward Primer	0.5 µM
Template DNA	100 ng
Q5 High-Fidelity DNA Polymerase	0.02U/µl
dH_2O	Make up 50 µl final

Primers used for amplification:

T7 forward: 5' - TAA TAC GAC TCA CTA TAG GG - 3'

BGH Reverse: 5' - TAG AAG GCA CAG TCG AGG - 3'

2.4.4. Agarose gel electrophoresis

Gels were made containing either 0.8% (w/v) or 1% (w/v) agar in 1X TAE buffer (40mM Tris pH 7.6, 20mM acetic acid, 1mM EDTA). 1 µg/ml ethidium bromide was used as a staining agent. Electrophoresis was performed at 100 V for approximately 1 h. Separated DNA bands were visualized using G-Box chemiluminescence and UV transilluminator (Syngene).

2.4.5. Ethanol precipitation of DNA

DNA precipitation was performed by adding 0.1 volume of 3M sodium acetate pH 5.2, followed by adding three volumes of 100% ethanol. The mixture was then incubated at -70˚C for 20 min followed by centrifugation at 16,000x g for 10 min at 4˚ C. The pellet was washed twice with 70% ethanol, then air-dried for 10 min and re-suspended in sterile water or TE (10mM Tris-HCl, 1mM EDTA).

2.4.6. Large scale DNA purification

Using a sterile pipette tip single colonies were picked from the LB plates streaked with *E.coli* cells and incubated at 37° C overnight containing the plasmid. The colony was then inoculated into 2 ml of LB medium containing appropriate antibiotic and cultured at 37°C in a shaking incubator for 6 h. The culture was then diluted at 1:500 in 100 ml of fresh LB medium containing appropriate antibiotic and cultured at 37° C in a shaking incubator for 16 h. The DNA was then purified using DNA maxiprep kit (Qiagen) according to manufacturer’s instructions.

2.4.7. Double digestion of plasmid using restriction enzymes

Restriction enzyme digest of the plasmid was performed by adding 1 µg of DNA to 1 µl of 10x enzyme buffer, 1 U of enzyme, then made up to 10 µl with either water of TE. The samples were then incubated at 37˚C for overnight. Plasmid was ethanol precipitated, pelleted in the tube by centrifuging and the supernatant was aspirated. Same volumes of second restriction enzyme was added and incubated at 37˚ C for 3 hours and analysed using DNA gel electrophoresis.

2.4.8. Gel purification of DNA fragments

After running the DNA on agarose gel, bands containing DNA fragments of interest were excised from the gel using a clean scalpel blade. The gel fragments were subsequently digested and purified from agarose using Qiagen gel extraction kit (Qiagen) following the manufacturer's protocol.

2.4.9. Addition of 3' A overhangs to linear plasmid

After amplification of VEGFR cDNA using PCR as described previously in 2.4.3. 3' A overhangs were added to generate sticky ends for direct cloning into TOPO vectors.

Table 2.3. Composition of PCR reaction mix for addition of 3' A overhangs

	Final concentration
Purified PCR product	0.30 pmol
dATP	0.2 mM
Taq PCR buffer (10X)	1X
Taq Polmerase	1 U
dH_2O	Make up 50 µl final

The reaction mixture was prepared as mentioned in Table 2.2 and then incubated for 25 min at 72°C in thermal cycler. 2µl of mixture was then used for ligation into TOPO vectors as described in 2.4.10

2.4.10. Ligation of VEGFR cDNA with 3' A overhangs into pCDNA5/FRT/TOPO vector

After addition of 3' A overhangs to VEGFR cDNA, 2µl of reaction mixture was used for direct cloning into pCDNA5/FRT/TOPO vector by preparing the following reaction mixture.

Table 2.4. Composition of PCR reaction mix for ligation

	Volume
Purified PCR product	2 µl
Salt solution 6X (1.2M NaCl, 60 mM $MgCl_2$)	1 µl (final concentration 200 mM NaCl, 6 mM $MgCl_2$)
dH_2O	2 µl
Linear TOPO vector	1 µl
Final volume	6 µl

The mixture was incubated on ice for 5 min and then added to *XL-10* competent cells prepared as mentioned in 2.4.1. The cells were further incubated on ice for 5 min, then heat shocked for 30 sec at 42°C and immediately transferred onto ice. 250 µl of SOC media was added and incubated at 37° C for 1 h with horizontal shaking. 100 µl of mixture was spread onto LB plate containing ampicillin (100µg/ml) for selection and incubated for 24 h at 37° C. After incubation 5 colonies were picked to screen for the presence of TOPO plasmid and VEGFR insert.

2.4.11. Plasmid DNA sequencing

Plasmid was isolated as previously described in **2.4.6** and sent to Source Bioscience (Nottingham, UK) for sequencing. Plasmids were sent at 100 ng/µl, primers at 3.2 pmol/µl, and PCR products at 10 ng/µl per. The following primers were used for sequencing

CMV forward: 5'- CGC AAA TGG GCG GTA GGC GTG - 3'

BGH Reverse: 5' - TAG AAG GCA CAG TCG AGG - 3'

2.5. Cell Culture

2.5.1. Cell Passage

Normal HEK293 cells are not resistant to zeocin, they acquire resistance to zeocin due to insertion Flp-in. Therefore, commercial HEK293 'Flp-In' cells were maintained in DMEM high glucose media with 5 µg/ml zeocin antibiotic and split every three days when they reach 80% confluency. The cells were setup for transfection at passage number 3 and continued monitoring their passage number after transfection.

2.5.2. Lipofectamine transfection

HEK293 cells were plated to reach the confluency of 50% on the day of transfection. For a 6 well plate, 2.5 µg of DNA was added to 125 µl of opti-MEM (solution A). 7.5 µl of Lipofectamine 2000 (ThermoFisher, UK) was added to 125 µl of opti-MEM and mixed well and incubated for 5 min at room temperature (solution B). Solutions A and B were mixed gently by pipetting and incubated at room temperature for 20 min. After incubation, the mixture was added to the cells slowly drop-wise and incubated at 37˚ C for 6-8 hours. Medium was replaced with complete medium and cells were allowed to grow. Two days after transfection, 3µg/ml puromycin was added and the clones generated were screened after 10 days

2.6. Protein analysis

Table 2.5. List of antibodies used

Antibody name	Source
Goat anti-VEGFR1	R & D systems
Goat anti-VEGFR2	R & D systems
Goat anti-VEGFR3	R & D systems
Mouse anti-FLAG	Sigma
Rabbit anti-sheep Alexa Fluor 488	Invitrogen

Rabbit anti-mouse Alexa Fluor 488	Invitrogen
Rabbit anti-VEGFR2 pY951	Cell Signaling Technology
Rabbit anti-VEGFR2 pY1175	Cell Signaling Technology
Rabbit anti-VEGFR2 pY1214	Cell Signaling Technology
Mouse anti-pY20	Abcam
Sheep anti-LOX-1	Santa Cruz Biotechnology
Mouse anti-actin	Abcam
Mouse anti-tubulin	Abcam
Mouse anti-goat IgG	R & D systems
Rabbit anti-mouse IgG	R & D systems
Mouse anti-rabbit IgG	R & D systems

2.6.1. Preparation of cell lysates

After aspirating off the media, cells were washed thrice with ice-cold PBS. Cells were then lysed with lysis buffer (2% (w/v) SDS, 50mM Tris-HCl pH 7.4, 150mM NaCl, 2mM ethylene diamine tetraacetic acid (EDTA), 2 mM ethylene glycol tetraacetic acid (EGTA), 1 mM phenylmethylsulfonyl fluoride (PMSF) in PBS). For Immunoblot analysis the lysates were boiled at 95˚ C for 5 mins and sonicated for 3 seconds. Lysates were flash frozen in liquid nitrogen and stored in -20˚ C.

2.6.2. BCA Assay

To estimate the concentration of total protein in lysates, bicinchoninic acid assays (BCA) were performed using a 96-well plate format. Total protein lysates were then added in duplicates of 5µl each. Bovine serum albumin was used a standard protein (2-10 ug range). After addition of BCA reagent, the plate was incubated at 37˚C for 15-20 minutes and then the absorbance was measured at 562 nm using a varioscan flash plate reader (ThermoFisher, UK). Based on the BSA absorbance values, a standard curve was plotted. The protein concentrations of the lysates were determined from the equation of the line fitted to the standard values.

2.6.3. SDS-PAGE

After quantification of protein in a cell lysate, volume required for 30 µg of protein was estimated, equal volume of 2X sample loading buffer (1 M Tris-HCl pH 6.8, 20 % (v/v) glycerol, 4 % (w/v) SDS, 0.1 % (w/v) bromophenol blue and 4 % (v/v) β-mercaptoethanol) was added and incubated for 5 minutes at 95˚C. Samples were then loaded onto 10% (w/v) SDS-polyacrylamide resolving gel containing 5 % (w/v) SDS-polyacrylamide stacking gel, and subjected to electrophoresis at 120-130V for 1.5-2 h at room temperature in SDS-running buffer (192 mM glycine, 25 mM Tris, 0.1 % (w/v) SDS) until the blue dye interface had run down to the bottom of the gel.

2.6.4. Blue native polyacrylamide gel electrophoresis

Purified samples were separated using blue native polyacrylamide gel electrophoresis using 4-16% NativePAGE Bis-Tris precast gels to validate the native state of the proteins. Samples were prepared using a Coomassie G-250 sample additive that displaces detergent from membrane proteins, converting hydrophobic sites to negatively charged sites required for NativePAGE electrophoresis. The NativePAGE 5% G-250 sample additive was added to detergent containing samples such that the final G-250 concentration is 1/4th of the detergent concentration. 4X NativePAGE sample buffer was added at the ratio of 1:4 prior to electrophoresis. Anode running buffer was prepared using 20X NativePAGE running buffer at 1:20 ratio using deionized water to make the final 1X concentration for outer buffer chamber. For inner chamber, Dark blue and light blue cathode buffers were made using 20X NativePAGE running buffer at 1:20 ratio, 20X NativePAGE cathode additive at 1:20 and 1:200 ratio respectively. Samples were loaded onto the gel prior to filling the cathode buffer chamber for easy visualization of sample wells, NativePAGE unstained protein marker was used as standard. After sample loading, the inner chamber was loaded with dark blue cathode buffer and the outer chamber with anode buffer. Electrophoresis was performed at 150 V constant for 90 min and the dark blue cathode buffer was then replaced with light blue cathode buffer and further electrophoresis was performed for 30 min. After electrophoresis, proteins were either transferred onto a PVDF membrane or stained with Coomassie blue as described in section 2.6.10. Proteins were transferred to the PVDF membrane only because the nitrocellulose is not compatible for blotting NativePAGE gels since the Coomassie G-250 dye binds very tightly to the membrane and also the membrane is not compatible for fixing, staining/destaining. Prior to transfer the PVDF membrane was activated by treating with 100% methanol for 30 seconds, Gel was then sandwiched between the blotting pads and membrane, transferred at 25 V constant for 1 hour according to manufacturer's instructions using XCell-II blot module (Invitrogen). After transfer, membrane was treated with 8% acetic acid for 15 min to fix the proteins, and the membrane was probed and developed using specific antibodies as described in 2.6.6.

2.6.5. Dot blotting

For dot blotting, 2-3 µl of protein samples were dotted onto a nitrocellulose membrane and let the blot dry for 5 mins. To block nonspecific binding, membranes were incubated in 5% skimmed milk in TBS-T (20 mM Tris-HCl pH 7.6, 137 mM NaCl, 0.1% (v/v) Tween-20) for 1 hr on the orbital rocker. Membranes were then probed with primary antibodies diluted in 2 % Bovine serum albumin (BSA), 1 mM sodium azide in TBS-T for overnight at 4˚C. Membranes were then washed three times for 10 min with TBS-T and probed with species-specific horseradish peroxide (HRP)- conjugated antibodies for 1-2 hrs at room temperature. Membranes were washed again three times for 10 min in TBS-T, and blots were developed by incubating briefly with EZ-ECL combined enhanced chemiluminescence for 2 min. Bound antibodies were then visualised using a G-Box (Syngene) workstation.

2.6.6. Western blotting

After electrophoresis, proteins were transferred onto a nitrocellulose membrane (0.2 µm pore size) (GE healthcare life sciences) in transfer buffer (106 mM glycine, 25 mM Tris, 0.1 % (w/v) SDS, 20 % (v/v) methanol) at 300mA for 3 hours or at 30mA for overnight at 4˚C. Membranes were briefly stained with Ponceau S stain to check if the transfer was successful, and rinsed briefly with TBS-T. To block nonspecific binding, membranes were incubated in 5% skimmed milk in TBS-T for 1 hr on the orbital rocker. Membranes were then probed with primary antibodies diluted in 2 % Bovine serum albumin (BSA), 1 mM sodium azide in TBS-T for overnight at 4˚C. Membranes were then washed three times for 10 min with TBS-T and probed with species-specific horseradish peroxide (HRP)-conjugated antibodies for 1-2 hrs at room temperature. Membranes were washed again three times for 10 min in TBS-T, and blots were developed by incubating briefly with EZ-ECL combined enhanced chemiluminescence for 2 min. Bound antibodies were then visualised using a G-Box (Syngene) workstation.

2.6.7. Coomassie staining of gels

Gels were routinely stained with G250 Coomassie Brilliant Blue stain or Quick Coomassie stain (Generon, UK). For Brilliant Blue staining, gels were removed after electrophoresis and fixed for 2 hours in fixing solution (25 % (v/v) propanol, 10 % (v/v) acetic acid) and then incubated in stain 1 (0.025 % (w/v) G250 Coomassie Brilliant Blue, 10% propanol, 10% (v/v) acetic acid) for 2 hours and then stain 2 (0.0025 % (w/v) G250 Coomassie Brilliant Blue, 10 % propanol, 10 % (v/v) acetic acid) for 2 hours. The gel was then de-stained with several changes of de-staining solution (10 % (v/v) acetic acid) typically for 2 hours to overnight to remove the background.

2.6.8. Silver staining of gels

The silver stain has sensitivity down to 0.25 ng per band while the typical Coomassie Brilliant Blue G250 has 30 ng per band detection limit. As a more sensitive alternative to Coomassie staining, gels were stained using Pierce^{TM} Silver Stain Kit (ThermoFisher Scientific) following manufacturer’s protocol.

2.6.9. Immunofluorescence analysis (IF)

Stably transfected HEK293s cells were seeded on to sterile coverslips precoated with 0.1% (w/v) pig skin gelatin or 0.01 % poly-L-lysine respectively at 60 % confluency in 24-well plates, and cells were rinsed thrice with 500 µl of PBS. Cells were fixed in 400 µl of pre-warmed Sigma-Fix fixative (Sigma-Aldrich) for 10 min at 37˚C. The fixative was aspirated and coverslips were rinsed thrice with 500µl of PBS. Cells were then incubated with 50mM ammonium chloride (NH_4Cl) in PBS to quench the free aldehyde groups. Fixed cells were then permeabilized for 4 mins in 500µl of 0.2 % (v/v) Triton X-100 in PBS at room temperature. Coverslips were washed three times in 500 µl PBS and incubated for 30 mins in blocking buffer (5 % (w/v) BSA/PBS/0.02 % sodium azide) to block nonspecific antibody binding to the cells. 20 µl of primary antibody in blocking buffer is added to the coverslip and incubated in a moist staining chamber for overnight at room temperature. Coverslips were washed three times with 500 µl of PBS and 20 µl of secondary antibody containing 4 µg/ml donkey Alexa Flour-conjugated secondary antibody (Invitrogen), 2 µg/ml 4,6-diamidino-2-phenylidole (DAPI) in 1 % (w/v) BSA in PBS is added to the coverslip and incubated at room temperature for 2 h. Coverslips were washed three times with 500 µl of PBS and mounted onto slides using Fluoromount G (Southern Biotech). Images were acquired using an EVOS-FL inverted digital microscope (Life Technologies, UK). The realtive protein levels were analysed and quantified using Image J software.

2.6.10. Microscopy based analysis and quantification of VEGFRs expression

Microscopy data was quantified using ImageJ software. The HEK293 cells expressing VEGFRs were probed with protein specific primary antibody followed by species specific alexafluor 488 secondary antibody. The cells fixed on coverslips were imaged using Auto EVOS 2 electron microscope (ThermoFisher) at 10x or 20x magnification using two different filter cubes. DAPI blue filter with excitation at ultra-violet light (wavelength 358 nm) and GFP filter with excitation at 488 nm were used. The images captured using two cubes were overlaid and processed for quantification. Using ImageJ, the images were split into different channels using RGB split function (blue and green) and the raw intense pixel density of green channel representing the protein levels were measured, followed by division with number of cells (DAPI) in the region of interest. The measured pixel densities were then background corrected by subtraction with background pixel densities. The final VEGFR levels were estimated by normalising the measured intensities with negative controls (uninduced VEGFR).

2.7. Protein purification from bacterial culture (*E.coli*)

2.7.1. Recombinant protein expression in bacteria

An overnight culture of 50-100 ml was prepared from either a single colony or 0.5 ml of overnight culture using the appropriate antibiotic. The culture was diluted 1:25-1:50 into 1 litre of medium (+ antibiotic) in a large 2 litre flask. $OD_{550-600}$ was measure after vigorous shaking for 1-2 hrs until it is approx. ~0.3-0.4. IPTG was added at 0.1 mM final concentration and grown for required period (6 hrs to overnight). Decanted into 500 ml bottles and spun at 4000 rpm for 20-30 mins (pellets stored at -70°C overnight if needed).

2.7.2. Purification of soluble recombinant proteins (sLOX-1)

The pellets were resuspended in isotonic lysis buffer and 1 mg/ml lysozyme, incubated on ice for 15-30 mins. Sonicated with 4 x 20-30 sec bursts using sonicator. Added 1% detergent (TX-100 or NP-40) to increase lysis and release of protein (optional). Incubated on ice for 30 min and spun at 100 000 g (30 000 rpm in a Ti45 rotor) to generate a pellet and supernatant. Added to pre-equilibrated nickel-agarose resin and incubated on rotating wheel at room temp for 15-30 mins. The resin was packed into a disposable Econo column (Bio-Rad) and washed extensively with 30-50 ml of lysis buffer, followed by 30-50 ml of lysis buffer + 1% detergent, 30-50 ml lysis buffer + 0.5 M NaCl, and 30-50 ml lysis buffer, no detergent. The elution steps were performed at 10 x 1 ml elution in buffer 0.1-0.5 M eluent (glutathione or imidazole, freshly made). The elutions were dialysed against PBS (+0.1 mM PMSF) or similar buffer, and protein concentration was measured using BCA assay (Pierce). Purified recombinant protein was then analysed by SDS-PAGE.

2.7.3. Purification of insoluble protein from inclusion bodies

The cells were resuspended in isotonic lysis buffer (1 mg/ml lysozyme) containing 1% NP-40 or TX-100, incubated on ice for 15-30 mins. The lysate was sonicated with 4 x 20-30 sec bursts using sonicator, incubated on ice again for 15-30 mins. The lysate was then spun at 15, 000 rpm for 20-30 mins (Sorvall or Beckman rotor) to generate a pellet and supernatant. The supernatant was removed, and the pellet was washed 3x with lysis buffer, fully resuspending pellet as much as possible - this removes contaminants from the inclusion bodies. Pellet was then solubilised in denaturing buffer (6 M GuHCl, 50 mM sodium phosphate pH 8.0) and placed on rotating for 30 mins to fully solubilise pellet. Centrifuged again at 15 000 rpm; pellet was kept for analysis (insoluble). Supernatant was added to Ni-NTA resin that has been pre-washed with denaturing buffer and incubated on rotating wheel for 60 mins. The resin and supernatant mixture was transferred to a column and washed extensively with 30-50 ml of denaturing buffer + 10-20 mM Imidazole, followed by 30-50 ml of lysis buffer + 1% detergent + 10-20 mM Imidazole, 30-50 ml lysis buffer + 1 M NaCl + 10-20 mM Imidazole, and 30-50 ml of denaturing buffer + 10-20 mM Imidazole. The elution steps were performed at 10 x 1 ml elution in buffer 0.1-0.5 M eluent (glutathione or imidazole, freshly made). 50 mM DTT was added to pooled fraction from a 1 M DTT stock. The fractions were dialysed extensively against denaturing buffer (+0.1 mM PMSF) and ensured that DTT levels are < 0.1 mM DTT. The protein concentration of the pooled fractions were measured using the BCA assay (Pierce) and SDS-PAGE. The recombinant protein was snap-frozen in liquid nitrogen and stored at -70°C.

2.8. Protein purification from HEK293 cells

2.8.1. Recombinant protein expression in Flp-In^{TM} HEK293T-Rex^{TM} cell line

The adherent HEK293 cells expressing VEGFRs were maintained in a T175 flask, split every three days using high glucose DMEM media into a new T175 flask at 1:5 dilution ratio. For large scale expression the cells were transferred into an 8 layered cell disc (Greiner bio-one) and induced with 1 μg/ml of tetracycline in 70

% ethanol for 36h. After induction, cells were removed by flushing with 5 mM EDTA in PBS 7.4 pH dissociating buffer. The cells were centrifuged to collect the pellets, flash frozen in liquid nitrogen and stored in -80° C for detergent solubilization studies and purification.

2.8.2. Detergent screening for membrane protein solubilisation

2.8.2.1. Purification from whole cell lysate

Cells induced with 1 μg/ml tetracycline for 36h were pooled and weighted. 8 g of cells were resuspended in 20 ml of lysis buffer (1% DDM or SMA, 1x EDTA free protease cocktail inhibitor, 1 mM PMSF). Cells were sonicated for 5 seconds on and 10 seconds off for 90 seconds, 10 U of benzonase nuclease was added to the mixture and incubated for 1h in the cold room (4° C). The solubilized lysate was centrifuged at 2000 *xg* for 20 min, the supernatant was transferred into a suitable ultracentrifuge tube and centrifuged using TLA 100 or TLA 110 rotor at 100,000 *xg*, at 4° C for 60 mins. The supernatant from ultracentrifugation was added to 500 µl of fresh monoclonal mouse anti-FLAG resin or used anti-FLAG resin washed with FLAG binding buffer (20 mM Tris.HCl, 100 mM NaCl, 10% (v/v) Glycerol, 1mM PMSF, 1x protease cocktail inhibitor, pH 7.5), incubated overnight at 4° C with end over end mixing. The resin was added to a 5 ml column the next day, the flow-through was collected and run through the column twice to further capture any unbound receptor and increase the efficiency. The resin was then washed with three column volumes (15 ml) of binding buffer (20 mM Tris.HCl, 100 mM NaCl, 1mM EDTA, 10% (v/v) Glycerol, 1mM PMSF, 1x protease cocktail inhibitor, pH 7.5 with 0.1% DDM), then washed again with three column volumes (15 ml) of high salt wash buffer (20 mM Tris.HCl, 500 mM NaCl, 1mM EDTA, 10% (v/v) Glycerol, 1mM PMSF, 1x protease cocktail inhibitor, pH 7.5 and 0.1 % DDM). The resin was washed with 1 column volume (5ml) of elution buffer (20 mM Tris.HCl, 300 mM NaCl, pH 7.5 and 0.1 % DDM) without FLAG peptide, and then eluted using 200 µl elution volume of 100 µg/ml FLAG peptide in elution buffer (20 mM Tris.HCl, 300 mM NaCl, pH 7.5 and 0.1 % DDM), five elutions were performed with 100 µg/ml FLAG peptide followed by five elutions with 200 µg/ml

FLAG peptide in elution buffer (20 mM Tris.HCl, 300 mM NaCl, pH 7.5 and 0.1 % DDM). The eluted protein was immediately used for EM studies or phosphorylation assays.

2.8.2.2. Purification from cell membrane

Similar to purification from whole cell lysate, the cells were induced with 1 μg/ml tetracycline for 36h were pooled and weighted. 8 gms of cells were resuspended in 20 ml of binding buffer (20 mM Tris.HCl, 100 mM NaCl, 10% (v/v) Glycerol, 1mM PMSF, 1x protease cocktail inhibitor, pH 7.5) without any detergent, sonicated for 15 seconds on and 1 min off for 6 cycles, spun at 110,000 *xg* at 4° C for 1h using TLA 100 or TLA 110 rotor. The supernatant was discarded, pellets were re-suspended in 10 ml of binding buffer containing 1 mM EDTA and centrifuged at 110,000 *xg* at 4° C for 30 min, supernatant was discarded again and then the pellets were re-suspended in high salt resuspension buffer (20 mM Tris.HCl, 500 mM NaCl, 1mM EDTA, 10% (v/v) Glycerol, 1mM PMSF, 1x protease cocktail inhibitor, pH 7.5). The mixture was spun again at 110,000 *xg* at 4° C for 30 min. The supernatant was discarded and the pellets (cell membranes) were re-suspended in 20 ml of binding buffer containing DDM of SMA detergent. Using a 10ml syringe and 22 gauge needle the pellets were mixed properly to obtain uniform mixture and incubated overnight at 4° C with end to end mixing. The next day the mixture was spun again at 110,000 *xg* at 4° C for 30 min to remove any insoluble membrane pellets which clog the resin. The supernatant was added to 500 µl of monoclonal mouse anti-FLAG resin and incubated for 2h at 4° C with gentle end to end mixing. The resin was added to a 5 ml column, the flow-through was collected and run through the column twice to further capture any unbound receptor and increase the efficiency. The resin was then washed with three column volumes (15 ml) of binding buffer (20 mM Tris.HCl, 100 mM NaCl, 1mM EDTA, 10% (v/v) glycerol, 1mM PMSF, 1x protease cocktail inhibitor, pH 7.5 with 0.1% DDM), then washed again with three column volumes (15 ml) of high salt wash buffer (20 mM Tris.HCl, 500 mM NaCl, 1mM EDTA, 10% (v/v) Glycerol, 1mM PMSF, 1x protease cocktail inhibitor, pH 7.5 and +/- 0.1 % DDM). The resin was washed with 1 column volume (5ml) of elution buffer (20 mM Tris.HCl, 300 mM NaCl, pH 7.5, and +/- 0.1 % DDM) without FLAG peptide, and then eluted using 200 µl elution volume of 100 µg/ml FLAG peptide in elution buffer (20 mM Tris.HCl, 300 mM NaCl, pH 7.5 and 0.1 % DDM), five elutions were performed with 100 µg/ml FLAG peptide followed by five elutions with 200 µg/ml FLAG peptide in elution buffer (20 mM Tris.HCl, 300 mM NaCl, pH 7.5 and +/- 0.1 % DDM). The eluted protein was immediately used for EM studies or phosphorylation assays

2.9. Mass spectrometry and protein ID analysis

The protein ID was performed using the Biomolecular Mass Spectrometry facility, University of Leeds. The proteins bands were manually excised from the gel and digested using Montage in-gel digest96 kit (Millipore, Germany) following the manufacturer's instructions. The sample was then desalted using µC18-Ziptips (Millipore), and loaded onto the nanoelectronspray capillary (Waters Micromass, UK). Using a tandem mass spectrometer (Waters Micromass, UK) the measurements were performed to determine the peptide sequences. The peptide fragments were analysed using TOF analyser and the data acquired was processed using MASSLYNX 3.5 software. The peptide sequences were the submitted to BLAST search for short matches on NCBI's database (http://www.ncbi.nlm.nih.gov/BLAST/).

2.10. Size exclusion chromatography of purified FLAG-tagged VEGFR2

The FLAG tagged VEGFR2 purified with FLAG peptide competitive elution as mentioned in sections 2.7.2.1 or 2.7.2.2 are subjected to size exclusion chromatography analysis using a superpose 6^{TM} increase 5/150 (GE Life Sciences). The elutions of VEGFR2 were pooled together (~ 600-800 µl) and concentrated using 100K molecular weight cutoff filter (Pierce^{TM} Protein Concentrators, 100 MWCO, 0.5 ml). The volume was brought down 50 µl by centrifugation at 4,000 *x* rpm for 10 min. Alternatively, the superpose column was washed with three column volumes of degassed distilled water and calibrated with two column volumes of binding buffer (20 mM Tris.HCl, 100 mM NaCl, pH 7.5, and +/- 0.1 % DDM). The concentrated VEGFR2 (50 µl) was loaded onto a Superose 6 column and run through the column at 0.1 ml per minute at 1 MPa pressure. The absorbance of elutions were measured at 216 nm and 280 nm wavelengths using two detectors. The elution volumes of each fraction were set at 100 µl and the collected fractions were analysed by dot blot or SDS-PAGE followed by western blot as mentioned in sections 2.6.5 or 2.6.6 respectively. The raw data from AKTA was collected and the chromatographs were generated using Origin Pro 8 software.

2.11. Protein activity assays

2.11.1 Cell based phosphorylation assay

The activity assays were performed in both endothelial cells (HUVECs) and HEK293 cells. For HUVECs the cells were starved for 30 min prior to stimulation with VEGF-A, whereas the HEK293 cells were induced with 1 µg/ml tetracycline for 36h prior to stimulation with VEGF-A. From stimulation the methodology was same for both cell lines. The cells were stimulated with different concnetrations of VEGF-A isoforms for different time periods. The cells were then lysed using lysis buffer (2% triton X100, 20 mM Tris 100 mM NaCl, 1 mM EDTA, 1 mM PMSF, 1X protease cocktail inhibitor, pH 7.5) or analysed using immunofluorescence as described in section 2.6.9. The cells lysates were analysed by SDS-PAGE and western blot as mentioned in sections 2.6.3 and 2.6.6 respectively.

2.11.2. *In vitro* phosphorylation assay

The *In vitro* phosphorylation was performed using a purified VEGFR2 receptor, the receptor was purified from HEK293 cell membranes solubilised in DDM detergent as mentioned in section 2.7.4, The BCA quantification method was unreliable for quantification of VEGFR2 due to impurities, therefore, the volume of receptor from the elution was kept consistent representing the same amount of VEGFR2 in all conditions. 8 µl of purified VEGFR2 was added to different concentration of VEGF-A_{165} (0.1-10 nM), 50 mM $MgCl_2$ was added along with different concentration of ATP (0-5000 µM). The mixture was made-up to 25 µl using 20 mM Tris, 100 mM NaCl, 1mM EDTA, 0.1 % DDM, pH 7.5, mixed gently by re-suspension and incubated for 30 min on ice. The reaction mixture was then analysed using SDS-PAGE and western blot as mentioned in sections 2.6.3 and 2.6.6 respectively. The same assay was also performed in the absence of VEGF-A_{165} ligand, with only difference being the volume of growth factor was replaced by 20 mM Tris, 100 mM NaCl, 1 mM EDTA, 0.1 % DDM, pH 7.5 buffer.

2.12. LDL and oxidised LDL preparation

2.12.1. Purification of LDL from blood

18 ml of blood was taken by a medical doctor from a consenting volunteer (under the University of Leeds, Faculty of Biological Sciences local ethical approval and license) and added to a tube containing 2 ml of 3.8 % (w/v) trisodium citrate to prevent coagulation. Plasma was then separated by centrifugation at 1500 *g* for 10 min. The plasma was transferred to a fresh tube and centrifuged again at 1500 *g* for 10 min. Plasma was mixed 4:1 with Opti-prep (Sigma) to give final concentration of 12 % (v/v) Iodaxinol, 1 ml of HBS (0.85% (w/v) NaCl, 10 mM HEPES pH 7.4) was added to 4.7 ml Beckman Opti-seal centrifuge tube. The plasma-Optiprep mix was layered under the HBS solution and centrifuged at 100,000 *g at* 16˚ C for 3 h. The different lipoprotein fractions form different bands in the tube. A deep orange band towards the top of the tube is formed by LDL, which was extracted using a 25 gauge needle attached to a 1 ml syringe. The extracted LDL was dialysed into PBS at 4˚C for 24 h. The concentration of LDL was measured by BCA assay.

2.12.2. Oxidation of LDL

After dialysis of LDL into PBS, native LDL was stored in an eppendorf tube containing 100 µM EDTA and 20 µM butylated hydroxytoluene (BHT) for storage. Oxidation is initiated by incubating LDL in 5 µM $CuSO_4$ for 24 h at 37˚C. After 24 h 100 µM EDTA and 20 µM BHT were added to terminate oxidation, and concentration of OxLDL was measured using BCA assay.

2.12.3. Agarose electrophoresis of lipid particles

The oxidation of LDL was verified using agarose gel electrophoresis and sudan black staining. The lipid was quantified using BCA assay and 4 µg of native LDL and oxidized LDL were loaded onto 0.5% (w/v) agarose gel in borate buffer (80 mM boric acid, 90 mM Tris-HCl pH 8.3, 3 mM EDTA) and run for 1 h at 100 V. The gel was fixed in fixing solution (75% (v/v) ethanol and 5 % (v/v) acetic acid for 15 min and then stained with sudan black solution (60 % (v/v) ethanol and 0.05 % (w/v) NaOH) for 3h. The gel was then washed with 50 % (v/v) ethanol to remove any excess unbound sudan black and imaged using G-Box (Syngene).

2.13. Size exclusion chromatography of lipoproteins

A 30 ml column was manually packed using Sephacryl S-100 High Resolution resin (GE, Life Sciences). The packed column was washed with three column volumes of degassed distilled water and calibrated with two column volumes of HEPES buffer (20 mM HEPES, 100 mM NaCl, pH 7.5). The lipoproteins (nLDL or OxLDL) (~500 µl) were loaded into the sephacryl S-100 column and run at 0.5 mL per minute at 2 MPa pressure and absorbance readings were measured at 216 nm and 280 nm wavelengths using two detectors. The elutions were collected at 200 µl fractions which were analysed on SDS-PAGE followed by western blot as mentioned in section 2.6.6. The raw data from AKTA was collected and chromatographs were generated using Origin Pro 8 software.

2.14. Microfluidic diffusion sizing (MDS) analysis

Microfluidic diffusion analysis was performed to measure the hydrodynamic radius (R_h) of purified lipoproteins and complexes. Fluidity one (Fluidic analytics, UK) equipment that works on dynamic light scattering (DLS) based microdiffusion technique was used. The lipoproteins (nLDL and OxLDL) that were run through the SEC column were used, 5 µl of purified lipoproteins were loaded on to the chip which was passed through the inlet reservoir, the auxillary fluid was loaded onto the second reservoir and both solutions were flown through a small capillary diffusion chamber where the lipoproteins diffused through based on size. At the

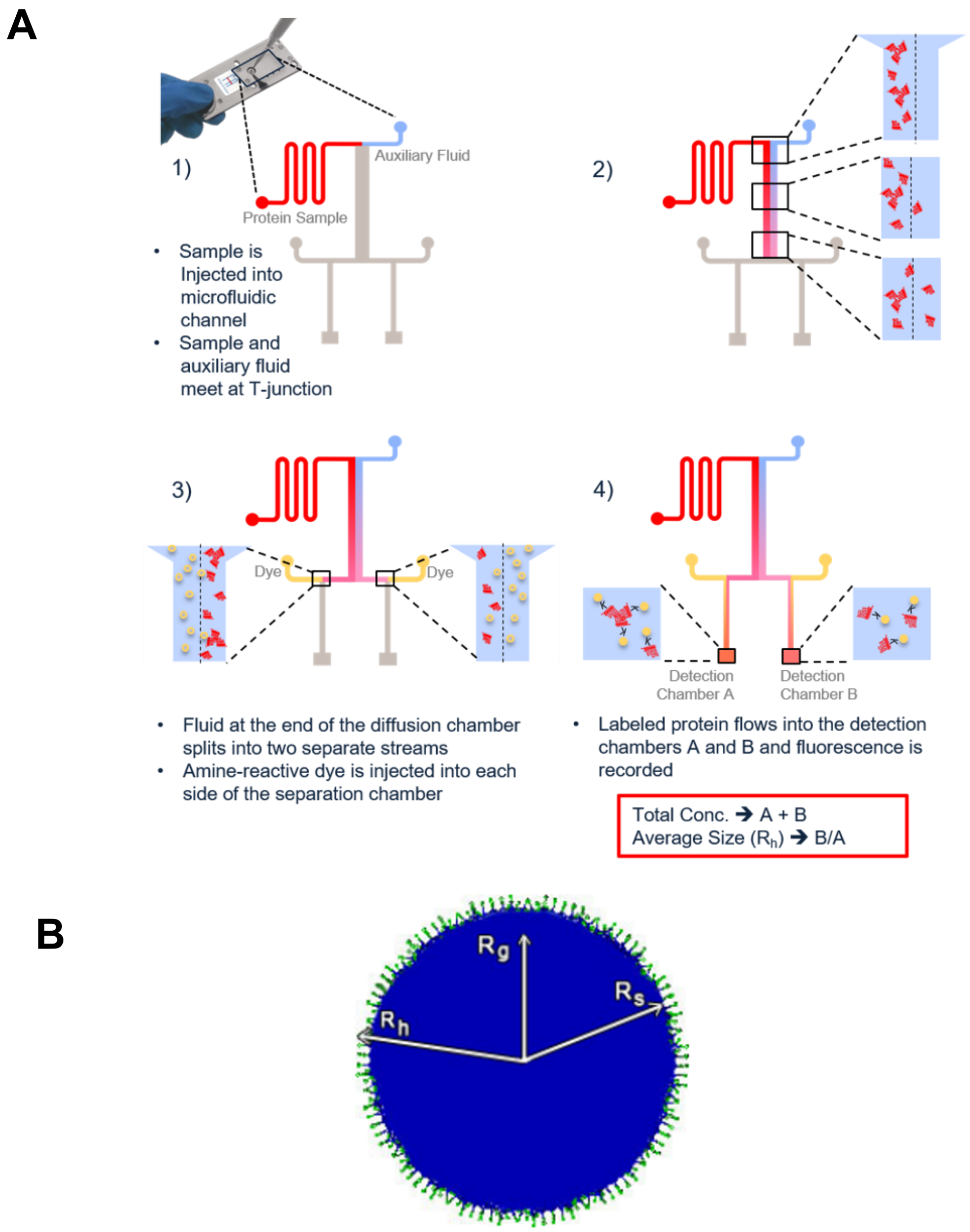

Figure 2.1. Dynamic light scattering-based microdiffusion technique for measurement of lipoprotein size. (A) Purified lipoprotein injected into a microfluidic chamber which meets the auxillary fluid at a T-junction, at the end of diffusion chamber the solution is split into two streams. Amine-reactive dye is injected into each chamber separately and the average protein size (R_h) is estimated based on protein flow in detection chamber. Image reproduced with permission from Arosio et al., 2016. **(B)** Comparison of various radius terms used to characterize proteins, hydrodynamic radius (R_h), radius of gyration (R_g), and stokes radius (R_s). The protein is represented as blue sphere. Image reference Brookhaven Instruments.

end of diffusion chamber the fluid is again split into two streams. An amine reactive dye (Alexa Fluor 488) is automatically injected in the separation chamber, by recording the fluorescence in detection chambers A and B the average size (hydrodynamic radius) of the particles were measured (Fig. 2.1). The traces of diffusion profiles and sizes were measured by automation using Fluidity One.

2.15. Negative stain grid preparation

Negative stain grids were prepared by pipetting 2 µl of purified protein onto a carbon coated copper grid charged with PELCO easiGlow glow-discharge unit for 30 seconds. Using a Whatman blotting paper the excess solution was removed and then stained by pipetting 3 µl of 1 % (w/v) uranyl acetate onto the grid and dried under the desk lamp for 1 min, the excess uranyl acetate was then removed with blotting paper. The staining with uranyl acetate was repeated again before blotting the excess. After drying the grids were stored until screening. Negative stained grids were imaged using either using FEI F20 or Technai T12 microscope fitted with a Lab6 source operating at 120 kV (Astbury Centre for Structure Molecular Biology). Micrographs were collected on Gatan CCD camera at 50,000X magnification with defocus set between 0.5 and 2 µm.

2.16. Cryo-EM grid preparation for single particle analysis

Holey carbon grids (Quantifoil, Agar Scientific) were glow discharged for 20 seconds using a TED-PELLA glow discharge unit. FEI Vitrobot Mark IV was the used to produce cryo grids using standard 100% humidity settings and blot times between 3 or 4s, and blot force set to -2 to -3. 3 µl of sample was loaded on the carbon side of the grid before being blotted and plunge-frozen in liquid ethane. Grid was then transferred into pre-cooled grid box and stored in liquid nitrogen for analysis. Micrographs were collected using Titan Krios (FEI, ThermoFisher) equipped with Gatan 300 keV X-FEG electron source (Astbury Centre for Structure Molecular Biology), Falcon III direct electron detector camera set at 25,000X magnification with defocus set between 0.5 and 2 µm.

2.17. Single particle data processing using RELION 3

The micrographs were collected from FEI F20 (negative stain-EM of VEGFR2) and Titan Krios (cryo-EM of OxLDL) and analysed using RELION 3 data processing software that works on Linux operating system (Fernandez-Leiro and Scheres, 2017, Zivanov et al., 2018). The Arc 3 high speed supercomputer (University of Leeds) was used with remote access for data processing. Firstly, the micrographs of OxLDL collected using Titan Krios were generated over the weekend with automation, therefore, micrograph movies were generated which were motion corrected to produce a beam induced motion correction files. Then the contrast transfer function (CTF) was estimated for each corrected micrograph and then processed for manual particle picking. Whereas, the micrographs of VEGFR2 from negative stain EM were manually collected using FEI F20 microscope, and they were directly processed for manual particle picking as the beam induced motion correction is not required for non-movie micrographs generated from negative stain. The particles picked were extracted with particle box size set at 300 Å for OxLDL and 250 Å for VEGFR2. The extracted particles were used for reference free 2D class averaging. The VEGFR2 classes didn’t exhibit enough views to produce a *de novo* 3D model; whereas, OxLDL 2D classes were used further to generate 3D model using C2 symmetry reconstruction.

2.18. 3-D modelling of lipoproteins using UCSF chimera

The model.mrc 3D extension file of OxLDL generated from RELION 3.0 was used for further processing using UCSF chimera program. The unwanted background density noise was removed using volume remover, and different side views with cross sections of the model were generated using volume viewer > density range option. The superimposed 3-D model of nLDL and OxLDL was generated using chimera by multireference aligning the density maps of both nLDL (EM ID:5239) and OxLDLmrc extension 3-D map. The overall dimensions (length x width x height) of OxLDL 3-D model was also generated using volume data > measure volume and volume tracer options on chimera.

2.19. Statistical analysis

This was performed using the unpaired two-tailed students *t*-test for two groups and one-way analysis of variance (ANOVA) followed by two-way ANOVA using GraphPad prism software (La Jolla, CA, USA). Significant differences between the control and test groups were evaluated with *p* values less than 0.05 (*), 0.01 (**), 0.001 (***) and 0.0001 (****) indicated on the graphs. Error bars in graphs denote ± SEM (standard error of mean)

CHAPTER 3

Construction and characterization of tetracycline-inducible VEGFR expressing human cell lines

3.1. INTRODUCTION

VEGFRs are associated with physiological and pathological angiogenesis, various types of cancers and neurodegenerative diseases (Schlessinger, 2000, Otrock et al., 2007, Stuttfeld and Ballmer-Hofer, 2009, Harris et al., 2018, Janelidze et al., 2015, Lim et al., 2012). VEGFRs have differing expression profiles, with VEGFR2 and VEGFR3 expressed largely in immune, vascular and neural tissues. The study of VEGFR function in an experimentally tractable system will be beneficial for relevance to diseases such as cancer, neurodegenerative disease, and immune dysfunction.

The choice of the mammalian expression system plays a crucial role in the quality and quantity of recombinant membrane protein expressed for functional and structural studies. The expression and purification of recombinant integral membrane proteins from bacteria, yeast, and insect cells have led to >300 diverse protein structures (Andréll and Tate, 2013). However, the frequent drawbacks in these expression systems include low expression, aggregation, insolubility, proteolysis, lack of post-translational modifications e.g. glycosylation, improper protein folding, and functionally inactive states (Vinothkumar and Henderson, 2010). To circumvent these issues mammalian expression systems based on Human Embryonic Kidney (HEK293), murine myeloma NS0 and Chinese Hamster Ovarian (CHO) immortalised cell lines have become a popular choice for membrane protein expression. Recombinant membrane proteins produced in these expression systems display native folding, retain tertiary structure, undergo appropriate post-translational modifications, and remain functionally active (Büssow, 2015, Berlec and Strukelj, 2013).

Since the VEGFRs are involved in cell proliferation, migration and survival, VEGFR overexpression can potentially burden the cells by unwanted activation of several signalling pathways (Moriya, 2015). Therefore, VEGFR expression needs to be tightly regulated. Using an inducible expression system would be one way of controlling VEGFR expression in such cell types. The mammalian Flp-In^{TM} HEK293 T-Rex^{TM} expression cell lines which are commercially available enable stable integration of a recombinant transgene and places gene transcription and protein expression under control of tetracycline (or doxycycline) addition (Gossen & Bujard, 1992). Based on the original system developed by Bujard and colleagues (Gossen & Bujard, 1992, Urlinger et al., 2000). The current commercially available system has a single FRT recombination site at the active locus which enables uniform protein expression across the cell population when transfected with Flp-In expression vector. These HEK293 T-Rex cells also stably express the engineered Tet-binding transactivator. Co-transfection of the recombinant transgene cloned into a Flp-In expression vector and Flp-In recombinase vector allows stable integration of the transgene into the FRT locus and now places expression under control of the Tet repressor (O'Gorman et al., 1991). In the absence of tetracycline, the Tet repressor forms a homodimer and binds with high affinity to two Tet responsive element (TRE) sequences upstream of the FRT locus thereby blocks gene transcription. This enables tight regulation and timing of gene expression and also eliminates variability in transgene expression (Fig. 3.1) (Das et al., 2016, O'Gorman et al., 1991).

For VEGFR-based studies, such an inducible mammalian expression system would be ideal, as the expression can be controlled by exogenous effector molecule, such as tetracycline. This human cell line expression platform also produces the human protein in its most relevant or native state. In this chapter, the objective was to construct inducible VEGFR1, VEGFR2, and VEGFR3 expression cell lines that could be useful platforms for biochemical, structural and cellular studies.

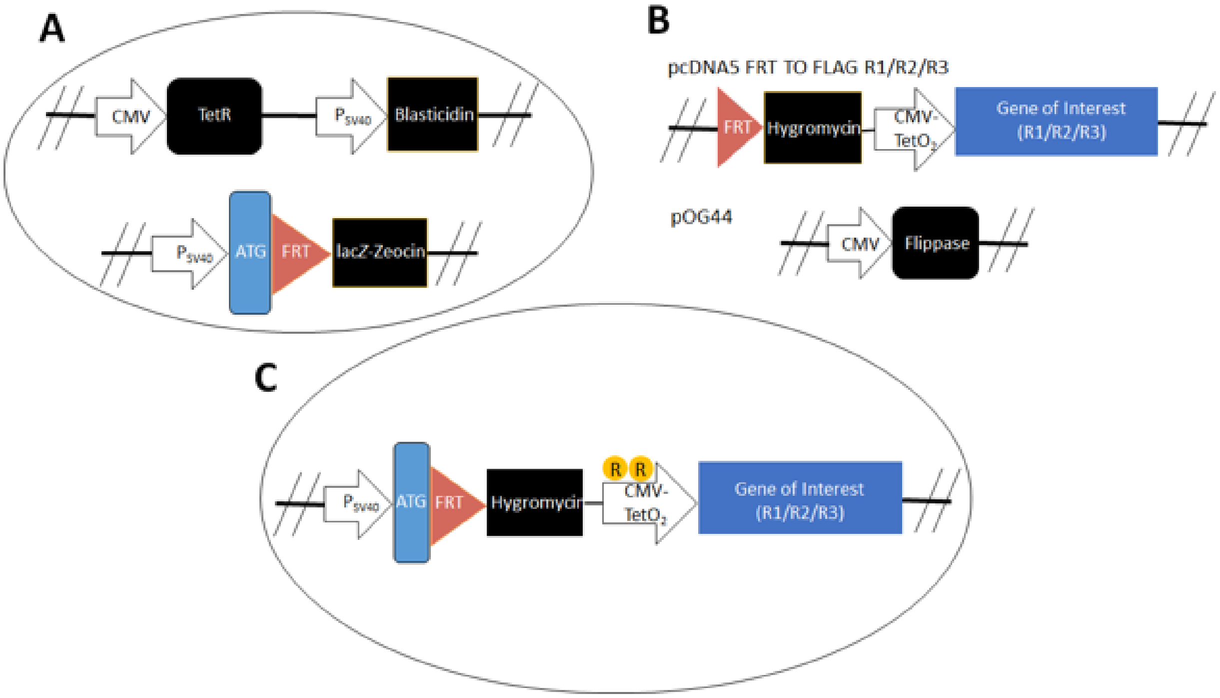

Figure 3.1. Schematic diagram of Flp-In T-Rex tetracycline-inducible expression system. (A) pFRT/lacZeo and pcDNA/TR integrated into the genome of Flip-In T-Rex HEK293 cell line. **(B)** Co-transfection of pcDNA5/FRT/TOPO VEGFR vector and pOG44 in the HEK293 T-Rex cell line. **(C)** Gene of interest (GOI) stably integrated for regulated expression by tetracycline. Tet repressor (yellow) binds to the promoter region and represses GOI transcription in the absence of tetracycline.

3.2. RESULTS

3.2.1. Generation of VEGFR expression constructs

3.2.1.1. Sub-cloning of human VEGFRs into the FLP Recombination Target (FRT) plasmid vector

The specific objective was to generate HEK293 Flp-In^{TM} T-Rex^{TM} cell lines for inducible expression of VEGFR1, VEGFR2 and VEGFR3. Following characterisation of the expression and localisation of recombinant VEGFRs in each cell line, receptor could be isolated to support biochemical and structural studies. The strategy used for building constructs and transfection of cells is shown in Fig. 3.2 pCMV3 constructs with a CD33 signal peptide (SP), N-terminal FLAG-tag and VEGFR cDNA inserts i.e pCMV3-SP-VEGFR1, pCMV3-SP-VEGFR2 and pCMV3-SP-VEGFR3 were purchased commercially and used as templates for subcloning the CD33 SP-FLAG-VEGFR cDNA into pCDNA5-TA-TOPO vector and transfected into HEK293 Flp-In^{TM} T-Rex^{TM} cells.

The schematic map of each open reading frame (ORF) comprising CD33 SP-FLAG-VEGFR constructs is shown in Fig. 3.2, with a *KpnI* restriction site located before the ATG start codon in the VEGFR hybrid cDNA construct, whereas *XbaI* is positioned after the stop codon at the 3' end. These hybrid constructs were digested using *KpnI* and *XbaI* to validate the presence of VEGFR cDNA inserts in the pCMV3 plasmid, and agarose gel electrophoresis was performed (Fig. 3.3). *KpnI* and *XbaI* were used for single and double digestion of constructs.

pCMV3-SP-FLAG-VEGFR1 (10.16 kb) plasmid digested with *KpnI* produced a linear single band at 10.16 Kb. Digestion with *XbaI* produced two fragments at 6.86 kb and 3.3 kb. Double digestion with *KpnI* and *XbaI* produced three fragments at 5.28 Kb, 3.3 kb and 1.58 kb respectively (Fig. 3.3A). Two fragments in *XbaI* digest and three fragments with double digestion were due to the presence of a digestion site for *XbaI* enzyme in VEGFR1 cDNA. The uncut pCMV3-SP-FLAG-VEGFR1 construct was used as a negative control.

pCMV3-SP-FLAG-VEGFR2 (10.21 kb) plasmid digested with *KpnI* and *XbaI* individually produced a linear single band at 10.21 kb. Double digestion with *KpnI* and *XbaI* produced two fragments at 6.13 kb and 4.94 kb respectively (Fig. 3.3B). Unlike VEGFR1 cDNA, VEGFR2 doesn't contain digestion sites for both restriction enzymes. Therefore, only two fragments representing plasmid at 6.13 kb and VEGFR2 cDNA at 4.94 kb were produced. Subsequently, plasmid pCMV3-SP-FLAG-VEGFR3 (10.04 kb) digested with *KpnI* and *XbaI* individually produced a linear single band at 10.04 kb. Double digestion with *KpnI* and *XbaI* produced two fragments at 6.14 kb and 4.7 kb respectively (Fig. 3.3C). Similar to VEGFR2, VEGFR3 cDNA doesn't contain digestion sites for both restriction enzymes, thereby both VEGFR2 and VEGFR3 constructs produced single linear band upon single digestion with both *KpnI* and *XbaI*, and plasmid and insert fragments upon double digestion. The sizes of fragments on agarose gel represent the sizes of respective VEGFRs cDNA inserts and the pCMV3 plasmid vector.

After validating the presence of VEGFR inserts in pCMV3 plasmids, a gradient PCR was performed with T7 forward primer and BGH reverse primer with annealing temperature ranging from 55-68° C (Fig. 3.4). The site of primer binding on the pCMV3 plasmid is shown (Fig. 3.2), and the transgenes amplified by PCR contain the CD33 signal peptide, FLAG, linker fused to the respective VEGFR ORF. PCR products analysed by agarose gel electrophoresis, showed 4 kb, 4.1 kb, and 3.9 kb fragments which correspond to the hybrid human VEGFR1, VEGFR2, and VEGFR3 constructs respectively (Fig 3.4).

The PCR products produced in these experiments have blunt ends, so *Taq* polymerase treatment was used to add a single deoxyadenosine (A) nucleotide to the 3' end of each PCR product. PCR product A-tailing was performed to enable cloning into linear pCDNA5-FRT/TA/TOPO vector which had a single overhanging 3' deoxythymidine (T) residues at the site of insertion. This allows efficient annealing and ligation of the PCR product into the TOPO expression vector.

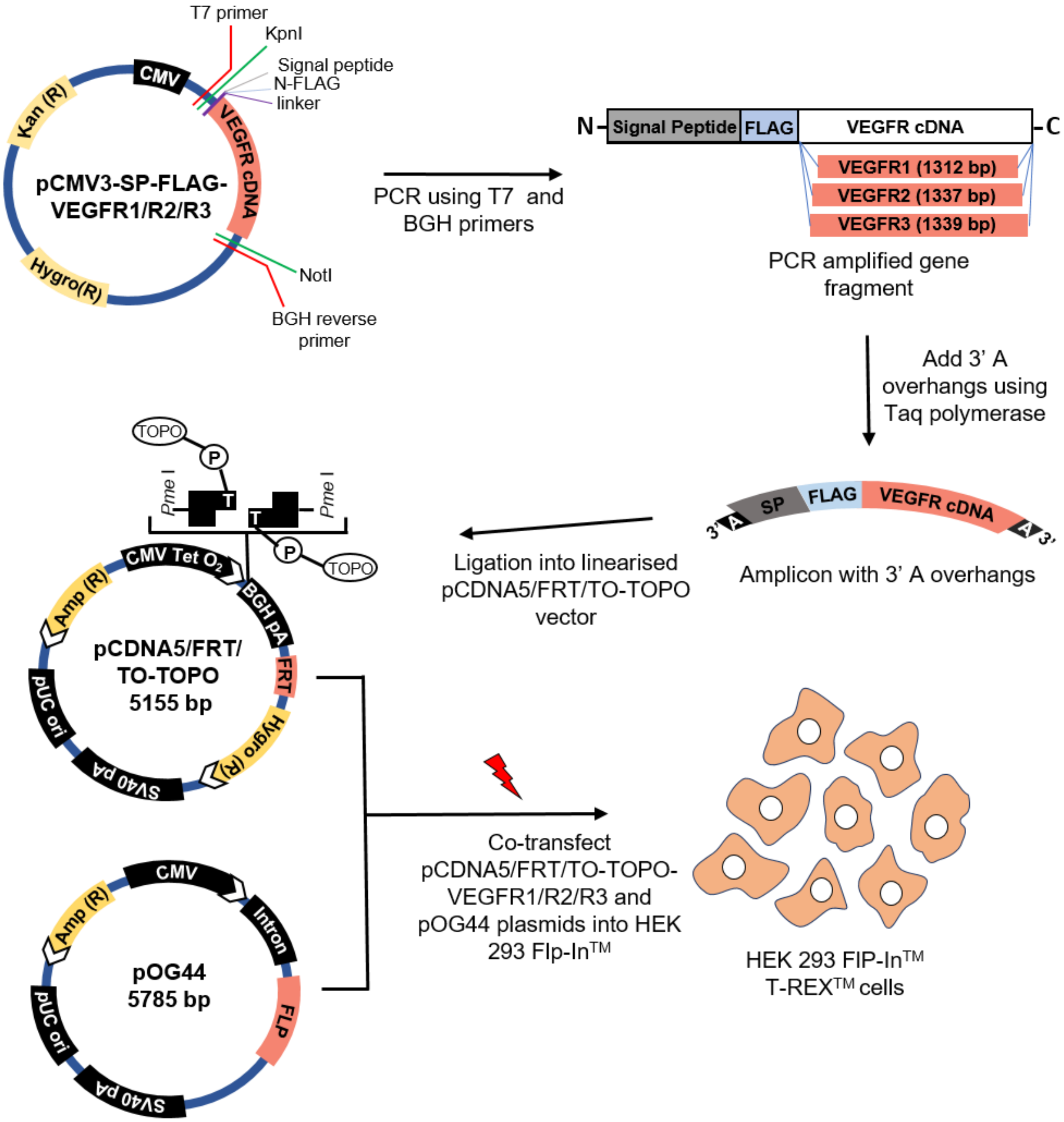

Figure 3.2. Schematic overview of construction of inducible FLAG-VEGFR cell lines. pCMV3 plasmids containing signal peptide (SP)-FLAG-VEGFR cDNAs were used to perform PCR amplification of the gene of interest (VEGFR cDNA) using an upstream T7 primer and downstream BGH primer. 3'-A overhangs added using Taq polymerase, before ligation into pcDNA5/FRT/TO/TOPO plasmid with complementary 3'-T sticky ends. HEK293 Flp-In^{TM} T-Rex^{TM} cells are co-transfected with pcDNA5/FRT/TO/TOPO/VEGFR and pOG44 plasmids for stable integration of transgene cassette into a genomic locus under control of the tetracycline repressor.

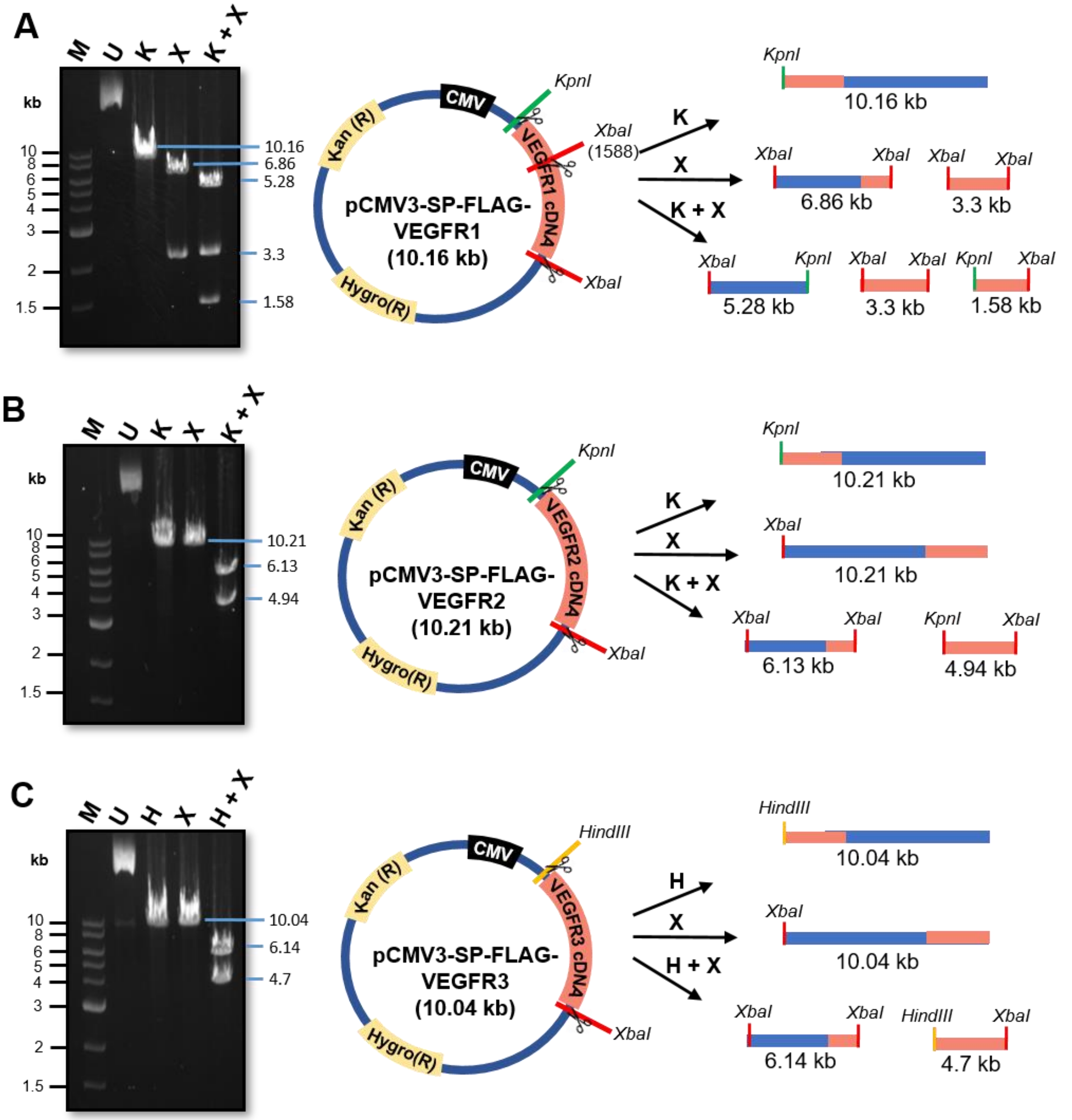

Figure 3.3. Analysis of recombinant pCMV3-FLAG-VEGFR constructs. Restriction digest and 1% agarose gel electrophoresis analysis of **(A)** pCMV3-SP-FLAG-VEGFR1, **(B)** pCMV3-SP-FLAG-VEGFR2, and **(C)** pCMV3-SP-FLAG-VEGFR3. 1 kb DNA marker (M), undigested plasmid (U), HindIII digest (H), XbaI digest (X), HindIII and XbaI double digest (H+X). Schematic representation of plasmid digests and fragment sizes indicated in each case.

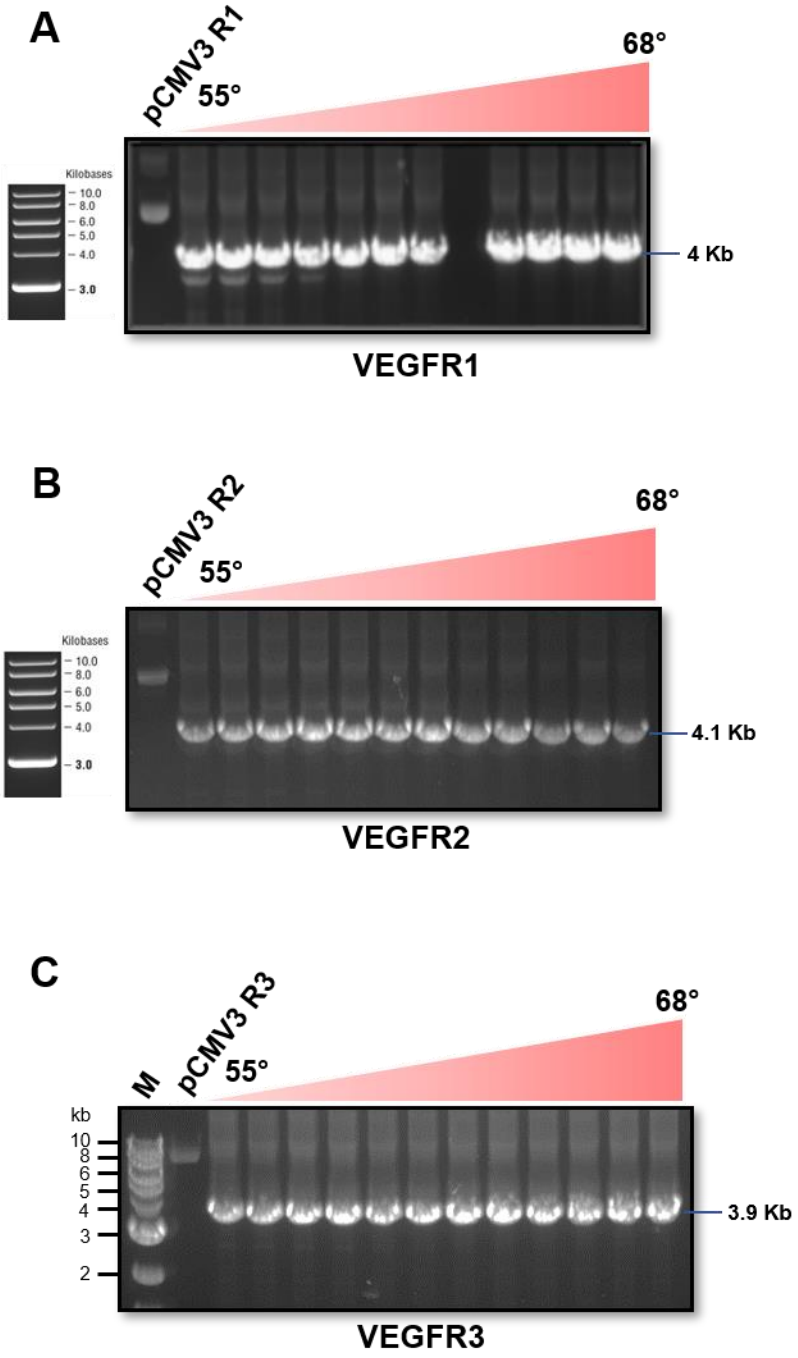

Figure 3.4. Gradient PCR amplification of VEGFR cDNAs. 1% Agarose gel electrophoresis of PCR amplification of **(A)** VEGFR1, **(B)** VEGFR2, and **(C)** VEGFR3 from pCMV3 vectors using T7 forward primer and BGH reverse primer. Lanes represent pCMV3 VEGFR vector, followed by PCR products with 1˚ rise in annealing temperature conditions from 55-68 ˚C respectively.

Transformation into the *XL-10 E.coli* strain was followed by screening clones for recombinant colonies. Four colonies were in each cloning experiment picked to analyse each VEGFR transgene inserted into pCDNA5-TO-TOPO plasmid vectors, followed by restriction digest analysis using the *PmeI* enzyme (Fig. 3.5). As shown in the schematic map of pCDNA5-TA-TOPO in Fig. 3.2, the site of the hybrid VEGFR cDNA insertion within the plasmid is located between two *PmeI* restriction sites. For VEGFR1 clones, only clone 3 showed two bands at 5.15 kb and 4 kb representing the plasmid and the insert in the correct orientation, the rest of the clones showed only one band at 5.15 kb but no insert. For VEGFR2 three clones out of four showed two bands each at 5.15 kb and 4.1 kb. Whereas for VEGFR3, all four clones showed bands at 5.15 kb and 3.9 kb respectively. These experiments showed successful production of recombinant plasmids carrying the hybrid VEGFR cDNAs cloned into the pCDNA5-TA-TOPO plasmid.

3.2.1.2. Checking the recombinant VEGFR sequence in pCDNA5-FRT-TO-TOPO plasmids

One limitation of using TA cloning is the possibility of changes in orientation and sequence at the site of insertion that may affect gene expression Sequencing was performed to verify the orientation of the VEGFR insert, and the sequence was translated to check for open reading frame (ORF) which showed the CD33 signal peptide (MPLLLLLPLLWAGALA), FLAG (DYKDDDDK), linker (GGGGS) followed by corresponding VEGFR ORFs (Fig. 3.6). The translation of the correctly oriented cDNA for each VEGFR ORF in the plasmid construct is shown (Fig. 3.6).

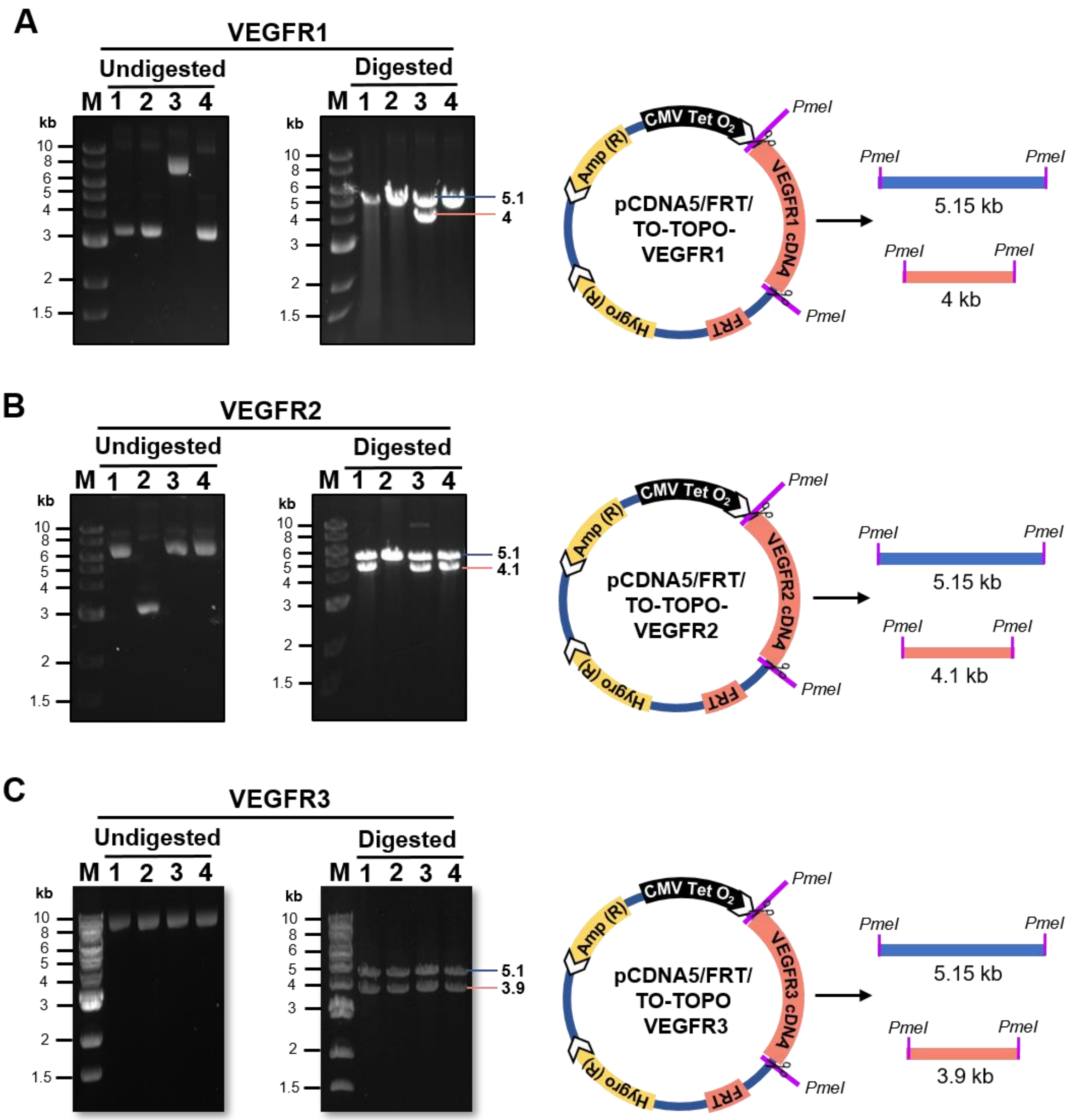

Figure 3.5. Screening clones of pCDNA5/FRT/TO-TOPO/VEGFR recombinant plasmids for the presence of DNA inserts. (A-C) Agarose gel electrophoresis showing plasmids purified from 4 selected colonies (labelled 1-4) from each cloning experiment. 1 kb DNA marker (M), undigested plasmid (1-4), and *Pme*I digest (1-4). Schematic representation of *PmeI* enzyme digest and fragment sizes produced. **(A)** pCDNA5/FRT/TO-TOPO/VEGFR1, **(B)** pCDNA5/FRT/TO-TOPO/VEGFR2, **(C)** pCDNA5/FRT/TO-TOPO/VEGFR3.

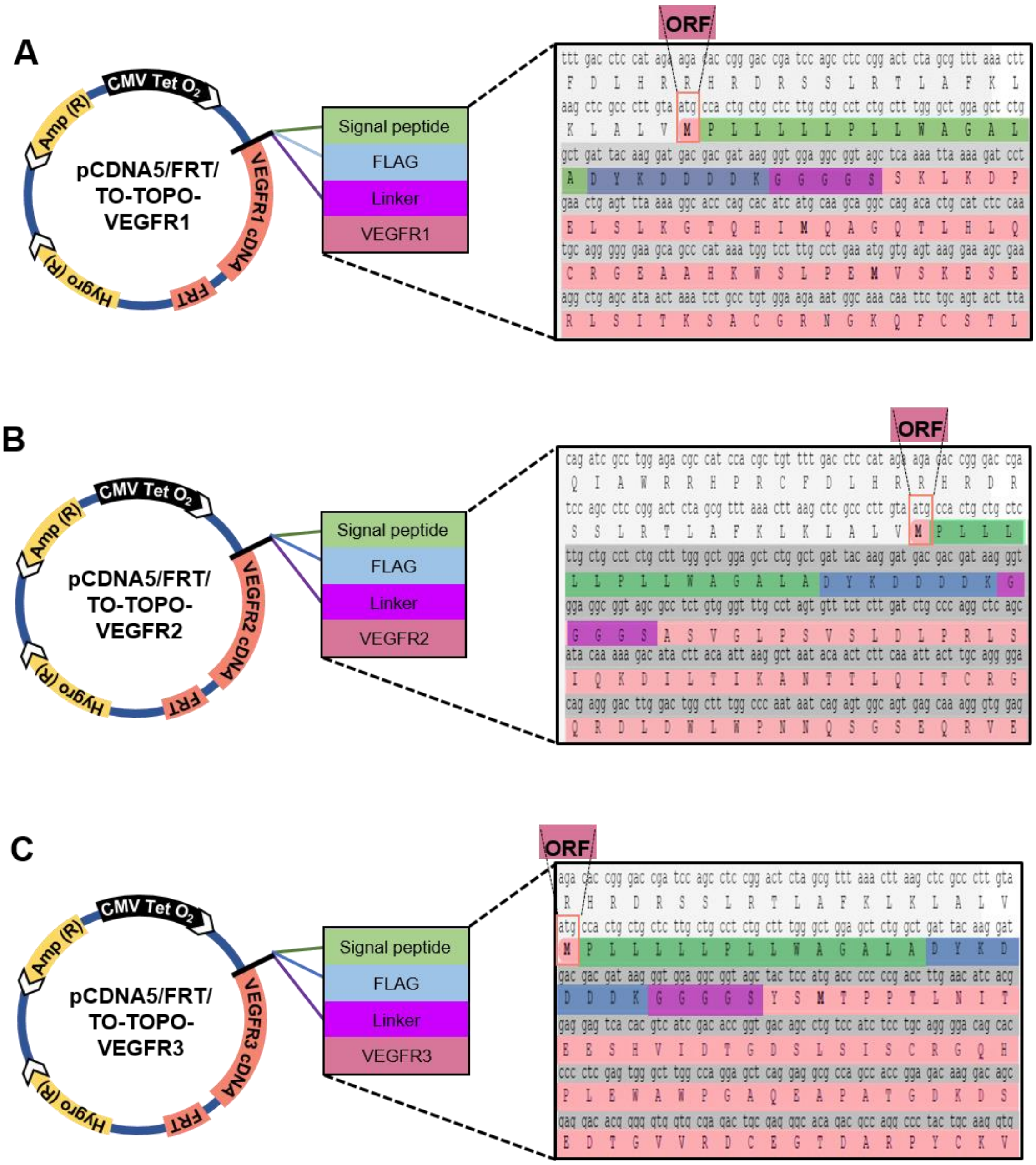

Figure 3.6. Sequence analysis of pCDNA5/FRT/TO-TOPO/VEGFR recombinants and open reading frames (ORFs). Plasmids containing inserts were sequenced to verify the orientation of insert, shows open reading frame (ORF) starting with Methionine (M) (pink); signal peptide (green); FLAG tag (blue); linker (purple), followed by receptor (pink). Analysis of recombinant plasmids corresponding to **(A)** pCDNA5/FRT/TO-TOPO/VEGFR1, **(B)** pCDNA5/FRT/TO-TOPO/VEGFR2, and **(C)** pCDNA5/FRT/TO-TOPO/VEGFR3.

3.2.2. Characterization of Flp-In^{TM} T-Rex^{TM} cell lines

To generate the stable HEK293 cell lines expressing the full-length hybrid VEGFRs, the commercially available HEK293 Flp-In^{TM} T-Rex^{TM} line was used. HEK293 Flp-In^{TM} T-Rex^{TM} cells were co-transfected with recombinant pcDNA5-FRT-TOPO-VEGFR plasmid and pOG44 plasmid (encoding the Flp recombinase). By stable integration pCDNA5-FRT-TOPO-plasmid and the VEGFR hybrid cDNA into the FRT site, the integrated plasmid confers cellular resistance to hygromycin B but now becomes sensitive to zeocin due to disruption of the FRT locus. An empty pCDNA5-FRT-TOPO plasmid vector without a cDNA insert was used as a negative control in these transfection experiments. The transfected cells were screened for sensitivity using hygromycin B selection marker with gradual increase in concentration from 25 µg/ml to 250 µg/ml over the course of 10 days, along with 15 µg/ml blasticidin. This ensured the elimination of parent non-transfected cells, thus allowed the growth of only stably integrated cells which acquired resistance to hygromycin B. After 10 days, the HEK293 T-Rex cells which developed resistance to hygromycin were pooled. The pooled cells were subjected to induction with 1 μg/ml of tetracycline for 24 h and then lysed to check for VEGFR expression using immunoblotting. Fig. 3.7 shows the Western blot of cell lines corresponding to the tetracycline-induced expression of all three VEGFRs; a mouse anti-FLAG antibody was used to detect FLAG-VEGFR protein expressed from the stably integrated transgenes. Untransfected HEK293 cells were used as a negative control and a purified FLAG-TRPM2 membrane protein (~170 kDa) was used as a positive control. After inducing with tetracycline, the parent HEK293 cells showed no bands, whereas each VEGFR stable cell line showed bands for VEGFR1 at 200 kDa, VEGFR2 at 250 kDa, and for VEGFR3, two bands were detected at ~ 230 kDa and 190 kDa. These two bands for VEGFR3 likely represent the mature glycosylated and immature partially glycosylated full-length forms before post-translational cleavage in the ER. The tubulin protein was used as a loading control for the quantification of relative VEGFR expression levels. The levels of VEGFR3 were four-fold higher in comparison to VEGFR2, whereas VEGFR1 expression levels

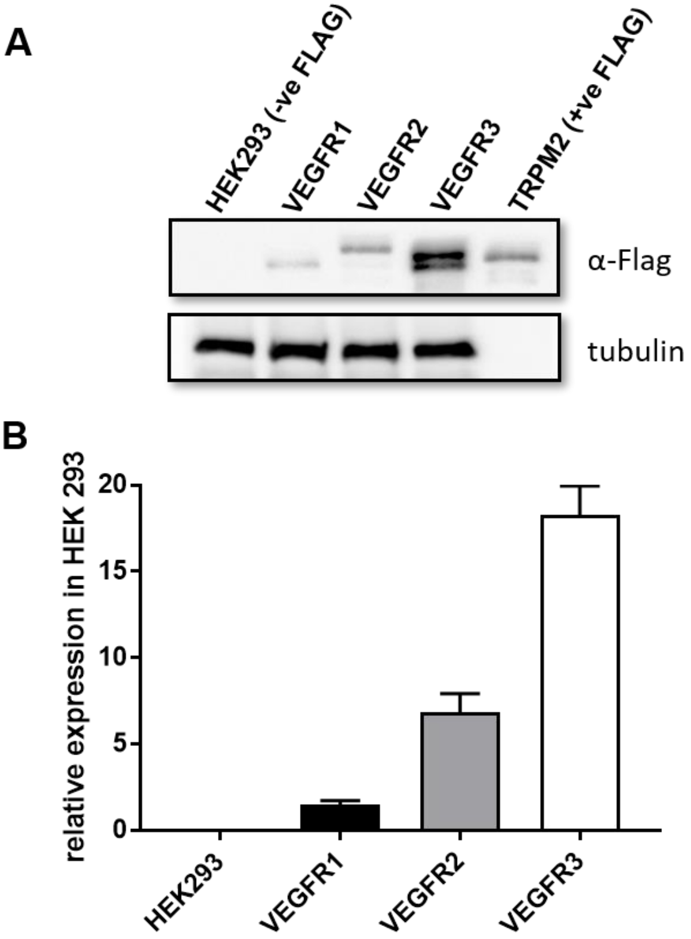

Figure 3.7. Inducible expression of VEGFR1, VEGFR2 and VEGFR3. Human embryonic kidney 293 Flp-In^{TM} T-Rex^{TM} cells were co-transfected with pOG44 and pCDNA5/FRT/TO-TOPO VEGFR1, VEGFR2, or VEGFR3 constructs to generate tetracycline-inducible stable expression systems. Stable clones were induced for 24 h with tetracycline (1 mg/ml), lysed and processed for immunoblotting. **(A)** Western blot showing lysates of untransfected HEK, cells stably transfected with VEGFR1, VEGFR2, and VEGFR3 plasmid constructs probed with mouse anti-FLAG primary antibody followed by goat anti-mouse HRP secondary antibody followed by ECL detection. A recombinant FLAG-TRPM2 recombinant protein was used as positive control and tubulin as loading control. **(B)** Quantification of relative expression levels of VEGFRs.

are relatively lower than both VEGFR2 and VEGFR3. This study confirmed the successful expression of full-length FLAG-tagged VEGFRs in HEK293 Flp^{TM} In^{TM} T-Rex cells.

3.2.3. Expression analysis of VEGFR cell lines

3.2.3.1. Comparison of endogenous and recombinant expression levels of VEGFRs in HEK293 cells

It was unknown whether the HEK293 cells express endogenous VEGFRs, which may affect subsequent studies. To check the endogenous and tetracycline-induced expression of all three VEGFRs a cell-based immunofluorescence analysis was performed. HEK293 cells expressing VEGFRs were uninduced or induced with tetracycline for 24 h, fixed and stained with VEGFR-specific antibodies and anti-FLAG antibodies and processed for microscopy (Fig. 3.8). Staining with anti-FLAG antibodies only allows the detection of recombinant hybrid VEGFRs, whereas VEGFR-specific antibodies detect both endogenous and recombinant VEGFRs. Non-transfected cells with tetracycline (+Tet) and transfected cells without tetracycline (-Tet) were used as negative controls (Fig. 3.8).

Both non-transfected/parent and uninduced transfected cells (-Tet) showed low levels of VEGFR1 staining within a juxtanuclear, Golgi-like compartment when probed with anti-VEGFR1 antibody (Fig. 3.8A). However, in FLAG-VEGFR1 transfected cells, tetracycline induction showed an almost 2-fold increase in VEGFR1 levels with a similar staining pattern (Fig. 3.8D). In contrast, no staining was visible for either VEGFR2 or VEGFR3 in parent cells or uninduced transfected cells (Fig. 3.8B and Fig. 3.8C). Endogenous VEGFR1 is clearly present, but VEGFR2 and VEGFR3 are absent in the parent HEK293 T-Rex cell line (Fig. 3.8D).

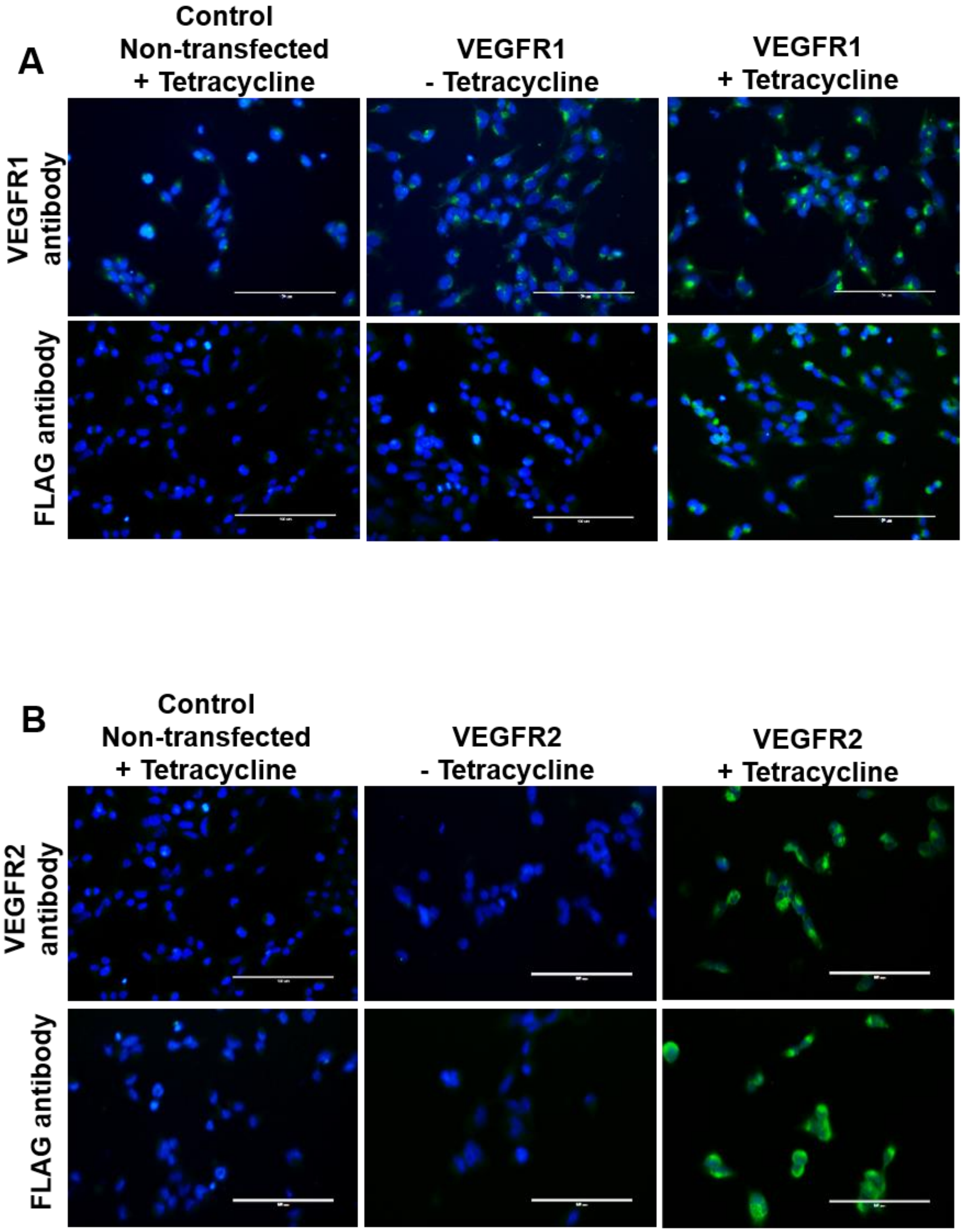
A
Control
Non-transfected
+ Tetracycline
VEGFR1
- Tetracycline
VEGFR1
+ Tetracycline
VEGFR1
antibody
FLAG antibody
B
Control
Non-transfected
+ Tetracycline
VEGFR2
- Tetracycline
VEGFR2
+ Tetracycline
VEGFR2
antibody
FLAG antibody

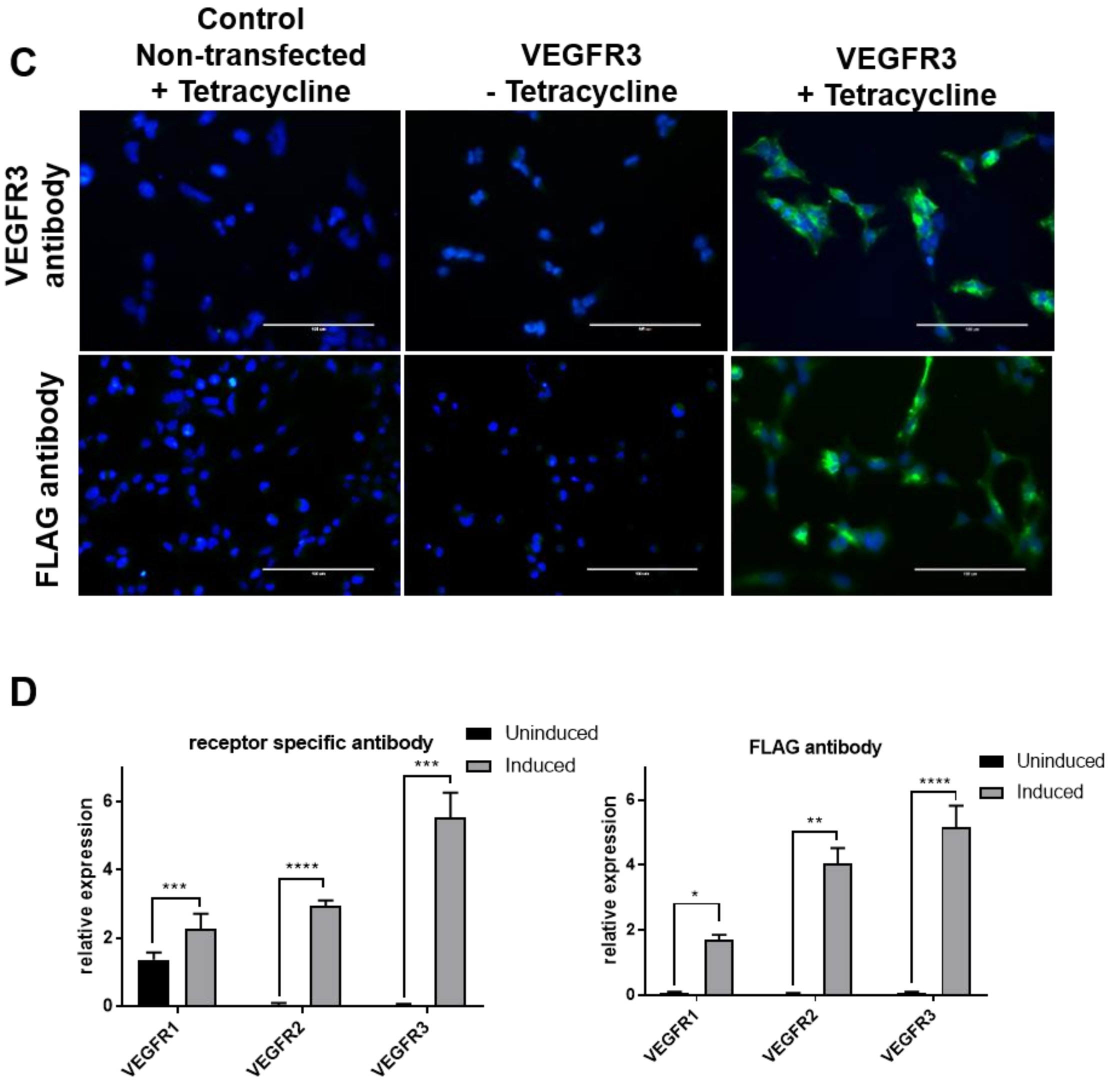

Figure 3.8. Analysis of inducible VEGFR1, VEGFR2 and VEGFR3 expression using microscopy. Human embryonic kidney 293 Flp-In^{TM} T-Rex^{TM} cells expressing VEGFRs were induced with of tetracycline (1 mg/ml) for 24 h, fixed and processed for immunofluorescence. **(A-C)** Indirect immunofluorescence labelling and microscopy using goat anti-VEGFR or mouse anti-FLAG antibodies respectively. Cells were then labelled with secondary anti-sheep AlexaFluor-488 or anti-mouse AlexaFluor-488 (green); nuclei stained with DAPI (blue). Scale bar, 100 µm. **(D)** Quantification of relative expression levels of VEGFRs probed with VEGFR- or FLAG-specific antibodies (left and right panels respectively). Quantification was performed as mentioned in methods. Error bars indicate ±SEM (n≥3). $p<0.05$ (*), $p<0.01$ (**).

3.2.3.2. Tetracycline induction and analysis of VEGFR1 and VEGFR2 expression in HEK293 T-Rex stable cell lines

To assess tetracycline-inducible VEGFR expression time-dependent immunoblot analysis was performed. VEGFR1 and VEGFR2 cell lines were treated with 1 µg/ml tetracycline for 0, 12, 24, 36, 48 and 72 h, then subjected to immunoblot analysis. The expression profiles of either VEGFR1 (Fig. 3.9A) or VEGFR2 (Fig. 3.9B) are shown when induced with tetracycline. Bands corresponding to mature VEGFR1 can be seen at ~200 kDa and for mature VEGFR2 at ~250 kDa when probed with goat anti-VEGFR1 and anti-VEGFR2 antibodies. Human endothelial cells (HUVECs) were used as a positive control for VEGFR expression, and non-transfected HEK293 lysate was used as a negative control (Fig. 3.9). As HEK293 cells endogenously express low levels of VEGFR1, relatively low levels of VEGFR1 are clearly evident at the 0 h time point (Fig. 3.9A). Tubulin protein was used as a loading control for normalisation of expression levels. The VEGFR tetracycline-induced expression profiles were relatively similar for both VEGFR1 and VEGFR2, with a gradual increase in expression from 0 h, which peaked at 36 h time point (post-stimulation) before declining. From these experiments, we concluded that the optimal time period for maximal VEGFR output is achieved between 24-36 h after the addition of tetracycline.

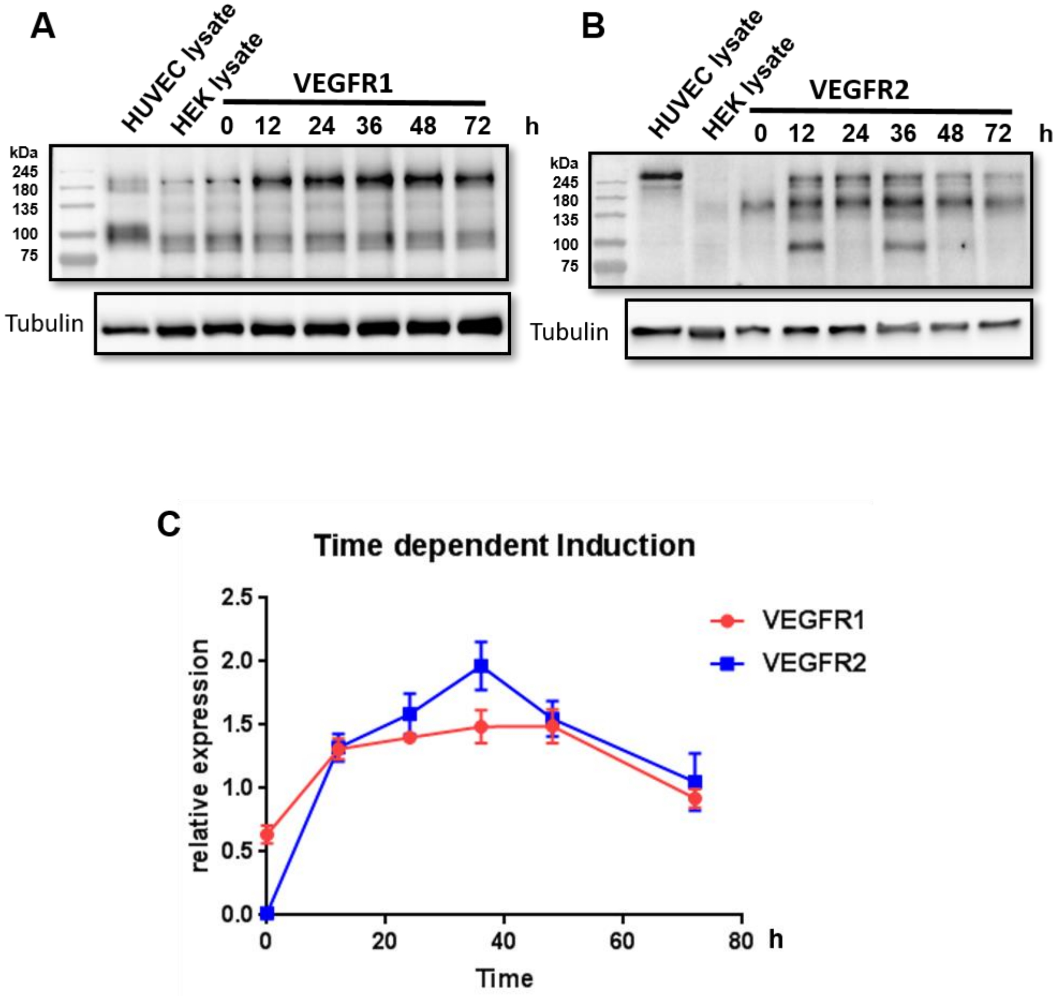

Figure 3.9. Time-dependent induction of VEGFR expression. HEK293 T-Rex stable cell lines expressing **(A)** FLAG-VEGFR1, or **(B)** FLAG-VEGFR2 were induced with tetracycline (1 µg/ml) for 0, 12, 24, 36, 48 or 72 h before cell lysis and immunoblotted. The western blots were probed with goat anti-VEGFR1 and goat anti-VEGFR2 primary antibodies respectively. **(C)** Quantification of relative FLAG-VEGFR1 and FLAG-VEGFR2 levels over time.

3.2.4. Analysis of cell surface VEGFR expression

We needed to demonstrate VEGFR cell surface localisation as a measure of delivery of properly folded and processed VEGFR to the plasma membrane. To do this, we quantified the percentage of intracellular and cell surface recombinant VEGFRs, by measuring VEGFR pools at the cell surface vs. total. Normally, secreted proteins that are delivered to have to also transit the ER, Golgi apparatus and endoplasmic reticulum, and can also accumulate in endosomes. By using detergent vs. non-detergent treatments in microscopy experiments, we can determine % staining patterns in total (+detergent) vs. cell surface (-detergent). As the FLAG tag attached to each VEGFR hybrid protein is located at the extreme N-terminus; this is also located within the membrane lumen or extracellular environment. Thus, accessibility to FLAG antibody labelling under detergent/no detergent conditions during microscopy can give staining patterns representative of total vs. cell surface FLAG-VEGFR distribution.

VEGFR1 and VEGFR2 cell lines were induced for 36 h with tetracycline, before PFA fixation which does not permeabilise the plasma membrane (Boocock, 1990). Cells were then either permeabilised or non-permeabilised with 0.2 % (w/v) Triton X-100 detergent and probed with either receptor-specific goat primary antibody or mouse anti-FLAG primary antibody. The respective fluorescent secondary antibodies were used to detect total or FLAG-VEGFR expression patterns (Fig. 3.10). Non-transfected HEK293 T-Rex cells and transfected but uninduced (-Tet) cells were used as negative controls. Fig. 3.10A shows the permeabilised and non-permeabilised VEGFR1 cell line probed with either goat anti-VEGFR1 antibody or mouse anti-FLAG antibody. As expected, because HEK cells endogenously express VEGFR1, non-transfected HEK control as well as VEGFR1 non-induced (-Tet) cells showed significant staining when probed with goat anti-VEGFR1 antibody, and no staining was seen with mouse anti-FLAG antibody (Fig. 3.10A). A key point is a 2-fold increase in VEGFR1 levels in permeabilised cells when compared to non-permeabilised cells in all conditions (Fig. 3.10B and 3.10C). Quantification of the total, intracellular and cell surface

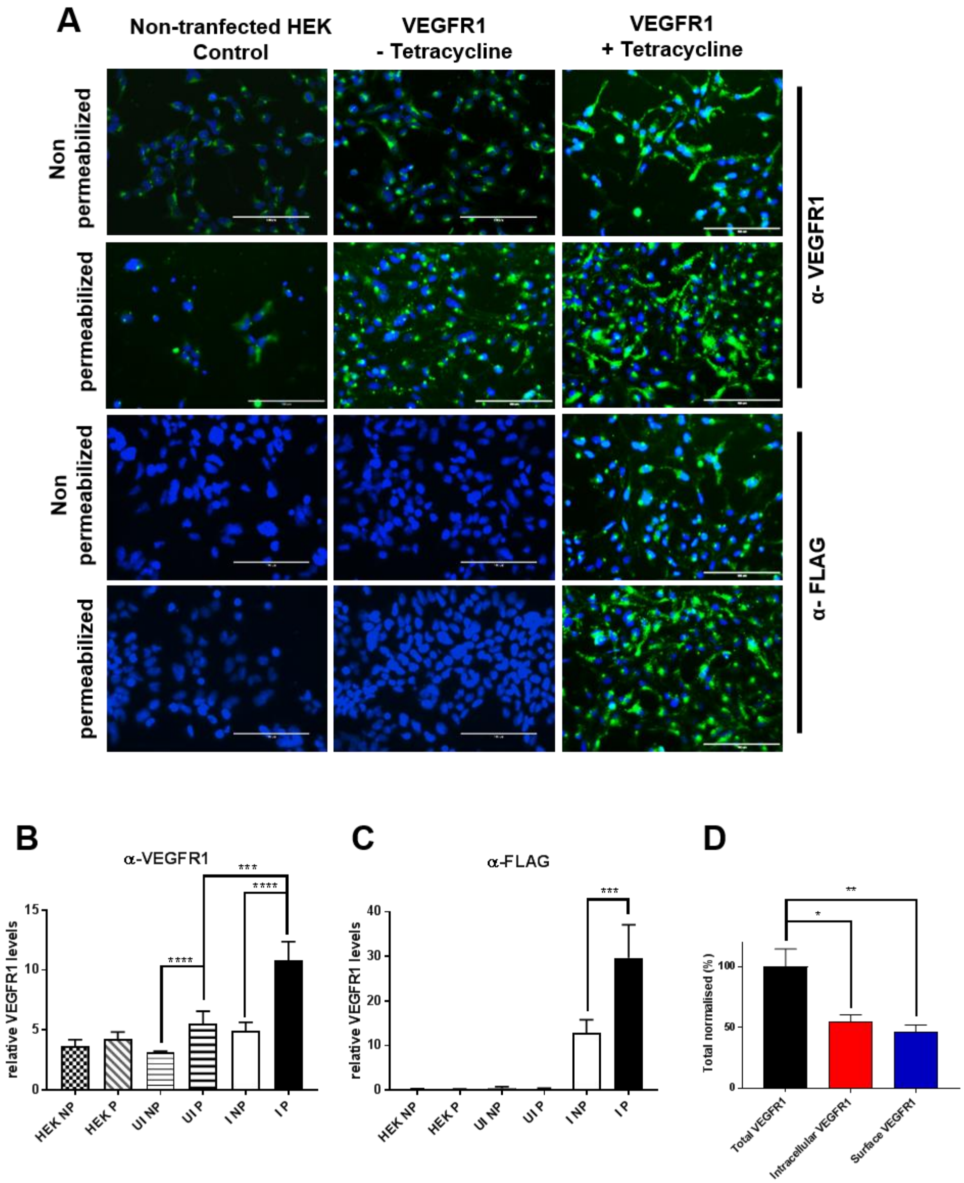

Figure 3.10. Analysis of VEGFR1 pools. (A) HEK293 T-Rex cells expressing FLAG-VEGFR1 were induced with tetracycline (1 mg/ml) for 36 h, fixed before either permeabilisation with 0.2% (w/v) Triton X-100 or non-permeabilisation, and processed for indirect immunofluorescence analysis. Cells were stained with primary goat anti-VEGFR1 or mouse anti-FLAG, then labelled with secondary anti-sheep AlexaFluor-488 or anti-mouse AlexaFluor-488 (green) and nuclear DNA stained with DAPI (blue). Scale bar, 100 µm. Quantification of **(B)** relative levels of VEGFR1. **(C)** FLAG staining in non-permeabilised (NP) and permeabilised (P) cells under uninduced (UI) or induced (I) conditions. **(D)** Quantification of relative intracellular and surface VEGFR1 levels relative to total VEGFR2. Error bars indicate ±SEM (n≥3). $p< 0.05$ (*), $p< 0.01$ (**), $p< 0.001$ (***), $p< 0.0001$ (****).

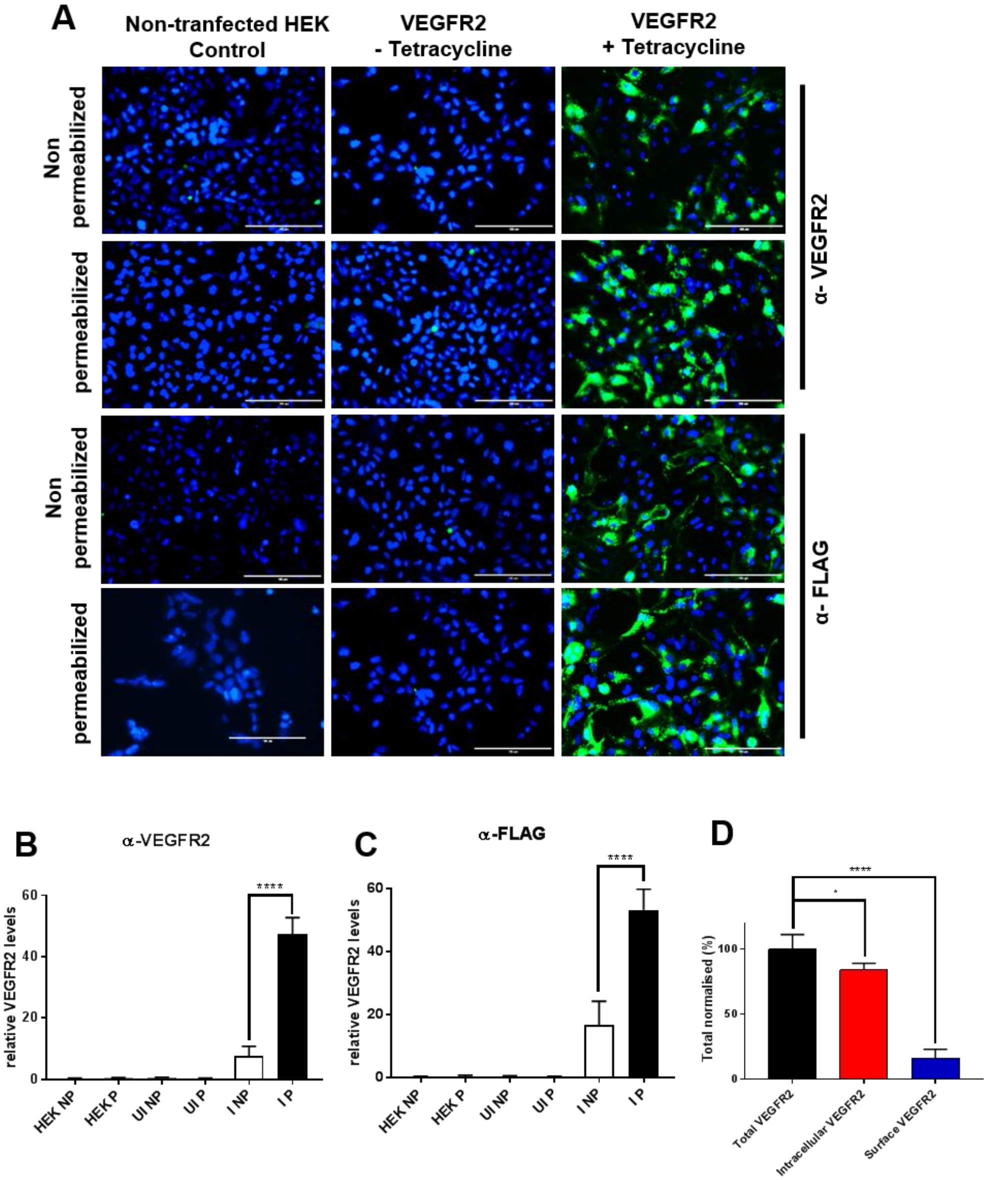

Figure 3.11. Analysis of VEGFR2 pools. (A) HEK293 T-Rex cells expressing FLAG-VEGFR2 were induced with tetracycline (1 mg/ml) for 36 h, fixed before either permeabilisation with 0.2% (w/v) Triton X-100 or non-permeabilisation, and processed for indirect immunofluorescence analysis. Cells were stained with primary goat anti-VEGFR2 or mouse anti-FLAG, then labelled with secondary anti-sheep AlexaFluor-488 or anti-mouse AlexaFluor-488 (green) and nuclear DNA stained with DAPI (blue). Scale bar, 100 µm. Quantification of **(B)** VEGFR2 staining or **(C)** FLAG staining in non-permeabilised (NP) and permeabilised (P) cells under uninduced (UI) or induced (I) conditions. **(D)** Quantification of relative intracellular and surface VEGFR2 levels relative to total VEGFR2. Error bars indicate ±SEM (n≥3). $p< 0.05$ (*), $p< 0.0001$ (****).

FLAG-VEGFR1 is shown in Fig. 3.10D at 36 h post-induction ~60% of VEGFR1 present in an internal pool whereas ~40% is present on a cell surface pool.

In the stable VEGFR2 HEK293 T-Rex cell line, there was no staining in non-transfected HEK293 controls, and transfected uninduced (-Tet) when probed with either goat anti-VEGFR2 antibody or mouse anti-FLAG antibody (Fig. 3.11A). There was a >4-fold increase in total VEGFR2 levels in permeabilised cells (Fig. 3.11B and 3.11C). When the VEGFR2 cell surface and intracellular levels were compared (Fig., 3.11D) ~75 % of VEGFR2 is present in an internal pool with only 25% on the cell surface or plasma membrane.

3.3. DISCUSSION

In this chapter, we produced three recombinant pCDNA5/FRT/TO VEGFR constructs to express processed N-terminal FLAG-tagged VEGFR1, VEGFR2, and VEGFR3 hybrid proteins in an inducible manner. Consequently, these constructs were stably integrated into HEK293 T-Rex cells and successfully produced tetracycline-inducible VEGFR expression. The Tet repressor protein binds to two Tet-Operator sequences to inhibit the transcription of the VEGFR transgenes. Therefore, tetracycline must be added to the culture media which diffuses into the cell nucleus and binds to the Tet repressor protein to enable a conformational change and release from the Tet-O operator: this now allows the transcription of VEGFR transgene, production of mRNA which is subsequently translated into VEGFR protein which is processed and secreted (Fig. 3.1.)

The FLAG peptide tag was added to the N-terminus of each VEGFR, as an in-frame fusion to the extracellular Ig domains for all three VEGFRs: this is because the cytoplasmic tyrosine kinase activity is likely regulated by the flexibility of the C-terminal tail such tags attached to the extreme C-terminus are known to modulate kinase activity (Yokoyama et al., 2005). The presence of the 8-residue FLAG peptide tag at the extreme N-terminus is also likely not to hinder or interfere with VEGF ligand binding which usually occurs via Ig domains D2 and/or D3 (Hubbard and Miller, 2007, Dionne et al., 2018). Recombinant FLAG-VEGFR1 expressed in HEK293 cells showed a band at ~200 kDa and a soluble isoform at

~110 kDa, For VEGFR2, a doublet band at ~250 and ~230 kDa indicated the presence of the mature and immature VEGFR2 forms; a band of ~160 kDa was also detected, which likely correlates to a VEGFR2 proteolytic fragment. For VEGFR3, a doublet at ~230 kDa and ~200 kDa was detected, corresponding to immature forms of the polypeptide before processing. The molecular mass of recombinant VEGFRs detected by anti-VEGFR antibodies corresponds to the molecular mass human VEGFRs expressed in primary human endothelial cells (Fearnley et al., 2015). Also, FLAG-VEGFR expression was not detected in uninduced cells, which demonstrates that VEGFR expression is tightly regulated (Baron and Bujard, 2000).

Signal peptides govern the intrinsic signals for transportation of proteins to their site of action which is subsequently cleaved from mature protein, Although, not all proteins have signal peptides, there is evidence that suggests in the absence of specific signal peptides, a sorting machinery incorporates the proteins into transport vesicles based on the biochemical properties and sequence motifs (i.e. extracellular/lumenal transmembrane, cytoplasmic domains) of the secreted protein (Ponnambalam and Baldwin, 2003). However VEGFRs expressed in endothelial cells have intrinsic signal peptides that are diverse in amino acid composition and length, with different residue lengths of 26 for VEGFR1, 19 for VEGFR2 and 24 for VEGFR3, respectively (Kendall and Thomas, 1993, Zhang and Henzel, 2004). Signal peptides are responsible for post-translational modifications such as glycosylation and protein folding. Detection of VEGFRs on the cell surface also indicates that human CD33 signal peptide facilitated efficient secretion of recombinant proteins and assisted in trafficking to the plasma membrane (Güler-Gane et al., 2016). The expression profiles of recombinant VEGFRs corresponds to the size of native VEGFRs in endothelial cells, suggesting the human CD33 signal peptide also facilitated native VEGFR processing and glycosylation (Güler-Gane et al., 2016).

VEGFR receptor numbers at the surface of transfected cells are reported to be between 500-50,000 for VEGFR1 and 6,000-150,000 for VEGFR2 per cell, whereas, their numbers in human endothelial cell surface on average are reported to be ~1800±100 for VEGFR1 and ~5800±300 for VEGFR2 (Imoukhuede et al., 2013, Imoukhuede and Popel, 2011). Human endothelial cells have ~3-5-fold more VEGFR2 on cell surface compared to VEGFR1 and their levels are regulated by intracellular trafficking process which are unique to each VEGFR (Imoukhuede and Popel, 2012). Cell-based studies showed that VEGFR1 is trafficked to the cell surface from the *trans*-Golgi network (Mittar et al., 2009). It has been estimated that ~80% VEGFR1 resides in an internal pool in the Golgi apparatus (Mittar et al., 2009, Imoukhuede and Popel, 2012). In contrast, VEGFR2 is constitutively delivered to the plasma membrane from the Golgi and internalised by endocytosis for delivery to endosomes (Ewan et al., 2006; Lampugnani et al., 2006; Gample et al., 2006). VEGFR2 is routed via late endosomes to either the lysosome for degradation (Bruns et al., 2010) or recycled from endosomes (Jopling et al., 2011, 204). It was estimated that at least 40% of total VEGFR2 resides intracellularly, either in trafficking compartments or stored in endosomal compartments (Jopling et al., 2014, Yokoyama et al., 2005). It is not possible to estimate the receptor numbers from our studies, but the proportion of VEGFR1 in the plasma membrane pool was estimated at ~40%. The corresponding VEGFR2 pool represented 25% of total receptor, which is relatively low and does not reflect the situation in human endothelial cells, but it is safe to say that the absolute numbers of receptors on the cell surface would be much higher in HEK293 cells due to recombinant overexpression.

CHAPTER 4

Purification and analysis of recombinant full-length VEGFR1 and VEGFR2 membrane proteins

4.1. INTRODUCTION

The key role of VEGF ligands and their cognate VEGFRs in angiogenesis, lymphangiogenesis, and cancer progression is well established (Hicklin and Ellis, 2005). Even though the mechanism of VEGF ligand binding to the VEGFR extracellular domain is well studied, how VEGF binding mediates tyrosine kinase activation in the cytoplasmic domain is still unclear. Resolving the structure of the VEGFR-VEGF complex is crucial and more detailed investigations are needed to improve our understanding of this important area of membrane biology linked to a variety of human diseases.

X-ray crystallography, nuclear magnetic resonance (NMR), and single-particle transmission electron microscopy (EM) are the important tools in biology which are being used to resolve high-resolution structures of various soluble and membrane proteins (Shi, 2014, Wang and Wang, 2017, Cavalli et al., 2007). Alternatively, small-angle x-ray scattering (SAXS) can be used to determine the oligomeric state and quaternary structures of proteins in solution, although to relatively low resolution (Korasick and Tanner, 2018). A key limitation of crystallography is the requirement for milligram amounts of highly purified membrane protein in detergent solution, and at >1mg/mL concentration (introducing additional potential problems around solubility). Without this, obtaining well-ordered crystals for diffraction would be essentially impossible. Where a mammalian cell expression system must be used, scale-up to achieve this is technically difficult and prohibitively costly (Ishchenko et al., 2017). Even with distinct challenges, the recent success in resolving the structure of membrane-bound G-protein coupled receptors (GPCRs) produced in baculovirus/insect cells has proved that the limitations can be overcomed (Palczewski et al., 2000, Topiol, 2018).

NMR spectroscopy is another important approach used in structural biology which provides the structural information of membrane proteins in detergent micelles and also in detergent-free native phospholipid bilayers (Columbus et al., 2009). However, there is a size limitation with NMR, even after 30 years of development, the membrane proteins that are largely studied are lower than 100 residues (Liang and Tamm, 2016). There are few exceptions such as chemokine receptor CXCR1 and *Anabaena* sensory rhodopsin (ASR) (Park et al., 2012, Wang et al., 2013). On the other hand, EM techniques are gaining prominence in studying structures of biological assemblies (Fig. 4.1A), and recent technical advances in electron microscopy (EM) field has allowed resolving structures of membrane proteins at atomic resolution (Gold et al., 2014, De Zorzi et al., 2015).

Historically x-ray crystallography was used to resolve the structures of individual Ig-like domains and kinase domain at resolution ranging from 1.7 - 4.2 Å (Table. 1.2). Even though high-resolution structures of individual Ig-like domains were available, the mechanism that drives the formation of homotypic contacts that lead to dimerization and subsequent tyrosine kinase activation are not clearly understood. Hofer and colleagues studied VEGFR2/VEGF ECD complex using SAXS and determined low-resolution structure of ECD in solution which provided first insights into orientation of Ig-like domains (Kisko et al., 2011). Later the same group has used the combination of negative stain-EM and x-ray crystal structures to resolve the structure of VEGFR1/VEGF ECD at 4 Å resolution (Table. 1.2). Thus, a combination of single-particle electron microscopy (EM), X-ray crystallography and small-angle X-ray scattering (SAXS), have revealed details of the ligand-binding to extracellular Ig-like domains and receptor-receptor interactions (Markovic-Mueller et al., 2017, Park et al., 2018, Ruch et al., 2007a).

The main aim of the work presented in this chapter is to understand the complete structural arrangement of at least one of the VEGFRs using negative stain electron microscopy (EM) and to try and extend this using cryo-EM. Inducible HEK293 stable cell lines expressing VEGFRs were generated and their expression was characterized in the previous Chapter 3. Optimisation of membrane protein solubilisation in detergent and purification is essential to

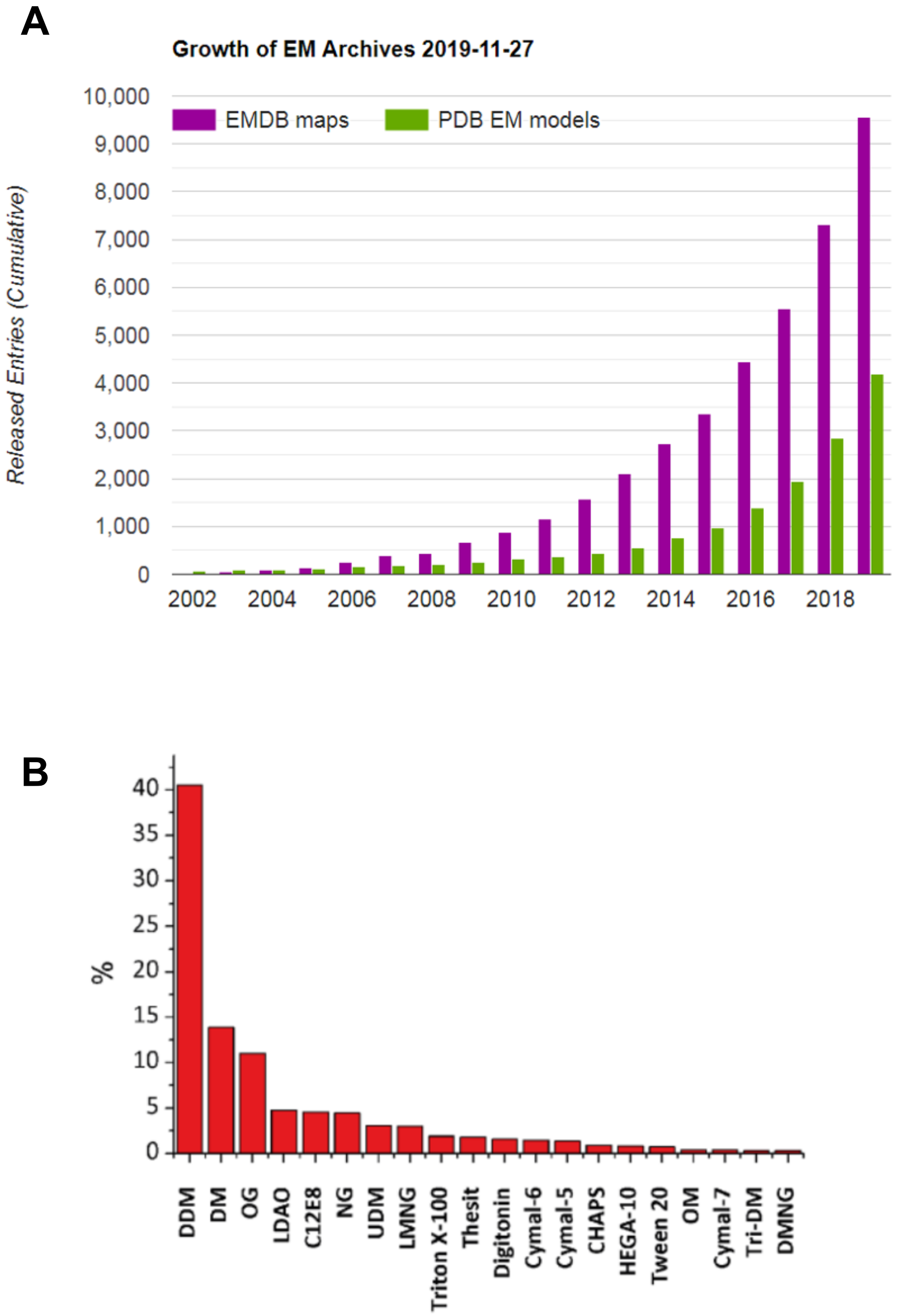

Figure 4.1. Structural and biochemical studies linked to protein structures in databases. (A) Cumulative entries of number of structures generated using EM deposited in Electron Microscopy Databank (EMDB) and Protein Databank (PDB) from 2002-2019. Image source https://www.emdataresource.org/statistics **(B)** Percentage of protein deposits of different detergents used for purification of membrane proteins in both EM and crystallography (adapted from Stetsenko and Guskov, 2017).

achieve sufficient quantity and quality of purified receptors in their active state. In this study, the purification of two full-length membrane receptors i.e. VEGFR1 and VEGFR2 were optimised using different detergent-based procedures, and purified complexes were analyzed using single-particle negative stain EM.

Membrane proteins are difficult to study, as they are required to extract from the membrane for structural studies. The hydrophobic surface areas of the proteins especially the transmembrane domains need to be in native lipids to maintain their active conformation (Garavito and Ferguson-Miller, 2001). Therefore, the proteins are extracted using agents that mimic the lipid membrane environment. Historically, the most widely used agents for membrane protein extraction are detergents (Kotov et al., 2019). These are amphipathic compounds that contain a hydrophilic head group (polar) and a hydrophobic tail (apolar), which act by dissolving the lipid membrane bilayer and solubilising the membrane proteins by burying the hydrophobic surface areas (e.g. transmembrane regions) into the hydrophobic interior of detergent micelles. The detergents form micelles only above the critical micellar concentration (CMC), which varies for each detergent; such detergents are usually monomers below the CMC (Stetsenko and Guskov, 2017). Therefore, proteins are isolated from the cell membrane in their native-like environment using such detergents that can allow the retention of key enzymatic and/or functional activities.

The choice of detergent is crucial for successful protein solubilisation and purification from cells and tissues. Generally, detergents are classified into three major classes: non-ionic, ionic and zwitterionic (Seddon et al., 2004, Garavito and Ferguson-Miller, 2001). Non-ionic detergents are uncharged and mild detergents which only disrupts the lipid-lipid interactions and protein-lipid interactions, without effecting protein-protein interactions (Schick, 1963). Ionic detergents are charged (either anionic or cationic), they are harsh detergents that completely denature the protein by disrupting the protein-protein interactions (Moriyon and Berman, 1982). On the other hand, zwitterionic detergents are mildly harsh detergents considered as an intermediate between nonionic and ionic detergent, they have both anionic and cationic polar head groups with an overall neutral net charge.

They break the protein bonds but don’t completely denature a protein like ionic detergents (Hjelmeland, 1980, Henningsen et al., 2002). For structural studies maintaining the native-like state of the protein is essential, therefore mild non-ionic detergent was used for solubilisation. The most commonly used detergents for membrane protein purification are n-dodecyl β-D-maltoside (DDM) followed by n-decyl-β-D-maltopyranoside (DM), n-octyl-β-D-glucopyranoside (OG) and n-Dodecyl-N,N-Dimethylamine-N-Oxide (LDAO) which are all nonionic and have been used extensively in structural biology, with DDM proving to be the most successful (Fig. 4.1B) (Stetsenko and Guskov, 2017). All these detergents are compatible with cryo-EM studies (Pryor and Travis, 2018).

However, there are possible side effects of removing the protein from its native environment using detergents, such as adoption of a non-native structure or even denaturation. Therefore, in recent years, polymers such as styrene-maleic acid (SMA) copolymer that preserve native protein-lipid interactions are becoming more widely used as alternative to detergents. This approach is used to extract the protein and natural cell membrane lipids into SMA-lipid particles (SMALPS). The integral membrane protein and its associated lipids are encircled by a ring of polymer, the hydrophilic parts of the SMA ensuring solubility of the overall complex. The SMA is amphipathic as it has an alternate hydrophobic (styrene) and hydrophilic (maleic acid) moieties, and extracts small discs of membrane lipid bilayer in which the membrane proteins are trapped, therefore the native environment of the protein and its activity are retained (Postis et al., 2015). These discs are relatively small (10-15 nm), hence there is a very low likelihood of mulitiple proteins being trapped in a single complex.

Furthermore, the objective of this chapter is to solubilise the VEGFRs in non-ionic DDM/SMA co-polymer and perform an affinity-based purification using FLAG fusion tag which consists of eight amino acids (DYKDDDDK) (Einhauer and Jungbauer, 2001), followed by size exclusion chromatography (SEC). Size exclusion chromatography or gel permeation chromatography is commonly used for purification, measuring the molecular weight (Mr) and characterization of protein complexes (Hong et al., 2012). The size exclusion chromatography as the name suggests allows separation of protein complexes based on their size. Protein mixture is passed through a column containing uniformly sized porous beads, proteins diffuse through the pores of the beads with different mobility based on their size, this allows the fractionation of protein complexes and removal of proteins and contaminants that are either smaller or larger than the target protein (Engelke et al., 2019). In this chapter, comparative optimisation studies of solubilisation using DDM detergent, SMA polymer, and purification were performed on VEGFRs for structural analysis using single-particle electron microscopy.

4.2. RESULTS

4.2.1. Immunoisolation of recombinant tagged VEGFR1, VEGFR2, and VEGFR3 membrane proteins

A small-scale immunoisolation was performed to check VEGFR1, VEGFR2 and VEGFR3 recovery from inducible HEK293 cell lines. Fig. 4.2A shows a Western blot of VEGFR elutions probed with mouse anti-FLAG antibody. The uninduced HEK cell lysates (-Tet) were used as a negative control for non-specific binding to protein G column and purified FLAG-TRPM2 membrane protein (170 kDa) was used as a positive control (Fig. 4.2A). VEGFR1 lane showed a band at ~190 kDa, VEGFR2 at >200 kDa, two bands (200 and 180 kDa) were detected in VEGFR3 (Fig. 4.2A). The top VEGFR3 band likely represents the mature glycosylated full-length VEGFR3 and the second smaller kDa band likely represents the immature partially glycosylated receptor. The uninduced negative control showed no bands, indicating that the DDM-solublised HEK293 lysates contained no polypeptides that bound non-specifically to the immunoaffinity matrix. Fig. 4.2B shows the quantification of relative levels of FLAG-VEGFRs isolated using this approach. Same volume of lysates of VEGFR1, VEGFR2 and VEGFR3 were added to the resin, the higher levels of VEGFR3 compared to VEGFR1 and VEGFR2 is potentially due to higher expression of VEGFR2 as evident from Fig. 3.7 and 3.8, this also indicate that final binding capacity of the resin was not reached. Further optimisation was carried out on VEGFR1 and VEGFR2 membrane proteins with a view to carrying out a detailed structural analysis of a specific VEGFR.

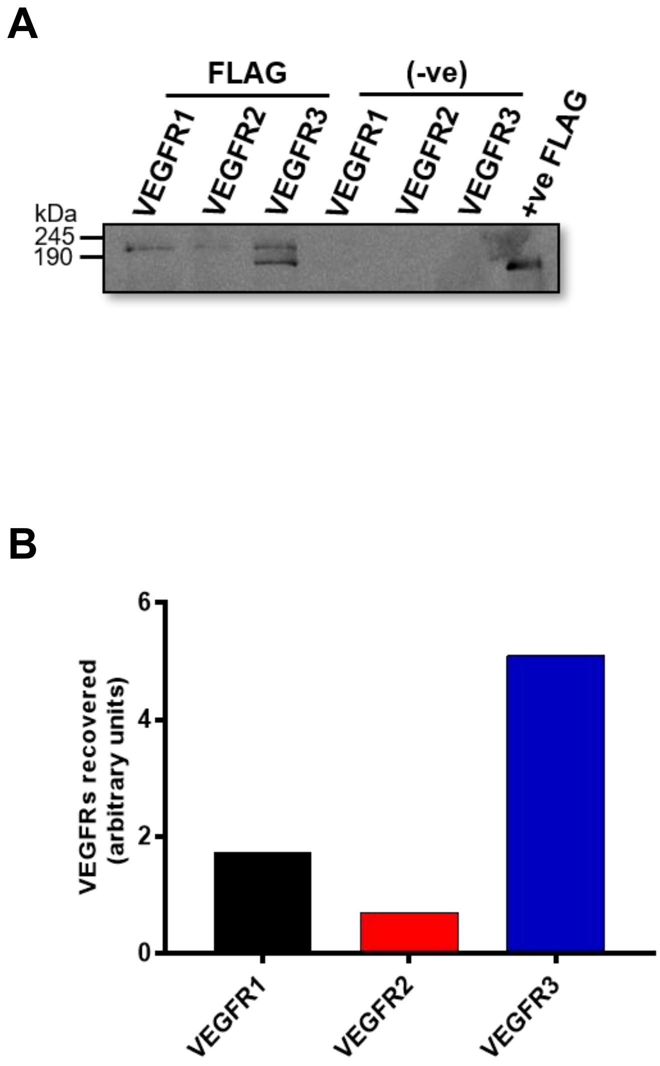

Figure 4.2. Immunoisolation of tagged VEGFRs. (A) Western blots showing immunoisolation of FLAG-tagged VEGFR1, VEGFR2 and VEGFR3 from HEK293 Flp-In$^{\text{TM}}$ T-Rex$^{\text{TM}}$ cell lines. Cells were solubilised in RIPA lysis buffer, incubated with mouse α-FLAG antibody, and immune complex isolated using rabbit α-mouse IgG-Protein G Sepharose beads. Anti-FLAG antibody was used to monitor recombinant VEGFR using immunoblotting. Purified FLAG-TRPM2 protein was used as a positive control (+ve FLAG). **(B)** Relative quantification of FLAG-VEGFR using immunoisolation technique.

4.2.2. Assessment of solubilisation of full-length VEGFR1 and VEGFR2

After validating the successful pulldown of VEGFRs using FLAG-affinity purification, solubilisation studies were performed to assess the ability to solubilise full-length VEGFR1 and VEGFR2 from cell membranes before purification. The activity and stability of purified membrane proteins depend upon the type of detergent used for membrane solubilisation. Initially, a milder non-ionic detergent like n-Dodecyl β-D-maltoside (DDM) which has longer aliphatic chains and very low critical micellar concentration (CMC) (0.17 mM) was used to solubilise the VEGFR from inducible HEK293 cell lines (Stetsenko and Guskov, 2017).

HEK293 cells expressing VEGFR1 and VEGFR2 were induced with 1 µg/ml of tetracycline for 36 h and cell membranes were prepared from 5 x 10^6 cells by sonicated and solubilised in 1% (w/v) DDM. To check for the solubility and protein recovery, the solubilised membranes were centrifuged at 4,000 xg low speed to collect the soluble supernatant (S1) and insoluble membrane pellet (P1). The supernatant (S1) was then further subjected to high-speed centrifugation to collect the soluble supernatant (S2) and insoluble membrane (P2). Both membrane pellets (P1) and (P2) were dissolved in an equivalent volume of SDS-PAGE sample buffer to the supernatant volumes so that the levels of receptor in all the samples could be directly compared. The final soluble supernatant (S2) was incubated with monoclonal antibody M2 FLAG resin and bound FLAG-VEGFR was eluted using glycine before neutralisation. The flow-through was also collected to check for the relative level of unbound VEGFRs (UB). Equal representative percentages of all fractions were loaded on to an SDS-PAGE gel and then transferred on to a western blot. Fig. 4.3A and 4.3B show the Western blot data of soluble, insoluble, unbound and eluted VEGFR1 and VEGFR2 probed with goat anti-VEGFR1 and goat anti-VEGFR2 primary antibodies respectively. The soluble supernatant 1 (S1) shows the full-length VEGFR1 at 190 kDa and other soluble fragments at sizes ~80, 65, 50, 40, 35 and 25 kDa (Fig. 4.3A). This indicates that the VEGFR1 undergoes proteolysis at multiple sites. Whereas, VEGFR2 soluble supernatant (S1) in shows a dominant clear band at ~250 kDa and a very faint band at ~60 kDa (Fig. 4.3B). This shows that VEGFR2 is more stable to proteolysis compared to VEGFR1. The relative quantification (Fig. 4.3C) of both VEGFR1 and VEGFR2 shows that less than 10% of full-length VEGFR1 was finally purified, whereas >80% of full-length VEGFR2 was retained in fraction E1. The total was calculated by adding the amount of S1 and P1.

Non-specific proteolysis or degradation of proteins during purification is a frequent hurdle. To assess whether this could be reduced, especially in the case of VEGFR1, solubilisation was performed presence of 2% (w/v) bovine serum albumin (BSA) to quench proteolysis effects. BSA can act as a decoy protein for non-specific proteases (Chakrabarti et al., 2016). Western blots of solubilised and purified VEGFR1 and VEGFR2 in the presence of BSA revealed no improvement in proteolytic degradation of VEGFR1 (Fig. 4.4C and 4.4E). However, VEGFR2 still remained stable with most of the receptor retained (Fig. 4.4D and 4.4E). Therefore, further optimisation studies were performed without BSA and focused largely on recombinant VEGFR2. These elutions were performed using 100 mM glycine HCl pH 3, even though low pH buffer completely dissociates the antigen-antibody interactions without permanently affecting the protein structure; nevertheless, low pH frequently leads to denaturation of proteins (Narhi et al., 1997). Therefore, further optimisation was performed to elute the FLAG-VEGFR using excess competing FLAG peptide to retain VEGFRs in a non-denatured state. Optimisation of elution of FLAG-VEGFR1 and FLAG-VEGFR2 was performed with stepwise increases in FLAG peptide concentrations followed by immunoblot analysis of eluted FLAG-VEGFR1 (Fig. 4.5A) or FLAG-VEGFR2 (Fig. 4.5B). Relative quantification of FLAG elution profiles of VEGFR1 and VEGFR2 (Figure 4.5C) showed some differences: FLAG-VEGFR1 maximally eluted at 75 µg/ml FLAG peptide, however, FLAG-VEGFR2 maximally eluted at 200 µg/ml FLAG peptide. Even though the working concentration of FLAG peptide to elute most FLAG fusion proteins is 100 µg/ml (Gerace and Moazed, 2015), FLAG-VEGFR2 elution required a higher working concentration.

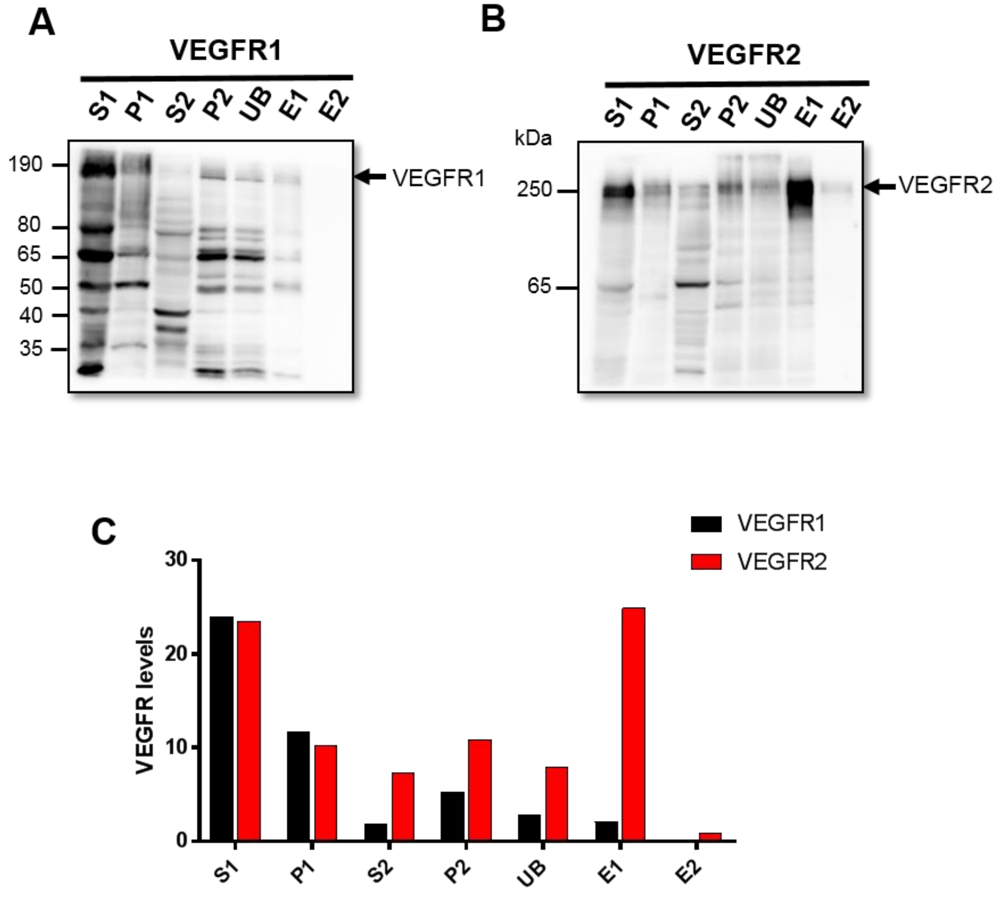

Figure 4.3. Detergent solubilisation of VEGFRs from membranes using DDM. Western blots showing VEGFRs solubilised in 1% (w/v) DDM and affinity purified using anti-FLAG M2 monoclonal antibody resin (see Materials and Methods), **(A)** VEGFR1, and **(B)** VEGFR2 probed with goat anti-VEGFR1 and goat anti-VEGFR2 primary antibodies respectively. **(C)** Relative quantities of different fractions supernatant 1 (S1), pellet 1 (P1), supernatant 2 (S2), pellet 2 (P2), unbound (UB), elution 1 (E1), and elution 2 (E2) are shown. VEGFR1 (black) or VEGFR2 (red) solubilisation and recovery.

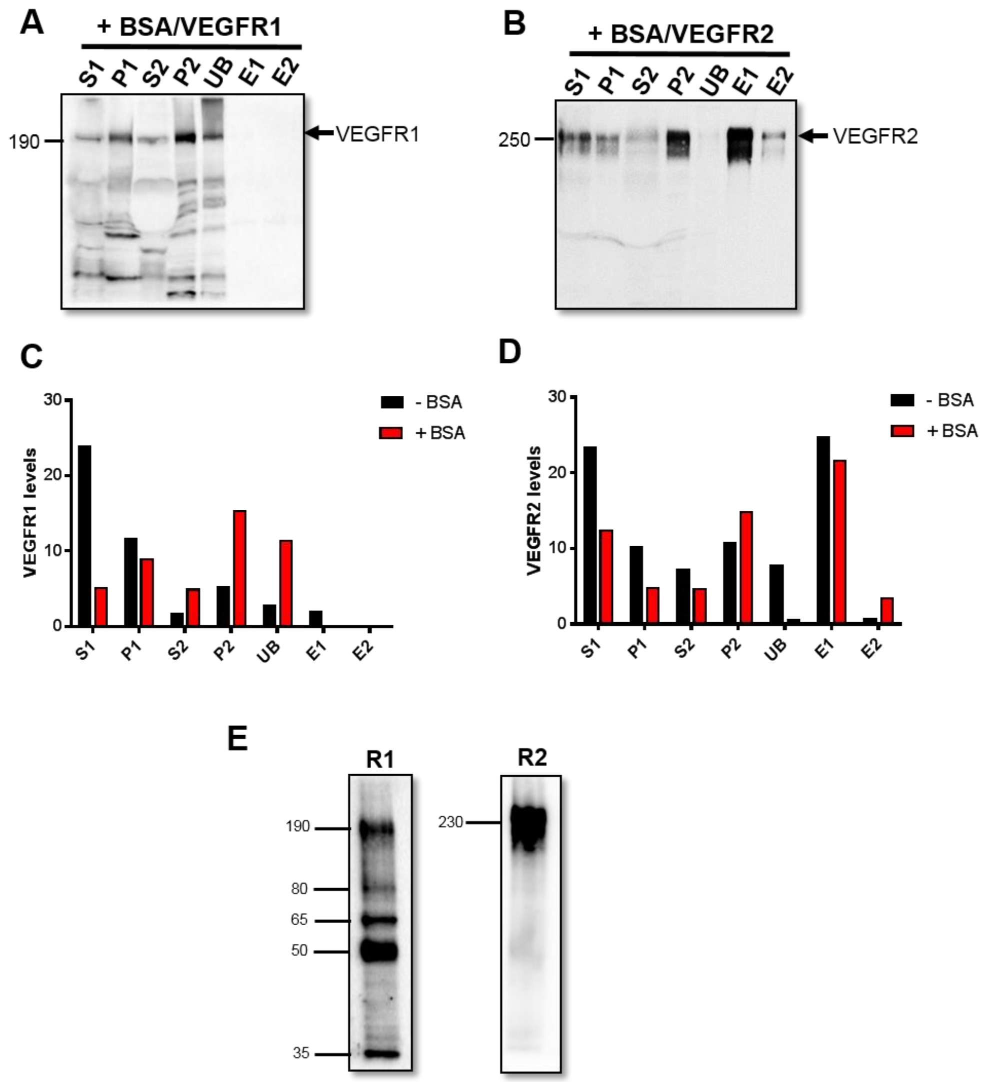

Figure 4.4. Blocking VEGFR proteolysis using BSA as a carrier protein. Western blots showing VEGFRs solubilised in 1% (w/v) DDM in the presence of 2% (w/v) BSA and affinity purified using anti-FLAG M2 mAb as previously described. VEGFR1 and VEGFR2 probed with goat anti-VEGFR1 and goat anti-VEGFR2 primary antibodies respectively. Relative quantities of different fractions supernatant 1 (S1), pellet 1 (P1), supernatant 2 (S2), pellet 2 (P2), unbound (UB), elution 1 (E1), and elution 2 (E2) are shown. Immunoblot analysis of purification for **(A)** VEGFR1, and **(B)** VEGFR2. **(C, D)** Relative quantification of full-length VEGFR solubilisation and recovery in the absence (black) or presence (red) of BSA. **(E)** Western blot of elution of either VEGFR1 or VEGFR2 in the presence of 2% BSA. VEGFR1 is highly sensitive to proteolysis, with breakdown products of VEGFR1 observed at ~80, 65, 50, and 35 kDa. On the other hand, only one band is detected for VEGFR2 at ~250 kDa indicating resistance to proteolysis.

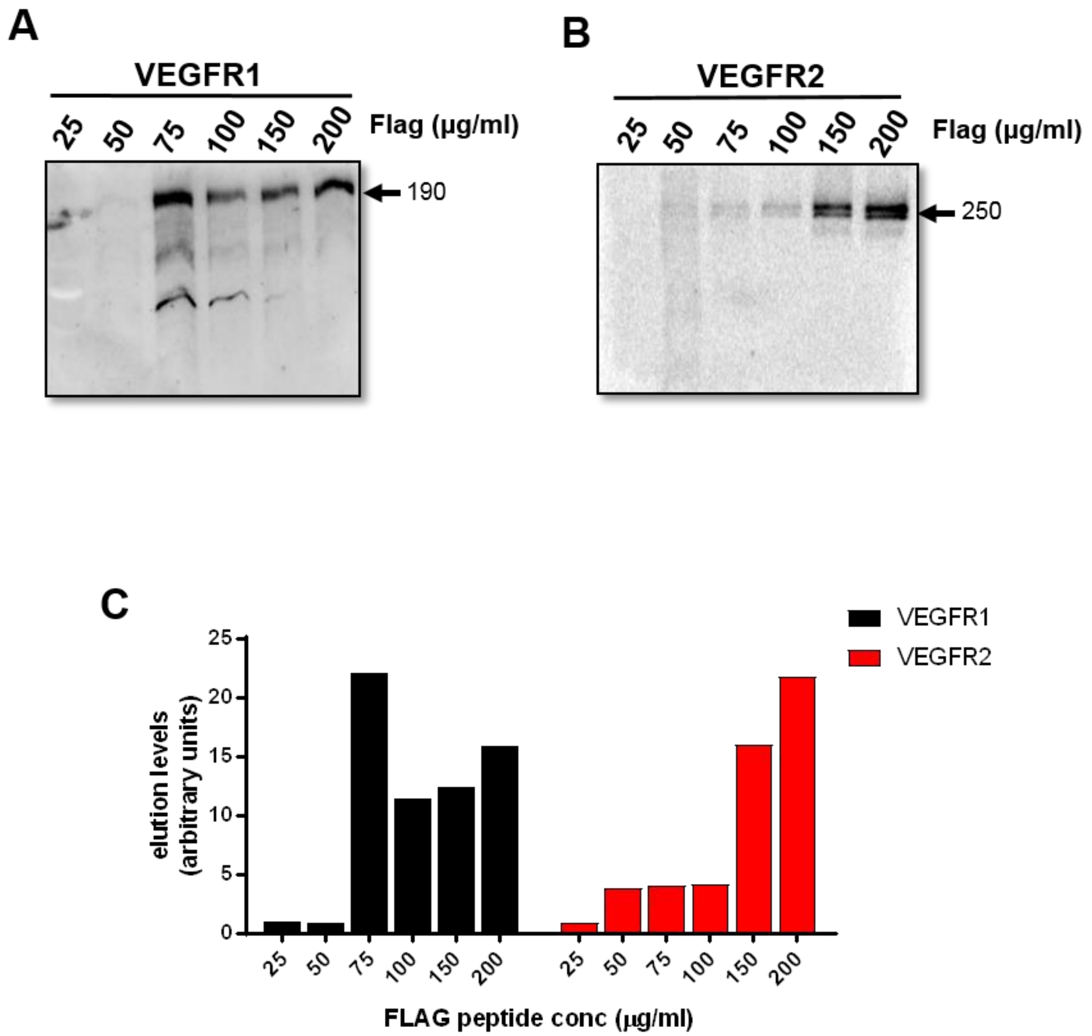

Figure 4.5. Elution of VEGFRs using FLAG peptide. Western blots showing VEGFRs solubilised in 1% (w/v) DDM and affinity purified using anti-FLAG M2 mAb. VEGFRs is eluted using either 25, 50, 75, 150 or 200 µg/ml FLAG peptide, VEGFR1 and VEGFR2 probed with goat anti-VEGFR1 and goat anti-VEGFR2 primary antibodies respectively. **(A)** VEGFR1, and **(B)** VEGFR2. **(C)** Relative quantification of VEGFR elution with different concentrations of FLAG peptide. VEGFR1 and VEGFR2 maximally elute at 75 and 200 µg/ml FLAG peptide respectively.

4.2.3. Effect of varying the protein:detergent ratio on receptor

Based on the above optimisation studies on proteolytic stability and protein retention, VEGFR2 was chosen for further analysis and EM studies. The protein-detergent mass ratio is also an important parameter for the solubilisation of cell membranes. Evidence suggests that higher detergent concentration doesn’t necessarily achieve higher solubilisation, whereas at lower concentrations the protein of interest might not retain its native state and gets degraded (Womack et al., 1983, Lichtenberg et al., 1983). It is important to characterize the detergent and total membrane protein mass ratio to measure the mass of detergent or polymer at which the maximal solubility is achieved. The solubility of VEGFR2 was initially analysed in 1% (w/v) DDM detergent, to further increase membrane protein solubility, a different mass ratio of DDM detergent and SMA polymer with total membrane protein were used.

The cell membranes containing recombinant VEGFR2, solubilised in different protein and detergent (w/w) ratios; optimisation was performed using DDM detergent and SMA polymer. Three fractions i.e. total (T), soluble (Sol), and insoluble (Insol) were collected and subjected to SDS-PAGE and western blot using an anti-VEGFR2 antibody (Fig. 4.6). Variation of DDM (Fig. 4.6A) or SMA (Fig. 4.6B) was used to evaluate optimal recombinant FLAG-VEGFR2 recovery. Quantification of these data suggests that using DDM, maximal solubilisation is achieved at 1:1 ratio (Fig. 4.6C), whereas using SMA, better solubilisation is achieved at 1:10 ratio of membrane protein:SMA (Fig. 4.6D). These data suggested that significant differences in membrane recovery using these two types of reagents for membrane protein solubilisation and purification.

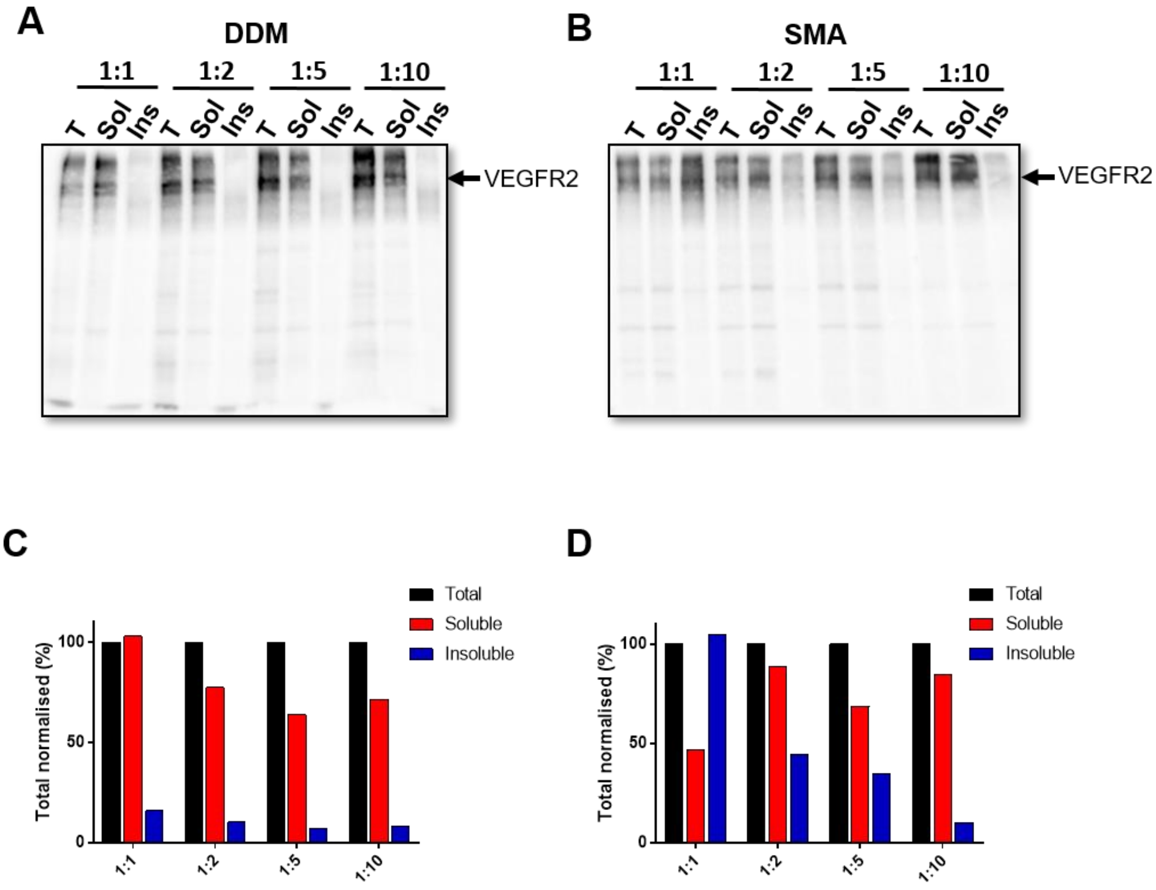

Figure 4.6. Comparison of VEGFR2 solubilisation with DDM and SMA (protein and detergent ratio (w/w)). Western blots showing solubilisation of VEGFR2 with equal quantities of each fraction analysed by immunoblotting. **(A)** DDM detergent, **(B)** SMA polymer comparison for VEGFR2 solubilisation. Total (T), soluble (S), and Insoluble (Insol). Relative quantification of soluble and insoluble VEGFR2 using **(C)** DDM or **(D)** SMA respectively. Western blots are developed by probing with goat anti-VEGFR2 antibody

4.2.4. Isolation and analysis of recombinant VEGFR2

For structural analysis using EM, recombinant FLAG-VEGFR2 needs to be pure and free of impurities, and a one-step FLAG-based immunoaffinity purification is estimated to produce moderately pure protein at ~50-60 % purity (Kimple et al., 2013, Lichty et al., 2005) which is sub-standard and not pure enough for EM analysis (Lyumkis, 2019). After establishing the solubility and elution parameters, purified FLAG-VEGFR2 was subjected to SDS-PAGE and the purity was estimated using Coomassie blue and silver staining (Mohan, 1992). Coomassie staining is able to detect as low as 0.2 μg of protein (He, 2011), but the more sensitive silver stain can detect protein as low as 10 ng (Chevallet et al., 2006). Using these two staining approaches the quantity and purity of FLAG-VEGFR2 were estimated (Fig. 4.7).

Based on previously established optimisation studies, FLAG-VEGFR2 was purified from HEK293 cell membranes by solubilising in 1:1 (total membrane protein:DDM) (w/w) and batch eluted by using 100 μg/ml and 200 μg/ml FLAG peptide (Fig. 4.7). At each FLAG peptide concentration, three elution fractions were collected i.e. 100 μg/ml (E1-E3) and 200 μg/ml (E4-E6). The unbound flow-through (UB) and elution fractions (E1-E6) were run on SDS-PAGE and probed by Western blot using the goat anti-VEGFR2 antibody (Fig. 4.7A). Full-length detergent-solubilised VEGFR2 eluted in fractions E5 and E6 as expected (Fig. 4.7A). The relative quantification of the amount of FLAG-VEGFR2 was estimated, showing a maximal recovery in fraction E6 (Fig. 4.7B). Fractions subjected to SDS-PAGE and Coomassie blue staining (Fig. 4.7C), or silver staining (Fig. 4.7D), both showed a band at ~250 kDa in all elutions (E1-E6) close to the expected size for FLAG-VEGFR2. Two other dominant bands were observed in elution fractions (E4-E6) at ~65 kDa and ~40 kDa. Even though the presence of VEGFR2 was clearly verified in E6 using western blot (Fig. 4.7A), a clear band for FLAG-VEGFR2 was not detected in E6 using Coomassie blue and silver staining (Fig. 4.7C and 4.7D).

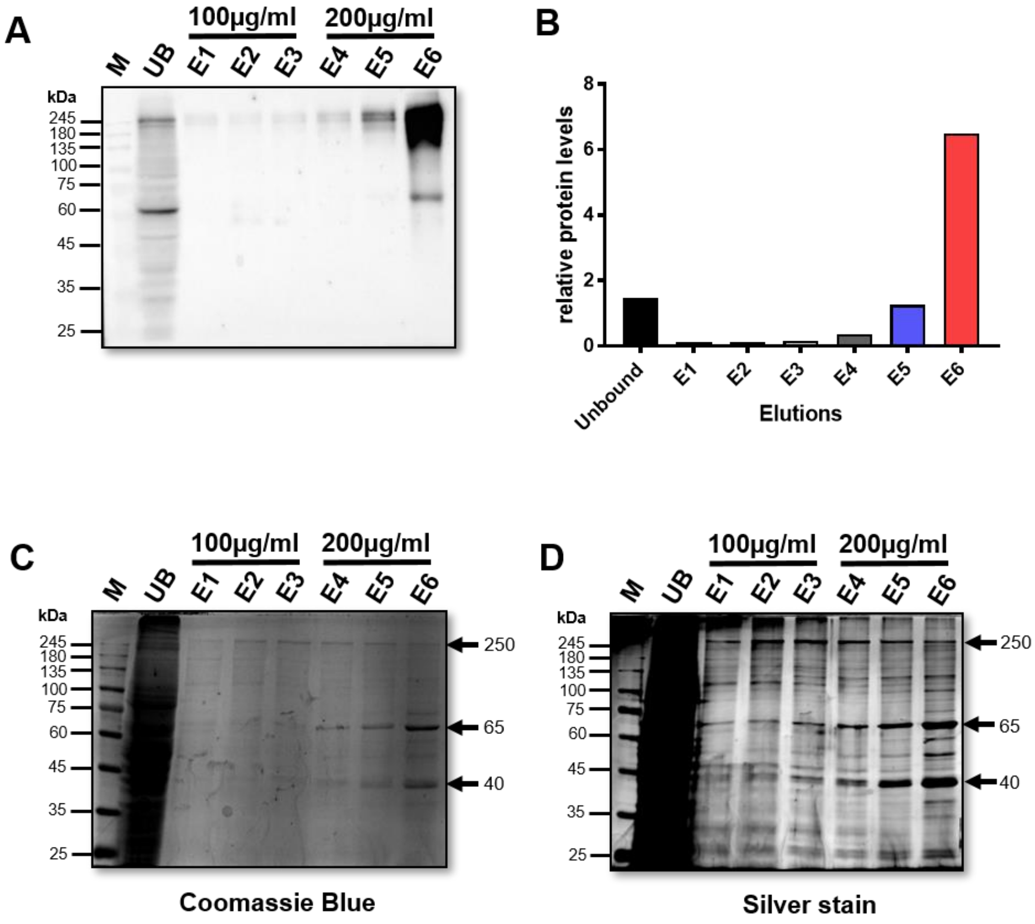

Coomassie Blue

Silver stain

Figure 4.7. SDS-PAGE analysis of purified VEGFR2 using DDM. VEGFR2 solubilised in DDM and affinity purified, eluted using sequential elutions of 100 µg/ml and 200 µg/ml FLAG peptide. Equal volumes of unbound (UB) and eluted fractions (E1-E6) were subjected to SDS-PAGE analysis. **(A)** Western blot of eluted VEGFR2 probed with goat anti-VEGFR2 primary antibody. **(B)** Relative quantification of VEGFR2 using DDM-based purification. **(C)** SDS-PAGE and Coomassie blue staining of VEGFR2 elutions. **(D)** SDS-PAGE and silver staining of VEGFR2 elutions. Multiple bands at various sizes were detected with Coomassie and silver stain, indicating impurities in the eluted fractions.

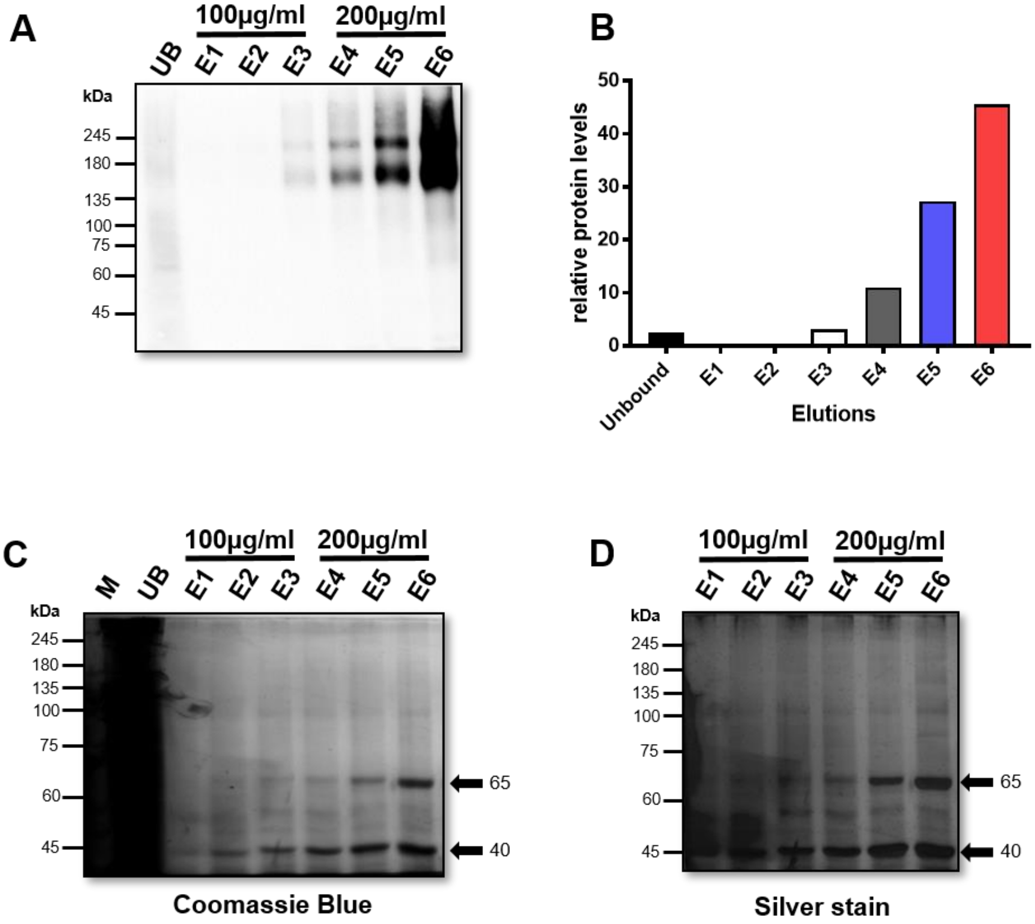

Figure 4.8. SDS-PAGE analysis of purified VEGFR2 using SMA. VEGFR2 solubilised in SMA and affinity purified, eluted using sequential elutions of 100 µg/ml and 200 µg/ml FLAG peptide. Equal volumes of unbound (UB) and eluted fractions (E1-E6) were subjected to SDS-PAGE analysis. **(A)** Western blot of eluted VEGFR2 probed with goat anti-VEGFR2 primary antibody. **(B)** Relative quantification of VEGFR2 using SMA-based purification. **(C)** SDS-PAGE and Coomassie blue staining of VEGFR2 elutions. **(D)** SDS-PAGE and silver staining of VEGFR2 elutions. Multiple bands at various sizes were detected with Coomassie and silver stain, indicating impurities in the eluted fractions.

Alternatively, solubilising cell membranes in 1:10 (total protein:SMA) (w/w) was subjected to a similar analysis using western blotting and purified FLAG-VEGFR2 evaluation (Fig. 4.8). The Western blot showed full-length VEGFR2 elution at 200 μg/ml FLAG peptide concentration (fractions E4-E6) (Fig. 4.8A). The relative quantification of FLAG-VEGFR2 elution showed the highest amounts of VEGFR2 in fraction E6 (Fig. 4.8B). These fractions were then analysed using SDS-PAGE and Coomassie blue or silver stain (Fig. 4.8C and 4.8D). Interestingly, the 250 kDa band observed during the DDM purification procedure was not detected when the membrane was solubilised in SMA, whereas the two dominant bands at ~65 kDa and ~40 kDa were still observed. Except for the 250 kDa band, the elution profiles look the same for DDM (Fig. 4.7) and SMA (Fig. 4.8). Overall, from this study, it can be said that a full-length VEGFR2 can be solubilised and isolated using DDM detergent and SMA polymer. Furthermore, no distinguishable bands were detected for FLAG-VEGFR2 which potentially indicates that the amount of purified VEGFR2 was still lower than the detection limit for Coomassie blue as well as a silver stain; multiple bands detected <200 kDa could either be proteolytic fragments of VEGFR2 or impurities. However, such bands were not detected on Western blotting using anti-VEGFR2, which indicates that they are impurities. Nonetheless, further analysis is needed to identify the proteins in those low molecular mass bands.

4.2.4.1. Extracted VEGFR2 analysis by mass spectrometry

Mass spectrometry (MS)-based protein analysis was performed to check the identity of polypeptides isolated as part of the FLAG-VEGFR2 purification (Fig. 4.9). The DDM-solubilised and extracted FLAG-VEGFR2 fraction was subjected to SDS-PAGE and silver staining (Fig. 4.9A). Three prominant bands labeled A, B and C (250, 65 and 40 kDa) (Fig. 4.9A, red boxes) were excised and analyzed using tryptic digestion and tandem MS to produce a peptide fingerprint of the polypeptide species present in each region of the gel. The tryptic fingerprint data were processed using MASSLYNX 3.5 software, and the peptide sequences obtained were submitted for BLAST search on NCBI (https://blast.ncbi.nlm.nih.gov/Blast.cgi) to identify the proteins (Table. 4.1). In band A (~250 kDa), four proteins were identified with different peptide coverages, VEGFR2 was also detected (Table 4.1). However, the number of peptides mapped and the percentage coverage of VEGFR2 was very low (Fig.4.9B). Two other proteins detected with more protein coverage were spectrin β chain (SPTB2) and spectrin α chain (SPTN1). Spectrin β and α are two subunits of the spectrin scaffold protein that link the plasma membrane to the actin cytoskeleton, which are involved in the arrangement of the cell structure (Hülsmeier et al., 2007). Usually, the sequence coverage directly depends on the relative abundance of each polypeptide in the gel; this indicates that the elution has more dominant impurities than the FLAG-VEGFR2. Moreover, no fragments of FLAG-VEGFR2 were detected in bands B (65 kDa) and C (40 kDa) (Appendix). The contaminants detected in those two bands are listed in supplementary Tables B1 and B2 (Appendix).

Furthermore, a similar MS analysis performed on FLAG-VEGFR2 solubilised in SMA polymer (Fig. 4.10). The protein gel was stained with silver stain and three bands A, B and C (Fig. 4.10A) were excised and analyzed using tryptic digestion and mass spectrometry. A very faint band was visible >200 kDa and this identified only VEGFR2 with very low coverage (Fig. 4.10B; Table 4.2). Other protein contaminants were detected in the other two bands B and C which are listed in Supplementary Tables B3 and B4 (Appendix B). This concludes that solubilisation in DDM detergent carries more impurities compared to SMA. However, it is crucial to note that the tryptic peptides identified in this analysis were derived from both the VEGFR2 extracellular domain and cytoplasmic tyrosine kinase domain (Fig. 4.9 and 4.10).

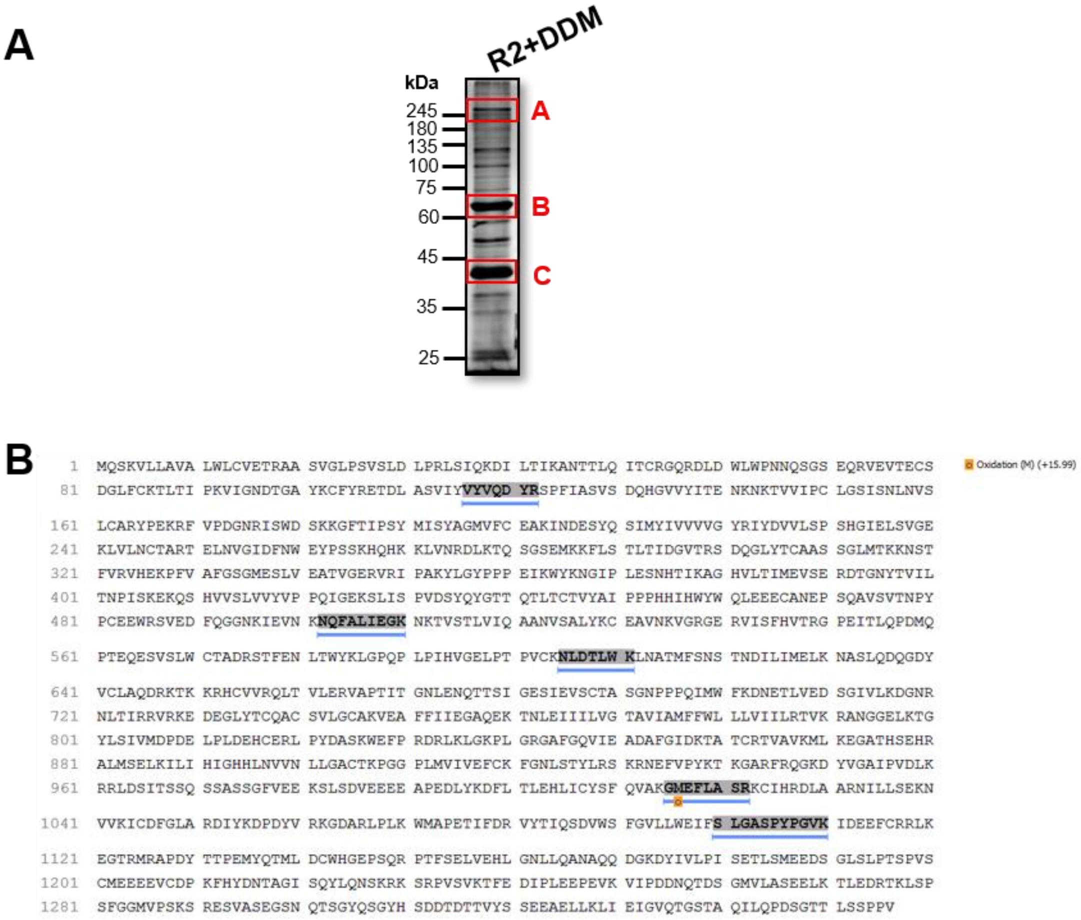

```
   1 MQSKVLLAVA LWLCVETRAA SVGLPSVSLD LPRLSIQKDI LTIKANTTLQ ITCRGQRDLD WLWPNNQSGS EQRVEVTECS
  81 DGLFCKTLTI PKVIGNDTGA YKCFYRETDL ASVIYVYVQD YRSPFIASVS DQHGVVYITE NKNKTVVIPC LGSISNLNVS
 161 LCARYPEKRF VPDGNRISWD SKKGFTIPSY MISYAGMVFC EAKINDESYQ SIMYIVVVVG YRIYDVVLSP SHGIELSVGE
 241 KLVLNCTART ELNVGIDFNW EYPSSKHQHK KLVNRDLKTQ SGSEMKKFLS TLTIDGVTRS DQGLYTCAAS SGLMTKKNST
 321 FVRVHEKPFV AFGSGMESLV EATVGERVRI PAKYLGYPPP EIKWYKNGIP LESNHTIKAG HVLTIMEVSE RDTGNYTVIL
 401 TNPISKEKQS HVVSLVVYVP PQIGEKSLIS PVDSYQYGTT QTLTCTVYAI PPPHHIHWYW QLEEECANEP SQAVSVTNPY
 481 PCEEWRSVED FQGGNKIEVN KNQFALIEGK NKTVSTLVIQ AANVSALYKC EAVNKVGRGE RVISFHVTRG PEITLQPDMQ
 561 PTEQESVSLW CTADRSTFEN LTWYKLGPQP LPIHVGELPT PVCKNLDTLW KLNATMFSNS TNDILIMELK NASLQDQGDY
 641 VCLAQDRKTK KRHCVVRQLT VLERVAPTIT GNLENQTTSI GESIEVSCTA SGNPPPQIMW FKDNETLVED SGIVLKDGNR
 721 NLTIRRVRKE DEGLYTCQAC SVLGCAKVEA FFIIEGAQEK TNLEIIILVG TAVIAMFFWL LLVIILRTVK RANGGELKTG
 801 YLSIVMDPDE LPLDEHCERL PYDASKWEFP RDRLKLGKPL GRGAFGQVIE ADAFGIDKTA TCRTVAVKML KEGATHSEHR
 881 ALMSELKILI HIGHHLNVVN LLGACTKPGG PLMVIVEFCK FGNLSTYLRS KRNEFVPYKT KGARFRQGKD YVGAIPVDLK
 961 RRLDSITSSQ SSASSGFVEE KSLSDVEEEE APEDLYKDFL TLEHLICYSF QVAKGMEFLA SRKCIHRDLA ARNILLSEKN
1041 VVKICDFGLA RDIYKDPDYV RKGDARLPLK WMAPETIFDR VYTIQSDVWS FGVLLWEIFS LGASPYPGVK IDEEFCRRLK
1121 EGTRMRAPDY TTPEMYQTML DCWHGEPSQR PTFSELVEHL GNLLQANAQQ DGKDYIVLPI SETLSMEEDS GLSLPTSPVS
1201 CMEEEEVCDP KFHYDNTAGI SQYLQNSKRK SRPVSVKTFE DIPLEEPEVK VIPDDNQTDS GMVLASEELK TLEDRTKLSP
1281 SFGGMVPSKS RESVASEGSN QTSGYQSGYH SDDTDTTVYS SEEAELLKLI EIGVQTGSTA QILQPDSGTT LSSPPV
```

Figure 4.9. Peptide identification VEGFR2 solubilized in DDM using mass spectrometry analysis. (A) Silver stained gel showing the purified VEGFR2 fraction was further analysed using mass spectrometry. The boxed bands labelled A, B and C (250, 65, and 40 kDa respectively) were excised, subjected to tryptic digestion, mass spectrometry, tryptic fingerprinting with database analysis. **(B)** Peptides identified in band A (250 kDa) confirm the identity of the protein as full-length VEGFR2 with the mixture of other protein impurities, Position of oxidation is highlighted (orange, o).

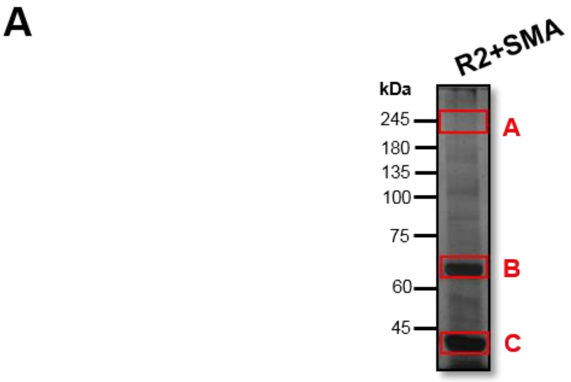

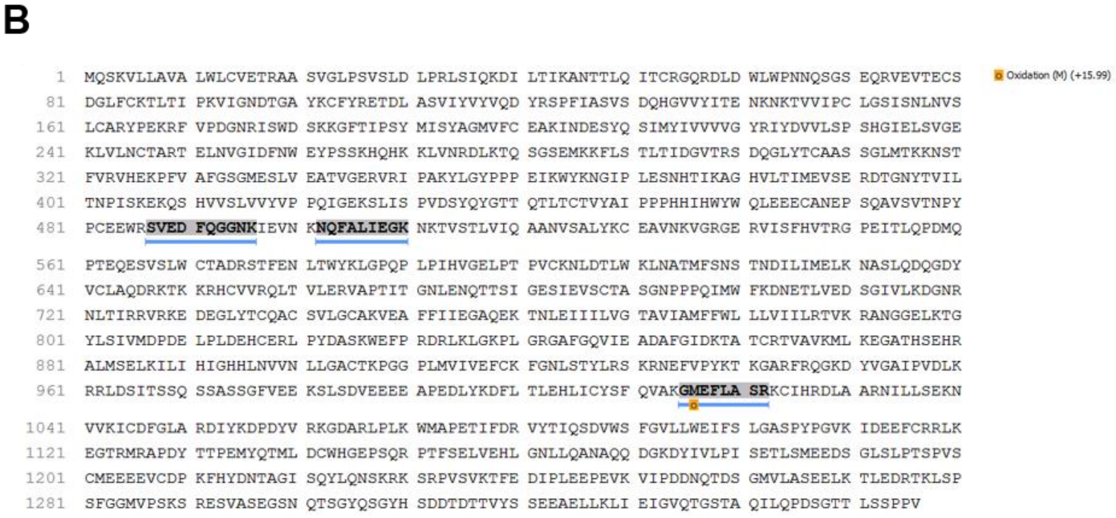

```
   1 MQSKVLLAVA LWLCVETRAA SVGLPSVSLD LPRLSIQKDI LTIKANTTLQ ITCRGQRDLD WLWPNNQSGS EQRVEVTECS
  81 DGLFCKTLTI PKVIGNDTGA YKCFYRETDL ASVIYVYVQD YRSPFIASVS DQHGVVYITE NKNKTVVIPC LGSISNLNVS
 161 LCARYPEKRF VPDGNRISWD SKKGFTIPSY MISYAGMVFC EAKINDESYQ SIMYIVVVVG YRIYDVVLSP SHGIELSVGE
 241 KLVLNCTART ELNVGIDFNW EYPSSKHQHK KLVNRDLKTQ SGSEMKKFLS TLTIDGVTRS DQGLYTCAAS SGLMTKKNST
 321 FVRVHEKPFV AFGSGMESLV EATVGERVRI PAKYLGYPPP EIKWYKNGIP LESNHTIKAG HVLTIMEVSE RDTGNYTVIL
 401 TNPISKEKQS HVVSLVVYVP PQIGEKSLIS PVDSYQYGTT QTLTCTVYAI PPPHHIHWYW QLEEECANEP SQAVSVTNPY
 481 PCEEWRSVED FQGGNKIEVN KNQFALIEGK NKTVSTLVIQ AANVSALYKC EAVNKVGRGE RVISFHVTRG PEITLQPDMQ
 561 PTEQESVSLW CTADRSTFEN LTWYKLGPQP LPIHVGELPT PVCKNLDTLW KLNATMFSNS TNDILIMELK NASLQDQGDY
 641 VCLAQDRKTK KRHCVVRQLT VLERVAPTIT GNLENQTTSI GESIEVSCTA SGNPPPQIMW FKDNETLVED SGIVLKDGNR
 721 NLTIRRVRKE DEGLYTCQAC SVLGCAKVEA FFIIEGAQEK TNLEIIILVG TAVIAMFFWL LLVIILRTVK RANGGELKTG
 801 YLSIVMDPDE LPLDEHCERL PYDASKWEFP RDRLKLGKPL GRGAFGQVIE ADAFGIDKTA TCRTVAVKML KEGATHSEHR
 881 ALMSELKILI HIGHHLNVVN LLGACTKPGG PLMVIVEFCK FGNLSTYLRS KRNEFVPYKT KGARFRQGKD YVGAIPVDLK
 961 RRLDSITSSQ SSASSGFVEE KSLSDVEEEE APEDLYKDFL TLEHLICYSF QVAKGMEFLA SRKCIHRDLA ARNILLSEKN
1041 VVKICDFGLA RDIYKDPDYV RKGDARLPLK WMAPETIFDR VYTIQSDVWS FGVLLWEIFS LGASPYPGVK IDEEFCRRLK
1121 EGTRMRAPDY TTPEMYQTML DCWHGEPSQR PTFSELVEHL GNLLQANAQQ DGKDYIVLPI SETLSMEEDS GLSLPTSPVS
1201 CMEEEEVCDP KFHYDNTAGI SQYLQNSKRK SRPVSVKTFE DIPLEEPEVK VIPDDNQTDS GMVLASEELK TLEDRTKLSP
1281 SFGGMVPSKS RESVASEGSN QTSGYQSGYH SDDTDTTVYS SEEAELLKLI EIGVQTGSTA QILQPDSGTT LSSPPV
```

Figure 4.10. Mass spectrometry analysis of SMA-based purified VEGFR2. (A) Silver stained gel showing the purified VEGFR2 fraction was further analysed using mass spectrometry. The boxed bands labelled A, B and C (250, 65, and 40 kDa respectively) were excised, subjected to tryptic digestion, mass spectrometry, tryptic fingerprinting with database analysis. **(B)** Peptides identified from band A confirm the identity of the protein as full-length VEGFR2 (250 kDa) with additional protein impurities. Position of oxidation is highlighted (orange, o).

Table 4.1. VEGFR2 and other proteins identified using tryptic digestion and mass spectrometry from band A (Figure 4.9A).VEGFR2 highlighted in red

Protein ID	Accession	Coverage (%)	Peptides	PTM	Avg. Mass	Description
474	Q01082|SPTB2_HUMAN	22	49	Y	274608	Spectrin beta chain, non-erythrocytic 1 OS=Homo sapiens GN=SPTBN1 PE=1 SV=2
475	Q13813|SPTN1_HUMAN	11	27	N	284538	Spectrin alpha chain, non-erythrocytic 1 OS=Homo sapiens GN=SPTAN1 PE=1 SV=3
477	P35968|VGFR2_HUMAN	3	5	Y	151526	Vascular endothelial growth factor receptor 2 OS= Homo sapiens GN=KDR PE=1 SV=2
11	P02768|ALBU_HUMAN	5	3	N	69367	Serum albumin OS=Homo sapiens GN=ALB PE=1 SV=2
Total proteins 4						

Table 4.2. VEGFR2 identified using tryptic digestion and mass spectrometry from band A (Figure 4.10A).. VEGFR2 peptide sequence highlighted in red.

Protein ID	Accession	Coverage (%)	Peptides	PTM	Avg. Mass	Description
5	P35968|VGFR2_HUMAN	2	3	Y	151526	Vascular endothelial growth factor receptor 2 OS=Homo sapiens GN=KDR PE=1 SV=2
Total proteins 1						

4.2.4.2. Preclearing the lysate with IgG improves the purity of extracted VEGFR2

Two main obstacles that needed to be addressed were the purity and the quantity of solubilised VEGFR2 before proceeding to EM analysis. A subsequent second purification can be performed using size exclusion chromatography (SEC) to separate the eluted proteins based on their molecular weight. However, the main concern was the ~200-250 kDa α and β chain spectrin as contaminants which are around the same molecular mass as full-length VEGFR2; other major contaminants are smaller than 150 kDa and can be eliminated by SEC.

The spectrin α and β chains are unlikely to bind to the anti-FLAG antibody and probably bind non-specifically to the FLAG mAb-agarose beads. To improve the purity, a pre-clearing step was introduced with mouse IgG-agarose beads. The membranes were solubilised with DDM or SMA and run-through the mouse IgG-agarose resin to trap and eliminate non-specific binding contaminants before adding it to mouse monoclonal M2 FLAG-agarose resin. VEGFR2 was then extracted from the pre-cleared lysate by competitive elution with FLAG peptide (Fig. 4.11). The eluted fractions were subjected to Western blotting for VEGFR2 (Fig. 4.11A and 4.11B). Interestingly, purified VEGFR2 eluted at 100 µg/ml FLAG peptide concentration. Silver staining was then used to further visualize protein content in eluates (Fig. 4.11C and 4.11D). In these experiments, spectrin and other high molecular mass contaminants were not detected (Fig. 4.11C and 4.11D). However, the two contaminants at ~65 kDa and 40 kDa were still observed which could be eliminated in the next purification step (Fig. 4.11C and 4.11D).

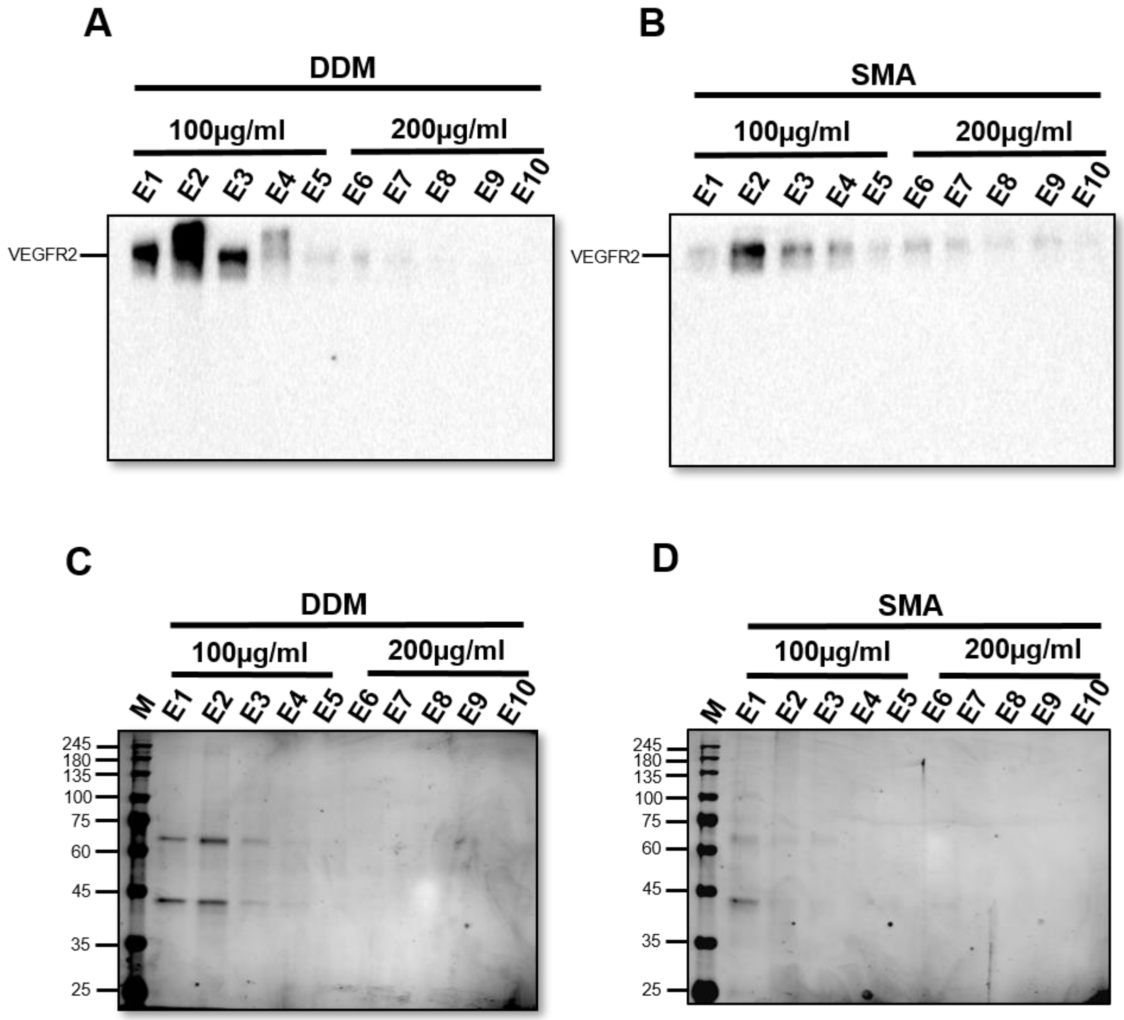

Figure 4.11. Refinement of VEGFR2 purification procedure. (A, B) Western blotting of DDM or SMA-based VEGFR2 purification procedures. Cell lysates were pre-cleared with Protein G-Sepharose resin before FLAG-based purification (see Materials and Methods), western blots were probed with goat anti-VEGFR2 primary antibody SDS-PAGE of purified VEGFR2 using either **(C)** DDM, or **(D)** SMA followed by silver staining and evaluation. IgG pre-clearing enabled the use of 100 µg/ml FLAG peptide for VEGFR2 elution, with less background contamination.

4.2.5. Molecular mass estimation of purified VEGFR2

Using denaturing SDS-PAGE and Western blotting, the size of glycosylated full-length VEGFR2 monomer was estimated at ~250 kDa (Fig. 4.3B). However, whether VEGFR2 is monomeric or dimeric after solubilisation in DDM detergent and the homogeneity was still unknown. Studies were carried out to characterize the multimeric status of extracted VEGFR2.

4.2.5.1. SEC analysis of DDM solubilised VEGFR2

To further improve the quality, a second step purification was performed using size exclusion chromatography (SEC). This gel filtration separates multiple protein mixture based on their size. Theoretically, large protein complexes elute faster as they move without diffusing through the pores whereas, smaller proteins are eluted slower due to diffusion (Hong et al., 2012). The objective of this study was to improve the purity of VEGFR2 by separating the impurities on the basis of their size, determine the molecular mass of the extracted VEGFR2 and estimate its molecular mass distribution.

Three elutions of VEGFR2 (E1, E2, and E3) (Fig. 4.12A) were pooled together and concentrated using a 100 kDa molecular weight cutoff (MWCO) filter to remove the impurities lower than 100 kDa. After quantification, approximately 50-100 µg of eluted protein was loaded onto a Superose 6 Increase 5/150 GL column. Fig. 4.12B shows the chromatogram of the concentrated VEGFR2 pool. The size exclusion elution profile showed five distinct peaks (labeled 1-5), the elution fractions were collected (A6-B12) and analyzed using antibody-based dot blots to detect VEGFR2 (Fig. 4.12C, top panel). The pool of soluble VEGFR2 was largely detected in fractions B2 and B3, and very less in B4 and B5 (Fig. 4.12C). Interestingly, none of the other peaks (with protein content) had immune-reactive VEGFR2 (Fig. 4.12C), indicating unwanted contaminants were successfully removed. This indicates that the pooled elutions after first step immunoaffinity purification still contained relatively higher levels of impurities compared to VEGFR2. The western blot of B2-B4 fractions show full-length intact VEGFR2 (Fi. 4.12C lower panel).

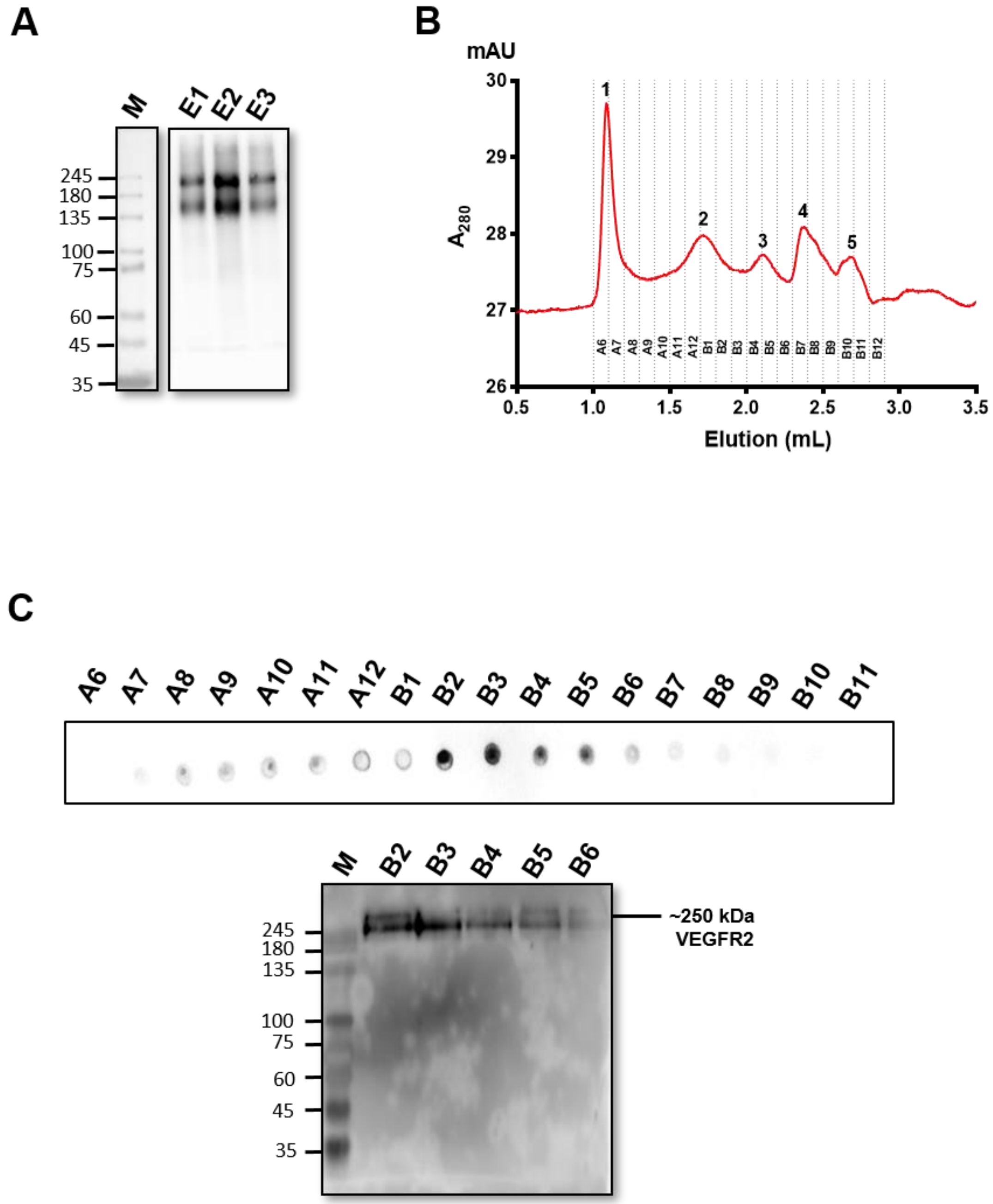

Figure 4.12. Size exclusion chromatography on purified FLAG-VEGFR2. (A) Eluted VEGFR2 fractions (E1, E2, E3). **(B)** Fractions E1-E3 were pooled, concentrated and loaded onto a Superose^{TM} 6 Increase 5/150 GL column and absorbance at 280 nm monitored. Fractions A6-B12 are shown on the trace diagram. **(C)** Equal volumes from each SEC fraction were immunoblotted using goat α-VEGFR2 antibody either as dot blots (upper panel) or SDS-PAGE (lower panel). Most full-length purified VEGFR2 was evident in fractions B2-B5.

The next objective was to identify the size of eluted VEGFR2. The Superose 6 5/150 GL column was calibrated using protein standards such as thyroglobulin (660 kDa), aldolase (158 kDa), creatinine phosphokinase (81 kDa dimer) and carbonic anhydrase (29 kDa) (Fig. 4.13). These protein standards were solubilised in a buffer containing DDM detergent and fractionated through the Superose 6 column (Fig. 4.13). The calibration curve was plotted using the gel-phase distribution coefficient (K_{av}) versus the logarithm molecular mass (Log MW). The estimated molecular mass range (kDa) of fractions containing VEGFR2 was measured and listed in Table. 4.3. The size of VEGFR2 eluted in fractions B2 and B3 (Fig. 4.13E) was estimated at 410.9 ± 68 and 301.55 ± 53 kDa respectively. The size of each DDM detergent micelle was reported to be 70 kDa (VanAken et al., 1986, Strop and Brunger, 2005). A full-length VEGFR2 (250 kDa) monomer trapped in 70 kDa DDM detergent micelle is approximately 320 kDa. This confirmed that DDM solubilized VEGFR2 is likely to be monomeric in nature.

Table 4.3. Estimated MW peaks during VEGFR2. The mass range of VEGFR2 fractions were measured by from fraction elution (V_E). The sizes represented are the maximum and minimum possible mass of each fraction.

Eluted fraction	Fraction V_E (mL)	Estimated M_r range in kDa
B2	1.8-1.9	410.9 ± 68
B3	1.9-2.0	301.55 ± 53
B4	2.0-2.1	203.35 ± 44.95
B5	2.1-2.2	118.9 ± 39.5

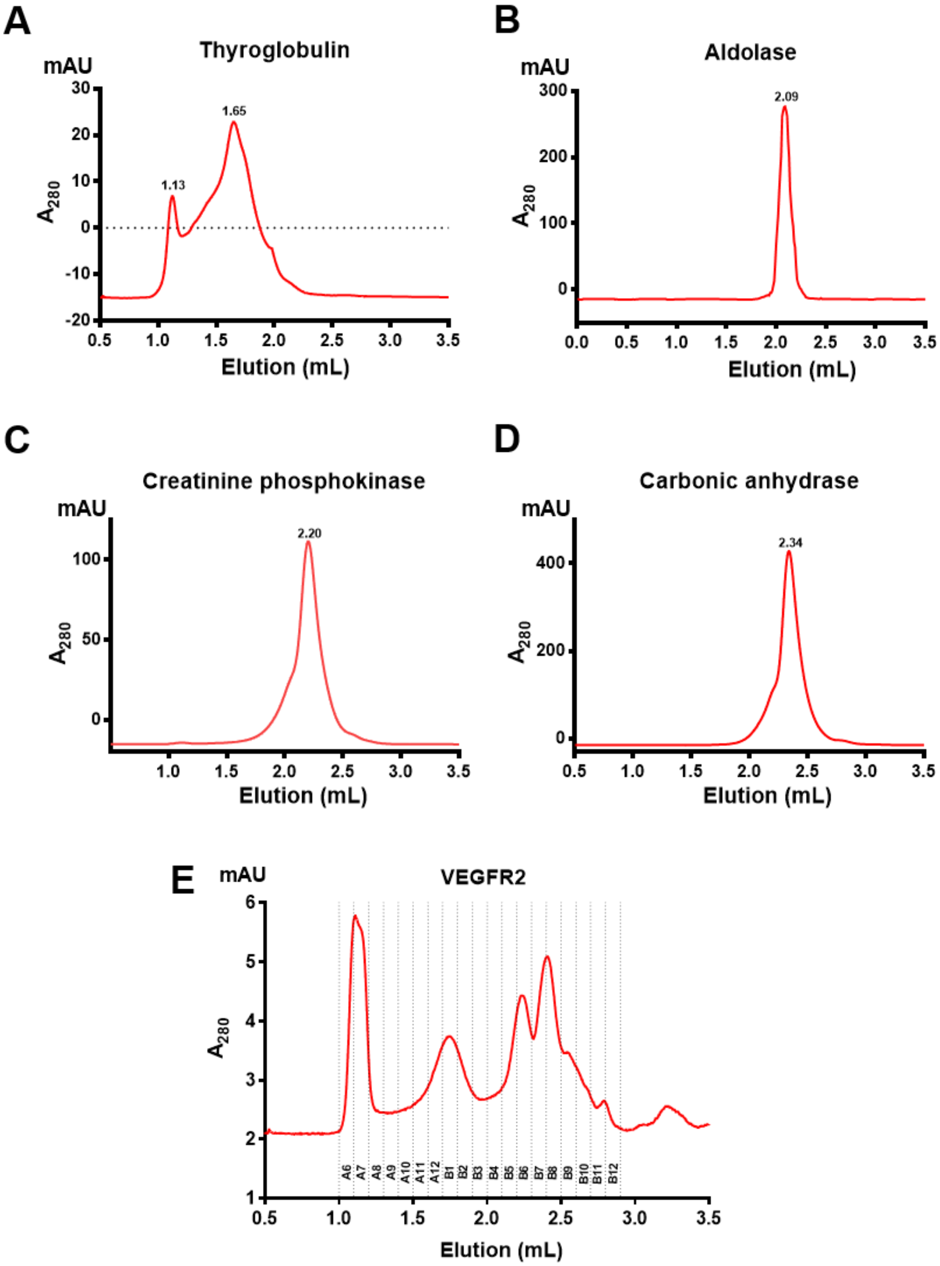

Figure 4.13. Molecular mass calibration of SEC column. Proteins of known molecular weights were solubilized in 0.05% (w/v) DDM and run through the Superpose 6 column to standardize their Mr elution and estimate the size of purified VEGFR2. Chromatograms of **(A)** thyroglobulin (660 kDa), **(B)** aldolase (158 kDa), **(C)** creatine phosphokinase (81 kDa dimer), **(D)** carbonic anhydrase (29 kDa), and **(E)** Purified VEGFR2 pool.

4.2.5.2. Native PAGE analysis of purified VEGFR2

A native PAGE analysis was used to further characterize purified VEGFR2 and also to test whether purified VEGFR2 could be induced to form dimers in the presence of VEGF-A ligand. In contrast to SDS-PAGE, native PAGE analysis allows separation of proteins in a native state by preserving the protein-protein interactions and multimeric complexes, therefore it is possible to estimate the size and multimeric state of soluble and membrane proteins under such conditions (Arndt et al., 2012). The eluted B2 fraction from previous SEC studies (Fig. 4.13E) was used in native PAGE analysis. A Western blot of blue native PAGE using goat-anti VEGFR2 antibody on VEGFR2 in the presence or absence of VEGF-A and ATP showed differing effects (Fig. 4.14A). Purified VEGFR2 was ~250-350 kDa in size but formed higher-order multimers of ~700-750 kDa in the presence of VEGF-A (Fig. 4.14A). There was no significant difference caused by the addition of ATP to these experiments (Fig. 4.14A). Immunoblotting these species using denaturing and reducing SDS-PAGE indicates that VEGF-A stabilises VEGFR2, but ATP does not significantly affect VEGFR2 levels in this analysis (Fig. 4.14B). These findings show that the purified VEGFR2 is likely monomeric and undergoes dimerisation due to VEGF-A addition.

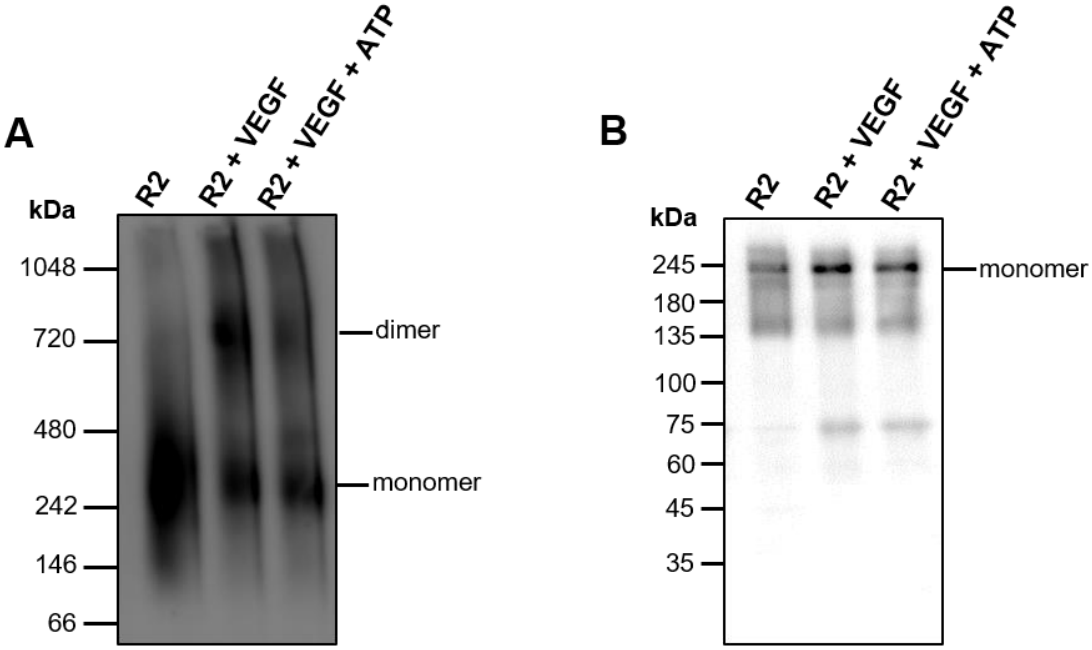

Figure 4.14. Dimerisation of VEGFR2 by VEGF-A ligand. (A) Western blot of purified VEGFR2 using native PAGE. Purified VEGFR2 (lane 1), VEGFR2/VEGF-A (lane 2) and VEGFR2/VEGF-A/ATP (lane 3). VEGFR2 is monomeric (~250-350 kDa) but binding to VEGF-A promoted higher order complexes (~600-750 kDa). **(B)** Western blot analysis of purified VEGFR2 complexes using reducing SDS-PAGE gel (control). VEGFR2 is monomeric in all three lanes due to reduction and denaturation. The blot was developed by probing with goat anti-VEGFR2 antibody.

4.2.6. Negative stain electron microscopy (EM) of VEGFR2

We established that full-length purified VEGFR2 could undergo dimerization using VEGF-A. The next step was structural analysis using electron microscopy (EM). Firstly, negative stain EM was used which provides a way to study and analyze the shape of the VEGFR2 complex and assess the heterogeneity of protein by image classification. It also allows assembling of a low-resolution model with low (micrograms) amounts of protein in the samples (Booth et al., 2011a).

4.2.6.1. ATP causes aggregation and form crystals in negative stain EM

Negative stain EM grids were made using uranyl acetate staining with purified VEGFR2 solubilised in DDM and SMA. For initial screening and to determine the quality of the receptor, grids were made with +/- VEGF and/or ATP. The objective was to assemble the VEGFR2 complex in different active and inactive states. The grids were screened with FEI F20 electron microscope, and micrographs were acquired for analysis. Fig.4.15 shows EM data collected on purified VEGFR2; purified VEGFR2 + 0.1 nM VEGF-A_{165}; VEGFR2 + 100 nM ATP; and VEGFR2 + 0.1 nM VEGF-A_{165} + 100 nM ATP solubilised in either DDM or SMA (Fig. 4.15 top panel and lower panel respectively). VEGFR2 monomers and potentially inactive dimers bound to VEGF-A_{165} respectively are shown (Fig. 4.15A, 4.15B, 4.15E and 4.15F). Even though both experiments showed monodisperse particle distribution and less background noise, particle heterogeneity was still observed. However, the experiments of interest were conditions of formation of an active VEGFR2 dimer complex with VEGF-A and ATP. Unfortunately, major clumps of aggregations and crystals were observed in micrographs with ATP (Fig. 4.15C, 4.15D, 4.15G and 4.15H). The grids were made repeatedly with freshly purified VEGFR2 with no improvement, protein aggregation and crystals were observed consistently. After troubleshooting, it was concluded that the crystalline precipitate was formed due to phosphate ions in ATP reacting with uranyl salts (Scarff et al., 2018, Gallagher et al., 2019). This proved to be a major hindrance in analysing the VEGFR2 dimer complex bound ATP and VEGF-A. Major optimisation studies are required to address the uranyl phosphate crystalline precipitate before such studies could provide meaningful structural information.

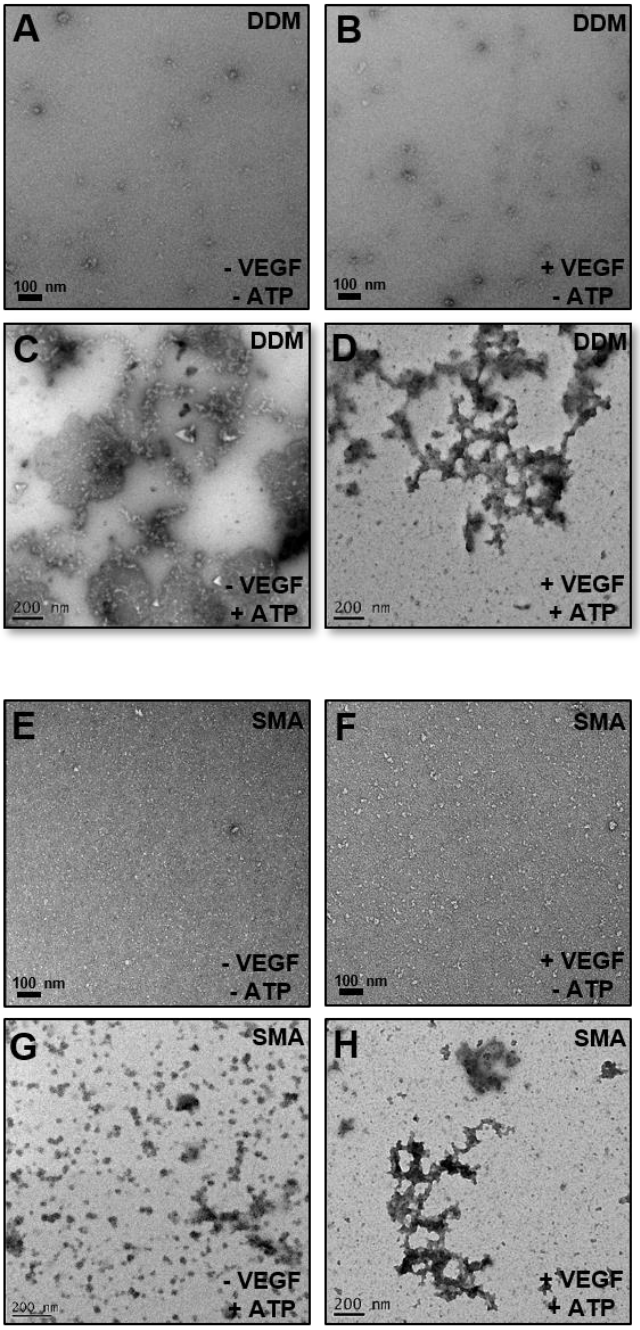

Figure 4.15. Negative stain EM analysis of purified VEGFR2/VEGF/ATP. Purified VEGFR2 fractions from SEC were used to generate negative micrographs. **(A-D)** Analysis of DDM-based purified VEGFR2. **(A)** Purified VEGFR2, **(B)** VEGFR2 plus 0.1 nM VEGF-A, **(C)** VEGFR2 plus 100 nM ATP, and **(D)** VEGFR2 plus 0.1 nM VEGF-A and 100 nM ATP. Bottom Panel VEGR2 solubilized in SMA. **(E-H)** Analysis of SMA-based purified VEGFR2. **(E)** Purified VEGFR2, **(F)** VEGFR2 plus 0.1 nM VEGF-A, **(G)** VEGFR2 plus 100 nM ATP, and **(H)** VEGFR2 plus 0.1 nM VEGF-A and 100 nM ATP. Protein aggregation was observed upon addition of ATP in both VEGFR2 preparations

4.2.6.2. EM analysis of VEGFR2 and VEGFR2/VEGF/Sutent complex

As the negative stain analysis of VEGFR2/VEGF-A_{165}/ATP complex were unsuccessful and required further optimisation studies, an attempt was made to assemble a VEGFR2 complex bound to VEGF-A_{165} at the extracellular domain and in the presence of a small molecule tyrosine kinase inhibitor (Sutent) which is an ATP mimetic and competitive inhibitor. This allows us to study the structural mechanism of receptor in an ATP-inhibited state. The VEGFR2 solubilised in DDM or SMA bound to FLAG M2 mAb resin was treated with VEGF-A_{165} and Sutent to stabilize the complex before elution with FLAG peptide. A Western blot of blue native PAGE was performed to confirm the dimerisation of VEGFR2 (Fig. 4.16A). Even though VEGFR2 recovery was very low compared to the previous purification approach, the successful dimerisation of VEGFR2 solubilised in both DDM and SMA (Fig. 4.16A) indicates that the membrane protein complex is potentially suitable for EM analysis.

EM studies of purified VEGFR2 and VEGFR2/VEGF-A_{165}/Sutent complex solubilised in DDM and SMA respectively were performed by collecting micrographs (Fig. 4.16B-E). VEGFR2 complex purified in DDM had multiple contaminants and aggregates (Fig 4.16B and 4.16C). Therefore, it was not good enough to further analysis, whereas the solubilisation in SMA had very fewer contaminants and also showed a monodisperse distribution of particles (Fig. 4.16D and 4.16E). The purified VEGFR2 molecule exhibited a beads-on-a-string appearance (Fig. 4.16D) and the VEGFR2 complex (VEGFR2/VEGF-A/Sutent) showed larger dimers with distinct orientation (Fig. 4.16E). Therefore, these data were further processed to generate 2-D class averages of the VEGFR2 complex.

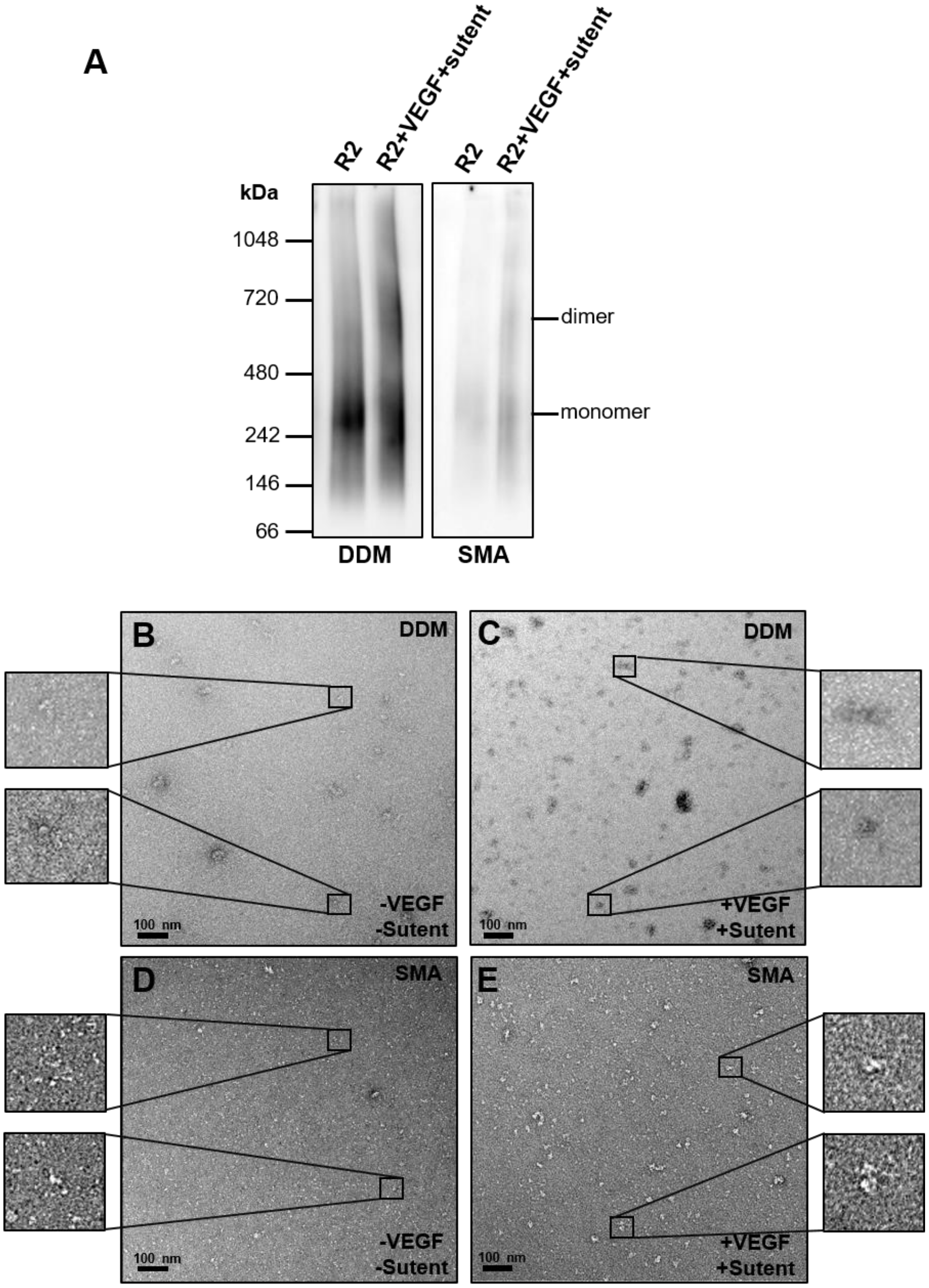

Figure 4.16. Negative stain EM analysis of purified VEGFR2/VEGF/Sutent. **(A)** Native PAGE Western blots of VEGFR2 and VEGFR2/VEGF-A/Sutent complexes in monomeric and dimeric states solubilised in DDM or SMA respectively. Western blots were probed with goat anti-VEGFR2 antibody. Negative stain EM analysis of **(B)** DDM-purified VEGFR2, **(C)** DDM-purified VEGFR2 plus 0.1 nM VEGF-A and 50 µM Sutent (tyrosine kinase inhibitor), **(D)** SMA-purified VEGFR2, and **(E)** SMA-purified VEGFR2 plus 0.1 nM VEGF-A and 50 µM Sutent (tyrosine kinase inhibitor). Scale bar indicate 100 nm.

4.2.6.2.1. 2-D models of the VEGFR2 complex

As explained earlier, purified monomeric VEGFR2 showed beads-on-a-string like appearance without any distinguishable features. Therefore, it is not viable to generate class averages of VEGFR2 monomers (without VEGFA).

In order to access the oligomeric state of VEGFR2 complex (VEGFR2/VEGF-A/Sutent), a total of 125 micrographs were collected. Using the RELION 3.0 software, 9,312 particles were picked to generate 60 class averages (Fig. 4.17A). The class averages exhibited conformations of various sizes, and possibly include both dimers and monomers. Fig. 4.17B shows 10 selected class averages showing similar architecture. The overall dimensions of VEGFR2/VEGF-A/Sutent were measured from class averages, the maximum average length measured along the axis was 20-25 nm (length) with maximum thickness ~10 nm (width) (Fig. 4.17C). This supports the heterogenous ECD particles of VEGFR2 observed by Hofer and group, again confirming that the observed class averages were mostly receptors (Stuttfeld and Ballmer-Hofer, 2009).

Furthermore, a graphic representation of the VEGFR2 complex showing three different conformations was generated (Fig. 4.17C). The class projection showed two receptor chains intertwined to form a dimer complex representing shape 8 with contacts at Ig domain 2, 5 and 7 (Fig. 4.17B, 4.17C). No distinct conformational features were observed for the Ig-like domain 1 (shown as blue strings). The VEGFR2 tyrosine kinase domain exhibited a small strand-like appearance without any specific orientation indicating that no sutent is bound within the kinase domain (Fig. 4.17C). These data indicate that VEGFR2 dimerisation occurs upon VEGF-A binding.

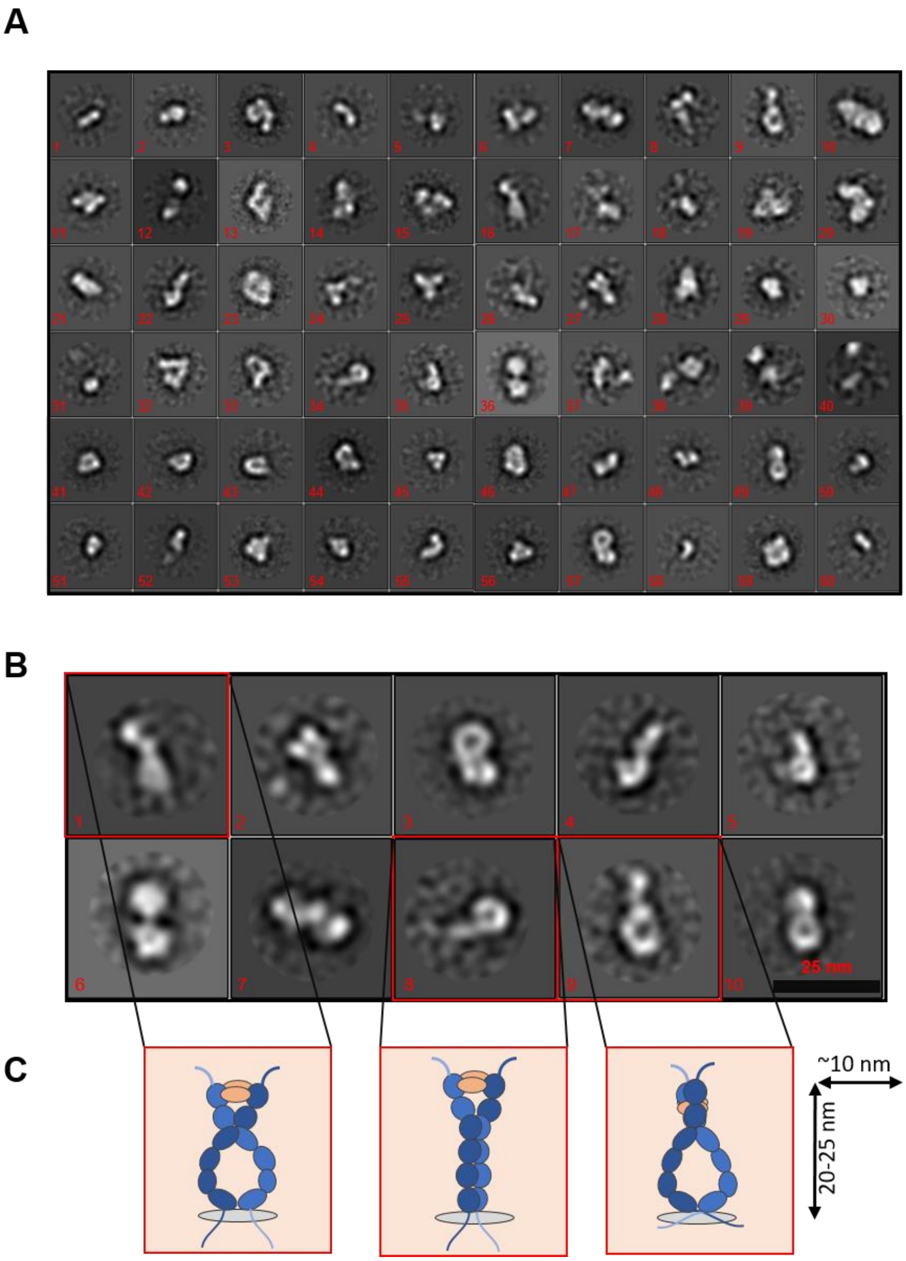

Figure 4.17. Negative stain EM-based 2-D classes of VEGFR2 complexes. (A) SMA-based purified VEGFR2-VEGF-A-Sutent imaged at 50 000X magnification**.** Class averages generated using RELION 3.0, 60 class averages are shown. **(B)** Selected class averages showing different orientation of VEGFR2-VEGF-A-Sutent complex. Scale bar, 25 nm. **(C)** Graphic representation three distinct class averages. Except for extracellular IgG domain 1, all extracellular domains (E2-E7) can be seen clearly with higher electron density distribution. The VEGFR2 tyrosine kinase domain did not show any distinguishable conformation. Length and thickness were measured at 20-25 nm and ~10 nm respectively.

4.3. DISCUSSION

The HEK293 cell lines with inducible VEGFR expression generated in the previous Chapter 3 were used for subsequent VEGFR purification. Solubilisation studies were carried out initially using the non-ionic DDM detergent. Comparative studies of VEGFR1 and VEGFR2 using DDM showed that VEGFR1 is more susceptible to proteolytic degradation under these conditions. Both anti-VEGFR1 and anti-VEGFR2 antibodies used only recognize the extracellular domains in each protein i.e. Sr27-H687 (VEGFR1) and A20-E764 (VEGFR2). Therefore, the bands recognized on Western blots are likely to be proteolytic fragments derived from full-length VEGFRs. The proteolytic cleavage of VEGFR1 was also observed in cell culture, suggesting a widespread phenomenon. Other work has found that VEGFR1 degradation, specifically domains D1-D3 occurs in both HEK293T and CHOK1SV GS-KO cells. Interestingly, growing cells at 30°C combined with protease cocktail inhibitor use improves VEGFR1 stability and inhibits proteolysis (Chakrabarti et al., 2016).

Compared to VEGFR1, VEGFR2 showed better stability and recovery during purification. Therefore, further structural studies were aimed at purified VEGFR2. Comparative studies were carried out on VEGFR2 solubilised in either DDM or SMA and showed similar solubilisation profiles at higher concentrations. Competitive elution is also affected by the high affinity of capture antibody binding which results in low recovery. Such cases require low pH or high acid elution to overcome the recovery issue, however, it can alter the activity and folding of the protein which compromises the functional activity of the protein (Di Russo et al., 2012). Therefore, such methods were not used here.

Mass spectrometry revealed VEGFR2 size at ~250 kDa and analysis has shown that VEGFR2-derived tryptic peptides are derived from both the extracellular and cytoplasmic domains. Even though the VEGFR2 peptide coverage was low, this was conclusive and clear (Baldwin, 2004). The mass spectrometry experiments confirmed that full-length VEGFR2 was present in the final purified fractions.

One of the major drawbacks in VEGFR2 purification has been the presence of a high amount of impurities in elutions. Obtaining highly pure protein is an important foundation of EM analysis. First step purification using FLAG peptide elution has produced VEGFR2 with low purity due to which a standard protein quantification BCA technique was unreliable (Walker, 1994). Interestingly, the recovery of VEGFR2 levels was very low using SMA extraction compared to DDM; however, the SMA-based VEGFR2 purity shows the mostly homogenous distribution of particles with different orientations (Ohi et al., 2004, Rames et al., 2014).

4.3.1. VEGFR2 is predominantly in the monomeric state after purification

Two major studies were carried out to verify the state of VEGFR2 in a detergent-solubilised native-like environment. Firstly, SEC analysis showed the VEGFR2 present mainly in a relatively narrow elution peak. The most dominant (concentrated) VEGFR2 peaks had an estimated molecular weight of 410.9 ±68 and 301.55 ± 53 kDa respectively. The size of the full-length monomeric VEGFR2 receptor is ~250 kDa (Fig. 4.3B) and each DDM micelle ranges from ~70-75 kDa (Garavito and Ferguson-Miller, 2001). Therefore, the size range suggests that purified VEGFR2 is monomeric. However, measurement of molecular weight (Mr) of a protein using size exclusion chromatography has certain limitations. Firstly, the shape of the protein significantly effects the size measurement. The ability of the protein to diffuse through the beads is due to its effective hydrodynamic radius. Asymmetric and elongated proteins have higher hydrodynamic radius compared to the globular proteins. This may sometime result in significant overestimation of molecular weight of a protein (Burgess, 2018). Therefore, a blue native PAGE analysis of purified VEGFR2 will give more accurate measurement of molecular weight. The blue native PAGE analysis of VEGFR2 solubilised in either DDM detergent or SMA polymer showed that VEGFR2 exists predominantly in the monomeric state. This study has also shown successful dimerisation of VEGFR2 upon the addition of VEGF-A_{165} ligand. Therefore, based on SEC and native PAGE we have confirmed the *in vitro* dimerisation of VEGFR2 by its VEGF-A ligand (Abhinand et al., 2016).

4.3.2. Structural features of VEGFR2 bound to VEGF-A

Furthermore, to gain the structural information on VEGFR2, we’ve analyzed the purified VEGFR2 solubilised in DDM and SMA using negative stain EM. Even though single particle cryo-EM is far more superior to negative stain-EM, it is extremely challenging to differentiate the broken-down contaminant products due to high contrast for non-symmetric and unstable protein complexes using cryo-EM. Thus, considering the amounts of contaminants and low yield of purified VEGFR2, negative stain EM was used in this chapter. It offers numerous advantages compared to cryo-EM such as less radiation damage to the proteins from absorbed electrons upon longer exposure (Rames et al., 2014). However, there are certain limitations. Uneven staining may produce artefacts which lead to higher contrast than normal. Furthermore, as a part of staining process the particle loose the hydration shall that may lead to distortion of its shape which is crucial especially for membrane proteins (De Carlo and Harris, 2011). Therefore, staining was performed carefully to obtain uniform staining without any artefacts. The purified VEGFR2 analysis showed to have a beads-on-a-string-like appearance randomly without any distinguishable conformation. This shows that the receptors are clearly monomeric with no specific features, therefore class averaging was not possible.

However, the main obstacle in this study was the aggregation of the receptor complex after the addition of ATP. All attempts to stabilize a homogenous complex of VEGFR2/VEGF-A/ATP for EM analysis was futile. No aggregation was observed in the absence of ATP. Excess ATP prompts the formation of a fine crystalline precipitate which masks the receptor on the grid, this is due to the phosphate ions in ATP reacting to uranyl salts which form crystals as seen in Fig. 4.15C and Fig. 4.15D (Juillerat et al., 2019, Morrison et al., 2016). Different molar concentrations of ATP were used, but the aggregates were persistent. This issue can potentially be addressed by making a stable complex of VEGFR2/VEGF-A/ATP before elution or using different ATP analogues (Suwal et al., 2012). Due to time constraints, an alternative approach was used to stabilize a VEGFR2/VEGF complex with a tyrosine kinase inhibitor (Sutent). Sutent competes with ATP and binds between the N and C lobes of the VEGFR2 tyrosine kinase domain (Roskoski, 2007b). The class averages of VEGFR2/VEGF-A/Sutent have shown complex as individual particles with two monomeric receptors held together. At one end, the receptors were seen bridged together by high-density VEGF-A ligand (Fig. 4.17B). However, the cytoplasmic tyrosine kinase domain still doesn’t seem to have any distinct features in the EM analysis. It was still unclear if the Sutent was bound in these structures.

The unbound state the VEGFR2 extracellular domain is highly flexible without any 3-D conformation. When associated with VEGF-A ligand, the extracellular Ig-like domains are stabilised via homotypic interactions. 3-D model construction was not possible due to limited views and sample size. Even though we’ve established a physiologically relevant VEGFR2-VEGF complex, it is crucial to validate the functional activity of the receptor, the functional studies were performed in the next chapter. To conclude, the single-particle analysis of VEGFR2 using negative stain EM has shown the preliminary structural characterization of the receptor, mainly ligand-bound and unbound states. Further optimisation is necessary to stabilize the complex with ATP or small molecular inhibitor bound in the kinase domain of VEGFR2 before assessing the samples for cryo-EM analysis (Skiniotis and Southworth, 2015).

CHAPTER 5

Biochemical studies on native and purified VEGFR2

5.1. INTRODUCTION

In the previous Chapter 4, attempts were made to analyse the structure of purified full-length recombinant VEGFR2 receptor. The main goal of the work in this chapter is to characterise and compare VEGFR2 activity in native and purified states. Native and recombinant membrane proteins contain numerous differences, especially post-translational modifications such as glycosylation and phosphorylation (Orlova et al., 2003). Protein glycosylation is an important post-translational modification process that is crucial in maintaining the tertiary and quaternary structures of a protein (Shental-Bechor and Levy, 2008, Xu and Ng, 2015). In RTKs, N-glycosylation plays a crucial role in ligand binding, stability and RTK trafficking (Itkonen and Mills, 2015b). The VEGFR2 extracellular Ig-like domains contain multiple N-glycosylation sites (Chandler et al., 2017).

Furthermore, many proteins have no enzymatic activity when expressed in a recombinant protein expression system, as some proteins also tend to misfold and lose their enzymatic activity after solubilisation and purification. Therefore, validation of the VEGFR2 enzymatic activity is important. VEGFR2 expressed on endothelial cells recognises growth factors such as VEGF-A and undergoes phosphorylation at specific tyrosine residues in the cytoplasmic domain; such modifications are linked to pro-angiogenic responses by endothelial cells (Basagiannis et al., 2016). There are multiple isoforms of VEGF-A such as VEGF-A_{121}, VEGF-A_{145}, VEGF-A_{148}, VEGF-A_{162}, VEGF-A_{165}, VEGF-A_{165b}, VEGF-A_{183}, VEGF-A_{189} and VEGF-A_{206} that are known to bind VEGFR2 and promote cell proliferation (Perrot-Applanat, 2012). However, VEGF-A_{165} and VEGF-A_{121} are the most common and most studied isoforms which are abundantly secreted by most cells and tissues (Harris et al., 2012). The residues that undergo phosphorylation in VEGFR2 are Y801, Y951, Y996, Y1054, Y1059, Y1175, Y1214, Y1223, Y1305, Y1309 and Y1319 (Clegg and Mac Gabhann, 2015). Firstly, the activated VEGFR2 is trafficked to endosomes followed by proteasomedependent cleavage and then trafficked into lysosomes for degradation (Simons, 2012). Furthermore, in endothelial cells, the activated and phosphorylated VEGFR2 undergoes ubiquitination and delivered to early endosomes, before proteolysis in late endosomes and lysosomes (Ewan et al., 2006; Bruns et al., 2010). Therefore, monitoring VEGFR2 proteolysis is also needed to ascertain the properties of recombinant tagged VEGFR2.

5.2. RESULTS

5.2.1. VEGF-A isoforms differentially regulate phosphorylation of VEGFR2

VEGF-A binding to VEGFR2 causes dimerisation and phosphorylation of multiple tyrosine residues in the cytoplasmic kinase domain (Fearnley et al., 2016). The VEGFR2 phosphotyrosine epitope pY1175 is present in the cytoplasmic domain and enables recruitment of both PLCγ1-dependent and PKA-dependent signalling pathways (Xie et al., 2019). To check for this, firstly, a time-dependent activation and phosphorylation of VEGFR2 were performed in primary endothelial cells (HUVECs). Two different VEGF-A isoforms of VEGF-A were used, and endothelial cells stimulated with 1 nM VEGF-A_{165} or VEGF-A_{121} for different time points (0, 5, 10 or 20 min) and analysed by Western blotting, total VEGFR2 and actin were used as loading controls (Fig. 5.1A). Quantification of relative VEGFR2-pY1175 levels showed little or no phosphorylation at 0 min time point as expected, with peak phosphorylation at 5 min for with VEGF-A_{165} (Fig. 5.1B). The VEGFR2-pY1175 levels declined rapidly to <25% of peak levels after 20 min (Fig. 5.1B). For VEGF-A_{121}, VEGFR2-pY1175 levels were rapid and maximal after 5 min; however, the levels persisted for much longer with ~75% of signal still detected after 20 min (Fig. 5.1B).

A similar study was performed on recombinant FLAG-VEGFR2 expressed in HEK293 cells. The cells were induced for 36 h to overexpress the VEGFR2 and then stimulated with 1 nM VEGF-A_{165} or VEGF-A_{121} (Fig. 5.2A). After VEGF-A stimulation for 0, 5, 10 or 20 min, cells were analysed by Western blotting probed

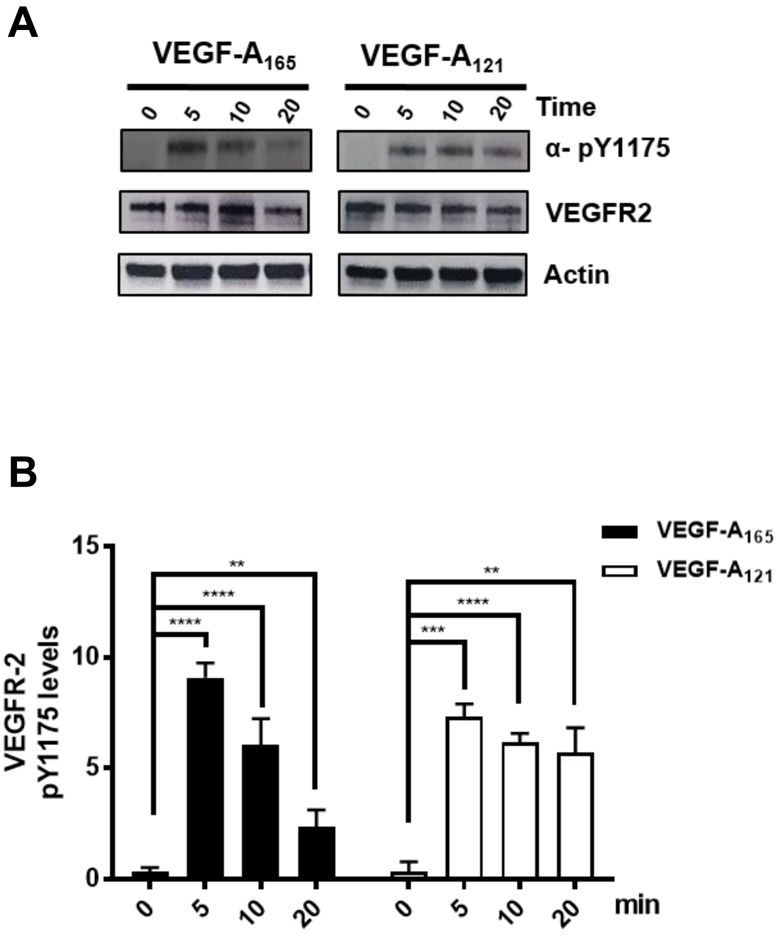

Figure 5.1. VEGF-A isoform-specific stimulation of VEGFR2-pY1175 levels in endothelial cells. (A) Human umbilical vein endothelial cells (HUVECs) were starved for 30 min in low serum media and then subjected to stimulation with 1 nM VEGF-A$_{165}$ or VEGF-A$_{121}$ for 0, 5, 10 or 20 min, lysed and analysed by Western blot for the phosphotyrosine pY1175 levels by probing with rabbit anti-pY1175 antibody. **(B)** Quantification of VEGFR2-pY1175 relative levels upon VEGF-A$_{165}$ or VEGF-A$_{121}$ stimulation. Error bars indicate ±SEM (n≥3). $p < 0.01$ (**)**,** $p < 0.001$ (***), $p < 0.0001$ (****)

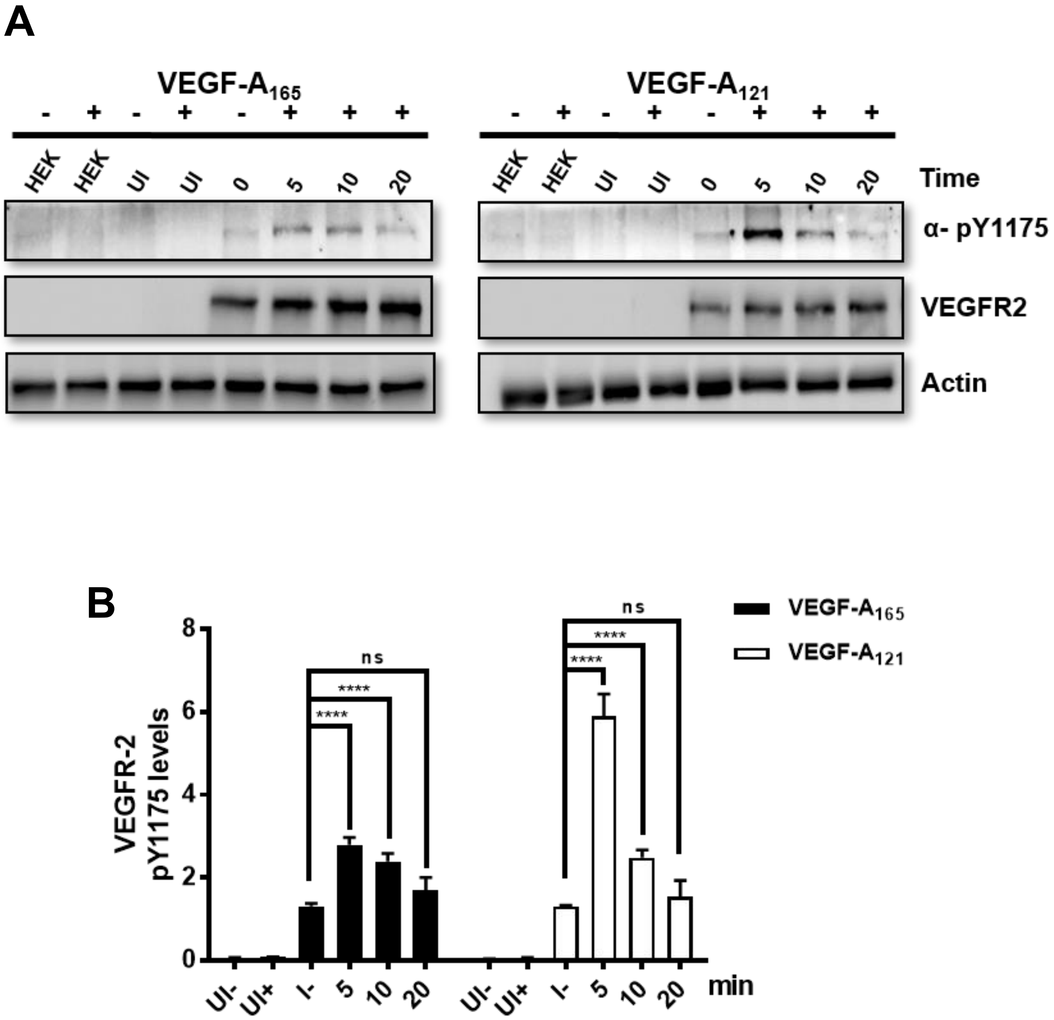

Figure 5.2. VEGF-A isoform-specific stimulation of recombinant FLAG-VEGFR2-pY1175 levels in HEK293 cells. **(A)** HEK293 cells expressing FLAG-VEGFR2 were induced with tetracycline (1 µg/ml) for 36 h, and then subjected to stimulation with 1 nM VEGF-A_{165} or VEGF-A_{121} for 0, 5, 10 or 20 min, lysed and analysed by Western blot for the phosphotyrosine VEGFR2-pY1175 levels by probing with rabbit anti-pY1175 antibody. **(B)** Quantification of VEGFR2-pY1175 relative levels upon VEGF-A_{165} or VEGF-A_{121} stimulation. Error bars indicate ±SEM (n≥3). $p < 0.0001$ (****).

with rabbit anti-VEGFR2-pY1175 (Fig. 5.2A). Non-transfected HEK293 cells and transfected but non-induced cells were used as a negative control, with total VEGFR2 and actin used as loading controls (Fig. 5.2A). Quantification of relative VEGFR2-pY1175 levels showed that maximal phosphorylation occurred after 5 min for both VEGF-A isoforms (Fig. 5.2B). Upon stimulation with VEGF-A$_{165}$ isoform, VEGFR2-pY1175 levels declined gradually from 5 to 20 min period (Fig. 5.2B), whereas for the VEGF-A$_{121}$ isoform, VEGFR2-PY1175 levels declined more rapidly with a ~70% decline after 20 min. This was different to that observed in endothelial cells.

5.2.2. VEGF-A isoforms program differential recombinant VEGFR2 degradation and proteolysis

In endothelial cells, VEGF-A binding to VEGFR2 promotes proteolysis and terminal degradation via the endosome-lysosome system (Ewan et al., 2006, Bruns et al., 2010). Isoforms of VEGF-A exhibit differential endocytosis and degradation of VEGFR2 (Fearnley et al., 2016). To investigate whether recombinant FLAG-VEGFR2 expressed in HEK293 cells also exhibits a similar degradation profile, the cells were subjected to tetracycline induction for 36 h to overexpress VEGFR2 and treated with different concentrations (0.1, 1 or 10 nM) of VEGF-A$_{165}$ for 0, 5, 15, 30 or 60 mins before microscopy analysis (Fig. 5.3). Cells were fixed and stained with an anti-VEGFR2 antibody to detect total VEGFR2 after stimulation with VEGF-A isoform (Fig. 5.3A). Induced cells expressing VEGFR2 but non-treated with VEGF-A were used as negative controls (Fig. 5.3). The quantification revealed a ~30-40 % reduction in basal VEGFR2 levels over 60 min with all three concentrations of VEGF-A$_{165}$ used (0.1, 1 and 10 nM) (Fig. 5.3B). Cells expressing FLAG-VEGFR2 treated with VEGF-A$_{121}$ isoform (0.1, 1 or 10 nM) also showed a similar profile of proteolysis (Fig. 5.4). Relative VEGFR2 quantification showed loss of VEGFR2 with a reduction of ~40 % upon treatment with 10 nM VEGF-A$_{121}$ after 60 min, and ~30 % reduction with 1 nM at 60 min (Fig. 5.4B). Furthermore, 0.1 nM VEGF-A$_{121}$ caused only ~10 % reduction in total VEGFR2 over the same time (Fig. 5.4B). Thus, the exogenously added VEGF-A isoforms have exhibited different effects on

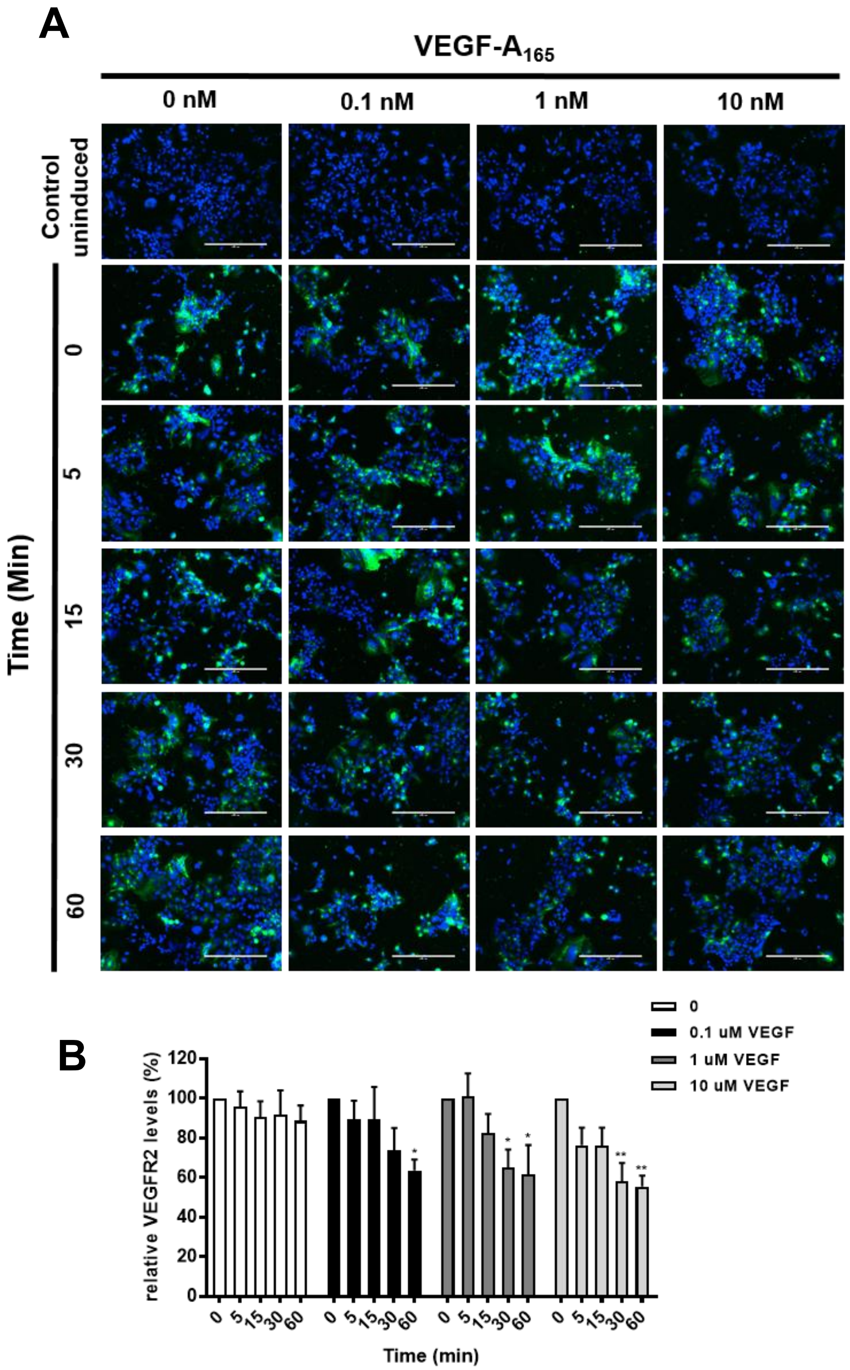

Figure 5.3. VEGF-A$_{165}$ modulation of VEGFR2 proteolysis. (A) HEK293 cells expressing FLAG-VEGFR2 were induced with tetracycline (1 mg/ml) for 36 h, treated with different VEGF-A$_{165}$ concentrations (0.1, 1 or 10 nM) for 0, 5, 15, 30 or 60 min and then fixed with parafromaldehyde before permeabilisation and staining with goat anti-VEGFR2 followed by secondary anti-goat AF488 conjugate (green), nuclei stained with DAPI (blue). Scale bar, 200 µm. **(B)** Quantification of relative VEGFR2 levels upon treatment with VEGF-A$_{165}$. Error bars indicate ±SEM (n≥3). *p*< 0.1 (*), *p*< 0.01 (**).

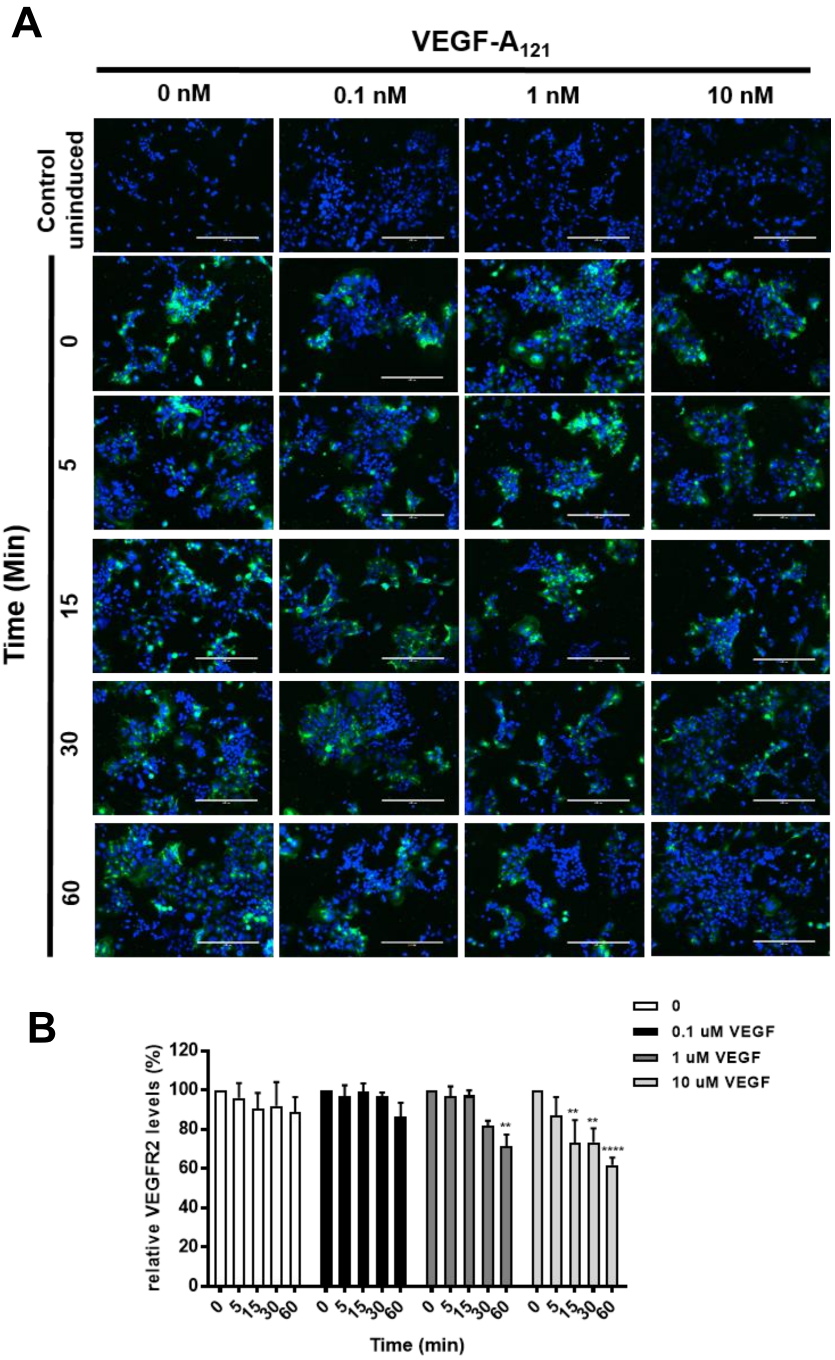

Figure 5.4. VEGF-A$_{121}$ modulation of VEGFR2 proteolysis. (A) HEK293 cells expressing FLAG-VEGFR2 were induced with tetracycline (1 mg/ml) for 36 h, treated with different VEGF-A$_{121}$ concentrations (0.1, 1 or 10 nM) for 0, 5, 15, 30 or 60 min and then fixed with paraformaldehyde before permeabilisation and staining with goat anti-VEGFR2 followed by secondary anti-goat AF488 conjugate (green), nuclei stained with DAPI (blue). Scale bar, 200 µm. **(B)** Quantification of relative VEGFR2 levels upon treatment with VEGF-A$_{121}$. Error bars indicate ±SEM (n≥3). $p < 0.1$ (*), $p < 0.01$ (**).

VEGFR2 associated with the endocytic pathway, especially at lower concentrations of VEGF-A_{165} (0.1 nM and 1 nM) higher degradation of VEGFR2 was observed compared to the same concentration of VEGF-A_{121}. This supports the degradation profile of VEGFR2 in endothelial cells upon stimulation with VEGF-A isoforms (Fearnley et al., 2016).

5.2.3. Purified VEGFR2 is N-glycosylated

The VEGFR2 extracellular domain is known to undergo N-glycosylation which plays a role in regulating ligand-dependent activation and signalling (Chandler et al., 2017). Therefore, it is essential to verify if the recombinant FLAG-VEGFR2 is N-glycosylated. To test this, the purified FLAG-VEGFR2 was analysed and subjected to deglycosylation with PNGase F enzyme which removes N-linked oligosaccharides (Fig. 5.5). PNGase-F is an amidase that cleaves the high mannose oligosaccharides attached to asparagine residues (Szigeti et al., 2016). Purified VEGFR2 deglycosylated with PNGase F was compared to untreated VEGFR2 as a negative control (con) (Fig. 5.5). In addition, VEGFR2 treated with PNGase F before and after denaturation and treatment with a reducing agent (DTT) (Fig. 5.5). Non-treated VEGFR2 (con) showed two bands at 250 and 200 kDa, whereas deglycosylated VEGFR2 under denaturing and non-denaturing conditions showed a band at ~160 kDa (Fig. 5.5). This increase in electrophoretic mobility with an apparent band change from ~250 to ~160 kDa upon treatment with PNGase F is due to the removal of N-linked oligosaccharides (Fig. 5.5). This confirms that FLAG-VEGFR2 undergoes N-glycosylation when expressed in HEK293 cells.

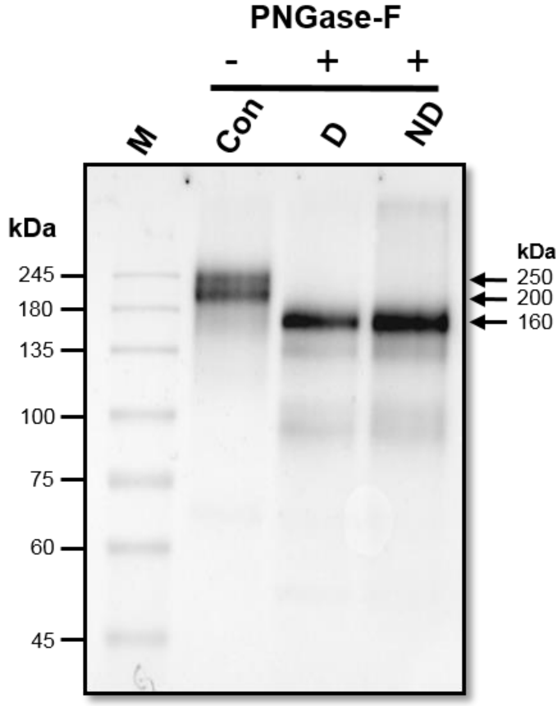

Figure 5.5. Purified VEGFR2 is N-glycosylated. Western blot of puridfied full-length VEGFR2 solubilised in DDM detergent, VEGFR2 was subjected to N-linked deglycosylation using PNGase F to cleave N-linked oligosaccharides. The blot was probed with goat anti-VEGFR2 antibody. Lanes represent protein marker (M), denatured VEGFR2 negative control (Con) without PNGase F, protein denatured before deglycosylation (D), and denatured after deglycosylation (ND). Non-treated VEGFR2 (con) showed two bands at 250 and 200 kDa, whereas deglycosylated VEGFR2 under both denaturing and non-denaturing conditions shows a band at ~160 kDa.

5.2.4. *In vitro* activation of purified VEGFR2

5.2.4.1. Activation of VEGFR2 by ATP and VEGF-A_{165} isoform

The tyrosine kinase of recombinant FLAG-VEGFR2 in HEK293 cells has been already validated (Fig. 5.2). However, the activity of purified recombinant VEGFR2 was still unknown. To test the tyrosine kinase activity of purified VEGFR2, an *in vitro* phosphorylation assay was performed. The purified VEGFR2 was treated with different concentrations of ATP and VEGF-A_{165}. The concentration of ATP in most eukaryote cells ranges from 1-10 mM (Zimmerman et al., 2011). Therefore, ATP titration was performed with 0, 1, 2, 5, 10, 100, 1000, or 5000 μM ATP in the presence of 0.1 nM, 1 nM or 10 nM VEGF-A_{165}. The purified VEGFR2 treated with ATP and VEGF-A_{165} was analysed using Western blotting using rabbit anti-VEGFR2-pY1175 as a measure of VEGFR2 activation and phosphorylation (Fig. 5.6A). ATP alone without VEGF-A_{165} was used as a negative control and total purified VEGFR2 was used as a loading control (Fig. 5.6A). Interestingly, purified FLAG-VEGFR2 was activated at >100 μM ATP alone, and also with three concentrations of VEGF-A_{165}. Trace amounts of VEGFR2-pY1175 was detected at lower ATP concentration and in the presence of VEGF-A (Fig. 5. 6B).

The EC_{50} (half-maximal response) of ATP was measured by plotting non-linear regression of ATP vs normalised response for all conditions (Fig. 5.6C). The EC_{50} of ATP alone is 70.05 μM, whereas the addition of 0.1, 1 or 10 μM of VEGF-A_{165} increased the EC_{50} of ATP fractionally to 84.22, 89.81 and 124.4 respectively. The addition of VEGF-A_{165} delayed VEGFR2 phosphorylation (based on EC_{50}). This suggests that ligand-bound VEGFR2 requires a higher concentration of ATP for activation, especially with an increase in VEGF-A_{165} concentration.

5.2.4.2. ATP stimulates phosphorylation of VEGFR2 tyrosine residues without VEGF-A

In vitro phosphorylation of VEGFR2-pY1175 suggests that ATP alone can cause such effects. To understand this further, the *in vitro* phosphorylation of different VEGFR2 phosphotyrosine epitopes was analysed (Fig. 5.7). The assay was

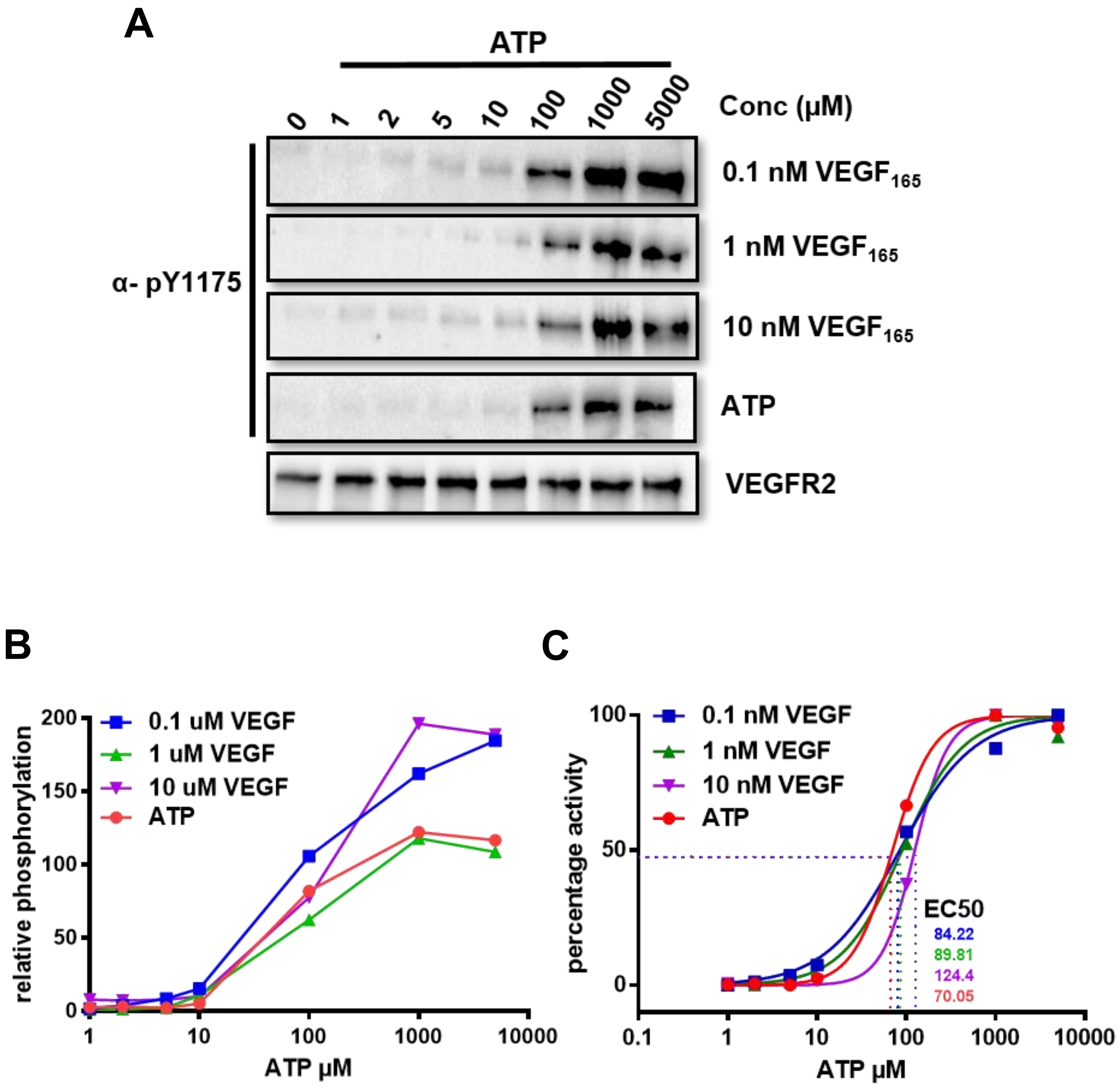

Figure 5.6. VEGF-A_{165} and ATP-dependent phosphorylation of Y1175 on recombinant VEGFR2. (A) Full-length VEGFR2 purified by DDM solubilisation subjected to stimulation with ATP and VEGF-A_{165}, processed for immunoblot analysis to assess relative levels of VEGFR2-pY1175. Purified VEGFR2 was used as a loading control. The western blot was developed by probing with rabbit anti-pY1175 antibody, **(B)** Quantification of relative VEGFR2-pY1175 levels upon treatment with ATP and VEGF-A_{165}. **(C)** EC_{50} measurement for ATP with different concentrations of VEGF-A_{165}.

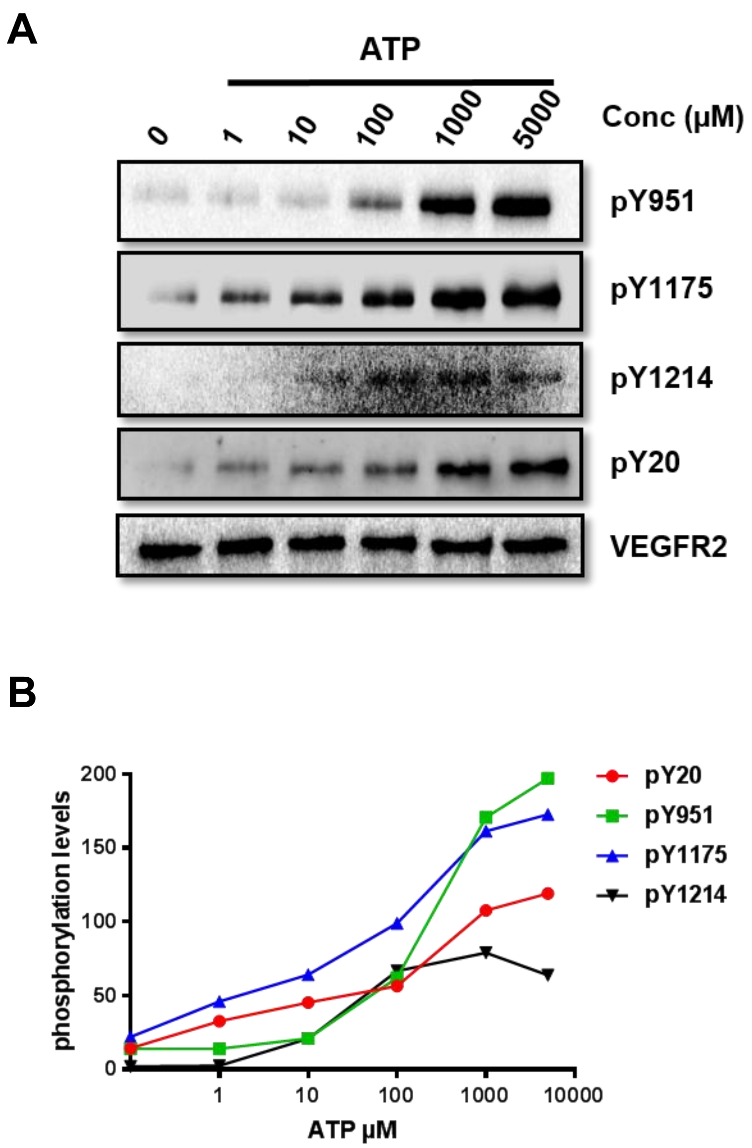

Figure 5.7. VEGF-A independent activation and VEGFR2 phosphrylation. (A) Full-length VEGFR2 purified in DDM detergent is subjected to different concentrations of ATP and processed for immunoblot analysis to assess the phosphorylation of four phosphotyrosine epitopes defined by PY20 (generic phosphotyrosine probe), pY951, pY1175 and pY1214 epitopes. Purified VEGFR2 was used as loading control. **(B)** Quantification of relative VEGFR2-pY levels upon treatment with ATP.

performed with ATP alone to test if multiple residues are phosphorylated by ATP without VEGF-A_{165}. The purified VEGFR2 was treated with gradient log concentrations of ATP (1, 10, 100, 1000, 5000 μM) for 30 min and analysed using Western blot (Fig. 5.7A). Multiple VEGFR2 phosphorylation sites were analysed: these included the pY951, pY1175 and pY1214 epitopes in the VEGFR2 cytoplasmic domain (Fearnley et al., 2016). The pY951 epitope is located in the tyrosine kinase domain, whereas pY1175 and pY1214 are located in the C-terminal flexible tail region (Dayanir et al., 2001). Alternatively, generic phosphotyrosine antibody (PY20) that recognises all phosphotyrosine residues was used as a probe (Tinti et al., 2012). Total VEGFR2 was used as a loading control (Fig. 5.7A). Phosphorylation was detected in all tyrosine residues caused by an increase in ATP concentration, and quantification revealed higher VEGFR2 phosphorylation of pY951 and pY1175 compared to pY1214 residues (Fig. 5.7B).

5.3. DISCUSSION

In this study, we showed that VEGF-A isoforms differentially promote ligand-dependent FLAG-VEGFR2 phosphorylation when expressed in HEK293 cells. In endothelial cells, the appearance of the VEGFR2-pY1175 epitope triggers multiple downstream signalling pathways such as ERK1/2, p38 and Akt (Olsson et al., 2006, Cross et al., 2003, Trinh et al., 2009). Studies show that VEGF-A_{165} stimulation promotes higher cell proliferation mediated by pY1175 via ERK1/2 and p38 pathways when compared to VEGF-A_{121} (Soker et al., 1997). However, unlike endothelial cells, recombinant FLAG-VEGFR2 in HEK293 cells showed higher VEGFR2-pY1175 levels with VEGF-A_{121} compared to VEGF-A_{165} isoform (Fig. 5.2). This suggests that VEGF-A_{121} potentially promotes more potent cellular responses than VEGF-A_{165} in our recombinant expression system. Furthermore, there are studies that show that most VEGF-A isoforms bind to VEGFR2 extracellular domain with similar binding affinity but have unique properties in VEGFR2 endocytosis, ubiquitination and degradation (Fearnley et al., 2014). In endothelial cells, elevation in VEGFR2 endocytosis is observed upon stimulation with VEGF-A_{165} compared to VEGF-A_{121} which showed negligible effects

(Fearnley et al., 2016). Similarly, our findings reveal that stimulation of VEGFR2 using VEGF-A_{165} led to a higher degradation of VEGFR2 over time compared to VEGF-$_{121}$ which showed degradation only at higher concentrations. We know that the degradation of VEGFR2 is linked to its ubiquitination and internalisation into the endosome-lysosome pathway (Smith et al., 2017). Therefore, our findings show that the recombinant VEGFR2 expressed in HEK293 cells exhibit similar trafficking and degradation profile of native VEGFR2 in endothelial cells.

Secretory protein N-glycosylation is a post-translational process that occurs in the ER and Golgi (Itkonen and Mills, 2015a). VEGFR2 is known to have 18 N-glycosylation sites in the extracellular domain which play a significant role in protein dimerisation (Chandler et al., 2016). Treatment of endothelial cells with a glucose analogue that interferes with N-glycosylation prevents endothelial cell proliferation and formation of capillaries (Kovacs et al., 2016). Therefore, the N-glycosylation of VEGFR2 is regarded as crucial for its activity. Treatment of VEGFR2 with PNGase F removes N-linked glycans from recombinant FLAG-VEGFR2. Thus, recombinant FLAG-VEGFR2 is likely to be functionally glycosylated and active.

VEGF-A ligand binding is known to bring together two monomeric receptors and promote dimerisation. The VEGFR dimerisation leads to orientation change in the tyrosine kinase domain that allows the RTKs to phosphorylate each other, the process is known as “transautophosphorylation” (Smith et al., 2016, Koch and Claesson-Welsh, 2012). Therefore, VEGFR dimerisation is essential for activation and tyrosine phosphorylation. Our studies revealed that VEGFR2 doesn’t always exist in the monomeric state as previously thought (Shibuya, 2011b). Cellular studies show that the activation of VEGFR2 is regulated by VEGF-A ligand, as expected (Fig. 5.8A). However, a supplying monomeric VEGFR2 with ATP initiates the “transautophosphorylation” of multiple tyrosine residues in the cytoplasmic domain (Fig. 5.8B). Therefore, our *in vitro* assay revealed four potential VEGFR2 species: (1) monomers, (2) VEGF-A unbound dimer with contacts in cytoplasmic domain, (3) VEGF-A unbound dimer with contacts in extracellular domain and cytoplasmic domains, and (4) VEGF-A-bound dimer with

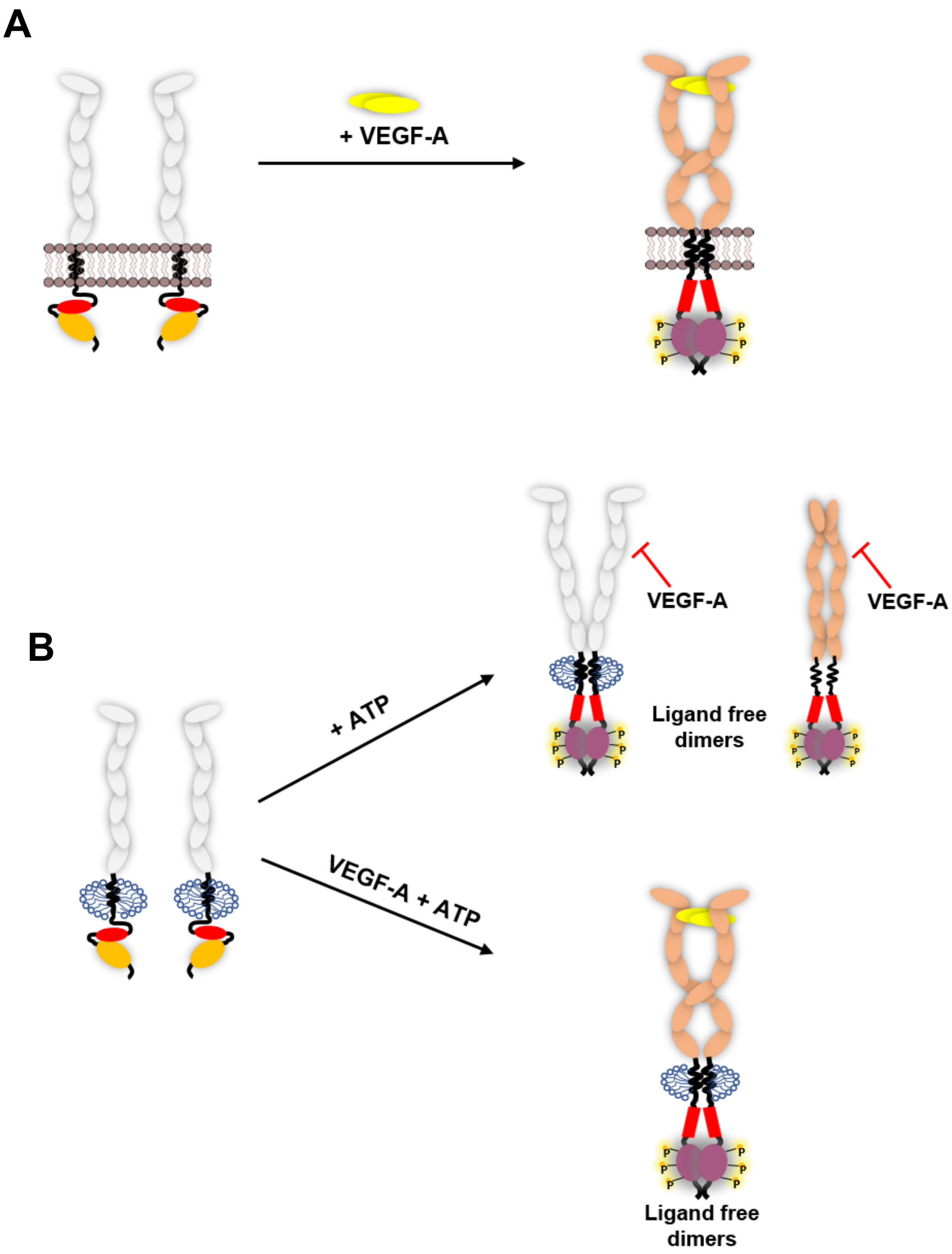

Figure 5.8. Schematic representation of VEGFR2 activation states. (A) VEGF-A binding to VEGFR2 activates the kinase domain and causes cytoplasmic phosphorylation on tyrosine residues, therefore VEGF-A dependent activation as demonstrated by cell based studies, **(B)** Purified VEGFR2 monomers, activated by ATP in the presence or absence of VEGF-A, gives rise to differentially activated VEGFR2 species (based on *in vitro* activation studies).

homotypic contacts in both extracellular domain and cytoplasmic domains (Fig. 5.8B).

Our studies have also shown that VEGFR2 only requires ~70-125 µM ATP for activation of the tyrosine kinase enzyme. Cells contain much higher cytoplasmic ATP concentrations (1-10 mM) than required for activation of VEGFR2 enzyme (Leist et al., 1997). This raises an obvious question: why doesn't cellular VEGFR2 undergo phosphorylation in the absence of VEGF-A ligand? We believe that the concentration of VEGFR2 and its distribution on the plasma membrane plays a crucial role in dimerisation and activation. VEGFR2 requires close proximity contacts for allosteric regulation, especially for VEGF-A independent activation. If the membrane receptors are in close proximity, they come in contact with each other which leads to a conformational change and easily allows access to ATP. Therefore, overexpression or overcrowding of the receptor by upregulation increases the ligand-independent phosphorylation levels of VEGFR2 (King and Hristova, 2019). Thus, the purified FLAG-VEGFR2 derived from overexpression in HEK293 cells dimerises and gets activated with greater efficiency due to the close proximity of membrane receptors. This also explains relatively higher basal phosphorylation levels in HEK293 cells compared to endothelial cells (Fearnley et al., 2016).

CHAPTER 6

Biochemical and structural analysis of LOX-1 scavenger receptor and OxLDL particles

6.1. INTRODUCTION

Atherosclerosis is a progressive phenomenon that is associated with numerous vascular disease states. The interaction between LOX-1 scavenger receptor on macrophages, endothelial cells, platelets and smooth muscle cells with OxLDL, and its subsequent recognition and internalisation is linked to the pathology of atherosclerosis (Figure 1.9) (Pirillo et al., 2013a). Even though the structure of LOX-1 was resolved to 1.4 Å resolution (Park et al., 2005), limited information on the structure of the OxLDL particle is a major barrier in further improving our understanding of atherosclerosis. The study of interactions between LOX-1 and OxLDL is needed to better understand atherosclerosis and to target such processes in therapeutic strategies.

Most of the LOX-1/OxLDL interaction studies have used *in vivo* animal models or *in vitro* cultured cells (Akhmedov et al., 2014, Al-Banna and Lehmann, 2013, Hofmann et al., 2017, Hu et al., 2008). Numerous studies have shown the recognition of OxLDL by LOX-1 and subsequent internalization into vascular and non-vascular cells. However, there is a very limited number of studies that explain the molecular basis for such recognition. The exact epitope on OxLDL recognised by LOX-1 is still unclear. Moreover, as the LOX-1 extracellular domain possesses a CTLD domain it is likely that carbohydrate and calcium ions are involved in such interactions (Park et al., 2005), but this remains to be proven. The CTLD of LOX-1 has a rare CTLD fold (Ohki et al., 2005), which may preclude calcium ion and/or carbohydrate recognition. There are two hypotheses on LOX-1 binding to OxLDL. The first hypothesis suggests that CTLD of LOX-1 binds covalently to phospholipid moiety of elevated lysine side chains of modified ApoB-100 protein (Park et al., 2005). Alternatively, an acidic patch on LOX-1 particularly involving K171, E170, K167, and E166 facilitates the direct binding to zwitterionic phospholipid headgroups on the surface of the OxLDL particle (Park et al., 2005). The crystal structure of LOX-1 shows a hydrophobic tunnel that runs through the entire LOX-1 molecule and is crucially involved in recognition and binding to OxLDL (Francone et al., 2009).

On the other hand, ApoB-100 is presumed to be a predominant binding region for LOX-1 on lipoprotein. The ApoB-100 polypeptide contains 4536 residues and is identified to have a pentapartiate structure $NH_2\text{-}\beta\alpha_1\text{-}\beta_1\text{-}\alpha_2\text{-}\beta_2\text{-}\alpha_3\text{-}COOH$. However, its morphology is still unclear. Two groups have investigated the structural morphology of ApoB-100 protein using small-angle neutron scattering (Johs et al., 2006) and negative stain electron microscopy (Gantz et al., 2000). They used lipid-free non-native ApoB-100 which impedes its physiological relevance compared to ApoB-100 associated with the lipid. The widely accepted opinion is that ApoB-100 wraps around the LDL particle in an elongated form (Yang et al., 1994a, Murtola et al., 2011). Numerous groups have attempted to resolve the structure of native LDL using X-ray crystallography. Prassl and colleagues were the first to crystallize the native LDL and observed diffraction spots at 29 Å (Prassl et al., 1996). Later, Ritter group was able to make crystals that diffracted at 15 Å (Ritter et al., 1999). Newhouse and colleagues succeeded in making two crystals that diffracted lower than 8 Å but decayed very rapidly, and the diffraction is currently limited to 9 Å (Newhouse et al., 2005). Afterward, no attempt was made by other groups for crystallizing the LDL. Three groups have tried to resolve the structure of LDL using a single-particle cryo-electron microscopy approach (Orlova et al., 1999b, Ren et al., 2010b, Kumar et al., 2011). *Orlova et.al* was the first to determine a structural model of LDL at 30 Å resolution using cryo-EM (Orlova et al., 1999b). Their 3-D model didn’t detect any symmetry in lipid core or ApoB-100 on the surface. Ren et al. (2010a) al resolved a structure of LDL bound to the LDL receptor (160 kDa glycoprotein) at 28 Å. They’ve observed juxtaposed stacking of cholesteryl esters in core and higher density outer shell which represent the ApoB-100 protein (Ren et al., 2010b). Later, the resolution of this particle was improved to 16 Å (Kumar et al., 2011). All the studies carried out by different groups so-far on ApoB-100 and LDL are focused only to address the structural aspects of “native LDL”. There were no reported structural studies on OxLDL and modified ApoB-100 of OxLDL. We know that the nLDL is not directly involved in atherosclerotic plaque formation, whereas it’s modified form i.e OxLDL is directly involved. The cell-based studies have already shown that the OxLDL is recognized and internalized by LOX-1 on cells. Therefore, understanding the binding molecular mechanism of OxLDL/LOX-1 has huge therapeutic potential.

Moreover, we know from the literature that free reactive oxygen species (ROS) particles produced in the endothelial cells as well as transition metals like Cu^{2+} initiate and promote the oxidation of LDL *in vivo* (Esterbauer et al., 1992)**.** Unlike nLDL, the OxLDL is not initially present in the blood, it is accumulated deeply in the thickened intima of human coronary artery and found in the sub-endothelium foam cells (atherosclerotic plaque). Therefore, it is not possible to isolate the *in vivo* OxLDL from the arterial walls in the quantities enough to perform biochemical studies (Fukuchi et al., 2002). However, nLDL is present in blood plasma in abundant quantities which is possible to isolate and perform *in vitro* oxidation by chemical basis. Oxidation can be carried out using different approaches, i.e oxidation using transitional metal ions such as iron and copper (Lopes-Virella et al., 2000, Yuan et al., 1996), oxidation with enzymes such as lipoxygenase and myeloperoxidase (Funk and Cyrus, 2001, Otero et al., 2002) or oxidation from glucose with glycation (Otero et al., 2002). In this chapter copper-based oxidation of LDL was performed for biochemical studies with LOX-1 scavenger receptor.

Furthermore, the precise size of LDL measured using various methods has always been inconsistent, the average size measured using NMR being smaller compared to gradient gel electrophoresis (Witte et al., 2004). Characterising the sizes of macromolecules under native conditions has always been challenging. Conventionally, the size and shape of macromolecules are estimated either by measuring the diffusion coefficient using techniques such as NMR, dynamic light scattering (DLS) and fluorescence correlation spectroscopy (FCS) (Patil et al., 2017) or by measuring the sedimentation coefficient using analytical ultracentrifugation method (Cole et al., 2008, Chaturvedi et al., 2018). These techniques work effectively with monodisperse and homogenous mixtures, evaluation of properties of polydisperse lipid particles such as lipoproteins is quite challenging. To overcome this issue, a fundamentally different approach known as microfluidic diffusion sizing (MDS) can be used to acquire the diffusion coefficient profiles of specific species directly in the solution (Arosio et al., 2016). The MDS is designed to determine the size from hydrodynamic radius of globular proteins using the laminar flow. This approach uses a quantitative latent labelling of proteins for size profiling using a fluorogenic dye under denaturing conditions in microfluidic channel (Fig. 2.1A). Therefore, this allows the characterisation of lipoproteins distribution in their native environment (Yates et al., 2015). The main focus of this chapter is to use the purified LOX-1 extracellular domain i.e. comprising the CTLD and neck domain and study interactions with OxLDL. The aim was to reconcile a biochemical study of the sLOX-1-OLDL complex with structural representation of the OLDL particle using cryoEM. Such work would provide the basis for better understanding how OxLDL structure can be reconciled with recognition by a specific receptor such as LOX-1.

6.2. RESULTS

6.2.1. Construction of pET15b-LOX-1 plasmid, expression, and purification of His-tagged sLOX-1 protein

One objective was to use the pET15b-sLOX-1 bacterial expression plasmid to express and purify soluble LOX-1 protein. Fig. 6.1A shows the schematic map of the pET15b-sLOX-1 construct previously constructed and cloned by Dr. Jane Murphy (University of Leeds) which was readily available. The construct has a T7 lac promoter and an ampicillin resistance selection marker. The LOX-1 extracellular domain (sLOX-1) containing residues (68-273) has a hexahistidine tag at N-terminus followed by a thrombin protease cleavage site and TEV protease site fused to sLOX-1 truncated cDNA or open reading frame, ORF (Fig. 6.1B). The thrombin and TEV protease sites were introduced to remove polyhistidine tag respectively from sLOX-1 if necessary (Raran-Kurussi et al., 2017). The pET15b-sLOX-1 plasmid was transformed into Rosetta-gami and BL21-codon plus *E.coli* strains: both strains utilise codon usage typically found in mammalian proteins such as LOX-1 (Fathi-Roudsari et al., 2016, Li et al., 2019).

The transformed cells were induced with 0.1 mM IPTG for 6 h before lysis and purification using previously established procedures (see Materials and Methods; Vohra et al., 2007). sLOX-1 was purified using Ni-NTA agarose, eluted using 250 mM imidazole and visualized on SDS-PAGE gel under reducing conditions. Fig. 6.2A shows the SDS-PAGE gel stained with Coomassie blue stain: LOX-1 monomer (~26 kDa) bands were seen in both Rosetta-gami and BL21-codon plus expression systems, whereas the expression levels in BL21-codon plus were relatively low. The purified sLOX-1 probed with sheep anti-LOX-1 by immunoblotting showed two bands of ~26 kDa and ~52 kDa (Fig. 6.2B), suggesting the presence of monomers and dimers of sLOX-1.

To check for the amount of sLOX-1 contained in inclusion bodies a solubilization study was performed by lysing the cells in a non-denaturing buffer (S1) and denaturing buffer (S2) (Fig. 6.2C). The majority of sLOX-1 was observed in inclusion bodies like many recombinant proteins, as expected. The purification of sLOX-1 was carried out under denaturing conditions; therefore, dialysis was performed to remove the denaturing buffer and allow the protein to refold. However, the removal of guanidine HCl caused the purified sLOX-1 to precipitate from the solution. This may be due to the formation of incorrect disulphide bonds and folding of sLOX-1 (Kosuri et al., 2012). To address this issue and properly refold the sLOX-1, DTT was used to reduce the disulphide bonds and then this was removed using dialysis. To further reduce the denaturant concentration, the purified sLOX-1 was diluted using a refolding buffer containing oxidised and reduced glutathione to facilitate the formation of correct disulphide bonds, using 0.5 M L-arginine to inhibit the aggregation of unfolded proteins (Tischer et al., 2010, Thomson et al., 2012). The buffer also contained low levels of divalent cations such as Ca^{2+}, Mg^{2+}, Cu^{2+}, Zn^{2+}, Fe^{2+}, Mn^{2+}, Co^{2+} to facilitate the refolding of C-type lectin-like domain (Zelensky and Gready, 2006). Most of the sLOX-1 was refolded without forming precipitated aggregates, and this sLOX-1 protein was used for subsequent studies.

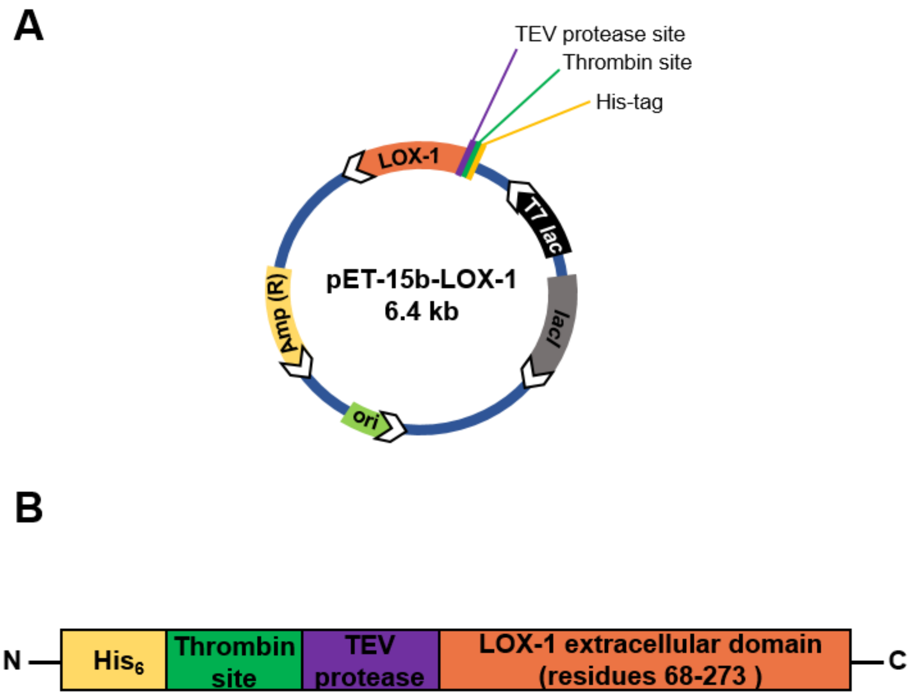

Figure 6.1. Schematic of sLOX-1 expression strategy. (A) Schematic map of pET-15b-LOX-1 recombinant plasmid containing the extracellular domain cDNA of LOX-1 (residues 68-273) cloned between *Nde*I and *Bam*HI restriction sites. **(B)** The sLOX-1 fusion protein contains a hexahistidine tag, a thrombin protease cleavage site, a TEV protease site followed by the sLOX-1 ORF sequence.

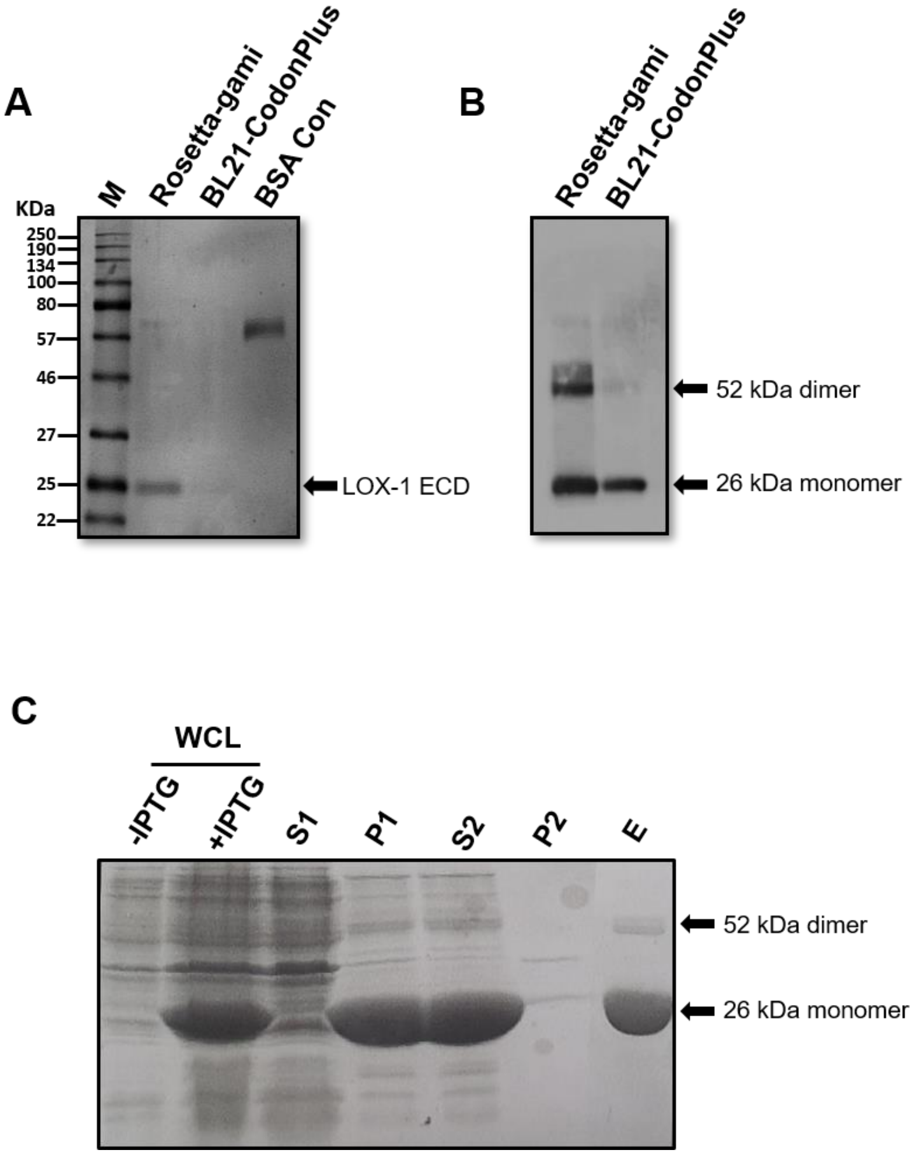

Figure 6.2. Bacterial expression and purification of sLOX-1 extracellular domain (sLOX-1-ECD). (A) *E.coli* strains Rosetta-gami(DE3)pLysS and BL21-CodonPlus(DE3)-RP were transformed pET-15b-LOX-1 plasmid were induced with IPTG and sLOX-1 purified as described in Materials and Methods. **(B)** Purified sLOX-1 was analysed by 12% SDS-PAGE and immunoblotting using sheep anti-LOX-1 primary antibody and mouse anti-goat IgG secondary antibody. **(C)** Rosetta-gami *E.coli* cells expressing sLOX-1 were induced with IPTG for 6 hours at 37° C, lysed in non-denaturing buffer and centrifuged at 10,000 g for 15 min, supernatant (S1) contain soluble protein and contain pellet (P1) contain insoluble LOX-1 in inclusion bodies, P1 was solubilized and centrifuged at 100,000 g to create supernatant (S2) containing sLOX-1 and pellet (P2). sLOX-1 was bound to Ni-NTA resin, and eluted (E) using Imidazole buffer. Samples were analysed by 12 % SDS-PAGE and visualized using Coomassie blue staining.

6.2.2. Purification, analysis, and oxidation of low-density lipoprotein particles

As explained earlier, circulating blood contains various lipid particles such as high-density lipoprotein (HDL), intermediate-density lipoprotein (IDL), low-density lipoprotein (LDL) and very-low-density lipoprotein (VLDL). The LOX-1 scavenger receptor recognizes the modified low-density lipoprotein known as oxidised low-density lipoprotein (OxLDL). To study the interactions between the LOX-1 and OxLDL, firstly, LDL was isolated and chemically modified into OxLDL. Plasma from human blood was subjected to high-speed ultracentrifugation using iodixanol gradient to separate the various lipoproteins based on their densities (Fig. 6.3A) (Graham et al., 1996). Self-generating iodixanol gradients allows separation of lipoprotein profiles into single fraction within very short centrifugation time of 3 h as opposed to conventional high salt-based sodium or potassium bromide gradients which require centrifugation for 78 h (Chung et al., 1980, Chapman et al., 1981) and high salt concentrations are also known to interfere or modify with the structure of lipoprotein particles (Kovanen and Kokkonen, 1991). Fig. 6.3A also shows the major human lipoprotein fractions of VLDL/Triglycerides, IDL, LDL, HDL, and other plasma proteins after a one-stop iodixanol gradient centrifugation. The LDL isolated from plasma was chemically oxidised using copper sulphate ($CuSO_4$) which produces an OxLDL. Copper sulphate dissolves into cupric ion (Cu^{2+}), there are different methods to oxidise LDL using other transition metals such as iron (Vlaminck et al., 2014, Smith et al., 1992).

Purified nLDL and OxLDL were analysed using agarose electrophoresis, nLDL (lane 1) and OxLDL (lane 2 & 3) were run on 0.5% (w/v) agarose gel and stained with an azo based Sudan Black dye that recognizes the triglycerides and lipids. (Fig. 6.3B). Oxidation leads to changes in protein components by aldehyde products thereby recognize the scavenger receptors and also create the net negative charge which is essential for its interaction with the receptors. The increase in net negative charge of modified LDL led to faster migration of lipids in comparison to native LDL as seen in Fig. 6.3B. Thus, the oxidation of LDL was confirmed.

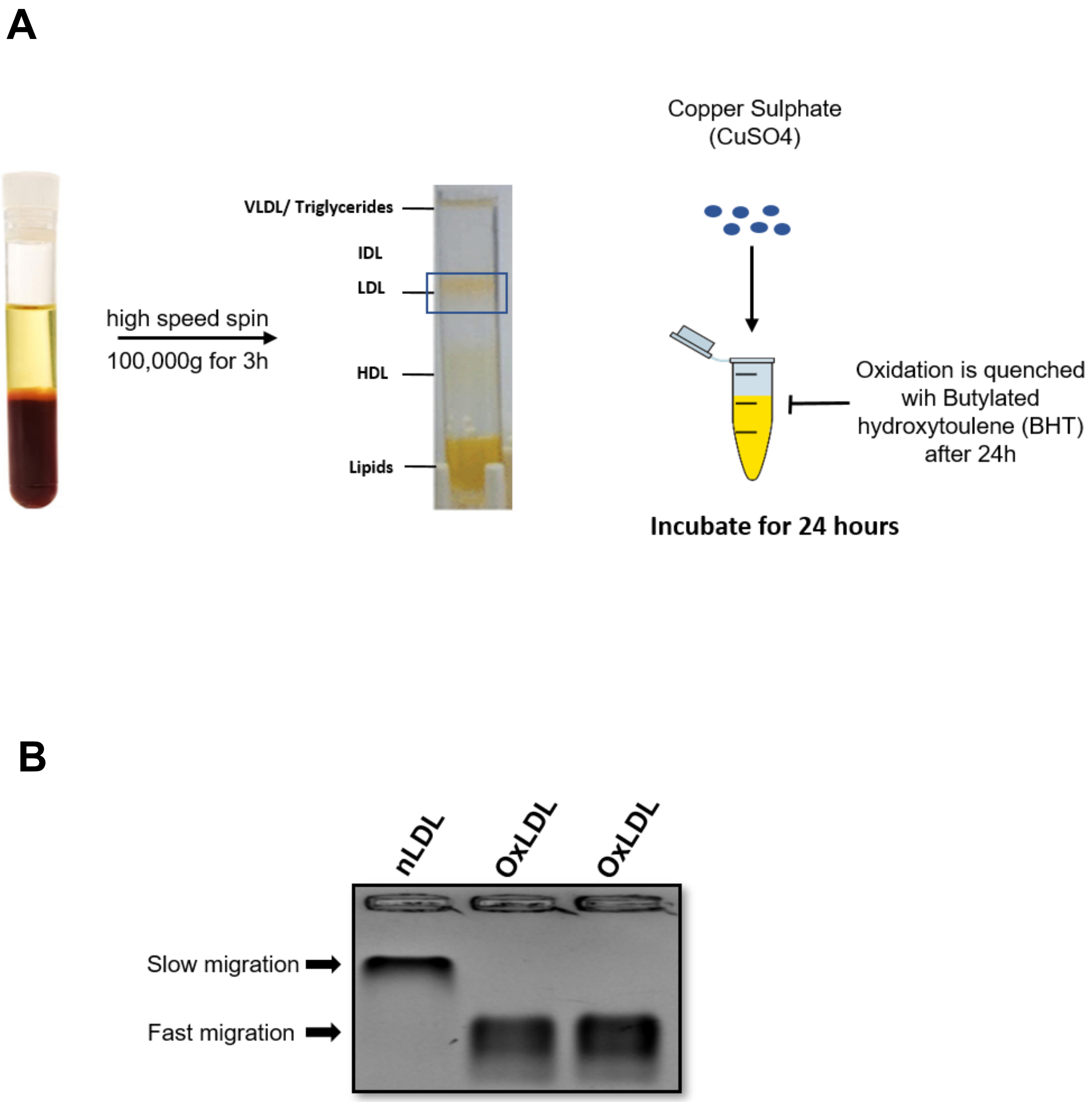

Figure 6.3. Purification and oxidation of low-density lipoprotein particles. (A) Schematic of isolation of native low-density lipoprotein (nLDL) from human plasma using ultracentrifugation and separation on iodixanol gradient; nLDL was then oxidised using 5 µM copper sulphate ($CuSO_4$) for 24 h at 37° C. Native LDL (nLDL) was used as control, incubated with 100 µM EDTA and 20 µM BHT at room temperature to stop the oxidation. **(B)** Lipid particles (4 µg) analysed by 0.5 % (w/v) agarose gel electrophoresis and Sudan Black staining. Native LDL (lane 1), OxLDL (lanes 2 and 3).

6.2.3. *In vitro* interaction studies on OxLDL and sLOX-1

It was essential to determine if OxLDL is recognised by the purified and refolded sLOX-1 protein. Previous studies suggested the LOX-1 only binds to OxLDL in the presence of millimolar calcium (Murphy et al., 2008). Therefore, 125 μg purified sLOX-1 was incubated with unmodified native LDL or OxLDL in the presence of 2 mM calcium chloride containing BHT anti-oxidant at 37°C physiological temperature for 1 hour and run through a size exclusion chromatography (SEC) column containing Sephacryl S-100 resin. SEC was performed to separate the protein-lipid complexes based on their size: the large protein complexes elute faster than the smaller complexes. The molecular weight of both native LDL and OxLDL ranges between ~1.5-4 MDa (Fisher et al., 1975a) with the ApoB-100 protein component itself constituting 550 kDa (Johs et al., 2006). However, the purified sLOX-1 monomer is ~26 kDa and dimer is ~52 kDa (Fig. 6.1C and 6.1D). Theoretically, the LDL and OxLDL particles elute faster through the column in comparison to the relatively small sLOX-1 polypeptide. This allows separation of free OxLDL, OxLDL/sLOX-1 complex, and free unbound sLOX-1.

The chromatograph nLDL with sLOX-1 showed three distinct peaks (Fig. 6.4A). Fig. 6.4B shows the monitoring of the OxLDL/sLOX-1 complex by SEC, which showed a similar elution profile as nLDL/sLOX-1 with three peaks. The chromatograph of control OxLDL alone also showed similar peaks (Fig. 6.4C). On the other hand, sLOX-1 alone showed a different elution profile with only two peaks (Fig. 6.4D) but no high molecular weight elution peak. The first peak of all three chromatographs containing lipoproteins (Fig. 6.4A, 6.4B and 6.4C) were fractions eluted closer to the void volume (35 mL CV). The elution fractions were collected and run on SDS-PAGE gel under reducing conditions and stained with Coomassie or probed by immunoblotting using primary sheep anti-LOX-1 antibody followed by secondary anti-goat HRP conjugate (Fig 6.4).

Figure 6.5A show nLDL/sLOX-1 SEC elution fractions (F1-F10) run on SDS-PAGE gel and stained with Coomassie blue: fractions F2 and F3 showed a band at ~150 kDa and another band >250 kDa, indicating the presence of ApoB-100 particle presence (Suto et al., 2013), a very faint band is can also be seen at ~100 kDa. No protein was detected in other fractions (F1, F4-F10), all fractions were transferred onto a western blot and probed with primary sheep anti-LOX-1 antibody and secondary anti-goat HRP, LOX-1 was not detected including fractions F2 and F3, indicating LOX-1 was not bound to LDL or ApoB-100 protein component of the LDL. 125 µg of OxLDL only was run through the SEC column as a negative control and the SEC fractions F1, F2 and F3 (Fig. 6.5B) representing the first peak (Fig. 6.4C) showed a band of ApoB-100 at much higher species of >250 kDa. Interestingly, no protein was detected in later fractions (F4-F10) representing the second peak. Furthermore, the first peak fractions (F1-F3) of OxLDL/sLOX-1 (Fig. 6.4B) stained with Coomassie blue showed numerous bands at sizes >250, 150, 100, 75 and ~25 kDa. Whereas, the second and third peak fractions (F5-F10) didn’t show any protein bands (Fig. 6.5C, upper panel).

The top three protein bands >250, 150, 100 kDa in the first peak of OxLDL/sLOX-1 were also detected in nLDL/sLOX-1; the additional bands at ~52 and ~26 kDa potentially represents the sLOX-1 protein. To verify the presence of sLOX-1 protein in the fractions, an immunoblot was performed using the primary sheep anti-LOX-1 antibody. Interestingly, multiple immunoreactive LOX-1-related bands were detected in the same fractions F1, F2 and F3 indicating existence of sLOX-1 multimers (Fig. 6.5C, lower panel). The sLOX-1 was thus evident as 4 bands of 26, 52, ~100, and >250 kDa molecular mass by reducing SDS-PAGE and immunoblot analysis. This indicated that the sLOX-1 monomer (26 kDa), dimer (52 kDa), tetramer (~100 kDa) and a possibly a higher multimer (>250 kDa). The analysis of the second and third peaks didn’t detect any free unbound sLOX-1. Furthermore, the SEC fractions of sLOX-1 alone (Fig. 6.4D) when analysed by immunoblotting also did not reveal sLOX-1. One possibility is due to the dilution of sLOX-1 due to high column volume (35 ml), causing an inability of our anti-LOX-1 antibody to detect very dilute amounts of sLOX-1 in these samples.

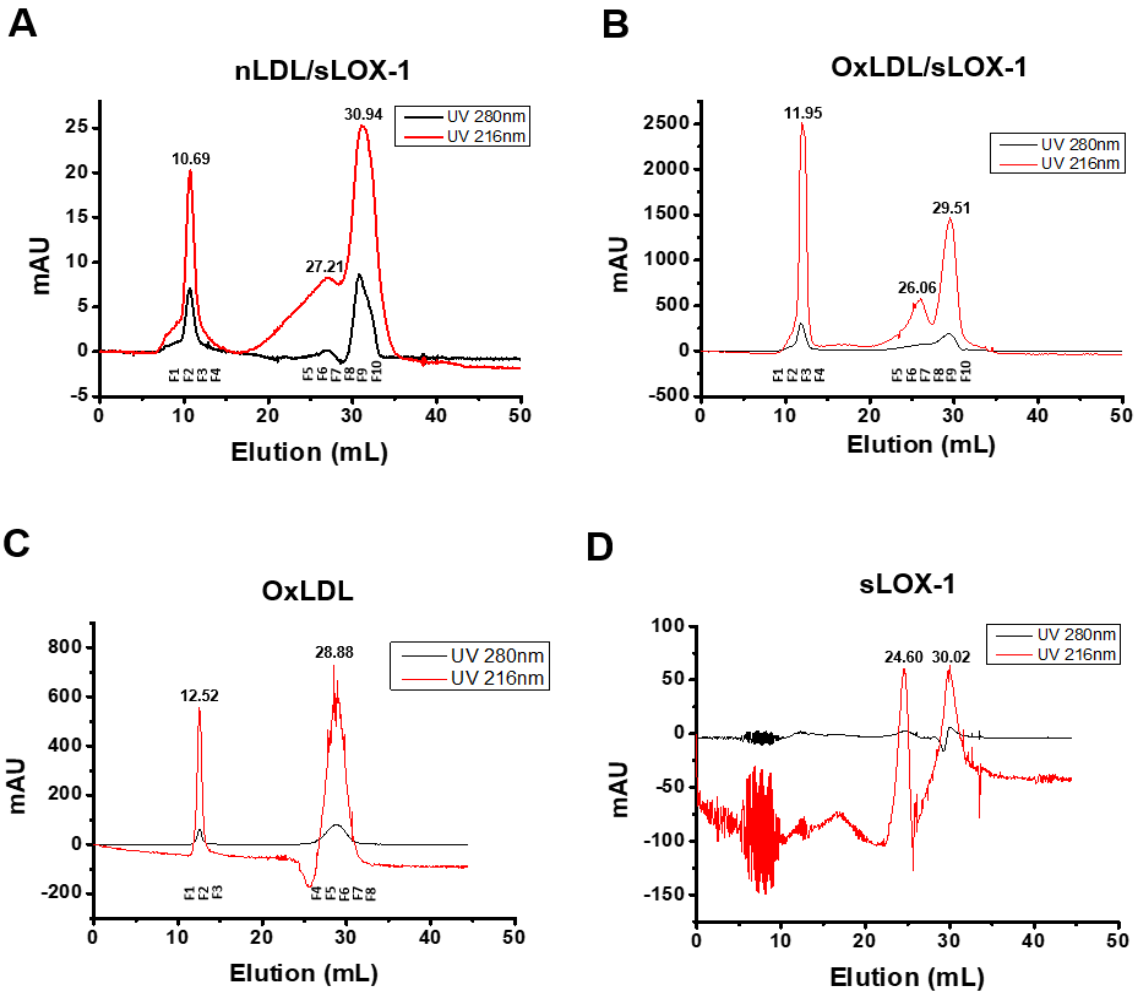

Figure 6.4. Size fractionation of lipid particle-sLOX-1 complexes. 125 µg of nLDL/sLOX-1, OxLDL/sLOX-1, OxLDL alone or sLOX-1 alone were incubated at 37˚C for 1 h and analysed using a Sephacryl S-100 size exclusion chromatography column. **(A)** Analysis of nLDL/sLOX-1 complex. **(B)** Analysis of OxLDL/sLOX-1 complex. Analysis of **(C)** OxLDL alone, or **(D)** sLOX-1 alone. Arrows indicate positions of sLOX-1 and lipid particles where appropriate. See Figure 6.5 for LOX-1 immunoblot analysis.

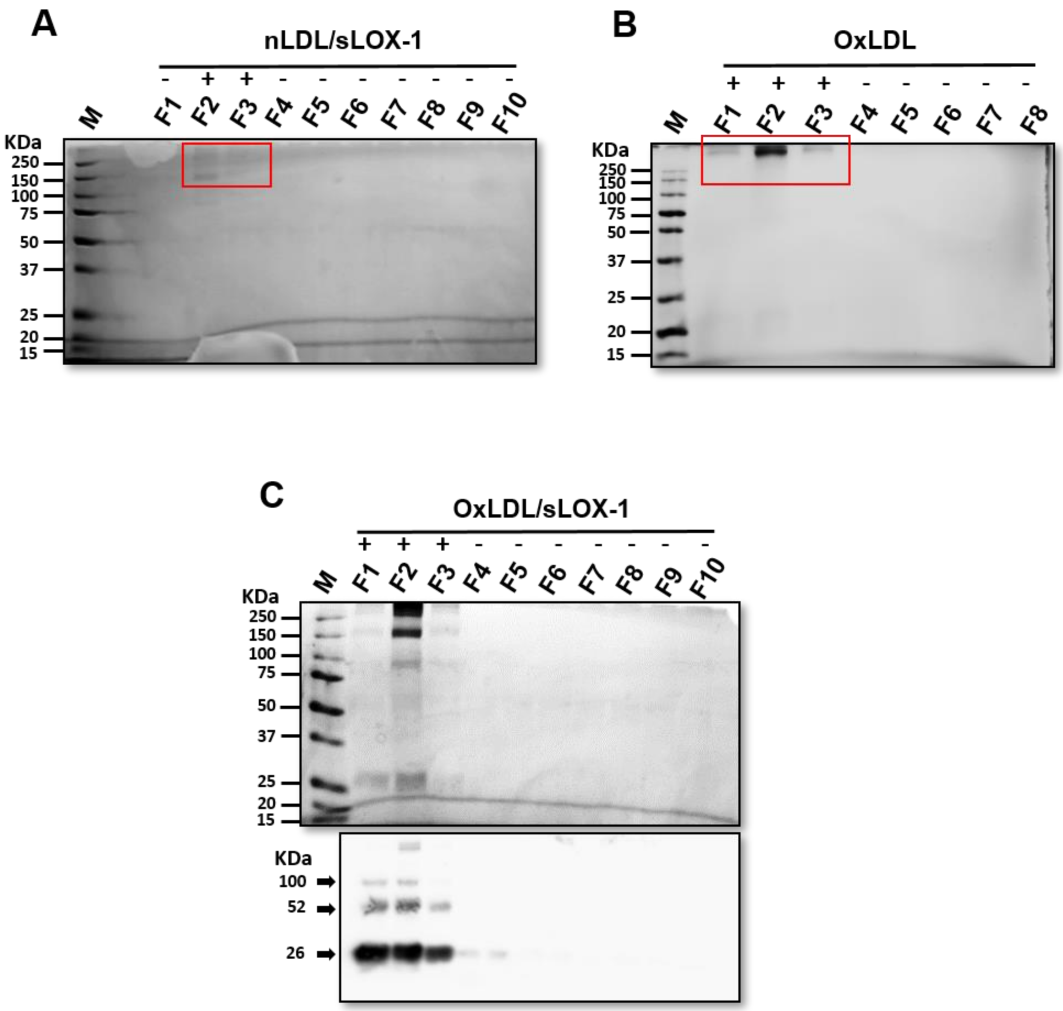

Figure 6.5. Analysis of protein content in size fractionation of lipid particle-sLOX-1 complexes. Fractions collected by size fractionation (see previously in Figure 6.3) were subjected to Coomassie blue staining or immunoblotting. **(A)** Fractions (F) of nLDL/sLOX-1 analysed by SDS-PAGE and Coomassie blue staining. Box in fractions F2 & F3 indicates ApoB-100 (lipid particle) presence. **(B)** OxLDL (-ve control) only fractions (F1, F2 and F3) show Apo-B100 presence, but as a high molecular weight species (>250 kDa). **(C)** Analysis of OxLDL/sLOX-1, fractions using SDS-PAGE and Coomassie staining (upper panel) showed both ApoB-100 (550 kDa) and sLOX-1 (25 kDa). Immunoblotting of these fractions using sheep anti-LOX-1 antibody indicated the presence of LOX-1 multimers indicated by 25 kDa, 50 kDa and 100 kDa immunoreactive bands.

6.2.4. Measurement of the molecular mass of lipid particles using microfluidic diffusion sizing (MDS) technique

Numerous studies have reported the average size of lipoproteins such as LDL, VLDL, HDL and chylomicrons using dynamic light scattering method (DLS) (Sakurai et al., 2010, O'Neal et al., 1998, Ruf and Gould, 1999). Using DLS, various subclasses of lipoprotein particles were investigated, however, no studies were performed to estimate the size of OxLDL. It was presumed that the size of OxLDL to be the same as nLDL (Chen and Khismatullin, 2015). In this study, a microfluidic diffusional sizing (MDS) method was used to estimate the size of OxLDL and nLDL. A microfluidic two-dimensional approach offers various advantages over conventional DLS technique as mentioned in materials and methods. This method uses two-dimensional microfluidic diffusion profiles based on Brownian motion of particles which are localized in a well-defined space over the same length on various time scales (Arosio et al., 2016). Using two streams of auxillary fluid the diffused and undiffused profiles were established for nLDL (Figure 6.6B), OxLDL (Figure 6.6C), and OxLDL/sLOX-1 complex (Figure 6.6D) 20 mM HEPES buffer was used as a control (Fig. 6.6A) (n=2).

Similar to DLS, the diffusion coefficient was used to measure the hydrodynamic radius (R_h) using the Stokes-Einstein equation (Tyn and Gusek, 1990)

$$\text{Hydrodynamic radius } (R_h) = kT/6\pi\eta D$$

k = Boltzmann’s constant

T = temperature

η = Solvent viscosity

D = diffusion coefficient

Table 6.1 shows the list of the average hydrodynamic radius (R_h) and hydrodynamic diameter of nLDL, OxLDL and OxLDL/sLOX-1 complex. The R_h was estimated using MDS, whereas, the relative molecular weights and the hydrodynamic diameter were measured using the R_h.

The diffusion coefficient rate of proteins varies based on their size and shape. The standard diffusion coefficient rates, relative R_h and molecular weight of the

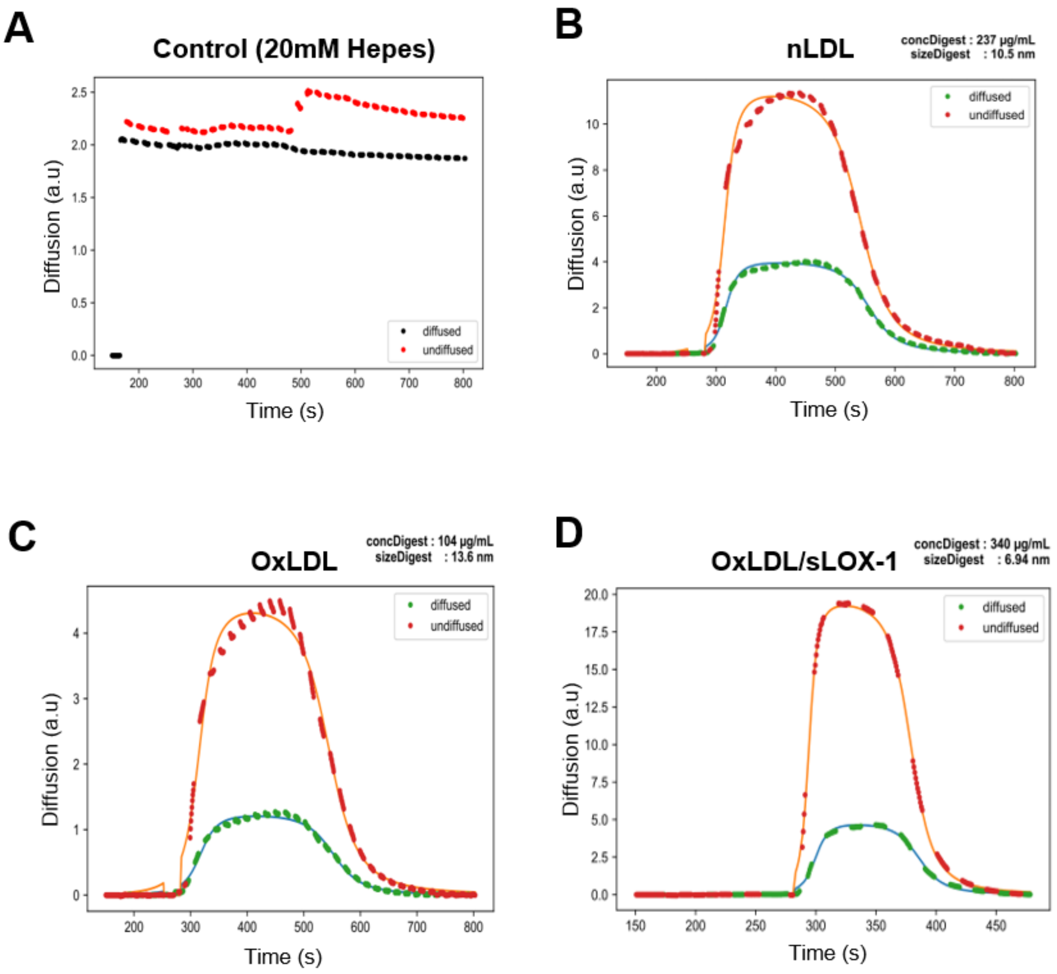

Figure 6.6. Diffusion profiles of lipoprotein particles and complexes using microfluidic diffusion technique. Graphs showing the traces of lipoproteins in microfluidic channel separated into diffused and undiffused split streams of **(A)** 20 mM Hepes buffer (control) **(B)** nLDL **(C)** OxLDL, and **(D)** OxLDL/sLOX-1 complex. Diffusion analysis is based on Brownian movement and the amine reactive dye used to label proteins and their fluorescence was measured to estimate the average hydrodynamic radius (Rh) using the Fluidity-1 system (see Materials and Methods).

Table 6.1. Estimation of lipoprotein particle and complex sizes using microfluidic diffusion technique (Fig. 2.1). The hydrodynamic radius of the lipoproteins was estimated using Stokes-Einstein equation**.**

Protein	Hydrodynamic radius in nm	Hydrodynamic diameter in nm
nLDL	10.8 ± 0.3	21.6 ± 0.6
OxLDL	13.48 ± 0.12	26.96 ± 0.24
OxLDL/sLOX-1	7.19 ± 0.26	14.38 ± 0.52

multiple broad range globular proteins and viruses (1.24 kDa - 5000 kDa) were generated by Tyn.et.al (Tyn and Gusek, 1990). Based on the existing molecular weight (kDa) and hydrodynamic radius values of folded globular proteins a calibration curve can be plotted to estimate the molecular weight of lipoproteins. A molecular weight converter (https://www.fluidic.com/support/faq/convert-hydrodynamic-radius-to-mw/) which works on the above principle was used to estimate the molecular weight of lipoproteins. Interestingly, the estimated hydrodynamic radius (R_h) of OxLDL (13.48 ± 0.12 nm) was higher than the nLDL (10.8 ± 0.3 nm). This confirms that oxidation leads to the change in the overall size of a lipoprotein. As expected, the significant decrease in the R_h value of OxLDL/sLOX-1 (7.19 ± 0.26 nm) complex is due to the limitation of the microfluidic diffusion sizing technique. Even though the average value of R_h is dominated significantly by larger species it also takes into account smaller free unbound sLOX-1 which conventionally brings the average value down significantly.

6.2.5. Cryo-electron microscopy (cryo-EM) analysis of OxLDL

To analyze the structure of OxLDL we've used cryo-EM technique. OxLDL was prepared as mentioned in materials and methods, purified OxLDL was dialyzed in Tris buffer. 1mg/ml OxLDL was used to make microscope specimens on Quantifoil holey carbon 400 mesh grids. The samples were plunge frozen using vitrobot (FEI) and 1431 micrographs were collected for 72 h using Titan Krios (FEI) equipped with Gatan K2 direct detection camera. Fig. 6.7A shows a mesh of quantifoil carbon grid with OxLDL particle distribution, Fig. 6.7B shows the micrograph of OxLDL particles embedded in vitrified ice taken at 50 000x magnification. The scale bar represents 50 nm and each lipid particle can be seen on average ~25 nm (250 Å) in diameter. The individual particles varied in size, as highlighted in red solid and dotted circles (Fig. 6.7B). Furthermore, the electron micrographs showed monodisperse particle distribution (Fig. 6.7B, black arrow heads), and homogenous samples with a clear background without much noise and particle movement in ice. These data indicated that this sample should be appropriate for further structural analysis.

6.2.5.1. EM class averages of OxLDL

From 1431 micrographs that were generated, 31,782 particles were manually picked using RELION 3.0 software to create 2-D class averages of the OxLDL particle. Fig. 6.7C shows 24 different class averages (labelled 1-24) generated by aligning all the particles using RELION 3.0. Two distinct classes were observed: the features observed in both raw micrographs and 2-D class averages were similar to class averages of LDL generated previously (Orlova et al., 1999a). The class averages showed two distinct appearances, most are round with no pattern, whereas, 8 classes (5, 6, 9, 14, 16, 17, 18 and 24) showed long striations appearance with different density distribution (Fig. 6.7C). This data suggests that they represent two different views of OxLDL, the round non-striations potentially represent the top or bottom view. 8 classes with striations represent the side views (Fig. 6.7D). The overall shape likely looks like an ellipsoidal particle. Similar to LDL, and the average length and height of OxLDL was also measured from 2-D classes (Fig. 6.6C & 6.6D). The OxLDL length and height dimensions measured were 150-160 Å and 210-240 Å respectively. Similar to nLDL, OxLDL also seems to have five striations in its lipid core and the number of striations remained the same in all eight 2-D class averages that were observed. The five higher density striations may act as internal walls and to separate the lower density compartments. This suggests that the OxLDL in its core has a consistent pattern of various higher density and lower density lipid distribution separately in compartments. Fig. 6.7D shows the cartoon representation of class averages generated in two different views. Firstly, a side view showing five higher density striations that formed four lower density compartments and a 90° rotation representing the top view which was oval.

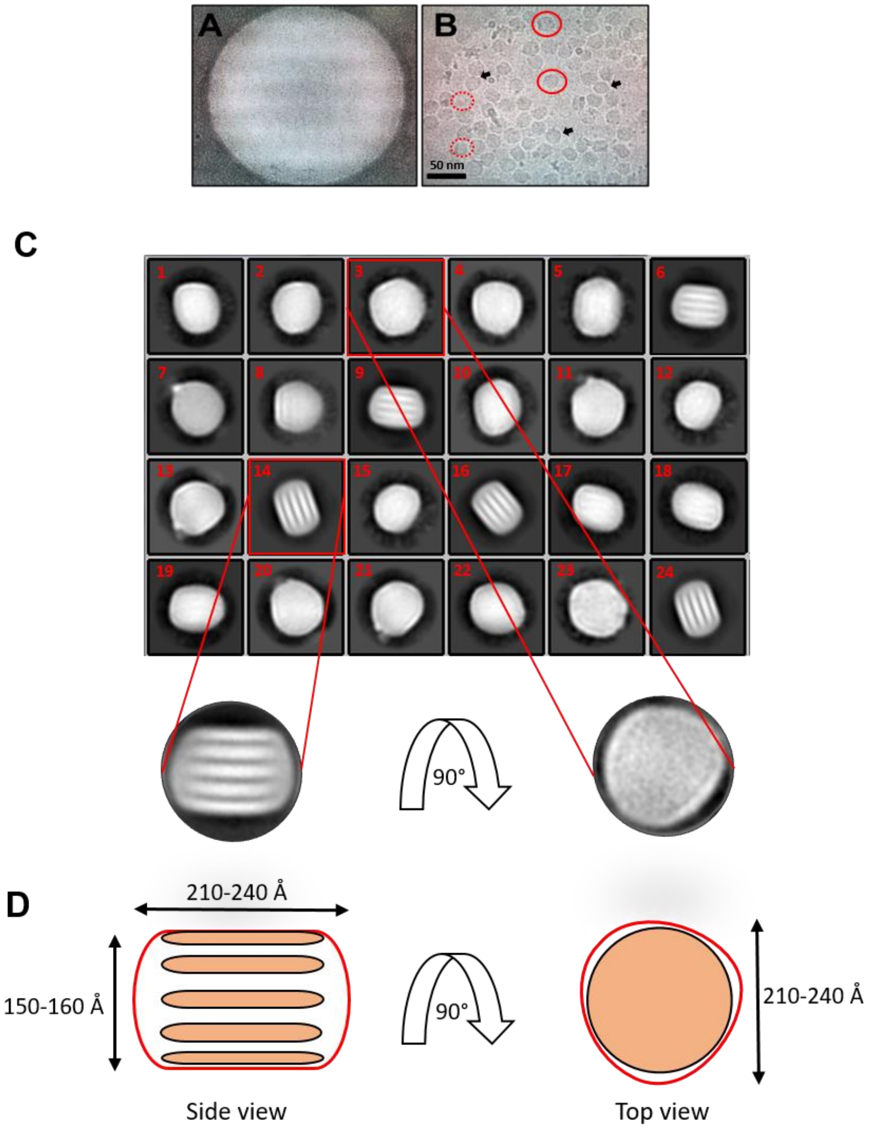

Figure 6.7. Analysis of purified OxLDL particles using cryo-electron microscopy. OxLDL was loaded onto electron microscopy grids and frozen before cryo-electron microscopy analysis (see Materials and Methods). **(A)** Quantifoil carbon grid mesh with OxLDL particles in vitrified ice. Mesh diameter, 2 µm. **(B)** OxLDL particles embedded in ice viewed at 50 000X magnification. Scale bar, 50 nm. Black arrow heads indicate electron density distribution across the surface of individual OxLDL particles. Each particle corresponds to ~250 Å (25 nm) diameter. **(C)** 2-D class averages of OxLDL profiles represented by 24 selected class averages generated (from 31,782 particles) using RELION 3.0 software. **(D)** Schematic representation of two views of OxLDL. Most of the 2-D averages which are large and round in appearance are possibly a a top view. Images 5, 6, 9, 14, 16, 17, 18 and 24 are non-circular and show three striations in the OxLDL core, probably indicating a side view showing regions of high and low fatty acyl chain density within the lipid particle.

6.2.5.2. 3-D reconstruction of a model of the OxLDL particle

All 24 2-D classes generated were clear without any background noise, consistent in size and represented different views of OxLDL. Therefore, no subset classes were selected to remove outliers. Using all 24 2-D classes, 30,688 particles were extracted from micrographs which were processed further to generate a 3-D model of OxLDL. Using the RELION 3.0 Stochastic Gradient Descent (SGD) algorithm, a 3-D *de novo* model based on the 2-D classes was generated (Fig. 6.8). C1 symmetry was used to align the 2-D classes, C1 consists of all the rotations about a fixed point by multiples of angle 360. Fig. 6.8 shows the 3-D model reconstruction of the OxLDL particle. The top panel of Fig. 6.8 shows 3-D electron density distribution of OxLDL from three different views, i.e. top view (Fig. 6.8A), bottom view (Fig. 6.8B), and side view (Fig. 6.8C). Surprisingly, and unlike nLDL, the overall shape is not a perfect ellipsoid. Upon close observation of the top right corner (Fig. 6.8C), a protrusion of higher electron density likely corresponding to a protein domain was detected. To further investigate the protrusion and interior core, multiple 3-D classes were generated which show the cross-sections of OxLDL and internal core density distribution from the side view. Fig. 6.8D shows the cross-section and the internal wall of OxLDL, Fig. 6.7E and 6.7F panels show the higher density internal striations and outer shell surface, a significantly higher density protrusion was also detected on the outer shell surface.

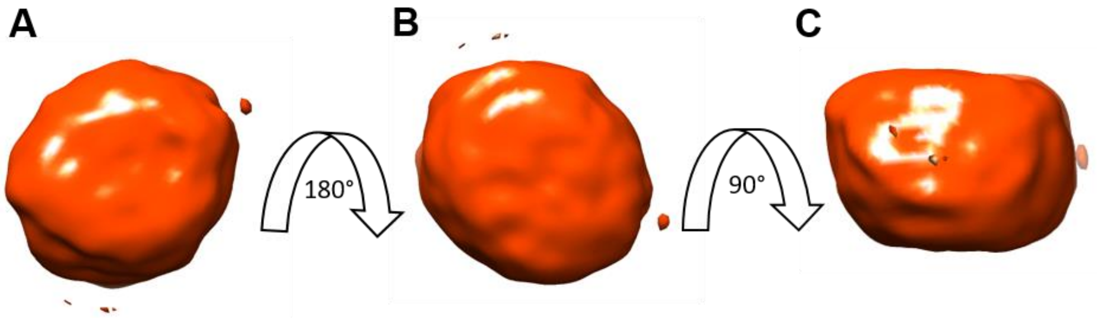

Top view

Bottom view

Side view

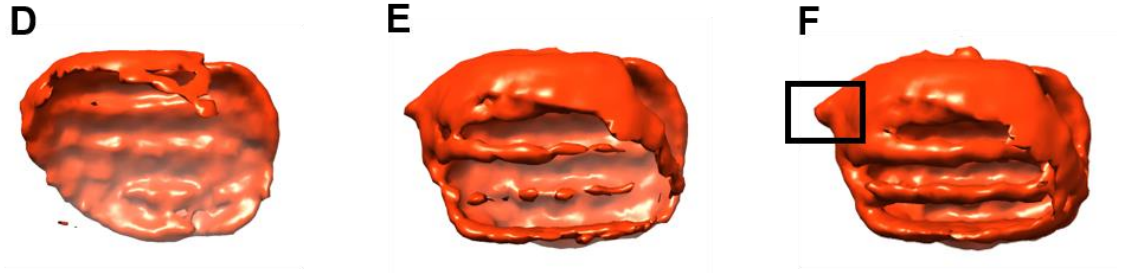

Figure 6.8. 3-D model representation of OLDL particles. Presentation of 3-D *de novo* model of OxLDL generated from 2-D classes using RELION 3.0 software. C1 symmetry was maintained to align the 2D classes. Top panel depicts different surface views in orange with **(A)** top view, **(B)** bottom view, and **(C)** side view. **(D)** Lower panel shows the cross section of side view. **(E)** Cross-section view of internal core arrangement with increase in density distribution of OxLDL. **(F)** Side view cross section shows a small protrusion of higher density on outer surface (black box).

6.2.5.3. Nanogold labeling of sLOX-1/OxLDL complex

After generating a 3-D model of OxLDL, an attempt was made to map the binding epitopes of OxLDL for the sLOX-1 protein. The cryo-EM conventionally doesn't detect the proteins that are lower than 200 kDa, and the size of monomeric sLOX-1 is only 26 kDa. We know that LOX-1 it binds to OxLDL as a dimer (52 kDa) or through potential multimers. Theoretically, it quite challenging to identify the small extracellular domain of LOX-1 dimer when bound to the surface of OxLDL due to its size being below the detection limit for cryo-EM analysis (Merk et al., 2016, Renaud et al., 2018). In order to map the number of LOX-1 binding sites on OxLDL and tackle the size limitation, a different approach of nanogold labeling was used. The Ni-NTA (nickel (II) nitrilotriacetic acid) nanogold particles can be visualized as dark electron-dense spots on micrographs and they have a very high affinity towards His-tag (Hainfeld et al., 1999). The purified sLOX-1 has a hexahistidine-tag at the N-terminus to which 5 nm Ni-NTA-nanogold particles can be directly linked and visualized under the microscope, therefore the surface localisation of sLOX-1 on OxLDL can be probed.

The schematic of interaction between the His-tagged protein and Ni-NTA nanogold (adapted from http://www.nanoprobes.com/MM05NTAGold.html) is shown in Fig. 6.9A) Each 5 nm gold particle is associated with multiple Ni-NTA functionalities, each Ni^{2+} binds to one NTA and two histidines from a recombinant hexahis-tagged protein; tight binding is achieved when three adjacent Ni-NTA bind to one hexahis-tag. Therefore, purified sLOX-1 with a hexahis-tag was incubated with >10-fold molar excess of 5 nm Ni-NTA nanogold for 30 min at room temperature and then the mixture was added to OxLDL. The complex was then incubated for 1 h at room temperature and run through the SEC containing Sephacryl S-100 column remove unbound nanogold particles. Fig. 6.9B and 6.9C show the chromatographs of OxLDL/Ni-NTA nanogold (control) and OxLDL/sLOX-1/Ni-NTA nanogold respectively. Both chromatographs showed a similar elution profile of OxLDL/sLOX-1 (Fig. 6.4B). Therefore, the elutions representing the first peak should contain sLOX-1 bound to OxLDL with potentially 5 nm Ni-NTA gold bound to sLOX-1. Cryo-grids were made with

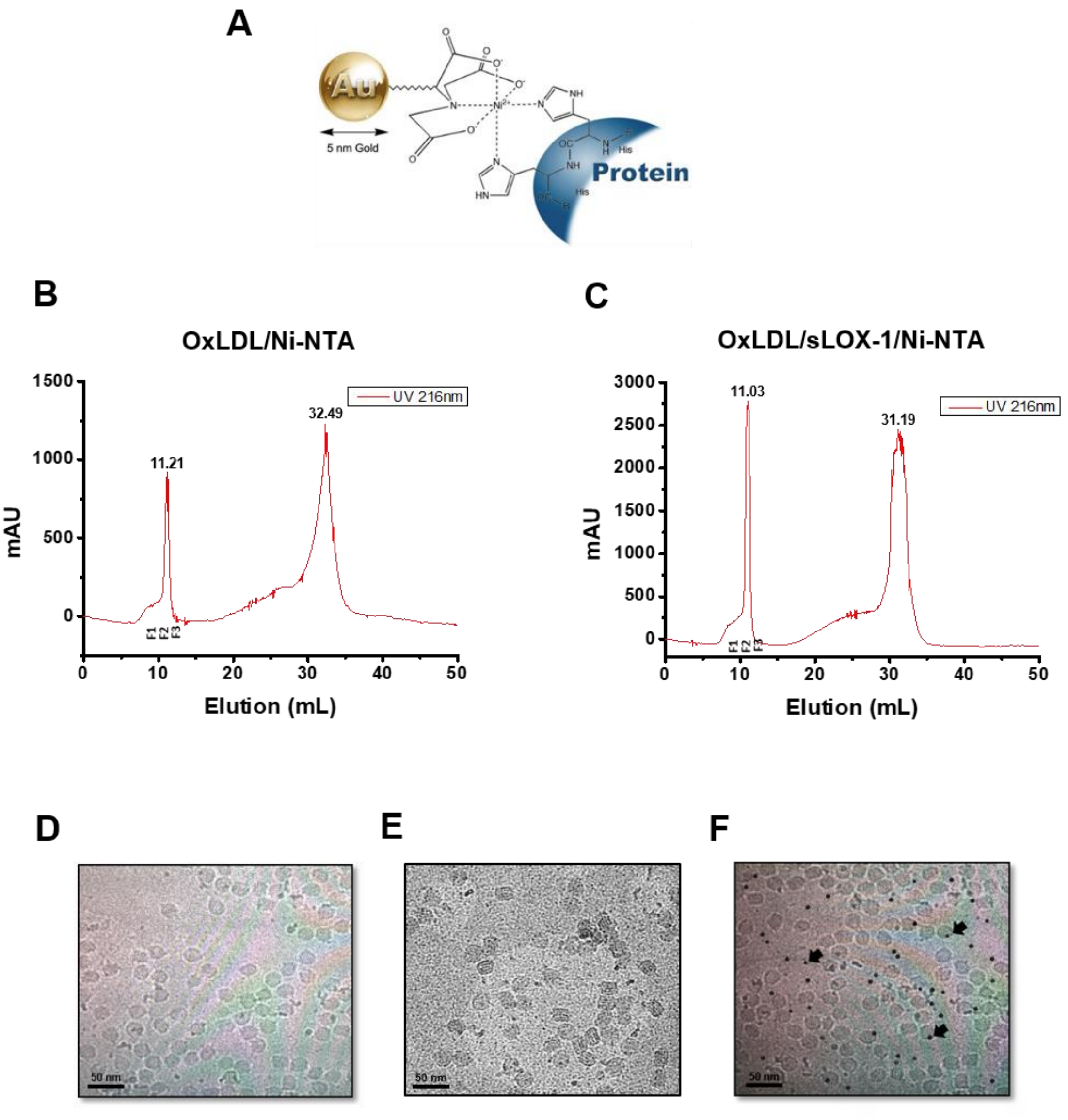

Figure 6.9. Nanogold labelling of sLOX-1/OxLDL complex. (A) Schematic representation of interaction between His_6-tagged protein and Ni-NTA-nanogold probe to detect hexahis-tagged proteins such as sLOX-1. **(B)** Size exclusion chromatography of OxLDL particles incubated with Ni-NTA probe with 5 nm diameter nanogold (negative control), and; **(C)** OxLDL/sLOX-1/Ni-NTA probe with 5 nm diameter nanogold complex. **(D, E)** Micrographs of fraction 2 (F2) collected from SEC of OxLDL/Ni-NTA nanogold and OxLDL/sLOX-1/Ni-NTA nanogold complexes respectively (magnification, 50 000X). Scale bar, 50 nm. **(F)** OxLDL/sLOX-1/Ni-NTA gold complex without size exclusion analysis (magnification, 50 000X). Gold particles (black arrow) can be seen but not directly bound to OxLDL/sLOX-1 complex. Scale bar, 50 nm.

fractions eluted from the first peak and micrographs were collected using Titan Krios to detect the complex (Fig. 6.9D & 6.9E). The micrograph showed monodisperse, uniform distribution of OxLDL. As expected, no gold particles were observed in the negative control (Fig. 6.9D). Unfortunately, no electron-dense gold particles were not detected in purified OxLDL/sLOX-1/Ni-NTA complexes (Fig. 6.9E). This suggests that Ni-NTA nanogold particles were not bound to sLOX-1 protein. Furthermore, cryo grids were made with OxLDL/sLOX-1/N-NTA nano gold complex before performing the SEC (Fig. 6.9F). OxLDL and nanogold particles indicated with black arrowheads are clearly visible however, gold particle localisation was not observed around the OxLDL profiles. In these experiments, the nanogold particles were not bound directly to OxLDL/sLOX-1 complex.

6.3. DISCUSSION

The main aims of this study were

- To generate and purify recombinant human extracellular domain LOX-1 for estimating the binding epitopes and number of LOX-1 receptors involved in binding to OxLDL.
- To establish a standard protocol to generate OxLDL that recognizes and binds to recombinant purified sLOX-1 invitro.
- To identify if LOX-1 binds to both ApoB100 and lipids or ApoB-100 alone.
- To generate a structure of OxLDL using cryo-EM and compare the structural features with native LDL.

Firstly, a bacterial sLOX-1 expression system was generated. Although milligram quantities of sLOX-1 protein were expressed, it was present in insoluble inclusion bodies. This is a common problem whilst expressing recombinant proteins in bacteria (Singh et al., 2015). sLOX-1 was successfully purified using Ni-NTA agarose and refolded after solubilizing the receptor in denaturant and reducing the incorrectly formed disulphide bonds. The LOX-1 contains one interchain and three intrachain disulphide bonds (Ohki et al., 2005). Attempt to refold the sLOX-1 were successful.

Although, the oxidation of lipoprotein is straightforward, monitoring the oxidation is crucial. The oxidation of LDL can be generally categorized into two types, minimally oxidized LDL (mOxLDL) and extensively oxidized LDL, the extent of oxidation of LDL mainly affects their ability to bind to LOX-1 scavenger receptor and internalization by phagocytic cells. (Lougheed and Steinbrecher, 1996). The minimally modified OxLDL is an early form of progression into extensively oxidized LDL, and it doesn't bind to the LOX-1 scavenger receptor but still retains the ability of nLDL to bind to LDL receptor (Boullier et al., 2006, Han and Pak, 1999).

Even though there are various methods to perform *in vitro* oxidation of LDL as previously described in introduction, in this chapter only copper-based oxidation was performed and the oxidation was verified using agarose gel electrophoresis. However, the extent of oxidation and the ability of OxLDL to recognize and bind to sLOX-1 was still unclear. This raises an obvious question: How is copper based *in vitro* oxidation of LDL relevant to the physiological process of oxidation? This relates to whether what happens during oxidation by free Cu (II) bears any relation to what happens in the body. Evidence suggest that reactive OH radicals that modify phenylalanine to o-tyrosine or m-tyrosine. Reduction to Cu(I), ironically by endogenous Vitamin E, drives decomposition of lipid hydroperoxides to fatty acid chain radicals (particularly if fatty acid is polyunsaturated) at the ApoB-100/lipid interface (Upston et al., 2002). These can modify other lipids or proteins (e.g. lysyl side-chains), a factor in binding other types of scavenger receptor (Biondi et al., 2001). To address if chemically oxidised LDL bear any resemblance to physiological LDL *In vitro* binding of refolded recombinant sLOX-1 to OxLDL was performed in the presence of divalent calcium ions, and SEC analysis showed that the OxLDL was able to form a stable complex with sLOX-1. Therefore, the recognition and binding of sLOX-1 to the LDL oxidized by copper as evidenced in this chapter support the idea of physiological process. The oxidation leads to modification of protein/lipid interface (ApoB-100/fatty acid) that in turn promote the recognition of OxLDL by LOX-1 scavenger receptor.

Using a radiolabelling approach, Goldstein, Brown, and colleagues determined that LDLR binds to LDL in 1:1 molar stoichiometry (Van Driel et al., 1989). Later experiments showed that LDLR specifically binds to the ApoB-100 moiety of LDL(Shireman et al., 1977, Lagor and Millar, 2010). The same approach can be tried for recognition of LOX-1 binding sites on OxLDL but this approach of solubilisation and delipidation of ApoB-100 of OxLDL compromises the modifications on ApoB-100 and also it doesn't address the question of sLOX-1 acid-base patch binding hypotheses which suggest that the charged and electrostatically neutral surface of sLOX-1 binding to zwitterionic polar head groups on the surface of OxLDL.

To address both these questions, a cryo-EM based approach of nanogold specific labelling was used. However, the attempt was unsuccessful and the nanogold particles identified on the cryo micrographs were not associated with OxLDL/sLOX-1 complex. The potential reason of Ni-NTA nanogold not being bound to the N-terminal hexahis-tag of sLOX-1 could be due to the hexahis-tag being buried by the dimers/multimers, or tag being inaccessible due to misfolding of the protein (Debeljak et al., 2006). Due to time constraints, it was not possible to perform extensive troubleshooting studies of His-tag accessibility and binding to nanogold. Further optimization of misfolding of sLOX-1 or by inserting a small flexible linker sequence can potentially limit the burying of the His-tag and give access for gold particles to bind to the tag (Chen et al., 2013).

6.3.1. Oxidation of LDL leads to potential structural rearrangement of ApoB-100 protein on the particle surface

The molecular mass of LDL was estimated to be 1.5–4 MDa (Fisher et al., 1975b). Campos and colleagues first measured the size of LDL particles approximately range from 22-27.5 nm in diameter (Campos et al., 1992). Scheffer and colleagues measured the size of native LDL using HPLC (Scheffer et al., 1997). Later, the same group measured the size of LDL from whole plasma by high-performance gel filtration chromatography using a fluorescent lipid probe (Scheffer et al., 1998). We know that LDL particles have a heterogeneous population with respect to size, composition, and density. Therefore, variation in size and the molecular weight is observed.

The sizes of lipoproteins are usually measured using electrophoresis and chromatography techniques. We know that the molar mass of LDL ranges from 1.5–4 MDa, and size from 22-27.5 nm in diameter respectively containing somewhere between ~3,000-6,000 lipid particles (Kaitosaari et al., 2006, Segrest et al., 2001). The huge variation in mass and size are due to lipoproteins being highly heterogeneous, with different composition and density of lipids. Unlike proteins, the lipoproteins with equal molecular weight (Mr) can potentially exhibit different sizes. Inversely, lipoproteins with the same size can also show difference in molecular weight based on packaging of lipids i.e densely packed lipids and loosely packed lipids, therefore, the molecular weight and size cannot be determined by elution alone using SEC (Hong et al., 2012, Osei et al., 2015, German et al., 2006). Considering that SEC mainly separates the molecules based on hydrodynamic radius but not Mr. Furthermore, mass spectrometry analysis of LDL and OxLDL allows the identification of changes in fatty acyl chain such as addition of any functional groups and their location on the fatty acyl chain (Rosario et al., 2008).

Both the lipoproteins were made by fractionation of blood from a single donor, with OxLDL being generated from purified LDL. The average hydrodynamic radius (R_h) measured using microfluidic diffusion has shown a change in the overall size (diameter) of lipoproteins. Surprisingly, the estimated average size of OxLDL (26.96 ± 0.24 nm) was larger than nLDL (21 ± 0.6 nm) (Table. 6.1). The measurement of average nLDL size was consistent with 20.3 ± 1.1 measured by Sakurai et.al using standard DLS technique (Sakurai et al., 2010). It was concluded that the proposed MDS can be used to differentiate the lipoprotein particle sizes and the oxidation of LDL leads to rearrangement of overall lipoprotein structure (German et al., 2006). In order to correlate the change in lipid particles due to oxidation, the change in the structural features were further investigated using cryo-EM for visualisation.

An attempt to resolve a high-resolution structure using single-particle cryo-EM is not a feasible approach for lipids due to heterogeneous lipid distribution (Zhang et al., 2011, Murray et al., 2016). However, a low-resolution structure of OxLDL would provide valuable information in identifying the difference in overall structural features of OxLDL when compared to native LDL. The 3-D structural model of native LDL exhibits an ellipsoid appearance (Fig. 6.10A), upon binding to the LDL receptor a small protrusion on the outer shell surface was detected (Fig. 6.10B) (Ren et al., 2010a). It was well-established that LDLR only binds to ApoB-100 protein of LDL but not the lipid components (Sakamoto and Rosenberg, 2011). There are two known binding sites for LDLR on ApoB-100 (residues 3147-3157 & 3359-3367) (Olsson et al., 1997). The bulge on the side of nLDL was the density distribution of LDLR bound to the LDL in 1:1 stoichiometry. Therefore, it has been proposed that the site of an ApoB-100 binding domain on LDL is located on one side of the lipoprotein particle (Ren et al., 2010a). Interestingly, the 3-D model of OxLDL we have generated in this study was more spheroidal, but not complete ellipsoid like native LDL. Also, a protein-based electron-dense protrusion was observed at a similar position on the outer shell surface without any bound LOX-1 receptor (sLOX-1) (Fig. 6.10C). This suggests that the bulge on the outer shell of OxLDL could be the LDLR ligand-binding domain of ApoB-100 protein. Therefore, we propose that the oxidation of native LDL leads to structural rearrangement of ApoB-100 and open the inaccessible domains which are possibly recognized by LOX-1 receptor. By analysing the nLDL/LDLr and OxLDL 3-D structures, it is crucial to note that the ApoB-100 binding region can potentially be the same for LOX-1 on OxLDL.

Furthermore, the 3D model of OxLDL generated was compared to native LDL by superimposing both the structures using the UCSF Chimera program (Fig. 6.11). Interestingly, the higher density regions were seen enlarged out from the surface of OxLDL which are not distinguishable by inspecting OxLDL alone. We know that the ApoB-100 exists in an elongated form and wraps around the LDL particle (Yang et al., 1994b). Presumably, the higher density projections observed on OxLDL are ApoB-100 protein unraveled from its native state (nLDL) due to the

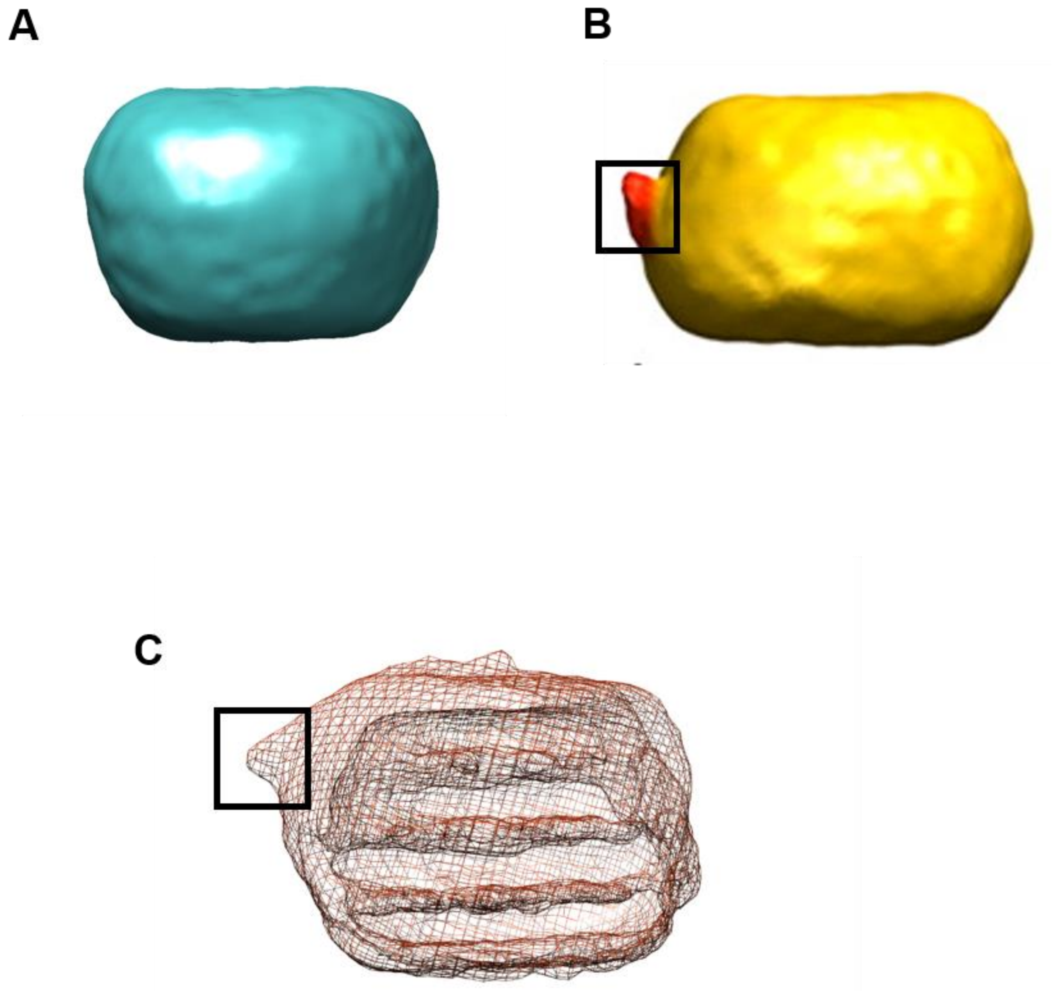

Figure 6.10. Comparison of 3-D models of native LDL and OxLDL particles. Side view of **t**hree dimensional density map of **(A)** native LDL (green) (EM ID:5239), **(B)** native LDL bound to LDL receptor (yellow) (EM ID:5158), the electron density distribution of LDL receptor can be seen as small protrusion on the side (indicated in black box), and **(C)** Three-dimensional reconstruction of OxLDL (orange mesh), with the internal core compartments and outer surface viewed separately. A higher density protrusion on the side can be observed in the absence of receptor (sLOX-1).

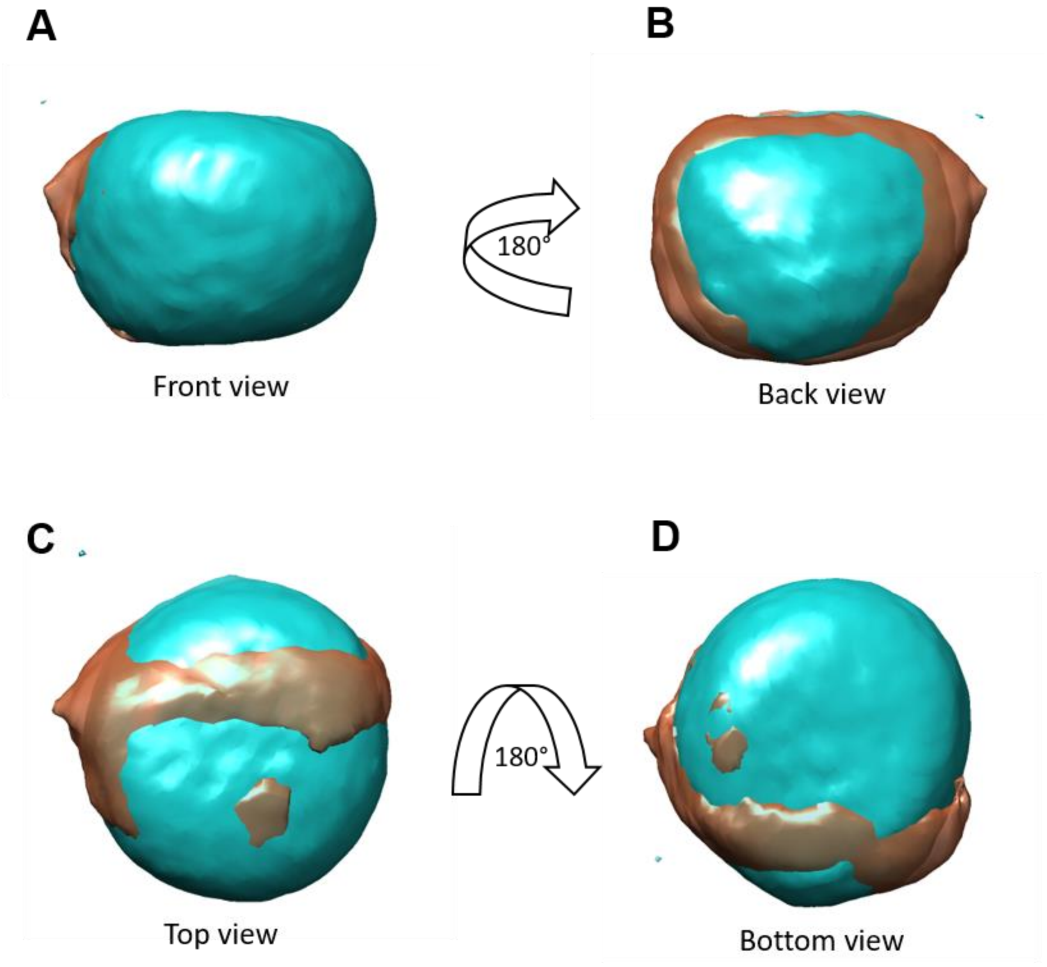

Figure 6.11. Lipid particle oxidation causes structural re-arrangement. 3-D model of nLDL (blue) (EMID:5239) is superimposed with OxLDL structure (light orange) using UCSF chimera software. Four orthogonal views are presented **(A)** front view, **(B)** back view, **(C)** top view, and **(D)** bottom view. Oxidation of LDL particle potentially re-distributes the apoB-100 protein density on the lipid particle surface. The density distribution of apoB-100 (brown) can be seen wrapped around the outer surface of lipoprotein (blue).

oxidation. It also explains the overall increase in the hydrodynamic radius of LDL upon oxidation. This study has also identified that the internal structural features of LDL don’t change upon oxidation, but the overall size of lipoprotein decreased in size possibly due to increase in tighter packing of phospholipids due to oxidation.

CHAPTER 7

GENERAL DISCUSSION

The studies presented in this thesis provided novel insights into the structural and biochemical aspects of the VEGFR2 activation mechanism. In addition, the studies on OxLDL and sLOX-1 have provided a new insight into lipid particle structure and mechanism of recognition. This chapter will provide an overview of our findings with respect to the current understanding within the field, future work to be done, and conclusions.

7.1. Overview of VEGFR studies

Despite the important role of VEGFRs in animal health and disease biology, we have limited information on the structure and mechanism of activation. Our study was aimed to resolve the mechanism of VEGFR2-VEGF-A activation using electron microscopy (EM) combined with biochemical and cellular approaches.

7.1.1. VEGFR2 forms homodimers and undergoes ligand-independent activation

A widely accepted mechanism for RTK activation is that cell surface VEGFR2 exists as monomers which dimerise upon VEGF-A leading to conformational changes in both extracellular and cytoplasmic domains; this further leads to tyrosine kinase activation and subsequent phosphorylation of specific tyrosine epitopes in the cytoplasmic domain (Fig. 6) (Shibuya, 2011b). However, recent studies using thermodynamics-based techniques has revealed that the VEGFR2 exists as both monomers and dimers, and VEGF-A is not absolutely required for activation (Brozzo et al., 2012, King and Hristova, 2019). The studies presented here support this idea that VEGFR2 can be activated and tyrosine phosphorylated in the absence of VEGF-A ligand. This was demonstrated using an *in vitro* assay using purified full-length VEGFR2 and titration of ATP. Interestingly, VEGFR2 undergoes constitutive phosphorylation at relatively low levels of ATP (sub-millimolar) which is at least 10-fold lower than predicted cytoplasmic 1-5 mM ATP concentrations. Cell-based studies also suggest basal tyrosine phosphorylation of recombinant VEGFR2 in the absence of exogenous VEGF-A ligand. One possibility is that such basal activation and tyrosine phosphorylation is caused by allosteric regulation with VEGFR2 moving between auto-inhibited and activated states depending on the local concentration of membrane receptor (King and Hristova, 2019).

By combining our EM, biochemical and cell biological data, we propose a mechanism for VEGFR2 activation (Fig. 7.1). VEGFR2 on the cell surface exist as both monomers and pre-assembled dimers. Approximately 10-50% of the cell surface VEGFR2 pool exists as a pre-assembled dimer which is actively phosphorylated in the absence of ligand. There are other studies that show phosphorylation of endothelial RTKs in the absence of ligand (Warren et al., 2014, Peach et al., 2018). that the pre-assembled homodimers must undergo a conformational switch to transition from a kinase inactive state to a kinase active state before specific tyrosine residues become phosphorylated in the active site. We can predict the likely existence of VEGFR2 in two types of pre-assembled homodimers: (1) homodimers exhibiting protein-protein contacts in both the extracellular and cytoplasmic domains, and (2) homodimers with free non-interacting extracellular domains but with protein-protein contacts in the cytoplasmic domains (Fig 7.1, blue boxes) (Sarabipour et al., 2016). However, the pre-assembled VEGFR2 homodimers and monomers are potentially in equilibrium, and ‘empty’ homodimers without ligand are highly unstable and relatively short-lived (Mac Gabhann and Popel, 2007).

The two forms of non-ligand ‘empty’ VEGFR2 homodimers are thus potential intermediates that exhibit basal kinase activity that may impact on downstream signal transduction and cellular responses (Sase et al., 2009b). The VEGFR2 monomer:homodimer ratio also is likely to also be influenced by the absolute levels of VEGFR2 present within the cell. In the case of tetracycline-inducible VEGFR2 expression, cell surface VEGFR2 levels could thus be relatively high, with an increase in the cell surface pool of ‘empty’ VEGFR2 homodimers. Furthermore, one likelihood is that the role of VEGF-A ligand is to induce VEGFR2 monomer dimerisation (Fig. 7.1 orange box), and stabilise pre-existing VEGFR2

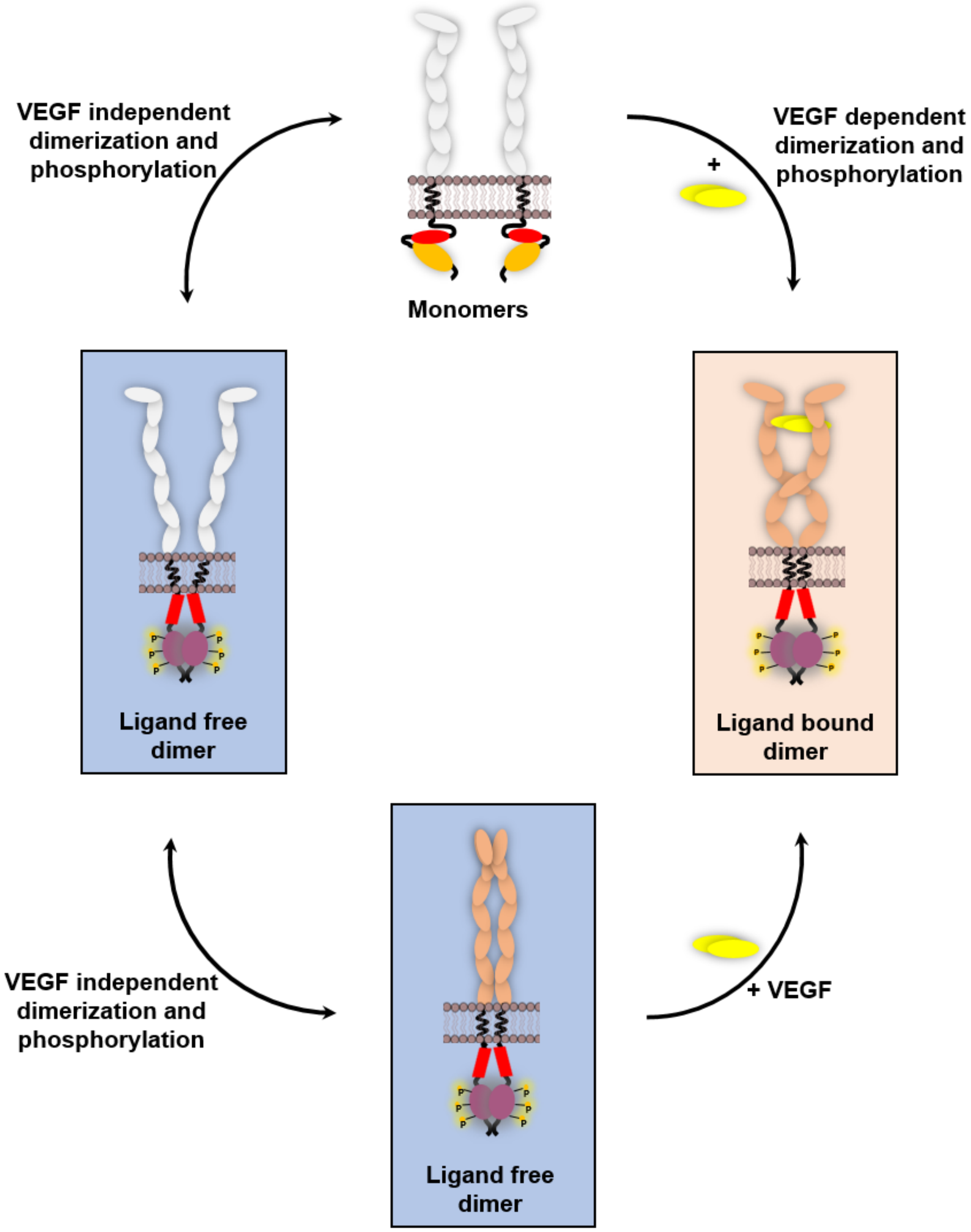

Figure 7.1. Proposed mechanism of VEGFR2-VEGF-A activation. The VEGFRs on the plasma membrane exist mostly as monomers and preassembled ligand-free dimers. This is via contacts in the extracellular domain and cytoplasmic domains (blue boxes). The VEGFR2 ligand-free dimers constitute ~10-50% of the pool and transautophosphorylate each other but are highly unstable and short-lived. Addition of VEGF-A ligand causes dimerisation of the extracellular domain, tyrosine phosphorylation in the cytoplasmic domain and VEGFR2 complex stabilisation (orange box).

homodimers. It was previously thought that the only major role of VEGF-A is to dimerise two VEGFR2 monomers to promote kinase activation; however, VEGF-A is likely to play more complex roles in homodimer stabilisation, conformational changes and protein-protein contacts within the VEGFR2 complex (Fig. 7.1).

7.1.2. Future work

There are still numerous questions to be addressed, similar studies are needed for VEGFR1 and VEGFR3 to understand their mechanistic insights. The proteolysis of VEGFR1 needs to be addressed before it can be purified for biochemical and structural studies (Farady and Craik, 2010, Zhang et al., 2001). Of note, it is of interest whether purified full-length VEGFR1 exhibits homodimer and heterodimer and formation with VEGFR2. Previous studies indicate that VEGFR1-VEGFR2 heterodimers exist and have functional signalling roles (Cudmore et al., 2012).

The major barrier for detailed structural studies on VEGFR2 was the lack of sufficient quantities of pure recombinant VEGFR2. Each purification prep required 10-20 grams of HEK293 cells, where the growth of these semi-adherent cells was highly time-consuming and a critical limiting factor. It would be beneficial to adapt the HEK293 cells into stirrer or suspension cultures to perform large scale VEGFR2 purifications to increase quantity and quality of purified protein (Portolano et al., 2014, Hunter et al., 2019).

7.1.2.1. Alternate detergents

It could be beneficial to explore more detergents for solubilization. There is a huge option of non-ionic detergents such as n-Decyl-β-D-Maltopyranoside (DM), n-Octyl-β-D-Glucopyranoside (OG) and n-Dodecyl-N,N-Dimethylamine-N-Oxide (LDAO) which are compatible with negative stain EM and cryo-EM studies. Alternatively, DDM and other non-ionic detergents can be used in combination with lipid analogues such as cholesteryl hemisuccinate (CHS). CHS is a cholesterol derivative that can be used to stabilise and incorporate membrane proteins into detergent micelles (Thompson et al., 2011).

7.1.2.2. VEGFR2 glycosylation

Further glycosylation studies could be performed on VEGFR2 to further characterise the N-glycosylation of the recombinant protein. Our recombinant purified VEGFR2 is heavily N-glycosylated but the functional role(s) of such modifications is poorly understood (Ferreira et al., 2018, Chandler et al., 2017). Therefore, we could further characterise the N-glycosylation sites on endothelial and HEK293-derived VEGFR2 using glycosidases and mass spectrometry. This would give us information about VEGFR2 N-glycan heterogeneity and possible effects on RTK activation and signalling (Chandler et al., 2017).

7.1.2.3. Tyrosine kinase inhibition using small molecules

We know that aberrant angiogenesis triggered by VEGFRs promotes various types of cancers (Cebe-Suarez et al., 2006). There are numerous small molecule VEGFR inhibitors in phase I, II and III clinical trials for treating cancer and other vascular disease states (Zirlik and Duyster, 2018, Qin et al., 2019). Our HEK293-VEGFR cell lines could be used for rapid screening of small molecule tyrosine kinase inhibitors. More importantly, the purified VEGFRs could be used for screening of ATP competitive inhibitors with ATP and rapidly map binding sites and inhibitory mechanisms of action.

7.1.2.4. Protein-protein interactions in the VEGFR2 homodimer

VEGFR2/VEGF-A binding to Ig-like domains 2 and 3, induces dimerization which further triggers homotypic contacts between Ig-like domains 4 and 7 (Hyde et al., 2012b). Our negative stain EM class averages have also shown contacts between regions of domains 2, 3, 4 and 7. We could further explore to understand the detailed role of each Ig-like domain in dimerisation and activation by site-directed mutagenesis of VEGFR2. We could study if the introduction of point mutations interferes with the VEGFR2/VEGF-A ligand-binding interface, thereby preventing dimerisation and kinase activation. We can also potentially explore the possibilities converting VEGF-A into an antagonist for VEGFR2 (Fuh et al., 1998).

Mutation of cytoplasmic tyrosine residues would provide insights into VEGFR2 signalling, trafficking and turnover. It is likely that different VEGFR2 phosphotyrosine residues are associated with different cellular responses to VEGF-A. Therefore, mutation of individual VEGFR2 tyrosine residues such as Y951, Y1175 and Y1214 to phenylalanine (F), could be performed within the HEK293 expression system to further understand the contribution of each residue to cellular responses.

7.2. Lipid particle and LOX-1 scavenger receptor study

The study presented here shows that the LOX-1 scavenger receptor specifically binds to OxLDL but not nLDL particles. We've also identified and showed a key structural difference between the nLDL and OxLDL. Therefore, based on our studies in Chapter 6 we propose a mechanism for OxLDL recognition by the LOX-1 scavenger receptor.

7.2.1. LOX-1 binding to OxLDL

The structure of native LDL, its binding mechanism to LDLR and physiology are well-studied (Jeon and Blacklow, 2005). Our 3-D structural model of OxLDL is the first work in this area. Based on our study we propose a mechanism for LOX-1 binding to OxLDL in the context of atherosclerotic plaque formation (Fig. 7.2). The nLDL particles carry cholesterol and lipids to tissues that require phospholipids and fuel for homeostasis and survival. The excess LDL in the bloodstream proceeds to the liver, binds to the LDLR on hepatocytes and gets internalised for recycling or metabolised and excreted (Wattis et al., 2008, Sirinian et al., 2005) (Fig 7.2, left blue panel). The ApoB-100 protein component (of nLDL) is recognised by LDLR, with two binding epitopes mapped on ApoB-100 (residues 3147-3157 and 3359-3367) which enable endocytosis (Sakamoto and Rosenberg, 2011). On the other hand, excess LDL in the bloodstream can be accumulated in arterial walls operating at high blood pressure where it undergoes oxidation by reactive oxygen species (ROS) generated by cells in the endothelium and vascular smooth muscle (Fig 7.2, orange panel step 1). This is well-studied and documented (Rafieian-Kopaei et al., 2014).

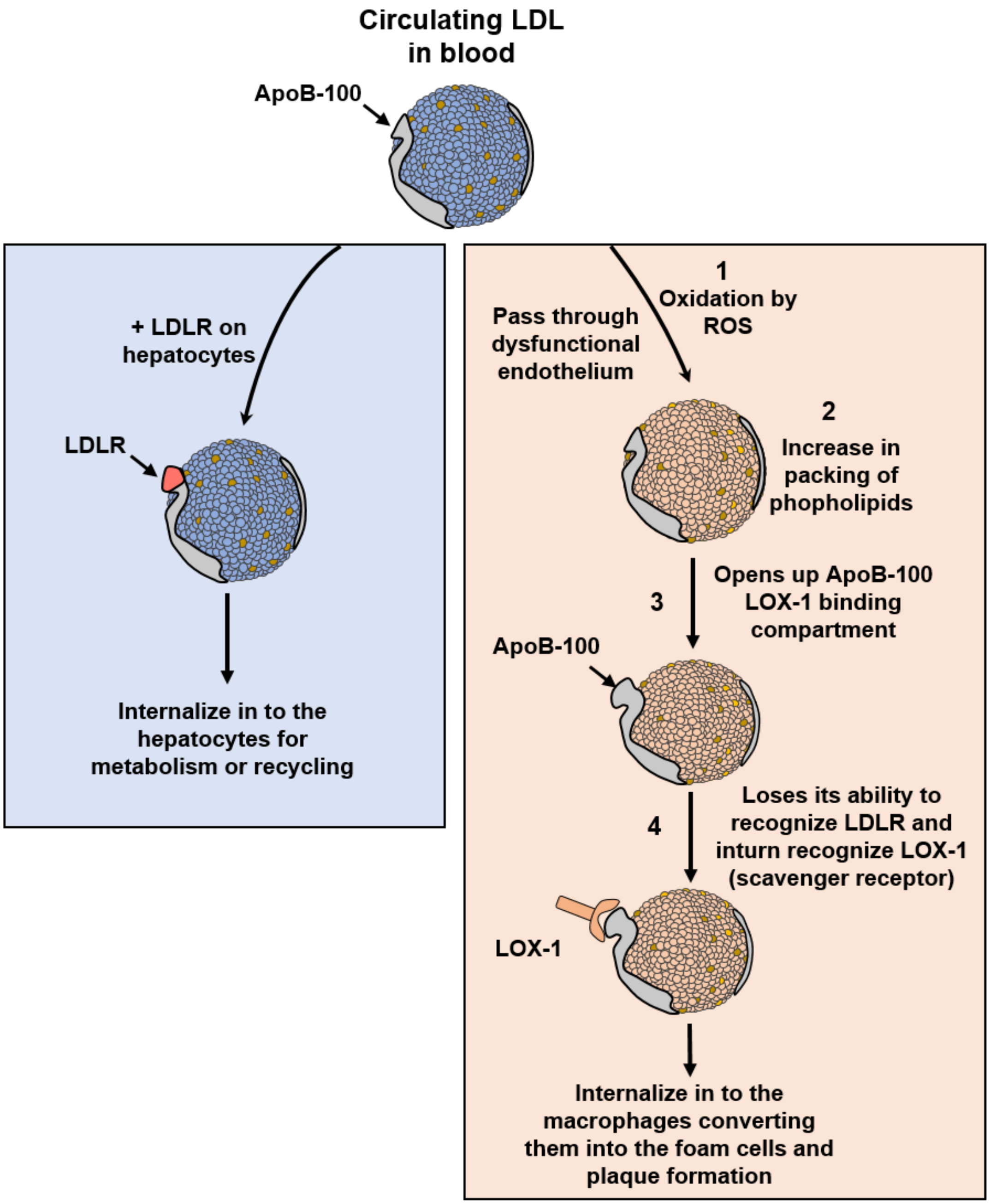

Figure 7.2. LDL fate and metabolism. Under normal physiological conditions, excess LDL proceeds to the liver and the LDLR receptor expressed on hepatocytes binds and helps internalisation and breakdown of LDL in lysosomes (blue panel). In atherosclerosis, excess circulating LDL enters into the subendothelial layer in arterial beds and becomes oxidised by ROS. LDL oxidation lead to tighter packing of phospholipids and unravels the inaccessible domains of ApoB-100 which are then recognised by LOX-1 scavenger receptor on macrophages (orange panel). This leads to OxLDL binding and uptake by macrophages and subsequent conversion into foam cells which eventually causes plaque formation and arterial disease.

The average dimensions of nLDL (~250 Å x ~240 Å x ~166 Å) (Ren et al., 2010c) compared to OxLDL (~228 Å x ~210.7 Å x ~157 Å) obtained from our study using 3-D reconstructions indicate an increase in particle density but decrease in lipoprotein size upon oxidation. Therefore, we propose that oxidation leads to more tighter lipid packing in OxLDL (Fig 7.2 orange panel steps 2 and 3). This could promote increased exposure of ApoB-100 on the OxLDL, thereby unravelling hitherto inaccessible or cryptic binding epitopes for LOX-1. We predict that the LOX-1 binding domain and LDLR binding domains on ApoB-100 are positioned closely in adjacent regions. The LOX-1 expressed on different vascular cells recognises and binds OxLDL via a newly accessible epitope on ApoB-100 due caused by conformational rearrangements caused by oxidation (Fig 7.2, orange panel step 4). Upon binding to LOX-1 on macrophages, the OxLDL particle undergoes endocytosis which leads to the development of the foam cell, which is a key event in atherosclerosis (Singh et al., 2002).

7.2.2. Future work

We predict that LOX-1 binds to the oxidised ApoB-100 protein component within OxLDL, similar to LDLR-mediated recognition of LDL. However, further biochemical and structural studies are needed to explore the role of carbohydrates and lipids in LOX-1-mediated recognition of OxLDL. Furthermore, using mass spectrometry and hydrogen-deuterium exchange (HDX) analysis could be used to map specific binding sites for LOX-1 on ApoB-100 and OxLDL.

7.2.2.1. Glycoproteomics study to map the LOX-1 binding sites

There are studies that show that oxidation of lipoproteins also effect the glycosylation profile of ApoB-100 (Meraji et al., 1992). It is likely that the ApoB-100 has N-linked and O-linked glycans which also contribute to LOX-1 recognition and binding. It is also essential to compare glycan contribution to ApoB-100-mediated binding to nLDL and OxLDL (Harazono et al., 2004, Clerc et al., 2016). This could be studied using specific proteases such as endoproteinase AspN, endoproteinase Glu-C, endoproteinase Lys-C and trypsin for digestion of OxLDL, followed by OxLDL-LOX-1 binding studies and re-purification (using SEC).

Trypsin digestion followed by LC-MS/MS combined with collision-induced dissociation (CID) could allow us to map protein and glycol-peptide identity (Harazono et al., 2004).

7.2.2.2. Other LOX-1-linked molecular determinants on OxLDL

We think that the nLDL is less compact (and larger) with a more relaxed lipid distribution, whereas OxLDL is more densely lipid packed. However, recent studies have shown that nLDL can be further categorized into multiple sub-classes based on lipid size and density distribution. These studies suggest that small and dense LDL particles get oxidized very quickly compared to less compact large buoyant LDL, additionally the small LDL also easily penetrates into the arterial wall to form deposits (Ivanova et al., 2017). Therefore, it is worth fractionating the native LDL based on size and density into different sub-classes and perform oxidation and binding studies with LOX-1. We know that not all LDL sub-classes undergo oxidation equally (Levitan et al., 2010, Pirillo et al., 2013a). Such work would potentially help us understand if all oxidised LDL sub-classes equally bind to LOX-1 irrespective of size or if there is any distinct category that specifically recognise and bind to LOX-1.

7.2.2.3. Structural approaches on LOX-1 binding to OxLDL

Cryo-EM has limitations in analysing heterogeneous lipid particles and it is not possible to achieve high resolution models (Lyumkis, 2019). Therefore, to better understand the 3-D model of OxLDL that has been generated in this work, cryo-electron tomography could be used. The density map of each lipoprotein particle can be constructed by an individual-particle electron tomography (IPET) reconstruction method (Yu et al., 2016, Meister and Blume, 2017). The 3-D reconstruction can also be used to examine OxLDL and LOX-1 interactions at different temperatures, which impact on lipid phase transition and lipid packing (Prassl, 2011).

7.3. Concluding remarks

In conclusion, this study has provided insights into creating stable mammalian expression cell lines for VEGFRs, their purification and structural analysis of VEGFR2 using negative stain EM. The VEGFR2 expression model will now provide a framework for numerous future studies. Our study was the first to investigate the structure of full-length recombinant VEGFR2 using negative stain-EM. Even though we could not resolve a complete structural model of full-length VEGFR2, our study has provided insights into the VEGFR2-VEGF-A mechanism on the cell membrane. Furthermore, this work has also shown differential activation of VEGFR2 receptor, its modulation in different states on the cell membrane against the widely accepted “one structure model”. Finally, we believe that to target and inhibit the VEGFR2 receptor, especially to hinder the signaling outcomes regulated by preassembled non-ligand bound dimers, targeting the VEGFR2 kinase domain using small molecule inhibitors approach would produce more positive therapeutic outcomes compared to inhibition in extracellular domain by protein based-therapies.

Furthermore, studies on LOX-1 and OxLDL over 20 years have yielded little insight into the exact mechanism of recognition. However, our studies in this thesis has now provided, for the first time, a 3-D model of the OxLDL particle. This work has also provided new insights into LOX-1 scavenger receptor-mediated recognition of OxLDL. Finally, understanding the interactions of LOX-1 and OxLDL at a molecular level by identifying the binding epitopes on both ApoB-100 and LOX-1 which potentially interact with each other would help us pave the way for new drugs and therapies for the treatment of atherosclerosis.

REFERENCES

ABDUL ZANI, I., STEPHEN, S. L., MUGHAL, N. A., RUSSELL, D., HOMER-VANNIASINKAM, S., WHEATCROFT, S. B. & PONNAMBALAM, S. 2015. Scavenger Receptor Structure and Function in Health and Disease. *Cells,* 4, 178-201.

ABHINAND, C. S., RAJU, R., SOUMYA, S. J., ARYA, P. S. & SUDHAKARAN, P. R. 2016. VEGF-A/VEGFR2 signaling network in endothelial cells relevant to angiogenesis. *Journal of cell communication and signaling,* 10, 347-354.

ABRAHAM, D., HOFBAUER, R., SCHAFER, R., BLUMER, R., PAULUS, P., MIKSOVSKY, A., TRAXLER, H., KOCHER, A. & AHARINEJAD, S. 2000. Selective downregulation of VEGF-A(165), VEGF-R(1), and decreased capillary density in patients with dilative but not ischemic cardiomyopathy. *Circ Res,* 87, 644-7.

AKHMEDOV, A., ROZENBERG, I., PANENI, F., CAMICI, G. G., SHI, Y., DOERRIES, C., SLEDZINSKA, A., MOCHARLA, P., BREITENSTEIN, A., LOHMANN, C., STEIN, S., VON LUKOWICZ, T., KURRER, M. O., BOREN, J., BECHER, B., TANNER, F. C., LANDMESSER, U., MATTER, C. M. & LUSCHER, T. F. 2014. Endothelial overexpression of LOX-1 increases plaque formation and promotes atherosclerosis in vivo. *Eur Heart J,* 35, 2839-48.

AL-BANNA, N. & LEHMANN, C. 2013. Oxidized LDL and LOX-1 in experimental sepsis. *Mediators of Inflammation,* 2013, 761789-761789.

AL-HALAFI, A. M. 2014. Vascular endothelial growth factor trap-eye and trap technology: Aflibercept from bench to bedside. *Oman journal of ophthalmology,* 7, 112-115.

ALONSO-GORDOA, T., GARCÍA-BERMEJO, M. L., GRANDE, E., GARRIDO, P., CARRATO, A. & MOLINA-CERRILLO, J. 2019. Targeting Tyrosine kinases in Renal Cell Carcinoma: "New Bullets against Old Guys". *International journal of molecular sciences,* 20, 1901.

ANDRÉLL, J. & TATE, C. G. 2013. Overexpression of membrane proteins in mammalian cells for structural studies. *Molecular membrane biology,* 30, 52-63.

ARIÖZ, C. 2014. *Exploring the Interplay of Lipids and Membrane Proteins.*

ARNDT, C., KORISTKA, S., BARTSCH, H. & BACHMANN, M. 2012. Native polyacrylamide gels. *Methods Mol Biol,* 869, 49-53.

AROSIO, P., MÜLLER, T., RAJAH, L., YATES, E. V., APRILE, F. A., ZHANG, Y., COHEN, S. I. A., WHITE, D. A., HERLING, T. W., DE GENST, E. J., LINSE, S., VENDRUSCOLO, M., DOBSON, C. M. & KNOWLES, T. P. J. 2016. Microfluidic Diffusion Analysis of the Sizes and Interactions of Proteins under Native Solution Conditions. *ACS Nano,* 10, 333-341.

ARRIETA, O., ZATARAIN-BARRON, Z. L., CARDONA, A. F., CARMONA, A. & LOPEZ-MEJIA, M. 2017. Ramucirumab in the treatment of non-small cell lung cancer. *Expert Opin Drug Saf,* 16, 637-644.

AUTIERO, M., LUTTUN, A., TJWA, M. & CARMELIET, P. 2003. Placental growth factor and its receptor, vascular endothelial growth factor receptor-1: novel targets for stimulation of ischemic tissue revascularization and inhibition of angiogenic and inflammatory disorders. *J Thromb Haemost,* 1, 1356-70.

BAKHEET, T. M. & DOIG, A. J. 2009. Properties and identification of human protein drug targets. *Bioinformatics,* 25, 451-457.

BALDWIN, M. A. 2004. Protein Identification by Mass Spectrometry. *Issues to be Considered,* 3, 1-9.

BALDWIN, M. E., HALFORD, M. M., ROUFAIL, S., WILLIAMS, R. A., HIBBS, M. L., GRAIL, D., KUBO, H., STACKER, S. A. & ACHEN, M. G. 2005. Vascular endothelial growth factor D is dispensable for development of the lymphatic system. *Mol Cell Biol,* 25, 2441-9.

BALDWIN, M. E., LIANG, X. H., RUCHATZ, A., BUSCH, J., GU, Z., ROOSE-GIRMA, M., OLSSON, C., ERICKSON, S., FERRARA, N. & GERBER, H.-P. 2004. Generation of mice carrying floxed VEGFR-1 and VEGFR-2 alleles to study the effects of postnatal gene ablation on angiogenesis and hematopoiesis. *Cancer Res,* 64, 596-596.

BANAI, S., SHWEIKI, D., PINSON, A., CHANDRA, M., LAZAROVICI, G. & KESHET, E. 1994. Upregulation of vascular endothelial growth factor expression induced by myocardial ischaemia: implications for coronary angiogenesis. *Cardiovasc Res,* 28, 1176-9.

BARLEON, B., SOZZANI, S., ZHOU, D., WEICH, H. A., MANTOVANI, A. & MARME, D. 1996. Migration of human monocytes in response to vascular endothelial growth factor (VEGF) is mediated via the VEGF receptor flt-1. *Blood,* 87, 3336-43.

BARON, U. & BUJARD, H. 2000. Tet repressor-based system for regulated gene expression in eukaryotic cells: Principles and advances. *In:* THORNER, J., EMR, S. D. & ABELSON, J. N. (eds.) *Methods Enzymol.* Academic Press.

BASAGIANNIS, D., ZOGRAFOU, S., MURPHY, C., FOTSIS, T., MORBIDELLI, L., ZICHE, M., BLECK, C., MERCER, J. & CHRISTOFORIDIS, S. 2016.

VEGF induces signalling and angiogenesis by directing VEGFR2 internalisation through macropinocytosis. *Journal of Cell Science,* 129, 4091-4104.

BERGHEANU, S. C., BODDE, M. C. & JUKEMA, J. W. 2017. Pathophysiology and treatment of atherosclerosis : Current view and future perspective on lipoprotein modification treatment. *Netherlands heart journal : monthly journal of the Netherlands Society of Cardiology and the Netherlands Heart Foundation,* 25, 231-242.

BERLEC, A. & STRUKELJ, B. 2013. Current state and recent advances in biopharmaceutical production in Escherichia coli, yeasts and mammalian cells. *J Ind Microbiol Biotechnol,* 40, 257-74.

BHATTACHARYA, R., FAN, F., WANG, R., YE, X., XIA, L., BOULBES, D. & ELLIS, L. M. 2017. Intracrine VEGF signalling mediates colorectal cancer cell migration and invasion. *Br J Cancer,* 117, 848-855.

BIONDI, R., XIA, Y., ROSSI, R., PAOLOCCI, N., AMBROSIO, G. & ZWEIER, J. L. 2001. Detection of hydroxyl radicals by D-phenylalanine hydroxylation: a specific assay for hydroxyl radical generation in biological systems. *Anal Biochem,* 290**,** 138-45.

BLANES, M. G., OUBAHA, M., RAUTUREAU, Y. & GRATTON, J. P. 2007. Phosphorylation of tyrosine 801 of vascular endothelial growth factor receptor-2 is necessary for Akt-dependent endothelial nitric-oxide synthase activation and nitric oxide release from endothelial cells. *J Biol Chem,* 282, 10660-9.

BOOCOCK, C. A. 1990. Double indirect-immunofluorescent labeling of cultured cells. *Methods Mol Biol,* 5, 473-85.

BOOTH, D. S., AVILA-SAKAR, A. & CHENG, Y. 2011a. Visualizing proteins and macromolecular complexes by negative stain EM: from grid preparation to image acquisition. *Journal of visualized experiments : JoVE*, 3227.

BOOTH, D. S., AVILA-SAKAR, A. & CHENG, Y. 2011b. Visualizing proteins and macromolecular complexes by negative stain EM: from grid preparation to image acquisition. *J Vis Exp*.

BOULLIER, A., LI, Y., QUEHENBERGER, O., PALINSKI, W., TABAS, I., WITZTUM, J. L. & MILLER, Y. I. 2006. Minimally oxidized LDL offsets the apoptotic effects of extensively oxidized LDL and free cholesterol in macrophages. *Arterioscler Thromb Vasc Biol,* 26, 1169-76.

BROZZO, M. S., BJELIC, S., KISKO, K., SCHLEIER, T., LEPPANEN, V. M., ALITALO, K., WINKLER, F. K. & BALLMER-HOFER, K. 2012.

Thermodynamic and structural description of allosterically regulated VEGFR-2 dimerization. *Blood,* 119, 1781-8.

BURGESS, R. R. 2018. A brief practical review of size exclusion chromatography: Rules of thumb, limitations, and troubleshooting. *Protein Expression and Purification,* 150**,** 81-85.

BÜSSOW, K. 2015. Stable mammalian producer cell lines for structural biology. *Current Opinion in Structural Biology,* 32, 81-90.

CABANILLAS, M. E. & HABRA, M. A. 2016. Lenvatinib: Role in thyroid cancer and other solid tumors. *Cancer Treat Rev,* 42, 47-55.

CAMPOS, H., BLIJLEVENS, E., MCNAMARA, J. R., ORDOVAS, J. M., POSNER, B. M., WILSON, P. W., CASTELLI, W. P. & SCHAEFER, E. J. 1992. LDL particle size distribution. Results from the Framingham Offspring Study. *Arteriosclerosis and Thrombosis: A Journal of Vascular Biology,* 12, 1410-1419.

CARMELIET, P. & DE ALMODOVAR, C. R. 2013. VEGF ligands and receptors: implications in neurodevelopment and neurodegeneration. *Cellular and Molecular Life Sciences,* 70, 1763-1778.

CARMELIET, P., FERREIRA, V., BREIER, G., POLLEFEYT, S., KIECKENS, L., GERTSENSTEIN, M., FAHRIG, M., VANDENHOECK, A., HARPAL, K., EBERHARDT, C., DECLERCQ, C., PAWLING, J., MOONS, L., COLLEN, D., RISAU, W. & NAGY, A. 1996. Abnormal blood vessel development and lethality in embryos lacking a single VEGF allele. *Nature,* 380, 435-9.

CARMELIET, P., MOONS, L., LUTTUN, A., VINCENTI, V., COMPERNOLLE, V., DE MOL, M., WU, Y., BONO, F., DEVY, L., BECK, H., SCHOLZ, D., ACKER, T., DIPALMA, T., DEWERCHIN, M., NOEL, A., STALMANS, I., BARRA, A., BLACHER, S., VANDENDRIESSCHE, T., PONTEN, A., ERIKSSON, U., PLATE, K. H., FOIDART, J. M., SCHAPER, W., CHARNOCK-JONES, D. S., HICKLIN, D. J., HERBERT, J. M., COLLEN, D. & PERSICO, M. G. 2001. Synergism between vascular endothelial growth factor and placental growth factor contributes to angiogenesis and plasma extravasation in pathological conditions. *Nat Med,* 7, 575-83.

CARRONI, M. & SAIBIL, H. R. 2016. Cryo electron microscopy to determine the structure of macromolecular complexes. *Methods,* 95, 78-85.

CAVALLI, A., SALVATELLA, X., DOBSON, C. M. & VENDRUSCOLO, M. 2007. Protein structure determination from NMR chemical shifts. *Proceedings of the National Academy of Sciences,* 104, 9615-9620.

CEBE-SUAREZ, S., GRUNEWALD, F. S., JAUSSI, R., LI, X., CLAESSON-WELSH, L., SPILLMANN, D., MERCER, A. A., PROTA, A. E. & BALLMER-

HOFER, K. 2008. Orf virus VEGF-E NZ2 promotes paracellular NRP-1/VEGFR-2 coreceptor assembly via the peptide RPPR. *FASEB J,* 22, 3078-86.

CEBE-SUAREZ, S., ZEHNDER-FJALLMAN, A. & BALLMER-HOFER, K. 2006. The role of VEGF receptors in angiogenesis; complex partnerships. *Cell Mol Life Sci,* 63, 601-15.

CHAKRABARTI, S., BARROW, C. J., KANWAR, R. K., RAMANA, V. & KANWAR, J. R. 2016. Studies to Prevent Degradation of Recombinant Fc-Fusion Protein Expressed in Mammalian Cell Line and Protein Characterization. *Int J Mol Sci,* 17.

CHANDLER, K. B., KHATRI, K., LEON, D. R., MEYER, R. D., RAHIMI, N. & COSTELLO, C. E. 2016. Analysis of Vascular Endothelial Growth Factor Receptor 2 (VEGFR-2) Glycosylation and its Role in Angiogenesis. *The FASEB Journal,* 30, 844.2-844.2.

CHANDLER, K. B., LEON, D. R., MEYER, R. D., RAHIMI, N. & COSTELLO, C. E. 2017. Site-Specific N-Glycosylation of Endothelial Cell Receptor Tyrosine Kinase VEGFR-2. *Journal of proteome research,* 16, 677-688.

CHAPMAN, M. J., GOLDSTEIN, S., LAGRANGE, D. & LAPLAUD, P. M. 1981. A density gradient ultracentrifugal procedure for the isolation of the major lipoprotein classes from human serum. *J Lipid Res,* 22, 339-58.

CHATURVEDI, S. K., MA, J., BROWN, P. H., ZHAO, H. & SCHUCK, P. 2018. Measuring macromolecular size distributions and interactions at high concentrations by sedimentation velocity. *Nature Communications,* 9**,** 4415.

CHEN, C. & KHISMATULLIN, D. B. 2015. Oxidized Low-Density Lipoprotein Contributes to Atherogenesis via Co-activation of Macrophages and Mast Cells. *PLOS ONE,* 10, e0123088.

CHEN, M., MASAKI, T. & SAWAMURA, T. 2002. LOX-1, the receptor for oxidized low-density lipoprotein identified from endothelial cells: implications in endothelial dysfunction and atherosclerosis. *Pharmacol Ther,* 95, 89-100.

CHEN, X., ZARO, J. L. & SHEN, W. C. 2013. Fusion protein linkers: property, design and functionality. *Adv Drug Deliv Rev,* 65, 1357-69.

CHENG, Y. 2015. Single-Particle Cryo-EM at Crystallographic Resolution. *Cell,* 161, 450-7.

CHENG, Y., GRIGORIEFF, N., PENCZEK, P. A. & WALZ, T. 2015. A primer to single-particle cryo-electron microscopy. *Cell,* 161, 438-49.

CHEVALLET, M., LUCHE, S. & RABILLOUD, T. 2006. Silver staining of proteins in polyacrylamide gels. *Nature protocols,* 1, 1852-1858.

CHISOLM, G. M. & STEINBERG, D. 2000. The oxidative modification hypothesis of atherogenesis: an overview. *Free Radic Biol Med,* 28, 1815-26.

CHIU, M. L. 2012. Introduction to membrane proteins. *Curr Protoc Protein Sci,* 29.

CHO, S.-J., PARK, M. H., HAN, C., YOON, K. & KOH, Y. H. 2017. VEGFR2 alteration in Alzheimer's disease. *Scientific Reports,* 7, 17713.

CHOI, K. J., SHIN, J. I. & LEE, S. H. 2018. Workflow of Cryo-Electron Microscopy and Status of Domestic Infrastructure. *Applied Microscopy,* 48, 6-10.

CHOUEIRI, T. K. & MOTZER, R. J. 2017. Systemic Therapy for Metastatic Renal-Cell Carcinoma. *N Engl J Med,* 376, 354-366.

CHRISTINGER, H. W., FUH, G., DE VOS, A. M. & WIESMANN, C. 2004. The crystal structure of placental growth factor in complex with domain 2 of vascular endothelial growth factor receptor-1. *J Biol Chem,* 279, 10382-8.

CHUNG, B. H., WILKINSON, T., GEER, J. C. & SEGREST, J. P. 1980. Preparative and quantitative isolation of plasma lipoproteins: rapid, single discontinuous density gradient ultracentrifugation in a vertical rotor. *J Lipid Res,* 21, 284-91.

CLEGG, L. W. & MAC GABHANN, F. 2015. Site-Specific Phosphorylation of VEGFR2 Is Mediated by Receptor Trafficking: Insights from a Computational Model. *PLoS computational biology,* 11, e1004158-e1004158.

CLERC, F., REIDING, K. R., JANSEN, B. C., KAMMEIJER, G. S. M., BONDT, A. & WUHRER, M. 2016. Human plasma protein N-glycosylation. *Glycoconj J,* 33, 309-343.

COLE, J. L., LARY, J. W., P MOODY, T. & LAUE, T. M. 2008. Analytical ultracentrifugation: sedimentation velocity and sedimentation equilibrium. *Methods in cell biology,* 84**,** 143-179.

COLUMBUS, L., LIPFERT, J., JAMBUNATHAN, K., FOX, D. A., SIM, A. Y., DONIACH, S. & LESLEY, S. A. 2009. Mixing and matching detergents for membrane protein NMR structure determination. *J Am Chem Soc,* 131, 7320-6.

CORRADO, A., FERRARI, S. M., POLITTI, U., MAZZI, V., MICCOLI, M., MATERAZZI, G., ANTONELLI, A., ULISSE, S., FALLAHI, P. & MICCOLI,

P. 2017. Aggressive thyroid cancer: targeted therapy with sorafenib. *Minerva Endocrinol,* 42, 64-76.

COSTACHE, M. I., IOANA, M., IORDACHE, S., ENE, D., COSTACHE, C. A. & SAFTOIU, A. 2015. VEGF Expression in Pancreatic Cancer and Other Malignancies: A Review of the Literature. *Rom J Intern Med,* 53, 199-208.

COWLEY, J. M. & BRIDGES, R. E. 1979. Phase and amplitude contrast in electron microscopy of stained biological objects. *Ultramicroscopy,* 4**,** 419-27.

CROSS, M. J., DIXELIUS, J., MATSUMOTO, T. & CLAESSON-WELSH, L. 2003. VEGF-receptor signal transduction. *Trends Biochem Sci,* 28, 488-94.

CUDMORE, M. J., HEWETT, P. W., AHMAD, S., WANG, K. Q., CAI, M., AL-ANI, B., FUJISAWA, T., MA, B., SISSAOUI, S., RAMMA, W., MILLER, M. R., NEWBY, D. E., GU, Y., BARLEON, B., WEICH, H. & AHMED, A. 2012. The role of heterodimerization between VEGFR-1 and VEGFR-2 in the regulation of endothelial cell homeostasis. *Nat Commun,* 3.

CUENDA, A., ROUSE, J., DOZA, Y. N., MEIER, R., COHEN, P., GALLAGHER, T. F., YOUNG, P. R. & LEE, J. C. 1995. SB 203580 is a specific inhibitor of a MAP kinase homologue which is stimulated by cellular stresses and interleukin-1. *FEBS Lett,* 364, 229-33.

DAS, A. T., TENENBAUM, L. & BERKHOUT, B. 2016. Tet-On Systems For Doxycycline-inducible Gene Expression. *Current gene therapy,* 16, 156-167.

DAYANIR, V., MEYER, R. D., LASHKARI, K. & RAHIMI, N. 2001. Identification of tyrosine residues in vascular endothelial growth factor receptor-2/FLK-1 involved in activation of phosphatidylinositol 3-kinase and cell proliferation. *J Biol Chem,* 276, 17686-92.

DE CARLO, S. & HARRIS, J. R. 2011. Negative staining and cryo-negative staining of macromolecules and viruses for TEM. *Micron (Oxford, England : 1993),* 42**,** 117-131.

DE VRIES, C., ESCOBEDO, J. A., UENO, H., HOUCK, K., FERRARA, N. & WILLIAMS, L. T. 1992. The fms-like tyrosine kinase, a receptor for vascular endothelial growth factor. *Science,* 255, 989.

DE ZORZI, R., MI, W., LIAO, M. & WALZ, T. 2015. Single-particle electron microscopy in the study of membrane protein structure. *Microscopy,* 65, 81-96.

DEBELJAK, N., FELDMAN, L., DAVIS, K. L., KOMEL, R. & SYTKOWSKI, A. J. 2006. Variability in the immunodetection of His-tagged recombinant proteins. *Analytical biochemistry,* 359, 216-223.

DI RUSSO, N. V., ESTRIN, D. A., MARTÍ, M. A. & ROITBERG, A. E. 2012. pH-Dependent conformational changes in proteins and their effect on experimental pK(a)s: the case of Nitrophorin 4. *PLoS computational biology,* 8, e1002761-e1002761.

DIFFENDERFER, M. R. & SCHAEFER, E. J. 2014. The composition and metabolism of large and small LDL. *Current Opinion in Lipidology,* 25, 221-226.

DIONNE, U., CHARTIER, F. J. M., LÓPEZ DE LOS SANTOS, Y., LAVOIE, N., BERNARD, D. N., BANERJEE, S. L., OTIS, F., JACQUET, K., TREMBLAY, M. G., JAIN, M., BOURASSA, S., GISH, G. D., GAGNÉ, J.-P., POIRIER, G. G., LAPRISE, P., VOYER, N., LANDRY, C. R., DOUCET, N. & BISSON, N. 2018. Direct Phosphorylation of SRC Homology 3 Domains by Tyrosine Kinase Receptors Disassembles Ligand-Induced Signaling Networks. *Molecular Cell,* 70, 995-1007.e11.

DRAUDE, G., HRBOTICKY, N. & LORENZ, R. L. 1999. The expression of the lectin-like oxidized low-density lipoprotein receptor (LOX-1) on human vascular smooth muscle cells and monocytes and its down-regulation by lovastatin. *Biochem Pharmacol,* 57, 383-6.

DUMONT, D. J., JUSSILA, L., TAIPALE, J., LYMBOUSSAKI, A., MUSTONEN, T., PAJUSOLA, K., BREITMAN, M. & ALITALO, K. 1998. Cardiovascular failure in mouse embryos deficient in VEGF receptor-3. *Science,* 282, 946-9.

EBOS, J. M. L., BOCCI, G., MAN, S., THORPE, P. E., HICKLIN, D. J., ZHOU, D., JIA, X. & KERBEL, R. S. 2004. A Naturally Occurring Soluble Form of Vascular Endothelial Growth Factor Receptor 2 Detected in Mouse and Human Plasma (J.M.L. Ebos); Sunnybrook Trust for Medical Research (G. Bocci); and NIH grant CA41223, Canadian Institutes for Health Research, and National Cancer Institute of Canada (R.S. Kerbel). *Molecular Cancer Research,* 2, 315-326.

EINHAUER, A. & JUNGBAUER, A. 2001. The FLAG peptide, a versatile fusion tag for the purification of recombinant proteins. *J Biochem Biophys Methods,* 49**,** 455-65.

EMAMI-NAEINI, P., DOHLMAN, T. H., OMOTO, M., HATTORI, T., CHEN, Y., LEE, H. S., CHAUHAN, S. K. & DANA, R. 2014. Soluble vascular endothelial growth factor receptor-3 suppresses allosensitization and promotes corneal allograft survival. *Graefe's archive for clinical and* *experimental ophthalmology = Albrecht von Graefes Archiv fur klinische und experimentelle Ophthalmologie,* 252, 1755-1762.

ENGELKING, L. R. 2015. Chapter 64 - Chylomicrons. *In:* ENGELKING, L. R. (ed.) *Textbook of Veterinary Physiological Chemistry (Third Edition).* Boston: Academic Press.

ENGELKE, J., BRANDT, J., BARNER-KOWOLLIK, C. & LEDERER, A. 2019. Strengths and limitations of size exclusion chromatography for investigating single chain folding – current status and future perspectives. *Polymer Chemistry,* 10**,** 3410-3425.

ESTERBAUER, H., WAEG, G., PUHL, H., DIEBER-ROTHENEDER, M. & TATZBER, F. 1992. Inhibition of LDL oxidation by antioxidants. *In:* EMERIT, I. & CHANCE, B. (eds.) *Free Radicals and Aging.* Basel: Birkhäuser Basel.

FARADY, C. J. & CRAIK, C. S. 2010. Mechanisms of macromolecular protease inhibitors. *Chembiochem : a European journal of chemical biology,* 11, 2341-2346.

FATHI-ROUDSARI, M., AKHAVIAN-TEHRANI, A. & MAGHSOUDI, N. 2016. Comparison of Three Escherichia coli Strains in Recombinant Production of Reteplase. *Avicenna journal of medical biotechnology,* 8, 16-22.

FEARNLEY, G. W., ODELL, A. F., LATHAM, A. M., MUGHAL, N. A., BRUNS, A. F., BURGOYNE, N. J., HOMER-VANNIASINKAM, S., ZACHARY, I. C., HOLLSTEIN, M. C., WHEATCROFT, S. B. & PONNAMBALAM, S. 2014. VEGF-A isoforms differentially regulate ATF-2-dependent VCAM-1 gene expression and endothelial-leukocyte interactions. *Molecular biology of the cell,* 25, 2509-2521.

FEARNLEY, G. W., SMITH, G. A., ABDUL-ZANI, I., YULDASHEVA, N., MUGHAL, N. A., HOMER-VANNIASINKAM, S., KEARNEY, M. T., ZACHARY, I. C., TOMLINSON, D. C., HARRISON, M. A., WHEATCROFT, S. B. & PONNAMBALAM, S. 2016. VEGF-A isoforms program differential VEGFR2 signal transduction, trafficking and proteolysis. *Biology Open,* 5, 571-583.

FEARNLEY, G. W., WHEATCROFT, S. B. & PONNAMBALAM, S. 2015. Detection and Quantification of Vascular Endothelial Growth Factor Receptor Tyrosine Kinases in Primary Human Endothelial Cells. *Methods Mol Biol*, 2917-7_4.

FEINGOLD, K. R. & GRUNFELD, C. *Introduction to Lipids and Lipoproteins*.

FELMEDEN, D. C., BLANN, A. D. & LIP, G. Y. H. 2003. Angiogenesis: basic pathophysiology and implications for disease. *European Heart Journal,* 24, 586-603.

FERNANDEZ-LEIRO, R. & SCHERES, S. H. W. 2017. A pipeline approach to single-particle processing in RELION. *Acta crystallographica. Section D, Structural biology,* 73, 496-502.

FERRARA, N., DAMICO, L., SHAMS, N., LOWMAN, H. & KIM, R. 2006. Development of ranibizumab, an anti-vascular endothelial growth factor antigen binding fragment, as therapy for neovascular age-related macular degeneration. *Retina,* 26, 859-70.

FERRARA, N., GERBER, H. P. & LECOUTER, J. 2003. The biology of VEGF and its receptors. *Nat Med,* 9, 669-76.

FERREIRA, I. G., PUCCI, M., VENTURI, G., MALAGOLINI, N., CHIRICOLO, M. & DALL'OLIO, F. 2018. Glycosylation as a Main Regulator of Growth and Death Factor Receptors Signaling. *Int J Mol Sci,* 19.

FINK, D. M., STEELE, M. M. & HOLLINGSWORTH, M. A. 2016. The lymphatic system and pancreatic cancer. *Cancer letters,* 381, 217-236.

FISHER, W. R., HAMMOND, M. G., MENGEL, M. C. & WARMKE, G. L. 1975a. A genetic determinant of the phenotypic variance of the molecular weight of low density lipoprotein. *Proc Natl Acad Sci U S A,* 72, 2347-51.

FISHER, W. R., HAMMOND, M. G., MENGEL, M. C. & WARMKE, G. L. 1975b. A genetic determinant of the phenotypic variance of the molecular weight of low density lipoprotein. *Proceedings of the National Academy of Sciences of the United States of America,* 72, 2347-2351.

FOLKMAN, J. 2008. History of Angiogenesis. *In:* FIGG, W. D. & FOLKMAN, J. (eds.) *Angiogenesis: An Integrative Approach From Science to Medicine.* Boston, MA: Springer US.

FONG, G. H., ROSSANT, J., GERTSENSTEIN, M. & BREITMAN, M. L. 1995. Role of the Flt-1 receptor tyrosine kinase in regulating the assembly of vascular endothelium. *Nature,* 376, 66-70.

FORDE, P. M. & ETTINGER, D. S. 2013. Targeted therapy for non-small-cell lung cancer: past, present and future. *Expert Rev Anticancer Ther,* 13, 745-58.

FRANCONE, O. L., TU, M., ROYER, L. J., ZHU, J., STEVENS, K., OLEYNEK, J. J., LIN, Z., SHELLEY, L., SAND, T., LUO, Y. & KANE, C. D. 2009. The hydrophobic tunnel present in LOX-1 is essential for oxidized LDL recognition and binding. *J Lipid Res,* 50, 546-55.

FREEDMAN, J. C. 2012. Chapter 3 - Cell Membranes. *In:* SPERELAKIS, N. (ed.) *Cell Physiology Source Book (Fourth Edition).* San Diego: Academic Press.

FREUND, K. B., MREJEN, S. & GALLEGO-PINAZO, R. 2013. An update on the pharmacotherapy of neovascular age-related macular degeneration. *Expert Opinion on Pharmacotherapy,* 14, 1017-1028.

FUCHS, C. S., TABERNERO, J., TOMÁŠEK, J., CHAU, I., MELICHAR, B., SAFRAN, H., TEHFE, M. A., FILIP, D., TOPUZOV, E., SCHLITTLER, L., UDREA, A. A., CAMPBELL, W., BRINCAT, S., EMIG, M., MELEMED, S. A., HOZAK, R. R., FERRY, D., CALDWELL, C. W. & AJANI, J. A. 2016. Biomarker analyses in REGARD gastric/GEJ carcinoma patients treated with VEGFR2-targeted antibody ramucirumab. *British journal of cancer,* 115, 974-982.

FUH, G., LI, B., CROWLEY, C., CUNNINGHAM, B. & WELLS, J. A. 1998. Requirements for binding and signaling of the kinase domain receptor for vascular endothelial growth factor. *J Biol Chem,* 273, 11197-204.

FUKUCHI, M., WATANABE, J., KUMAGAI, K., BABA, S., SHINOZAKI, T., MIURA, M., KAGAYA, Y. & SHIRATO, K. 2002. Normal and Oxidized Low Density Lipoproteins Accumulate Deep in Physiologically Thickened Intima of Human Coronary Arteries. *Laboratory Investigation,* 82**,** 1437-1447.

FUNK, C. D. & CYRUS, T. 2001. 12/15-lipoxygenase, oxidative modification of LDL and atherogenesis. *Trends Cardiovasc Med,* 11**,** 116-24.

GALLAGHER, J. R., KIM, A. J., GULATI, N. M. & HARRIS, A. K. 2019. Negative-Stain Transmission Electron Microscopy of Molecular Complexes for Image Analysis by 2D Class Averaging. *Curr Protoc Microbiol,* 54, 90.

GANTZ, D. L., WALSH, M. T. & SMALL, D. M. 2000. Morphology of sodium deoxycholate-solubilized apolipoprotein B-100 using negative stain and vitreous ice electron microscopy. *Journal of Lipid Research,* 41, 1464-1472.

GARAVITO, R. M. & FERGUSON-MILLER, S. 2001. Detergents as tools in membrane biochemistry. *J Biol Chem,* 276, 32403-6.

GERACE, E. & MOAZED, D. 2015. Affinity Pull-Down of Proteins Using Anti-FLAG M2 Agarose Beads. *Methods Enzymol,* 559, 99-110.

GERBER, H. P., CONDORELLI, F., PARK, J. & FERRARA, N. 1997. Differential transcriptional regulation of the two vascular endothelial growth factor receptor genes. Flt-1, but not Flk-1/KDR, is up-regulated by hypoxia. *J Biol Chem,* 272, 23659-67.

GERMAN, J. B., SMILOWITZ, J. T. & ZIVKOVIC, A. M. 2006. Lipoproteins: When size really matters. *Current opinion in colloid & interface science,* 11, 171-183.

GHASEMI, N., RAZAVI, S. & NIKZAD, E. 2017. Multiple Sclerosis: Pathogenesis, Symptoms, Diagnoses and Cell-Based Therapy. *Cell journal,* 19, 1-10.

GILLE, H., KOWALSKI, J., YU, L., CHEN, H., PISABARRO, M. T., DAVIS-SMYTH, T. & FERRARA, N. 2000. A repressor sequence in the juxtamembrane domain of Flt-1 (VEGFR-1) constitutively inhibits vascular endothelial growth factor-dependent phosphatidylinositol 3'-kinase activation and endothelial cell migration. *EMBO J,* 19, 4064-4073.

GINSBERG, H. N. 1998. LIPOPROTEIN PHYSIOLOGY. *Endocrinology and Metabolism Clinics of North America,* 27, 503-519.

GIROLAMO, F., COPPOLA, C., RIBATTI, D. & TROJANO, M. 2014. Angiogenesis in multiple sclerosis and experimental autoimmune encephalomyelitis. *Acta neuropathologica communications,* 2, 84-84.

GLAESER, R. M. 2008. Retrospective: radiation damage and its associated "information limitations". *J Struct Biol,* 163, 271-6.

GLAESER, R. M. 2018. PROTEINS, INTERFACES, AND CRYO-EM GRIDS. *Current opinion in colloid & interface science,* 34, 1-8.

GLASS, C. K. & WITZTUM, J. L. 2001. Atherosclerosis: The Road Ahead. *Cell,* 104, 503-516.

GLEN, H. 2016. Lenvatinib therapy for the treatment of patients with advanced renal cell carcinoma. *Future Oncol,* 12, 2195-204.

GOLD, V. A. M., IEVA, R., WALTER, A., PFANNER, N., VAN DER LAAN, M. & KÜHLBRANDT, W. 2014. Visualizing active membrane protein complexes by electron cryotomography. *Nat Commun,* 5, 4129.

GOLDENBERG, M. M. 2012. Multiple sclerosis review. *P & T : a peer-reviewed journal for formulary management,* 37, 175-184.

GOLDSTEIN, J. L. & BROWN, M. S. 2009. History of Discovery: The LDL Receptor. *Arteriosclerosis, thrombosis, and vascular biology,* 29, 431-438.

GRAHAM, J. M., HIGGINS, J. A., GILLOTT, T., TAYLOR, T., WILKINSON, J., FORD, T. & BILLINGTON, D. 1996. A novel method for the rapid separation of plasma lipoproteins using self-generating gradients of iodixanol. *Atherosclerosis,* 124, 125-135.

GREIG, S. L. & KEATING, G. M. 2015. Ramucirumab: A Review in Advanced Gastric Cancer. *BioDrugs,* 29, 341-351.

GRIZEL, A. V., GLUKHOV, G. S. & SOKOLOVA, O. S. 2014. Mechanisms of activation of voltage-gated potassium channels. *Acta naturae,* 6, 10-26.

GRUNEWALD, F. S., PROTA, A. E., GIESE, A. & BALLMER-HOFER, K. 2010. Structure-function analysis of VEGF receptor activation and the role of coreceptors in angiogenic signaling. *Biochim Biophys Acta,* 1804, 567-80.

GÜLER-GANE, G., KIDD, S., SRIDHARAN, S., VAUGHAN, T. J., WILKINSON, T. C. I. & TIGUE, N. J. 2016. Overcoming the Refractory Expression of Secreted Recombinant Proteins in Mammalian Cells through Modification of the Signal Peptide and Adjacent Amino Acids. *PLoS One,* 11, e0155340.

HADI, H. A. R., CARR, C. S. & AL SUWAIDI, J. 2005. Endothelial dysfunction: cardiovascular risk factors, therapy, and outcome. *Vascular health and risk management,* 1, 183-198.

HAINFELD, J. F., LIU, W., HALSEY, C. M. R., FREIMUTH, P. & POWELL, R. D. 1999. Ni–NTA–Gold Clusters Target His-Tagged Proteins. *Journal of Structural Biology,* 127, 185-198.

HAMILTON, J. L., NAGAO, M., LEVINE, B. R., CHEN, D., OLSEN, B. R. & IM, H. J. 2016. Targeting VEGF and Its Receptors for the Treatment of Osteoarthritis and Associated Pain. *J Bone Miner Res,* 31, 911-24.

HAN, C. Y. & PAK, Y. K. 1999. Oxidation-dependent effects of oxidized LDL: proliferation or cell death. *Exp Mol Med,* 31, 165-73.

HARAZONO, A., KAWASAKI, N., KAWANISHI, T. & HAYAKAWA, T. 2004. Site-specific glycosylation analysis of human apolipoprotein B100 using LC/ESI MS/MS. *Glycobiology,* 15, 447-462.

HARRIS, H., WOLK, A., LARSSON, A., VASSON, M.-P. & BASU, S. 2016. Soluble vascular endothelial growth factor receptors 2 (sVEGFR-2) and 3 (sVEGFR-3) and breast cancer risk in the Swedish Mammography Cohort. *International journal of molecular epidemiology and genetics,* 7, 81-86.

HARRIS, R., MINERS, J. S., ALLEN, S. & LOVE, S. 2018. VEGFR1 and VEGFR2 in Alzheimer's Disease. *J Alzheimers Dis,* 61, 741-752.

HARRIS, S., CRAZE, M., NEWTON, J., FISHER, M., SHIMA, D. T., TOZER, G. M. & KANTHOU, C. 2012. Do Anti-Angiogenic VEGF (VEGFxxxb) Isoforms Exist? A Cautionary Tale. *PLoS One,* 7, e35231.

HE, F. 2011. Coomassie Blue Staining. *Bio-protocol,* 1, e78.

HENNINGSEN, R., GALE, B. L., STRAUB, K. M. & DENAGEL, D. C. 2002. Application of zwitterionic detergents to the solubilization of integral membrane proteins for two-dimensional gel electrophoresis and mass spectrometry. *Proteomics,* 2, 1479-88.

HENRIKSEN, T., MAHONEY, E. M. & STEINBERG, D. 1981. Enhanced macrophage degradation of low density lipoprotein previously incubated with cultured endothelial cells: recognition by receptors for acetylated low density lipoproteins. *Proceedings of the National Academy of Sciences,* 78, 6499.

HEVONOJA, T., PENTIKÄINEN, M. O., HYVÖNEN, M. T., KOVANEN, P. T. & ALA-KORPELA, M. 2000. Structure of low density lipoprotein (LDL) particles: Basis for understanding molecular changes in modified LDL. *Biochimica et Biophysica Acta (BBA) - Molecular and Cell Biology of Lipids,* 1488, 189-210.

HICKLIN, D. J. & ELLIS, L. M. 2005. Role of the vascular endothelial growth factor pathway in tumor growth and angiogenesis. *J Clin Oncol,* 23, 1011-27.

HIRATSUKA, S., MINOWA, O., KUNO, J., NODA, T. & SHIBUYA, M. 1998. Flt-1 lacking the tyrosine kinase domain is sufficient for normal development and angiogenesis in mice. *Proc Natl Acad Sci U S A,* 95, 9349-54.

HITE, R. K., YUAN, P., LI, Z., HSUING, Y., WALZ, T. & MACKINNON, R. 2015. Cryo-electron microscopy structure of the Slo2.2 Na(+)-activated K(+) channel. *Nature,* 527, 198-203.

HJELMELAND, L. M. 1980. A nondenaturing zwitterionic detergent for membrane biochemistry: design and synthesis. *Proceedings of the National Academy of Sciences of the United States of America,* 77, 6368-6370.

HOEBEN, A., LANDUYT, B., HIGHLEY, M. S., WILDIERS, H., VAN OOSTEROM, A. T. & DE BRUIJN, E. A. 2004. Vascular endothelial growth factor and angiogenesis. *Pharmacol Rev,* 56, 549-80.

HOFMANN, A., BRUNSSEN, C., POITZ, D. M., LANGBEIN, H., STRASSER, R. H., HENLE, T., RAVENS, U. & MORAWIETZ, H. 2017. Lectin-like oxidized low-density lipoprotein receptor-1 promotes endothelial dysfunction in LDL receptor knockout background. *Atheroscler Suppl,* 30, 294-302.

HONG, P., KOZA, S. & BOUVIER, E. S. P. 2012. Size-Exclusion Chromatography for the Analysis of Protein Biotherapeutics and their Aggregates. *Journal of liquid chromatography & related technologies,* 35, 2923-2950.

HSIEH, J. J., PURDUE, M. P., SIGNORETTI, S., SWANTON, C., ALBIGES, L., SCHMIDINGER, M., HENG, D. Y., LARKIN, J. & FICARRA, V. 2017. Renal cell carcinoma. *Nature reviews. Disease primers,* 3, 17009-17009.

HU, C., DANDAPAT, A., SUN, L., CHEN, J., MARWALI, M. R., ROMEO, F., SAWAMURA, T. & MEHTA, J. L. 2008. LOX-1 deletion decreases collagen accumulation in atherosclerotic plaque in low-density lipoprotein receptor knockout mice fed a high-cholesterol diet. *Cardiovasc Res,* 79, 287-93.

HUBBARD, S. R. 1999. Structural analysis of receptor tyrosine kinases. *Prog Biophys Mol Biol,* 71, 343-58.

HUBBARD, S. R. & MILLER, W. T. 2007. Receptor tyrosine kinases: mechanisms of activation and signaling. *Curr Opin Cell Biol,* 19, 117-23.

HÜLSMEIER, J., PIELAGE, J., RICKERT, C., TECHNAU, G. M., KLÄMBT, C. & STORK, T. 2007. Distinct functions of α-Spectrin and β-Spectrin during axonal pathfinding. *Development,* 134, 713-722.

HUNTER, M., YUAN, P., VAVILALA, D. & FOX, M. 2019. Optimization of Protein Expression in Mammalian Cells. *Current protocols in protein science,* 95, 28.

HWANG-BO, J., PARK, J. H., BAE, M. G. & CHUNG, I. S. 2016. Recombinant canstatin inhibits VEGF-A-induced lymphangiogenesis and metastasis in an oral squamous cell carcinoma SCC-VII animal model. *Cancer Med,* 5, 2977-2988.

HYDE, C. A., GIESE, A., STUTTFELD, E., ABRAM SALIBA, J., VILLEMAGNE, D., SCHLEIER, T., BINZ, H. K. & BALLMER-HOFER, K. 2012a. Targeting extracellular domains D4 and D7 of vascular endothelial growth factor receptor 2 reveals allosteric receptor regulatory sites. *Mol Cell Biol,* 32, 3802-13.

HYDE, C. A. C., GIESE, A., STUTTFELD, E., ABRAM SALIBA, J., VILLEMAGNE, D., SCHLEIER, T., BINZ, H. K. & BALLMER-HOFER, K. 2012b. Targeting extracellular domains D4 and D7 of vascular endothelial growth factor receptor 2 reveals allosteric receptor regulatory sites. *Mol Cell Biol,* 32, 3802-3813.

IANCU, C. V., TIVOL, W. F., SCHOOLER, J. B., DIAS, D. P., HENDERSON, G. P., MURPHY, G. E., WRIGHT, E. R., LI, Z., YU, Z., BRIEGEL, A., GAN, L., HE, Y. & JENSEN, G. J. 2006. Electron cryotomography sample preparation using the Vitrobot. *Nat Protoc,* 1, 2813-9.

IGARASHI, K., ISOHARA, T., KATO, T., SHIGETA, K., YAMANO, T. & UNO, I. 1998a. Tyrosine 1213 of Flt-1 is a major binding site of Nck and SHP-2. *Biochem Biophys Res Commun,* 246, 95-9.

IGARASHI, K., SHIGETA, K., ISOHARA, T., YAMANO, T. & UNO, I. 1998b. Sck interacts with KDR and Flt-1 via its SH2 domain. *Biochem Biophys Res Commun,* 251, 77-82.

IKEDA, K., OKI, E., SAEKI, H., ANDO, K., MORITA, M., ODA, Y., IMAMURA, M., KAKEJI, Y. & MAEHARA, Y. 2014. Intratumoral lymphangiogenesis and prognostic significance of VEGFC expression in gastric cancer. *Anticancer Res,* 34, 3911-5.

IMOUKHUEDE, P. I., DOKUN, A. O., ANNEX, B. H. & POPEL, A. S. 2013. Endothelial cell-by-cell profiling reveals the temporal dynamics of VEGFR1 and VEGFR2 membrane localization after murine hindlimb ischemia. *American Journal of Physiology-Heart and Circulatory Physiology,* 304, H1085-H1093.

IMOUKHUEDE, P. I. & POPEL, A. S. 2011. Quantification and cell-to-cell variation of vascular endothelial growth factor receptors. *Experimental cell research,* 317, 955-965.

IMOUKHUEDE, P. I. & POPEL, A. S. 2012. Expression of VEGF receptors on endothelial cells in mouse skeletal muscle. *PLoS One,* 7, 12.

ISHCHENKO, A., ABOLA, E. E. & CHEREZOV, V. 2017. Crystallization of Membrane Proteins: An Overview. *Methods Mol Biol*, 7000-1_5.

ITKONEN, H. M. & MILLS, I. G. 2015a. Studying N-Linked Glycosylation of Receptor Tyrosine Kinases. *In:* GERMANO, S. (ed.) *Receptor Tyrosine Kinases: Methods and Protocols.* New York, NY: Springer New York.

ITKONEN, H. M. & MILLS, I. G. 2015b. Studying N-linked glycosylation of receptor tyrosine kinases. *Methods Mol Biol*, 1789-1_10.

IVANOVA, E. A., MYASOEDOVA, V. A., MELNICHENKO, A. A., GRECHKO, A. V. & OREKHOV, A. N. 2017. Small Dense Low-Density Lipoprotein as Biomarker for Atherosclerotic Diseases. *Oxidative medicine and cellular longevity,* 2017, 1273042-1273042.

IYER, S., DARLEY, P. I. & ACHARYA, K. R. 2010. Structural insights into the binding of vascular endothelial growth factor-B by VEGFR-1(D2): recognition and specificity. *J Biol Chem,* 285, 23779-89.

JANELIDZE, S., LINDQVIST, D., FRANCARDO, V., HALL, S., ZETTERBERG, H., BLENNOW, K., ADLER, C. H., BEACH, T. G., SERRANO, G. E., VAN WESTEN, D., LONDOS, E., CENCI, M. A. & HANSSON, O. 2015. Increased CSF biomarkers of angiogenesis in Parkinson disease. *Neurology,* 85, 1834-42.

JEON, H. & BLACKLOW, S. C. 2005. Structure and physiologic function of the low-density lipoprotein receptor. *Annu Rev Biochem,* 74, 535-62.

JIN, K., ZHU, Y., SUN, Y., MAO, X. O., XIE, L. & GREENBERG, D. A. 2002. Vascular endothelial growth factor (VEGF) stimulates neurogenesis in vitro and in vivo. *Proc Natl Acad Sci U S A,* 99, 11946-50.

JOHS, A., HAMMEL, M., WALDNER, I., MAY, R. P., LAGGNER, P. & PRASSL, R. 2006. Modular structure of solubilized human apolipoprotein B-100. Low resolution model revealed by small angle neutron scattering. *J Biol Chem,* 281, 19732-9.

JOPLING, H. M., ODELL, A. F., PELLET-MANY, C., LATHAM, A. M., FRANKEL, P., SIVAPRASADARAO, A., WALKER, J. H., ZACHARY, I. C. & PONNAMBALAM, S. 2014. Endosome-to-Plasma Membrane Recycling of VEGFR2 Receptor Tyrosine Kinase Regulates Endothelial Function and Blood Vessel Formation. *Cells,* 3, 363-385.

JUILLERAT, C. A., KOCEVSKI, V., BESMANN, T. M. & ZUR LOYE, H.-C. 2019. Observation of the Same New Sheet Topology in Both the Layered Uranyl Oxide-Phosphate Cs11[(UO2)12(PO4)3O13] and the Layered Uranyl Oxyfluoride-Phosphate Rb11[(UO2)12(PO4)3O12F2] Prepared by Flux Crystal Growth. *Frontiers in Chemistry,* 7.

KAITOSAARI, T., RONNEMAA, T., VIIKARI, J., LEINO, A., JOKINEN, E. & SIMELL, O. 2006. Low-density lipoprotein (LDL) particle size in healthy prepubertal children: the STRIP study. *Acta Paediatr,* 95, 1668-73.

KARKKAINEN, M. J., HAIKO, P., SAINIO, K., PARTANEN, J., TAIPALE, J., PETROVA, T. V., JELTSCH, M., JACKSON, D. G., TALIKKA, M., RAUVALA, H., BETSHOLTZ, C. & ALITALO, K. 2004. Vascular endothelial growth factor C is required for sprouting of the first lymphatic vessels from embryonic veins. *Nat Immunol,* 5, 74-80.

KAZAZI-HYSENI, F., BEIJNEN, J. H. & SCHELLENS, J. H. M. 2010. Bevacizumab. *Oncologist,* 15, 819-825.

KENDALL, R. L. & THOMAS, K. A. 1993. Inhibition of vascular endothelial cell growth factor activity by an endogenously encoded soluble receptor. *Proc Natl Acad Sci U S A,* 90, 10705-9.

KIBA, A., YABANA, N. & SHIBUYA, M. 2003. A set of loop-1 and -3 structures in the novel vascular endothelial growth factor (VEGF) family member, VEGF-ENZ-7, is essential for the activation of VEGFR-2 signaling. *J Biol Chem,* 278, 13453-61.

KILIC, I., GULDIKEN, S., SIPAHI, T., PALABIYIK, O., AKKER, M., CELIK, O., SOYSAL-ATILE, N., TUNCBILEK, N., GUVEN, H. M., GUNDOGDU, A. S. & SUT, N. 2016. Investigation of VEGF and IL-8 Gene Polymorphisms in Patients with Differentiated Thyroid Cancer. *Clin Lab,* 62, 2319-2325.

KIM, G., MCKEE, A. E., NING, Y. M., HAZARIKA, M., THEORET, M., JOHNSON, J. R., XU, Q. C., TANG, S., SRIDHARA, R., JIANG, X., HE, K., ROSCOE, D., MCGUINN, W. D., HELMS, W. S., RUSSELL, A. M., MIKSINSKI, S. P., ZIRKELBACH, J. F., EARP, J., LIU, Q., IBRAHIM, A., JUSTICE, R. & PAZDUR, R. *FDA approval summary: vemurafenib for treatment of unresectable or metastatic melanoma with the BRAFV600E mutation*, Clin Cancer Res. 2014 Oct 1;20(19):4994-5000. doi: 10.1158/1078-0432.CCR-14-0776. Epub 2014 Aug 5.

KIMPLE, M. E., BRILL, A. L. & PASKER, R. L. 2013. Overview of affinity tags for protein purification. *Current protocols in protein science,* 73, 9.9.1-9.9.23.

KING, C. & HRISTOVA, K. 2019. Direct measurements of VEGF-VEGFR2 binding affinities reveal the coupling between ligand binding and receptor dimerization. *J Biol Chem,* 294, 9064-9075.

KISKO, K., BROZZO, M. S., MISSIMER, J., SCHLEIER, T., MENZEL, A., LEPPÄNEN, V.-M., ALITALO, K., WALZTHOENI, T., AEBERSOLD, R. & BALLMER-HOFER, K. 2011. Structural analysis of vascular endothelial growth factor receptor-2/ligand complexes by small-angle X-ray solution scattering. *The FASEB Journal,* 25, 2980-2986.

KOCH, S. & CLAESSON-WELSH, L. 2012. Signal transduction by vascular endothelial growth factor receptors. *Cold Spring Harbor perspectives in medicine,* 2, a006502-a006502.

KONG, D.-H., KIM, M. R., JANG, J. H., NA, H.-J. & LEE, S. 2017. A Review of Anti-Angiogenic Targets for Monoclonal Antibody Cancer Therapy. *Int J Mol Sci,* 18, 1786.

KORASICK, D. A. & TANNER, J. J. 2018. Determination of protein oligomeric structure from small-angle X-ray scattering. *Protein Sci,* 27, 814-824.

KOSURI, P., ALEGRE-CEBOLLADA, J., FENG, J., KAPLAN, A., INGLÉS-PRIETO, A., BADILLA, C. L., STOCKWELL, B. R., SANCHEZ-RUIZ, J. M., HOLMGREN, A. & FERNÁNDEZ, J. M. 2012. Protein folding drives disulfide formation. *Cell,* 151, 794-806.

KOTOV, V., BARTELS, K., VEITH, K., JOSTS, I., SUBHRAMANYAM, U. K. T., GÜNTHER, C., LABAHN, J., MARLOVITS, T. C., MORAES, I., TIDOW, H., LÖW, C. & GARCIA-ALAI, M. M. 2019. High-throughput stability screening for detergent-solubilized membrane proteins. *Sci Rep,* 9, 10379-10379.

KOVACS, K., DECATUR, C., TORO, M., PHAM, D. G., LIU, H., JING, Y., MURRAY, T. G., LAMPIDIS, T. J. & MERCHAN, J. R. 2016. 2-Deoxy-Glucose Downregulates Endothelial AKT and ERK via Interference with N-

Linked Glycosylation, Induction of Endoplasmic Reticulum Stress, and GSK3beta Activation. *Mol Cancer Ther,* 15, 264-75.

KOVANEN, P. T. & KOKKONEN, J. O. 1991. Modification of low density lipoproteins by secretory granules of rat serosal mast cells. *J Biol Chem,* 266, 4430-6.

KROEZE, W. K., SHEFFLER, D. J. & ROTH, B. L. 2003. G-protein-coupled receptors at a glance. *Journal of Cell Science,* 116, 4867-4869.

KUMAR, V., BUTCHER, S. J., OORNI, K., ENGELHARDT, P., HEIKKONEN, J., KASKI, K., ALA-KORPELA, M. & KOVANEN, P. T. 2011. Three-dimensional cryoEM reconstruction of native LDL particles to 16A resolution at physiological body temperature. *PLoS One,* 6, 0018841.

KWONG-KWOK, W. 2009. Recent Developments in Anti-Cancer Agents Targeting the Ras/Raf/ MEK/ERK Pathway. *Recent Patents on Anti-Cancer Drug Discovery,* 4, 28-35.

LAGOR, W. & MILLAR, J. 2010. Overview of the LDL receptor: Relevance to cholesterol metabolism and future approaches for the treatment of coronary heart disease. *Journal of Receptor, Ligand and Channel Research,* 3, 1-14.

LAKKIREDDY, S., AULA, S., KAPLEY, A., SWAMY, A. V., DIGUMARTI, R. R., KUTALA, V. K. & JAMIL, K. 2016. Association of Vascular Endothelial Growth Factor A (VEGFA) and its Receptor (VEGFR2) Gene Polymorphisms with Risk of Chronic Myeloid Leukemia and Influence on Clinical Outcome. *Mol Diagn Ther,* 20, 33-44.

LALAN, M., BAGCHI, T. & MISRA, A. 2011. 1 - The Cell. *In:* MISRA, A. (ed.) *Challenges in Delivery of Therapeutic Genomics and Proteomics.* London: Elsevier.

LALI, F. V., HUNT, A. E., TURNER, S. J. & FOXWELL, B. M. 2000. The pyridinyl imidazole inhibitor SB203580 blocks phosphoinositide-dependent protein kinase activity, protein kinase B phosphorylation, and retinoblastoma hyperphosphorylation in interleukin-2-stimulated T cells independently of p38 mitogen-activated protein kinase. *J Biol Chem,* 275, 7395-402.

LEE, S. J., LEE, S. Y., LEE, W. S., YOO, J. S., SUN, J.-M., LEE, J., PARK, S. H., PARK, J. O., AHN, M.-J., LIM, H. Y., KANG, W. K. & PARK, Y. S. 2017. Phase I trial and pharmacokinetic study of tanibirumab, a fully human monoclonal antibody to vascular endothelial growth factor receptor 2, in patients with refractory solid tumors. *Investigational New Drugs,* 35, 782-790.

LEE, W. S., PYUN, B.-J., KIM, S.-W., SHIM, S. R., NAM, J. R., YOO, J. Y., JIN, Y., JIN, J., KWON, Y.-G., YUN, C.-O., NAM, D.-H., OH, K., LEE, D.-S., LEE, S. H. & YOO, J.-S. 2015. TTAC-0001, a human monoclonal antibody targeting VEGFR-2/KDR, blocks tumor angiogenesis. *mAbs,* 7, 957-968.

LEIST, M., SINGLE, B., CASTOLDI, A. F., KÜHNLE, S. & NICOTERA, P. 1997. Intracellular adenosine triphosphate (ATP) concentration: a switch in the decision between apoptosis and necrosis. *The Journal of experimental medicine,* 185, 1481-1486.

LEMMON, M. A. & SCHLESSINGER, J. 2010. Cell signaling by receptor tyrosine kinases. *Cell,* 141, 1117-34.

LENGFELD, J., CUTFORTH, T. & AGALLIU, D. 2014. The role of angiogenesis in the pathology of multiple sclerosis. *Vascular Cell,* 6, 23.

LEPPANEN, V. M., PROTA, A. E., JELTSCH, M., ANISIMOV, A., KALKKINEN, N., STRANDIN, T., LANKINEN, H., GOLDMAN, A., BALLMER-HOFER, K. & ALITALO, K. 2010. Structural determinants of growth factor binding and specificity by VEGF receptor 2. *Proc Natl Acad Sci U S A,* 107, 2425-30.

LEPPANEN, V. M., TVOROGOV, D., KISKO, K., PROTA, A. E., JELTSCH, M., ANISIMOV, A., MARKOVIC-MUELLER, S., STUTTFELD, E., GOLDIE, K. N., BALLMER-HOFER, K. & ALITALO, K. 2013. Structural and mechanistic insights into VEGF receptor 3 ligand binding and activation. *Proc Natl Acad Sci U S A,* 110, 12960-5.

LEVITAN, I., VOLKOV, S. & SUBBAIAH, P. V. 2010. Oxidized LDL: diversity, patterns of recognition, and pathophysiology. *Antioxidants & redox signaling,* 13, 39-75.

LI, D., JI, F., HUANG, C. & JIA, L. 2019. High Expression Achievement of Active and Robust Anti-β2 microglobulin Nanobodies via E.coli Hosts Selection. *Molecules (Basel, Switzerland),* 24, 2860.

LI, X., LEE, C., TANG, Z., ZHANG, F., ARJUNAN, P., LI, Y., HOU, X., KUMAR, A. & DONG, L. 2009. VEGF-B: a survival, or an angiogenic factor? *Cell Adh Migr,* 3, 322-7.

LIAN, L., LI, X.-L., XU, M.-D., LI, X.-M., WU, M.-Y., ZHANG, Y., TAO, M., LI, W., SHEN, X.-M., ZHOU, C. & JIANG, M. 2019. VEGFR2 promotes tumorigenesis and metastasis in a pro-angiogenic-independent way in gastric cancer. *BMC Cancer,* 19, 183.

LIANG, B. & TAMM, L. K. 2016. NMR as a tool to investigate the structure, dynamics and function of membrane proteins. *Nature Structural & Molecular Biology,* 23, 468-474.

LIAO, M., CAO, E., JULIUS, D. & CHENG, Y. 2013. Structure of the TRPV1 ion channel determined by electron cryo-microscopy. *Nature,* 504, 107-12.

LICHTENBERG, D., ROBSON, R. J. & DENNIS, E. A. 1983. Solubilization of phospholipids by detergents. Structural and kinetic aspects. *Biochim Biophys Acta,* 737, 285-304.

LICHTY, J. J., MALECKI, J. L., AGNEW, H. D., MICHELSON-HOROWITZ, D. J. & TAN, S. 2005. Comparison of affinity tags for protein purification. *Protein Expr Purif,* 41, 98-105.

LIM, L. S., MITCHELL, P., SEDDON, J. M., HOLZ, F. G. & WONG, T. Y. 2012. Age-related macular degeneration. *Lancet,* 379, 1728-38.

LIN, X., KHALID, S., QURESHI, M. Z., ATTAR, R., YAYLIM, I., UCAK, I., YAQUB, A., FAYYAZ, S., FAROOQI, A. A. & ISMAIL, M. 2016. VEGF mediated signaling in oral cancer. *Cell Mol Biol,* 62, 64-68.

LLEVADOT, J. & ASAHARA, T. 2002. [Effects of statins on angiogenesis and vasculogenesis]. *Rev Esp Cardiol,* 55, 838-44.

LONGO, V., GNONI, A., CASADEI GARDINI, A., PISCONTI, S., LICCHETTA, A., SCARTOZZI, M., MEMEO, R., PALMIERI, V. O., APRILE, G., SANTINI, D., NARDULLI, P., SILVESTRIS, N. & BRUNETTI, O. 2017. Immunotherapeutic approaches for hepatocellular carcinoma. *Oncotarget,* 8, 33897-33910.

LOPES-VIRELLA, M. F., KOSKINEN, S., MIRONOVA, M., HORNE, D., KLEIN, R., CHASSEREAU, C., ENOCKSON, C. & VIRELLA, G. 2000. The preparation of copper-oxidized LDL for the measurement of oxidized LDL antibodies by EIA. *Atherosclerosis,* 152**,** 107-15.

LOUGHEED, M. & STEINBRECHER, U. P. 1996. Mechanism of Uptake of Copper-oxidized Low Density Lipoprotein in Macrophages Is Dependent on Its Extent of Oxidation. *Journal of Biological Chemistry,* 271, 11798-11805.

LU, P., BAI, X. C., MA, D., XIE, T., YAN, C., SUN, L., YANG, G., ZHAO, Y., ZHOU, R., SCHERES, S. H. & SHI, Y. 2014. Three-dimensional structure of human gamma-secretase. *Nature,* 512, 166-70.

LUSIS, A. J. 2000. Atherosclerosis. *Nature,* 407, 233-241.

LYUMKIS, D. 2019. Challenges and opportunities in cryo-EM single-particle analysis. *J Biol Chem,* 294, 5181-5197.

MAC GABHANN, F. & POPEL, A. S. 2007. Dimerization of VEGF receptors and implications for signal transduction: a computational study. *Biophysical chemistry,* 128, 125-139.

MANSBACH, C. M., 2ND & SIDDIQI, S. 2016. Control of chylomicron export from the intestine. *Am J Physiol Gastrointest Liver Physiol,* 310, 25.

MARKOVIC-MUELLER, S., STUTTFELD, E., ASTHANA, M., WEINERT, T., BLIVEN, S., GOLDIE, K. N., KISKO, K., CAPITANI, G. & BALLMER-HOFER, K. 2017. Structure of the Full-length VEGFR-1 Extracellular Domain in Complex with VEGF-A. *Structure,* 25, 341-352.

MATSUMOTO, M., ROUFAIL, S., INDER, R., CAESAR, C., KARNEZIS, T., SHAYAN, R., FARNSWORTH, R. H., SATO, T., ACHEN, M. G., MANN, G. B. & STACKER, S. A. 2013. Signaling for lymphangiogenesis via VEGFR-3 is required for the early events of metastasis. *Clin Exp Metastasis,* 30, 819-32.

MCTIGUE, M. A., WICKERSHAM, J. A., PINKO, C., SHOWALTER, R. E., PARAST, C. V., TEMPCZYK-RUSSELL, A., GEHRING, M. R., MROCZKOWSKI, B., KAN, C. C., VILLAFRANCA, J. E. & APPELT, K. 1999. Crystal structure of the kinase domain of human vascular endothelial growth factor receptor 2: a key enzyme in angiogenesis. *Structure,* 7, 319-30.

MEISTER, A. & BLUME, A. 2017. (Cryo)Transmission Electron Microscopy of Phospholipid Model Membranes Interacting with Amphiphilic and Polyphilic Molecules. *Polymers,* 9, 521.

MENG, J., LIU, Y., HAN, J., TAN, Q., CHEN, S., QIAO, K., ZHOU, H., SUN, T. & YANG, C. 2017. Hsp90beta promoted endothelial cell-dependent tumor angiogenesis in hepatocellular carcinoma. *Mol Cancer,* 16, 017-0640.

MERAJI, S., MOORE, C. E., SKINNER, V. O. & BRUCKDORFER, K. R. 1992. The Importance of Oxidation or Glycosylation of Low-density Lipoproteins in Relation to Platelet Activation. *Platelets,* 3, 155-62.

MERK, A., BARTESAGHI, A., BANERJEE, S., FALCONIERI, V., RAO, P., DAVIS, M. I., PRAGANI, R., BOXER, M. B., EARL, L. A., MILNE, J. L. S. & SUBRAMANIAM, S. 2016. Breaking Cryo-EM Resolution Barriers to Facilitate Drug Discovery. *Cell,* 165, 1698-1707.

MITTAR, S., ULYATT, C., HOWELL, G. J., BRUNS, A. F., ZACHARY, I., WALKER, J. H. & PONNAMBALAM, S. 2009. VEGFR1 receptor tyrosine kinase localization to the Golgi apparatus is calcium-dependent. *Exp Cell Res,* 315, 877-89.

MIYAZAWA, A., FUJIYOSHI, Y., STOWELL, M. & UNWIN, N. 1999. Nicotinic acetylcholine receptor at 4.6 A resolution: transverse tunnels in the channel wall. *J Mol Biol,* 288, 765-86.

MOHAN, S. B. 1992. Determination of purity and yield. *Methods Mol Biol,* 11, 307-23.

MORIYA, H. 2015. Quantitative nature of overexpression experiments. *Molecular biology of the cell,* 26, 3932-3939.

MORIYON, I. & BERMAN, D. T. 1982. Effects of nonionic, ionic, and dipolar ionic detergents and EDTA on the Brucella cell envelope. *J Bacteriol,* 152, 822-828.

MORRISON, G., SMITH, M. D. & ZUR LOYE, H.-C. 2016. Understanding the Formation of Salt-Inclusion Phases: An Enhanced Flux Growth Method for the Targeted Synthesis of Salt-Inclusion Cesium Halide Uranyl Silicates. *Journal of the American Chemical Society,* 138, 7121-7129.

MUKHERJI, S. K. 2010. Bevacizumab (Avastin). *American Journal of Neuroradiology,* 31, 235-236.

MURPHY, J. E., VOHRA, R. S., DUNN, S., HOLLOWAY, Z. G., MONACO, A. P., HOMER-VANNIASINKAM, S., WALKER, J. H. & PONNAMBALAM, S. 2008. Oxidised LDL internalisation by the LOX-1 scavenger receptor is dependent on a novel cytoplasmic motif and is regulated by dynamin-2. *Journal of Cell Science,* 121, 2136-2147.

MURRAY, S. C., GILLARD, B. K., LUDTKE, S. J. & POWNALL, H. J. 2016. Direct Measurement of the Structure of Reconstituted High-Density Lipoproteins by Cryo-EM. *Biophysical journal,* 110, 810-816.

MURTOLA, T., VUORELA, T. A., HYVÖNEN, M. T., MARRINK, S.-J., KARTTUNEN, M. & VATTULAINEN, I. 2011. Low density lipoprotein: structure, dynamics, and interactions of apoB-100 with lipids. *Soft Matter,* 7, 8135-8141.

NAKAJIMA, K., NAGAMINE, T., FUJITA, M. Q., AI, M., TANAKA, A. & SCHAEFER, E. 2014. Apolipoprotein B-48: a unique marker of chylomicron metabolism. *Adv Clin Chem,* 64, 117-77.

NARHI, L. O., CAUGHEY, D. J., HORAN, T., KITA, Y., CHANG, D. & ARAKAWA, T. 1997. Effect of three elution buffers on the recovery and structure of monoclonal antibodies. *Anal Biochem,* 253, 236-45.

NAVARATNA, D., GUO, S., ARAI, K. & LO, E. H. 2009. Mechanisms and targets for angiogenic therapy after stroke. *Cell adhesion & migration,* 3, 216-223.

NEWHOUSE, Y., PETERS-LIBEU, C. & WEISGRABER, K. H. 2005. Crystallization and preliminary X-ray diffraction analysis of apolipoprotein E-containing lipoprotein particles. *Acta crystallographica. Section F, Structural biology and crystallization communications,* 61, 981-984.

NOGALES, E. & SCHERES, S. H. 2015. Cryo-EM: A Unique Tool for the Visualization of Macromolecular Complexity. *Mol Cell,* 58, 677-89.

O'GORMAN, S., FOX, D. T. & WAHL, G. M. 1991. Recombinase-mediated gene activation and site-specific integration in mammalian cells. *Science,* 251, 1351-5.

O'NEAL, D., HARRIP, P., DRAGICEVIC, G., RAE, D. & BEST, J. D. 1998. A comparison of LDL size determination using gradient gel electrophoresis and light-scattering methods. *J Lipid Res,* 39, 2086-90.

ODORISIO, T., SCHIETROMA, C., ZACCARIA, M. L., CIANFARANI, F., TIVERON, C., TATANGELO, L., FAILLA, C. M. & ZAMBRUNO, G. 2002. Mice overexpressing placenta growth factor exhibit increased vascularization and vessel permeability. *J Cell Sci,* 115, 2559-67.

OHI, M., LI, Y., CHENG, Y. & WALZ, T. 2004. Negative Staining and Image Classification - Powerful Tools in Modern Electron Microscopy. *Biological procedures online,* 6, 23-34.

OHKI, I., ISHIGAKI, T., OYAMA, T., MATSUNAGA, S., XIE, Q., OHNISHI-KAMEYAMA, M., MURATA, T., TSUCHIYA, D., MACHIDA, S., MORIKAWA, K. & TATE, S. 2005. Crystal structure of human lectin-like, oxidized low-density lipoprotein receptor 1 ligand binding domain and its ligand recognition mode to OxLDL. *Structure,* 13, 905-17.

OHOLENDT, A. L. & ZADLO, J. L. 2015. Ramucirumab: A New Therapy for Advanced Gastric Cancer. *Journal of the advanced practitioner in oncology,* 6, 71-75.

OLSSON, A. K., DIMBERG, A., KREUGER, J. & CLAESSON-WELSH, L. 2006. VEGF receptor signalling - in control of vascular function. *Nat Rev Mol Cell Biol,* 7, 359-71.

OLSSON, U., CAMEJO, G., HURT-CAMEJO, E., ELFSBER, K., WIKLUND, O. & BONDJERS, G. 1997. Possible functional interactions of apolipoprotein B-100 segments that associate with cell proteoglycans and the ApoB/E receptor. *Arterioscler Thromb Vasc Biol,* 17, 149-55.

ORLOVA, E. V., SHERMAN, M. B., CHIU, W., MOWRI, H., SMITH, L. C. & GOTTO, A. M. 1999a. Three-dimensional structure of low density lipoproteins by electron cryomicroscopy. *Proceedings of the National Academy of Sciences,* 96, 8420-8425.

ORLOVA, E. V., SHERMAN, M. B., CHIU, W., MOWRI, H., SMITH, L. C. & GOTTO, A. M. 1999b. Three-dimensional structure of low density lipoproteins by electron cryomicroscopy. *Proceedings of the National Academy of Sciences of the United States of America,* 96, 8420-8425.

ORLOVA, M. A., CHUBAR, T. A., FECHINA, V. A., IGNATENKO, O. V., BADUN, G. A., KSENOFONTOV, A. L., UPOROV, I. V. & GAZARYAN, I. G. 2003. Conformational differences between native and recombinant horseradish peroxidase revealed by tritium planigraphy. *Biochemistry,* 68, 1225-30.

OSEI, M., GRIFFIN, J. L. & KOULMAN, A. 2015. Hyphenating size-exclusion chromatography with electrospray mass spectrometry; using on-line liquid-liquid extraction to study the lipid composition of lipoprotein particles. *Rapid communications in mass spectrometry : RCM,* 29, 1969-1976.

OTERO, P., HERRERA, E. & BONET, B. 2002. Dual effect of glucose on LDL oxidation: dependence on vitamin E. *Free Radic Biol Med,* 33**,** 1133-40.

OTROCK, Z. K., MAKAREM, J. A. & SHAMSEDDINE, A. I. 2007. Vascular endothelial growth factor family of ligands and receptors: review. *Blood Cells Mol Dis,* 38, 258-68.

OVERINGTON, J. P., AL-LAZIKANI, B. & HOPKINS, A. L. 2006. How many drug targets are there? *Nat Rev Drug Discov,* 5, 993-6.

PALCZEWSKI, K., KUMASAKA, T., HORI, T., BEHNKE, C. A., MOTOSHIMA, H., FOX, B. A., TRONG, I. L., TELLER, D. C., OKADA, T., STENKAMP, R. E., YAMAMOTO, M. & MIYANO, M. 2000. Crystal Structure of Rhodopsin: A G Protein-Coupled Receptor. *Science,* 289, 739-745.

PAPADOPOULOS, N., MARTIN, J., RUAN, Q., RAFIQUE, A., ROSCONI, M. P., SHI, E., PYLES, E. A., YANCOPOULOS, G. D., STAHL, N. & WIEGAND, S. J. 2012. Binding and neutralization of vascular endothelial growth factor (VEGF) and related ligands by VEGF Trap, ranibizumab and bevacizumab. *Angiogenesis,* 15, 171-85.

PARK, H., ADSIT, F. G. & BOYINGTON, J. C. 2005. The 1.4 angstrom crystal structure of the human oxidized low density lipoprotein receptor lox-1. *J Biol Chem,* 280, 13593-9.

PARK, S. A., JEONG, M. S., HA, K.-T. & JANG, S. B. 2018. Structure and function of vascular endothelial growth factor and its receptor system. *BMB reports,* 51, 73-78.

PARK, S. H., DAS, B. B., CASAGRANDE, F., TIAN, Y., NOTHNAGEL, H. J., CHU, M., KIEFER, H., MAIER, K., DE ANGELIS, A. A., MARASSI, F. M. & OPELLA, S. J. 2012. Structure of the chemokine receptor CXCR1 in phospholipid bilayers. *Nature,* 491, 779-83.

PARTHASARATHY, S., RAGHAVAMENON, A., GARELNABI, M. O. & SANTANAM, N. 2010. Oxidized Low-Density Lipoprotein. *Methods in Molecular Biology (Clifton, N.j.),* 610, 403-417.

PATEL, N. S., MATHURA, V. S., BACHMEIER, C., BEAULIEU-ABDELAHAD, D., LAPORTE, V., WEEKS, O., MULLAN, M. & PARIS, D. 2010. Alzheimer's beta-amyloid peptide blocks vascular endothelial growth factor mediated signaling via direct interaction with VEGFR-2. *J Neurochem,* 112, 66-76.

PATIL, S. M., KEIRE, D. A. & CHEN, K. 2017. Comparison of NMR and Dynamic Light Scattering for Measuring Diffusion Coefficients of Formulated Insulin: Implications for Particle Size Distribution Measurements in Drug Products. *The AAPS journal,* 19**,** 1760-1766.

PEACH, C. J., MIGNONE, V. W., ARRUDA, M. A., ALCOBIA, D. C., HILL, S. J., KILPATRICK, L. E. & WOOLARD, J. 2018. Molecular Pharmacology of VEGF-A Isoforms: Binding and Signalling at VEGFR2. *International journal of molecular sciences,* 19, 1264.

PERROT-APPLANAT, M. 2012. VEGF isoforms. *Cell adhesion & migration,* 6, 526-527.

PETIOT, A., FAURE, J., STENMARK, H. & GRUENBERG, J. 2003. PI3P signaling regulates receptor sorting but not transport in the endosomal pathway. *J Cell Biol,* 162, 971-9.

PEZZELLA, F., HARRIS, A. L., TAVASSOLI, M. & GATTER, K. C. 2015. Blood vessels and cancer much more than just angiogenesis. *Cell death discovery,* 1, 15064-15064.

PIPERDI, B., MERLA, A. & PEREZ-SOLER, R. 2014. Targeting angiogenesis in squamous non-small cell lung cancer. *Drugs,* 74, 403-13.

PIRILLO, A., NORATA, G. D. & CATAPANO, A. L. 2013a. LOX-1, OxLDL, and atherosclerosis. *Mediators Inflamm,* 152786, 10.

PIRILLO, A., NORATA, G. D. & CATAPANO, A. L. 2013b. LOX-1, OxLDL, and Atherosclerosis. *Mediators of Inflammation,* 2013, 152786.

POEWE, W., GAUTHIER, S., AARSLAND, D., LEVERENZ, J. B., BARONE, P., WEINTRAUB, D., TOLOSA, E. & DUBOIS, B. 2008. Diagnosis and management of Parkinson's disease dementia. *International journal of clinical practice,* 62, 1581-1587.

PONNAMBALAM, S. & BALDWIN, S. A. 2003. Constitutive protein secretion from the trans -Golgi network to the plasma membrane (Review). *Molecular membrane biology,* 20, 129-139.

PORTOLANO, N., WATSON, P. J., FAIRALL, L., MILLARD, C. J., MILANO, C. P., SONG, Y., COWLEY, S. M. & SCHWABE, J. W. R. 2014. Recombinant protein expression for structural biology in HEK 293F suspension cells: a novel and accessible approach. *Journal of visualized experiments : JoVE*, e51897-e51897.

POSTIS, V., RAWSON, S., MITCHELL, J. K., LEE, S. C., PARSLOW, R. A., DAFFORN, T. R., BALDWIN, S. A. & MUENCH, S. P. 2015. The use of SMALPs as a novel membrane protein scaffold for structure study by negative stain electron microscopy. *Biochimica et Biophysica Acta (BBA) - Biomembranes,* 1848, 496-501.

PRASSL, R. 2011. Human low density lipoprotein: the mystery of core lipid packing. *Journal of Lipid Research,* 52, 187-188.

PRASSL, R., CHAPMAN, J. M., NIGON, F., SARA, M., ESCHENBURG, S., BETZEL, C., SAXENA, A. & LAGGNER, P. 1996. Crystallization and preliminary X-ray analysis of a low density lipoprotein from human plasma. *J Biol Chem,* 271, 28731-3.

PRYOR, E. & TRAVIS, B. 2018. An update on detergent usage in cryo-EM structure determination of membrane proteins. *Acta Crystallographica Section A,* 74, a228.

QIN, S., LI, A., YI, M., YU, S., ZHANG, M. & WU, K. 2019. Recent advances on anti-angiogenesis receptor tyrosine kinase inhibitors in cancer therapy. *J Hematol Oncol,* 12, 27.

RAFIEIAN-KOPAEI, M., SETORKI, M., DOUDI, M., BARADARAN, A. & NASRI, H. 2014. Atherosclerosis: process, indicators, risk factors and new hopes. *International journal of preventive medicine,* 5, 927-946.

RAMAKRISHNAN, S., ANAND, V. & ROY, S. 2014. Vascular endothelial growth factor signaling in hypoxia and inflammation. *Journal of neuroimmune pharmacology : the official journal of the Society on NeuroImmune Pharmacology,* 9, 142-160.

RAMES, M., YU, Y. & REN, G. 2014. Optimized negative staining: a high-throughput protocol for examining small and asymmetric protein structure by electron microscopy. *Journal of visualized experiments : JoVE*, e51087-e51087.

RANIOLO, S., VINDIGNI, G. & BIOCCA, S. 2016. Cholesterol level regulates lectin-like oxidized low-density lipoprotein receptor-1 function. *Biomedical Spectroscopy and Imaging,* 5**,** S87-S99.

RARAN-KURUSSI, S., CHERRY, S., ZHANG, D. & WAUGH, D. S. 2017. Removal of Affinity Tags with TEV Protease. *Methods Mol Biol*, 6887-9_14.

REN, G., RUDENKO, G., LUDTKE, S. J., DEISENHOFER, J., CHIU, W. & POWNALL, H. J. 2010a. Model of human low-density lipoprotein and bound receptor based on CryoEM. *Proceedings of the National Academy of Sciences,* 107, 1059-1064.

REN, G., RUDENKO, G., LUDTKE, S. J., DEISENHOFER, J., CHIU, W. & POWNALL, H. J. 2010b. Model of human low-density lipoprotein and bound receptor based on cryoEM. *Proc Natl Acad Sci U S A,* 107, 1059-64.

REN, G., RUDENKO, G., LUDTKE, S. J., DEISENHOFER, J., CHIU, W. & POWNALL, H. J. 2010c. Model of human low-density lipoprotein and bound receptor based on CryoEM. *Proceedings of the National Academy of Sciences of the United States of America,* 107, 1059-1064.

RENAUD, J.-P., CHARI, A., CIFERRI, C., LIU, W.-T., RÉMIGY, H.-W., STARK, H. & WIESMANN, C. 2018. Cryo-EM in drug discovery: achievements, limitations and prospects. *Nature Reviews Drug Discovery,* 17, 471.

RIBATTI, D. 2008. Judah Folkman, a pioneer in the study of angiogenesis. *Angiogenesis,* 11, 3-10.

RICHARDSON, P. G., ENG, C., KOLESAR, J., HIDESHIMA, T. & ANDERSON, K. C. 2012. Perifosine , an oral, anti-cancer agent and inhibitor of the Akt pathway: mechanistic actions, pharmacodynamics, pharmacokinetics, and clinical activity. *Expert opinion on drug metabolism & toxicology,* 8, 623-633.

RITTER, S., DIEDERICHS, K., FREY, I., BERG, A., KEUL, J. & BAUMSTARK, M. W. 1999. Crystallization of human low density lipoprotein (LDL), a large lipid–protein complex: Collection of X-ray data at very low resolution. *Journal of Crystal Growth,* 196, 344-349.

ROSENBAUM, D. M., RASMUSSEN, S. G. F. & KOBILKA, B. K. 2009. The structure and function of G-protein-coupled receptors. *Nature,* 459, 356-363.

ROSKOSKI, R. 2007a. Sunitinib: A VEGF and PDGF receptor protein kinase and angiogenesis inhibitor. *Biochemical and Biophysical Research Communications,* 356, 323-328.

ROSKOSKI, R., JR. 2007b. Sunitinib: a VEGF and PDGF receptor protein kinase and angiogenesis inhibitor. *Biochem Biophys Res Commun,* 356, 323-8.

ROSS, R. 1993. The pathogenesis of atherosclerosis: a perspective for the 1990s. *Nature,* 362, 801-9.

ROSS, R., GLOMSET, J. & HARKER, L. 1977. Response to injury and atherogenesis. *The American journal of pathology,* 86, 675-684.

RUCH, C., SKINIOTIS, G., STEINMETZ, M. O., WALZ, T. & BALLMER-HOFER, K. 2007a. Structure of a VEGF-VEGF receptor complex determined by electron microscopy. *Nat Struct Mol Biol,* 14, 249-50.

RUCH, C., SKINIOTIS, G., STEINMETZ, M. O., WALZ, T. & BALLMER-HOFER, K. 2007b. Structure of a VEGF–VEGF receptor complex determined by electron microscopy. *Nature Structural &Amp; Molecular Biology,* 14, 249.

RUF, H. & GOULD, B. J. 1999. Size distributions of chylomicrons from human lymph from dynamic light scattering measurements. *Eur Biophys J,* 28, 1-11.

SAKAMOTO, N. & ROSENBERG, A. S. 2011. Apolipoprotein B binding domains: evidence that they are cell-penetrating peptides that efficiently deliver antigenic peptide for cross-presentation of cytotoxic T cells. *J Immunol,* 186, 5004-11.

SAKURAI, T., TRIRONGJITMOAH, S., NISHIBATA, Y., NAMITA, T., TSUJI, M., HUI, S. P., JIN, S., SHIMIZU, K. & CHIBA, H. 2010. Measurement of lipoprotein particle sizes using dynamic light scattering. *Ann Clin Biochem,* 47, 476-81.

SANDHOFER, F. 1994. [Physiology and pathophysiology of the metabolism of lipoproteins]. *Wien Med Wochenschr,* 144, 286-90.

SARABIPOUR, S., BALLMER-HOFER, K. & HRISTOVA, K. 2016. VEGFR-2 conformational switch in response to ligand binding. *Elife,* 7, 13876.

SASE, H., WATABE, T., KAWASAKI, K., MIYAZONO, K. & MIYAZAWA, K. 2009a. VEGFR2-PLCgamma1 axis is essential for endothelial specification of VEGFR2+ vascular progenitor cells. *J Cell Sci,* 122, 3303-11.

SASE, H., WATABE, T., KAWASAKI, K., MIYAZONO, K. & MIYAZAWA, K. 2009b. VEGFR2-PLCγ1 axis is essential for endothelial specification of VEGFR2⁺ vascular progenitor cells. *Journal of Cell Science,* 122, 3303-3311.

SATHASIVAM, S. 2008. VEGF and ALS. *Neurosci Res,* 62, 71-7.

SAWANO, A., TAKAHASHI, T., YAMAGUCHI, S. & SHIBUYA, M. 1997. The phosphorylated 1169-tyrosine containing region of flt-1 kinase (VEGFR-1) is a major binding site for PLCgamma. *Biochem Biophys Res Commun,* 238, 487-91.

SCARFF, C. A., FULLER, M. J. G., THOMPSON, R. F. & IADAZA, M. G. 2018. Variations on Negative Stain Electron Microscopy Methods: Tools for Tackling Challenging Systems. *Journal of visualized experiments : JoVE*, 57199.

SCHACHTER, A. S. & DAVIS, K. L. 2000. Alzheimer's disease. *Dialogues in clinical neuroscience,* 2, 91-100.

SCHAEFER, E. J., ANTHANONT, P. & ASZTALOS, B. F. 2014. High-density lipoprotein metabolism, composition, function, and deficiency. *Current Opinion in Lipidology,* 25, 194-199.

SCHEFFER, P. G., BAKKER, S. J. L., HEINE, R. J. & TEERLINK, T. 1997. Measurement of low-density lipoprotein particle size by high-performance gel-filtration chromatography. *Clinical Chemistry,* 43, 1904-1912.

SCHEFFER, P. G., BAKKER, S. J. L., HEINE, R. J. & TEERLINK, T. 1998. Measurement of LDL particle size in whole plasma and serum by high performance gel-filtration chromatography using a fluorescent lipid probe. *Clinical Chemistry,* 44, 2148-2151.

SCHICK, M. 1963. Physical chemistry of nonionic detergents. *Journal of the American Oil Chemists' Society,* 40, 680-687.

SCHLESSINGER, J. 2000. Cell signaling by receptor tyrosine kinases. *Cell,* 103, 211-25.

SCHLESSINGER, J. 2014. Receptor tyrosine kinases: legacy of the first two decades. *Cold Spring Harb Perspect Biol,* 6.

SCOTT, L. J. 2018. Apatinib: A Review in Advanced Gastric Cancer and Other Advanced Cancers. *Drugs,* 78, 747-758.

SEDDON, A. M., CURNOW, P. & BOOTH, P. J. 2004. Membrane proteins, lipids and detergents: not just a soap opera. *Biochimica et Biophysica Acta (BBA) - Biomembranes,* 1666, 105-117.

SEGREST, J. P., JONES, M. K., DE LOOF, H. & DASHTI, N. 2001. Structure of apolipoprotein B-100 in low density lipoproteins. *J Lipid Res,* 42, 1346-67.

SHAHSUVARYAN, M. L. 2017. Therapeutic Potential of Ranibizumab in Corneal Neovascularization. *Trends Pharmacol Sci,* 38, 667-668.

SHALABY, F., ROSSANT, J., YAMAGUCHI, T. P., GERTSENSTEIN, M., WU, X. F., BREITMAN, M. L. & SCHUH, A. C. 1995. Failure of blood-island formation and vasculogenesis in Flk-1-deficient mice. *Nature,* 376, 62-6.

SHAO, J., CHOUDHARY, M. M. & SCHACHAT, A. P. 2016. Neovascular Age-Related Macular Degeneration. *Dev Ophthalmol,* 55, 125-36.

SHENTAL-BECHOR, D. & LEVY, Y. 2008. Effect of glycosylation on protein folding: A close look at thermodynamic stabilization. *Proceedings of the National Academy of Sciences,* 105, 8256-8261.

SHI, Y. 2014. A glimpse of structural biology through X-ray crystallography. *Cell,* 159, 995-1014.

SHIBUYA, M. 2011a. Vascular Endothelial Growth Factor (VEGF) and Its Receptor (VEGFR) Signaling in Angiogenesis: A Crucial Target for Anti- and Pro-Angiogenic Therapies. *Genes Cancer,* 2, 1097-105.

SHIBUYA, M. 2011b. Vascular Endothelial Growth Factor (VEGF) and Its Receptor (VEGFR) Signaling in Angiogenesis: A Crucial Target for Anti- and Pro-Angiogenic Therapies. *Genes & cancer,* 2, 1097-1105.

SHIBUYA, M. 2014. VEGF-VEGFR Signals in Health and Disease. *Biomolecules & therapeutics,* 22, 1-9.

SHIREMAN, R., KILGORE, L. L. & FISHER, W. R. 1977. Solubilization of apolipoprotein B and its specific binding by the cellular receptor for low density lipoprotein. *Proc Natl Acad Sci U S A,* 74, 5150-4.

SIDAWAY, P. 2019. Alpelisib effective in advanced-stage disease. *Nat Rev Clin Oncol,* 24, 019-0234.

SIMONS, M. 2012. An inside view: VEGF receptor trafficking and signaling. *Physiology (Bethesda, Md.),* 27, 213-222.

SINGH, A., UPADHYAY, V., UPADHYAY, A. K., SINGH, S. M. & PANDA, A. K. 2015. Protein recovery from inclusion bodies of Escherichia coli using mild solubilization process. *Microbial Cell Factories,* 14, 41.

SINGH, A. D. & PARMAR, S. 2015. Ramucirumab (Cyramza): A Breakthrough Treatment for Gastric Cancer. *P & T : a peer-reviewed journal for formulary management,* 40, 430-468.

SINGH, N., TIEM, M., WATKINS, R., CHO, Y. K., WANG, Y., OLSEN, T., UEHARA, H., MAMALIS, C., LUO, L., OAKEY, Z. & AMBATI, B. K. 2013. Soluble vascular endothelial growth factor receptor 3 is essential for corneal alymphaticity. *Blood,* 121, 4242-9.

SINGH, R. B., MENGI, S. A., XU, Y.-J., ARNEJA, A. S. & DHALLA, N. S. 2002. Pathogenesis of atherosclerosis: A multifactorial process. *Experimental and clinical cardiology,* 7, 40-53.

SINI, P., BAFFERT, F., WOOD, J. & HYNES, N. E. 2006. Role of VEGFR signaling in tumor cells. *Cancer Res,* 66, 659-659.

SIRINIAN, M. I., BELLEUDI, F., CAMPAGNA, F., CERIDONO, M., GAROFALO, T., QUAGLIARINI, F., VERNA, R., CALANDRA, S., BERTOLINI, S., SORICE, M., TORRISI, M. R. & ARCA, M. 2005. Adaptor protein ARH is recruited to the plasma membrane by low density lipoprotein (LDL) binding and modulates endocytosis of the LDL/LDL receptor complex in hepatocytes. *J Biol Chem,* 280, 38416-23.

SKINIOTIS, G. & SOUTHWORTH, D. R. 2015. Single-particle cryo-electron microscopy of macromolecular complexes. *Microscopy,* 65, 9-22.

SMITH, C., MITCHINSON, M. J., ARUOMA, O. I. & HALLIWELL, B. 1992. Stimulation of lipid peroxidation and hydroxyl-radical generation by the contents of human atherosclerotic lesions. *Biochemical Journal,* 286, 901-905.

SMITH, G. A., FEARNLEY, G. W., ABDUL-ZANI, I., WHEATCROFT, S. B., TOMLINSON, D. C., HARRISON, M. A. & PONNAMBALAM, S. 2016. VEGFR2 Trafficking, Signaling and Proteolysis is Regulated by the Ubiquitin Isopeptidase USP8. *Traffic (Copenhagen, Denmark),* 17, 53-65.

SMITH, G. A., FEARNLEY, G. W., ABDUL-ZANI, I., WHEATCROFT, S. B., TOMLINSON, D. C., HARRISON, M. A. & PONNAMBALAM, S. 2017. Ubiquitination of basal VEGFR2 regulates signal transduction and endothelial function. *Biology Open,* 6, 1404-1415.

SOKER, S., GOLLAMUDI-PAYNE, S., FIDDER, H., CHARMAHELLI, H. & KLAGSBRUN, M. 1997. Inhibition of vascular endothelial growth factor (VEGF)-induced endothelial cell proliferation by a peptide corresponding to the exon 7-encoded domain of VEGF165. *J Biol Chem,* 272, 31582-8.

SPRATLIN, J. 2011. Ramucirumab (IMC-1121B): Monoclonal Antibody Inhibition of Vascular Endothelial Growth Factor Receptor-2. *Curr Oncol Rep,* 13, 97-102.

SPRATLIN, J. L., COHEN, R. B., EADENS, M., GORE, L., CAMIDGE, D. R., DIAB, S., LEONG, S., O'BRYANT, C., CHOW, L. Q. M., SERKOVA, N. J., MEROPOL, N. J., LEWIS, N. L., CHIOREAN, E. G., FOX, F., YOUSSOUFIAN, H., ROWINSKY, E. K. & ECKHARDT, S. G. 2010. Phase I pharmacologic and biologic study of ramucirumab (IMC-1121B), a fully human immunoglobulin G1 monoclonal antibody targeting the vascular endothelial growth factor receptor-2. *Journal of clinical oncology : official journal of the American Society of Clinical Oncology,* 28, 780-787.

SRABOVIC, N., MUJAGIC, Z., MUJANOVIC-MUSTEDANAGIC, J., SOFTIC, A., MUMINOVIC, Z., RIFATBEGOVIC, A. & BEGIC, L. 2013. Vascular

Endothelial Growth Factor Receptor-1 Expression in Breast Cancer and Its Correlation to Vascular Endothelial Growth Factor A. *International Journal of Breast Cancer,* 2013, 6.

STACKER, S. A., CAESAR, C., BALDWIN, M. E., THORNTON, G. E., WILLIAMS, R. A., PREVO, R., JACKSON, D. G., NISHIKAWA, S., KUBO, H. & ACHEN, M. G. 2001. VEGF-D promotes the metastatic spread of tumor cells via the lymphatics. *Nat Med,* 7, 186-91.

STACKER, S. A., WILLIAMS, S. P., KARNEZIS, T., SHAYAN, R., FOX, S. B. & ACHEN, M. G. 2014. Lymphangiogenesis and lymphatic vessel remodelling in cancer. *Nature Reviews Cancer,* 14, 159.

STEINBERG, D. 1987. Lipoproteins and the pathogenesis of atherosclerosis. *Circulation,* 76, 508-14.

STEINBERG, D., PARTHASARATHY, S., CAREW, T. E., KHOO, J. C. & WITZTUM, J. L. 1989. Beyond cholesterol. Modifications of low-density lipoprotein that increase its atherogenicity. *N Engl J Med,* 320, 915-24.

STETSENKO, A. & GUSKOV, A. 2017. An Overview of the Top Ten Detergents Used for Membrane Protein Crystallization. *Crystals,* 7, 197.

STROP, P. & BRUNGER, A. T. 2005. Refractive index-based determination of detergent concentration and its application to the study of membrane proteins. *Protein science : a publication of the Protein Society,* 14, 2207-2211.

STUDENTOVA, H., VITASKOVA, D. & MELICHAR, B. 2018. Lenvatinib for the treatment of kidney cancer. *Expert Rev Anticancer Ther,* 18, 511-518.

STUTTFELD, E. & BALLMER-HOFER, K. 2009. Structure and function of VEGF receptors. *IUBMB Life,* 61, 915-22.

SUTO, A., YAMASAKI, M., TAKASAKI, Y., FUJITA, Y., ABE, R., SHIMIZU, H., OHTA, H. & TAKIGUCHI, M. 2013. LC-MS/MS analysis of canine lipoproteins fractionated using the ultracentrifugation-precipitation method. *J Vet Med Sci,* 75, 1471-7.

SUWAL, S., SENEVIRATHNE, C., GARRE, S. & PFLUM, M. K. H. 2012. Structural analysis of ATP analogues compatible with kinase-catalyzed labeling. *Bioconjugate chemistry,* 23, 2386-2391.

SZIGETI, M., BONDAR, J., GJERDE, D., KERESZTESSY, Z., SZEKRENYES, A. & GUTTMAN, A. 2016. Rapid N-glycan release from glycoproteins using immobilized PNGase F microcolumns. *J Chromatogr B Analyt Technol Biomed Life Sci,* 1, 139-143.

TAKAHASHI, H., HATTORI, S., IWAMATSU, A., TAKIZAWA, H. & SHIBUYA, M. 2004. A novel snake venom vascular endothelial growth factor (VEGF) predominantly induces vascular permeability through preferential signaling via VEGF receptor-1. *J Biol Chem,* 279, 46304-14.

TAKAHASHI, H. & SHIBUYA, M. 2005. The vascular endothelial growth factor (VEGF)/VEGF receptor system and its role under physiological and pathological conditions. *Clin Sci (Lond),* 109, 227-41.

TAMMELA, T. & ALITALO, K. 2010. Lymphangiogenesis: Molecular Mechanisms and Future Promise. *Cell,* 140, 460-476.

THAKKAR, S., WANG, X., KHAIDAKOV, M., DAI, Y., GOKULAN, K., MEHTA, J. L. & VARUGHESE, K. I. 2015. Structure-based Design Targeted at LOX-1, a Receptor for Oxidized Low-Density Lipoprotein. *Sci Rep,* 5, 16740-16740.

THOMPSON, A. A., LIU, J. J., CHUN, E., WACKER, D., WU, H., CHEREZOV, V. & STEVENS, R. C. 2011. GPCR stabilization using the bicelle-like architecture of mixed sterol-detergent micelles. *Methods (San Diego, Calif.),* 55, 310-317.

THOMSON, C. A., OLSON, M., JACKSON, L. M. & SCHRADER, J. W. 2012. A Simplified Method for the Efficient Refolding and Purification of Recombinant Human GM-CSF. *PLOS ONE,* 7, e49891.

TINTI, M., NARDOZZA, A. P., FERRARI, E., SACCO, F., CORALLINO, S., CASTAGNOLI, L. & CESARENI, G. 2012. The 4G10, pY20 and p-TYR-100 antibody specificity: profiling by peptide microarrays. *N Biotechnol,* 29, 571-7.

TISCHER, A., LILIE, H., RUDOLPH, R. & LANGE, C. 2010. L-arginine hydrochloride increases the solubility of folded and unfolded recombinant plasminogen activator rPA. *Protein science : a publication of the Protein Society,* 19, 1783-1795.

TOLOSA, L., MIR, M., ASENSIO, V. J., OLMOS, G. & LLADÓ, J. 2008. Vascular endothelial growth factor protects spinal cord motoneurons against glutamate-induced excitotoxicity via phosphatidylinositol 3-kinase. *Journal of Neurochemistry,* 105, 1080-1090.

TOPIOL, S. 2018. Current and Future Challenges in GPCR Drug Discovery. *Methods Mol Biol*, 7465-8_1.

TOVAR-Y-ROMO, L. B., ZEPEDA, A. & TAPIA, R. 2007. Vascular Endothelial Growth Factor Prevents Paralysis and Motoneuron Death in a Rat Model of Excitotoxic Spinal Cord Neurodegeneration. *Journal of Neuropathology & Experimental Neurology,* 66, 913-922.

TRINH, X. B., TJALMA, W. A., VERMEULEN, P. B., VAN DEN EYNDEN, G., VAN DER AUWERA, I., VAN LAERE, S. J., HELLEMAN, J., BERNS, E. M., DIRIX, L. Y. & VAN DAM, P. A. 2009. The VEGF pathway and the AKT/mTOR/p70S6K1 signalling pathway in human epithelial ovarian cancer. *Br J Cancer,* 100, 971-8.

TYN, M. T. & GUSEK, T. W. 1990. Prediction of diffusion coefficients of proteins. *Biotechnol Bioeng,* 35, 327-38.

ULLRICH, A. & SCHLESSINGER, J. 1990. Signal transduction by receptors with tyrosine kinase activity. *Cell,* 61, 203-12.

UPSTON, J. M., NIU, X., BROWN, A. J., MASHIMA, R., WANG, H., SENTHILMOHAN, R., KETTLE, A. J., DEAN, R. T. & STOCKER, R. 2002. Disease stage-dependent accumulation of lipid and protein oxidation products in human atherosclerosis. *The American journal of pathology,* 160**,** 701-710.

VAN DRIEL, I. R., BROWN, M. S. & GOLDSTEIN, J. L. 1989. Stoichiometric binding of low density lipoprotein (LDL) and monoclonal antibodies to LDL receptors in a solid phase assay. *J Biol Chem,* 264, 9533-8.

VANAKEN, T., FOXALL-VANAKEN, S., CASTLEMAN, S. & FERGUSON-MILLER, S. 1986. Alkyl glycoside detergents: synthesis and applications to the study of membrane proteins. *Methods Enzymol,* 125, 27-35.

VIALLARD, C. & LARRIVÉE, B. 2017. Tumor angiogenesis and vascular normalization: alternative therapeutic targets. *Angiogenesis,* 20, 409-426.

VINOTHKUMAR, K. R. 2015. Membrane protein structures without crystals, by single particle electron cryomicroscopy. *Curr Opin Struct Biol,* 33, 103-14.

VINOTHKUMAR, K. R. & HENDERSON, R. 2010. Structures of membrane proteins. *Quarterly Reviews of Biophysics,* 43, 65-158.

VLAMINCK, B., CALAY, D., GENIN, M., SAUVAGE, A., NINANE, N., ZOUAOUI BOUDJELTIA, K., RAES, M. & MICHIELS, C. 2014. Effects of copper sulfate-oxidized or myeloperoxidase-modified LDL on lipid loading and programmed cell death in macrophages under hypoxia. *Hypoxia (Auckland, N.Z.),* 2, 153-169.

VON HEIJNE, G. 2006. Membrane-protein topology. *Nat Rev Mol Cell Biol,* 7, 909-918.

WADA, T., HAIGH, J. J., EMA, M., HITOSHI, S., CHADDAH, R., ROSSANT, J., NAGY, A. & VAN DER KOOY, D. 2006. Vascular Endothelial Growth Factor Directly Inhibits Primitive Neural Stem Cell Survival But Promotes

Definitive Neural Stem Cell Survival. *The Journal of Neuroscience,* 26, 6803-6812.

WALKER, J. M. 1994. The bicinchoninic acid (BCA) assay for protein quantitation. *Methods Mol Biol,* 32, 5-8.

WALLER, D. G. & SAMPSON, A. P. 2018. 1 - Principles of pharmacology and mechanisms of drug action. *In:* WALLER, D. G. & SAMPSON, A. P. (eds.) *Medical Pharmacology and Therapeutics (Fifth Edition).* Elsevier.

WANDER, S. A., HENNESSY, B. T. & SLINGERLAND, J. M. 2011. Next-generation mTOR inhibitors in clinical oncology: how pathway complexity informs therapeutic strategy. *J Clin Invest,* 121, 1231-41.

WANG, H. W. & WANG, J. W. 2017. How cryo-electron microscopy and X-ray crystallography complement each other. *Protein Sci,* 26, 32-39.

WANG, S., MUNRO, R. A., SHI, L., KAWAMURA, I., OKITSU, T., WADA, A., KIM, S. Y., JUNG, K. H., BROWN, L. S. & LADIZHANSKY, V. 2013. Solid-state NMR spectroscopy structure determination of a lipid-embedded heptahelical membrane protein. *Nat Methods,* 10, 1007-12.

WARREN, C. M., ZIYAD, S., BRIOT, A., DER, A. & IRUELA-ARISPE, M. L. 2014. A ligand-independent VEGFR2 signaling pathway limits angiogenic responses in diabetes. *Science signaling,* 7, ra1-ra1.

WATTIS, J. A. D., O'MALLEY, B., BLACKBURN, H., PICKERSGILL, L., PANOVSKA, J., BYRNE, H. M. & JACKSON, K. G. 2008. Mathematical model for low density lipoprotein (LDL) endocytosis by hepatocytes. *Bulletin of mathematical biology,* 70, 2303-2333.

WEATHERS, S. P. & DE GROOT, J. 2015. VEGF Manipulation in Glioblastoma. *Oncology,* 29, 720-7.

WELLER, J. & BUDSON, A. 2018. Current understanding of Alzheimer's disease diagnosis and treatment. *F1000Research,* 7, F1000 Faculty Rev-1161.

WHITELEGGE, J. P. 2013. Integral membrane proteins and bilayer proteomics. *Anal Chem,* 85, 2558-68.

WIESMANN, C., FUH, G., CHRISTINGER, H. W., EIGENBROT, C., WELLS, J. A. & DE VOS, A. M. 1997. Crystal Structure at 1.7 Å Resolution of VEGF in Complex with Domain 2 of the Flt-1 Receptor. *Cell,* 91, 695-704.

WILLIAMS, K. J. & TABAS, I. 1995. The response-to-retention hypothesis of early atherogenesis. *Arterioscler Thromb Vasc Biol,* 15, 551-61.

WITTE, D. R., TASKINEN, M. R., PERTTUNEN-NIO, H., VAN TOL, A., LIVINGSTONE, S. & COLHOUN, H. M. 2004. Study of agreement between LDL size as measured by nuclear magnetic resonance and gradient gel electrophoresis. *J Lipid Res,* 45**,** 1069-76.

WOMACK, M. D., KENDALL, D. A. & MACDONALD, R. C. 1983. Detergent effects on enzyme activity and solubilization of lipid bilayer membranes. *Biochim Biophys Acta,* 733, 210-5.

XIAO, Z., LUO, G., LIU, C., WU, C., LIU, L., LIU, Z., NI, Q., LONG, J. & YU, X. 2014. Molecular mechanism underlying lymphatic metastasis in pancreatic cancer. *BioMed research international,* 2014, 925845-925845.

XIE, Y., MANSOURI, M., RIZK, A. & BERGER, P. 2019. Regulation of VEGFR2 trafficking and signaling by Rab GTPase-activating proteins. *Sci Rep,* 9, 13342.

XU, C. & NG, D. T. W. 2015. Glycosylation-directed quality control of protein folding. *Nature Reviews Molecular Cell Biology,* 16, 742-752.

XU, S., OGURA, S., CHEN, J., LITTLE, P. J., MOSS, J. & LIU, P. 2013. LOX-1 in atherosclerosis: biological functions and pharmacological modifiers. *Cellular and molecular life sciences : CMLS,* 70, 2859-2872.

YANG, C.-Y., GU, Z.-W., YANG, M. & GOTTO, A. M. 1994a. Primary structure of apoB-100. *Chem Phys Lipids,* 67-68, 99-104.

YANG, C., GU, Z. W., YANG, M. & GOTTO, A. M., JR. 1994b. Primary structure of apoB-100. *Chem Phys Lipids,* 68, 99-104.

YANG, H., HIGGINS, B., KOLINSKY, K., PACKMAN, K., GO, Z., IYER, R., KOLIS, S., ZHAO, S., LEE, R., GRIPPO, J. F., SCHOSTACK, K., SIMCOX, M. E., HEIMBROOK, D., BOLLAG, G. & SU, F. 2010a. RG7204 (PLX4032), a selective BRAFV600E inhibitor, displays potent antitumor activity in preclinical melanoma models. *Cancer Res,* 70, 5518-27.

YANG, S., ZHAO, J. & SUN, X. 2016. Resistance to anti-VEGF therapy in neovascular age-related macular degeneration: a comprehensive review. *Drug Des Devel Ther,* 10, 1857-67.

YANG, W.-H., XU, J., MU, J.-B. & XIE, J. 2017. Revision of the concept of anti-angiogenesis and its applications in tumor treatment. *Chronic Diseases and Translational Medicine,* 3, 33-40.

YANG, Y., XIE, P., OPATOWSKY, Y. & SCHLESSINGER, J. 2010b. Direct contacts between extracellular membrane-proximal domains are required for VEGF receptor activation and cell signaling. *Proc Natl Acad Sci U S A,* 107, 1906-11.

YATES, E. V., MÜLLER, T., RAJAH, L., DE GENST, E. J., AROSIO, P., LINSE, S., VENDRUSCOLO, M., DOBSON, C. M. & KNOWLES, T. P. J. 2015. Latent analysis of unmodified biomolecules and their complexes in solution with attomole detection sensitivity. *Nature Chemistry,* 7**,** 802-809.

YOKOYAMA, N., ISCHENKO, I., HAYMAN, M. J. & MILLER, W. T. 2005. The C Terminus of RON Tyrosine Kinase Plays an Autoinhibitory Role. *Journal of Biological Chemistry,* 280, 8893-8900.

YOSHIMOTO, R., FUJITA, Y., KAKINO, A., IWAMOTO, S., TAKAYA, T. & SAWAMURA, T. 2011. The discovery of LOX-1, its ligands and clinical significance. *Cardiovasc Drugs Ther,* 25, 379-91.

YUAN, X. M., LI, W., OLSSON, A. G. & BRUNK, U. T. 1996. Iron in human atheroma and LDL oxidation by macrophages following erythrophagocytosis. *Atherosclerosis,* 124**,** 61-73.

YU, Y., KUANG, Y.-L., LEI, D., ZHAI, X., ZHANG, M., KRAUSS, R. M. & REN, G. 2016. Polyhedral 3D structure of human plasma very low density lipoproteins by individual particle cryo-electron tomography1. *Journal of Lipid Research,* 57, 1879-1888.

ZELENSKY, A. & GREADY, J. 2006. The C-type lectin-like domain superfamily. *The FEBS journal,* 272, 6179-217.

ZENG, H., SANYAL, S. & MUKHOPADHYAY, D. 2001. Tyrosine residues 951 and 1059 of vascular endothelial growth factor receptor-2 (KDR) are essential for vascular permeability factor/vascular endothelial growth factor-induced endothelium migration and proliferation, respectively. *J Biol Chem,* 276, 32714-9.

ZHANG, L., SONG, J., CAVIGIOLIO, G., ISHIDA, B. Y., ZHANG, S., KANE, J. P., WEISGRABER, K. H., ODA, M. N., RYE, K.-A., POWNALL, H. J. & REN, G. 2011. Morphology and structure of lipoproteins revealed by an optimized negative-staining protocol of electron microscopy. *Journal of lipid research,* 52, 175-184.

ZHANG, Y., GUESSOUS, F., KOFMAN, A., SCHIFF, D. & ABOUNADER, R. 2010. XL-184, a MET, VEGFR-2 and RET kinase inhibitor for the treatment of thyroid cancer, glioblastoma multiforme and NSCLC. *IDrugs,* 13, 112-21.

ZHANG, Z. & HENZEL, W. J. 2004. Signal peptide prediction based on analysis of experimentally verified cleavage sites. *Protein Sci,* 13, 2819-24.

ZHANG, Z., LY, T. & KODADEK, T. 2001. An inhibitor of sequence-specific proteolysis that targets the substrate rather than the enzyme. *Chemistry & Biology,* 8, 391-397.

ZHENG, C., NENNESMO, I., FADEEL, B. & HENTER, J.-I. 2004. Vascular endothelial growth factor prolongs survival in a transgenic mouse model of ALS. *Annals of Neurology,* 56, 564-567.

ZHU, G., HUANG, Q., ZHENG, W., HUANG, Y., HUA, J., YANG, S., ZHUANG, J., WANG, J., CHANG, J., XU, J. & YE, J. 2016. LPS Upregulated VEGFR-3 Expression Promote Migration and Invasion in Colorectal Cancer via a Mechanism of Increased NF-kappaB Binding to the Promoter of VEGFR-3. *Cell Physiol Biochem,* 39, 1665-1678.

ZHU, X. & ZHOU, W. 2015. The Emerging Regulation of VEGFR-2 in Triple-Negative Breast Cancer. *Front Endocrinol,* 6.

ZIMMERMAN, J. J., VON SAINT ANDRÉ-VON ARNIM, A. & MCLAUGHLIN, J. 2011. Chapter 74 - Cellular Respiration. *In:* FUHRMAN, B. P. & ZIMMERMAN, J. J. (eds.) *Pediatric Critical Care (Fourth Edition).* Saint Louis: Mosby.

ZIRLIK, K. & DUYSTER, J. 2018. Anti-Angiogenics: Current Situation and Future Perspectives. *Oncology Research and Treatment,* 41, 166-171.

ZIVANOV, J., NAKANE, T., FORSBERG, B. O., KIMANIUS, D., HAGEN, W. J. H., LINDAHL, E. & SCHERES, S. H. W. 2018. New tools for automated high-resolution cryo-EM structure determination in RELION-3. *Elife,* 7, e42166.

APPENDIX

Supplementary Tables

Table B1. List of proteins identified using tryptic digestion and mass spectrometry on band B (Figure 4.9A).

Protein ID	Accession	Coverage (%)	#Peptides	PTM	Avg. Mass	Description
1	O14744|ANM5_HUMAN	61	73	Y	72684	Protein arginine N-methyltransferase 5 OS=Homo sapiens GN=PRMT5 PE=1 SV=4
173	P0DMV8|HS71A_HUMAN	28	17	Y	70052	Heat shock 70 kDa protein 1A OS=Homo sapiens GN =HSPA1A PE=1 SV=1
174	P0DMV9|HS71B_HUMAN	28	17	Y	70052	Heat shock 70 kDa protein 1B OS=Homo sapiens GN =HSPA1B PE=1 SV=1
2	P23588|IF4B_HUMAN	12	8	N	69151	Eukaryotic translation initiation factor 4B OS=Homo sapiens GN=EIF4B PE=1 SV=2
175	P11142|HSP7C_HUMAN	13	7	Y	70898	Heat shock cognate 71 kDa protein OS=Homo sapiens GN=HSPA8 PE=1 SV=1
6	Q9BQA1|MEP50_HUMAN	22	6	N	36724	Methylosome protein 50 OS=Homo sapiens GN=WDR77 PE=1 SV=1
11	P02768|ALBU_HUMAN	5	3	N	69367	Serum albumin OS=Homo sapiens GN=ALB PE=1 SV =2
Total 7 proteins						

Table B2. List of proteins identified using tryptic digestion and mass spectrometry on band C (Figure 4.9A).

Protein ID	Accession	Coverage (%)	#Peptides	PTM	Avg. Mass	Description
180	P60709|ACTB_HUMAN	10	3	N	41737	Actin, cytoplasmic 1 OS=Homo sapiens GN=ACTB PE =1 SV=1
181	P63261|ACTG_HUMAN	10	3	N	41793	Actin, cytoplasmic 2 OS=Homo sapiens GN=ACTG1 PE=1 SV=1
183	P14678|RSMB_HUMAN	6	2	N	24610	Small nuclear ribonucleoprotein-associated proteins B and B' OS=Homo sapiens GN=SNRPB PE=1 SV=2
184	P63162|RSMN_HUMAN	6	2	N	24614	Small nuclear ribonucleoprotein-associated protein N OS=Homo sapiens GN=SNRPN PE=1 SV=1
78	Q12802|AKP13_HUMAN	0	2	N	307550	A-kinase anchor protein 13 OS=Homo sapiens GN=AKAP13 PE=1 SV=2
Total 5 proteins						

APPENDIX

Supplementary Tables

Table B3. List of proteins identified using tryptic digestion and mass spectrometry on band B (Figure 4.10A).

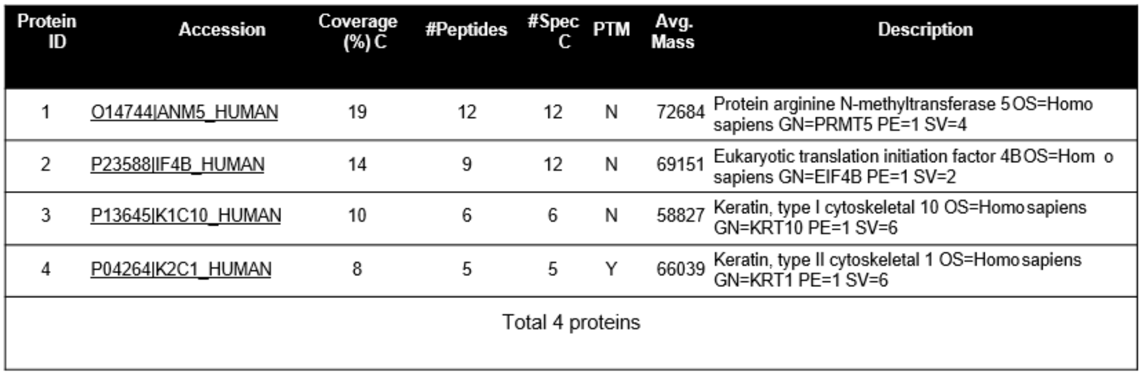

Protein ID	Accession	Coverage (%) C	#Peptides	#Spec C	PTM	Avg. Mass	Description
1	O14744|ANM5_HUMAN	19	12	12	N	72684	Protein arginine N-methyltransferase 5 OS=Homo sapiens GN=PRMT5 PE=1 SV=4
2	P23588|IF4B_HUMAN	14	9	12	N	69151	Eukaryotic translation initiation factor 4B OS=Hom o sapiens GN=EIF4B PE=1 SV=2
3	P13645|K1C10_HUMAN	10	6	6	N	58827	Keratin, type I cytoskeletal 10 OS=Homo sapiens GN=KRT10 PE=1 SV=6
4	P04264|K2C1_HUMAN	8	5	5	Y	66039	Keratin, type II cytoskeletal 1 OS=Homo sapiens GN=KRT1 PE=1 SV=6
Total 4 proteins							

Table B4. List of proteins identified using tryptic digestion and mass spectrometry on band C (Figure 4.10A).

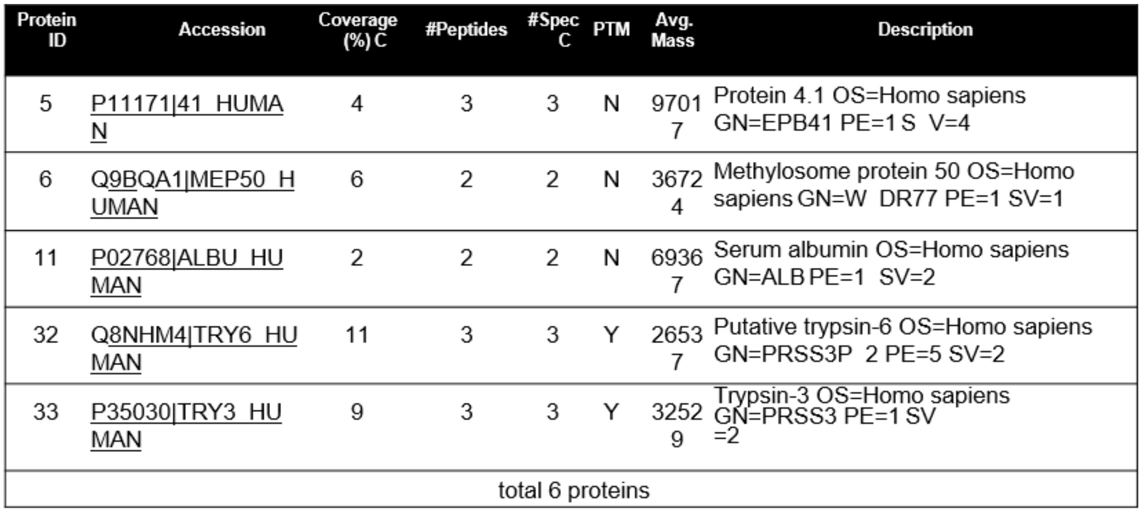

Protein ID	Accession	Coverage (%) C	#Peptides	#Spec C	PTM	Avg. Mass	Description
5	P11171|41_HUMAN	4	3	3	N	97017	Protein 4.1 OS=Homo sapiens GN=EPB41 PE=1 S V=4
6	Q9BQA1|MEP50_HUMAN	6	2	2	N	36724	Methylosome protein 50 OS=Homo sapiens GN=W DR77 PE=1 SV=1
11	P02768|ALBU_HUMAN	2	2	2	N	69367	Serum albumin OS=Homo sapiens GN=ALB PE=1 SV=2
32	Q8NHM4|TRY6_HUMAN	11	3	3	Y	26537	Putative trypsin-6 OS=Homo sapiens GN=PRSS3P 2 PE=5 SV=2
33	P35030|TRY3_HUMAN	9	3	3	Y	32529	Trypsin-3 OS=Homo sapiens GN=PRSS3 PE=1 SV =2
total 6 proteins							